UNIVERSITY OF BIRMINGHAM

UNDERSTANDING THE STABILITY AND PROPERTIES OF BULK NANOBUBBLES

by

Gianluca Ferraro

A thesis submitted to
The University of Birmingham
for the degree of
DOCTOR OF PHILOSOPHY

School of Chemical Engineering
College of Engineering and Pysical Sciences
The University of Birmingham
August 2020

"Observe what happens when sunbeams are admitted into a building and shed light on its shadowy places. You will see a multitude of tiny particles mingling in a multitude of ways… their dancing is an actual indication of underlying movements of matter that are hidden from our sight... It originates with the atoms which move of themselves. Then those small compound bodies that are least removed from the impetus of the atoms are set in motion by the impact of their invisible blows and in turn cannon against slightly larger bodies. So the movement mounts up from the atoms and gradually emerges to the level of our senses, so that those bodies are in motion that we see in sunbeams, moved by blows that remain invisible."

(Lucretius, "On the Nature of Things" c.60 BC).

Abstract

The existence of bubbles in the nanoscale is an object of debates and disputes in recent years. New types of nanoscale bubble systems have been reported, and among these, *Bulk Nanobubbles* represent a challenging problem due to their extraordinary stability experimental reported. In pure water, the pressure estimated from the Young-Laplace equation inside a nanobubble of 100 nm diameter will be close to ~30 atm, therefore, questions of their existence/ stability inevitably arise considering that the lifetime of macrobubbles (>1 mm) is on the order of minutes and that of microbubbles (1-1000 μm) is on the order of seconds, whereas bulk nanobubbles (50-300 nm) have been reported to last for days or weeks. Bulk nanobubbles have a higher curvature leading to a higher Laplace pressure, and a larger interfacial area for gas to diffuse out and should be in principle less stable. Reports stated that they are negatively charged, and speculations arise on the stability mechanism that could affect their stability against the bubble dissolution theories. Bulk nanobubbles are recent, and their research is still in its infancy; however, many applications have been reported and tested, and it appears that there is immense scope for nanobubbles to impact and perhaps revolutionise many current industrial sectors and medical processes.

Acknowledgements

First and foremost, I would like to express my sincere gratitude to Professor Mostafa Barigou, my research supervisor, for his patient guidance, encouragement, and useful critiques of this research work. It has been a privilege and immense pleasure to work with him.

I would like to thank Dr Neelkanth Nirmalkar, Dr Mandar Badve, and Dr Ananda J. Jadhav, for their assistance and valuable input throughout the course of this research. Their diligence, meticulousness and attitude to work have been a great help and a significant example. I would also like to thank Lynn Draper, Dave Boylin and all the other great people from the Chemical Engineering Department for their friendship and continuous support. Financial support was provided by the Engineering and Physical Sciences Research Council (UK) through Grant EP/L025108/1 and is gratefully acknowledged.

I would like to thank all the people that have been part of my life during this research, valuable friends and colleagues, that helped and supported me in any moment. In particular, I would like to thank Douglas, Mostapha, Gilmore, Lais, Alberto, Ioannis, Alex and Dan but also all the other international people I have had the pleasure to meet.

Throughout the last few years, I had the pleasure also to take part in amazing dinners that represented not only a way of recreation but were an opportunity to know well special people like Laura and Barbara. An incommensurable thank to Laura who has supported me in any moment in the final stage of writing.

A special thank to Daniele and Giorgia for their valuable moral support during the last year of this project and the difficult period everyone is facing due to the pandemic.

I would like to acknowledge, finally, my family for their encouragement and understanding during these years.

Table of Contents

List of Figures

List of Tables

Abbreviations

A/D	Analogic/Digital	-
BNBs	Bulk Nanobubbles	-
CDRI	Common rail direct injection	-
CFD	Computational fluid dynamics	-
DH	Disintegrating Head	-
DLS	Dynamic Light Scattering	-
DLVO	Deryagin-Landau-Verwey-Overbeck theory	-
DO	Dissolved Oxygen	-
FEH	Fine Emulsor Head	-
GC-MS	Gas Chromatography-Mass Spectroscopy	-
HSM	High Shear Mixer	-
ICP-MS	Inductively Coupled Plasma–Mass Spectroscopy	-
LDA	Laser Doppler Anemometry	-
NBs	Nanobubbles	-
NTA	Nanoparticle Tracking Analysis	-
PI	Polydispersity index	
PIV	Particle Image Velocimetry	-
PTFE	PolyTetraFluoro-Ethylene	-
SEH	Standard Emulsor Head	-
SHH	Square Hole Head	-
SNBs	Surface nanobubbles	-

TFE	PolyTetraFluoro-Ethylene	-
UFBs	Ultrafine bubbles	-
VSH	Vertical Slotted Head	-

Notations

A	Amplitude	-
B	Baseline at infinite time	-
γ	Surface tension	N/m
c	Constant	-
C	Gas solubility	M
c_∞	Concentration of co-ions in the bulk	$1/m^3$
c_i	Concentration	mol/L
$\Delta\rho$	Difference in density	kg/m^3
δ	Measurement error	-
ΔH	Heat of solution	Joule (J)
d	Point in space	-
D	Translational diffusion coefficient	m^2/s
D_H	Hydrodynamic diameter	m
$D_{r,o}$	Outer rotor diameter	m
ε	Absolute permettivity	F/m
ε_0	Vacuum permittivity	F/m
ε_r	Relative permittivity	-

e	Elementary charge	C
E_0	Amplitude electric field	W/m^2
E_i	Electric field	N/C
F	Force	Newton (N)
G	Autocorrelation function	-
g	Gravity	$m \cdot s^{-2}$
H	Hamaker constant	J
h	Surface separation between particles	m
θ	Detection angle	degrees
i	Type of ion	-
I	Intensity	W/m^2
Is	Ionic strength	mol/L
κ^{-1}	Inverse Debye length	nm
k_B	Boltzmann constant	$1.380648 \times 10\text{-}23 m^2 \cdot kg \cdot s^{-2}$ K^{-1}
K_H	Henry's law constant	M/atm
$\hat{k}$	Unit vector	-
k_i	Wave vector of the incident light	-
λ_0	Laser wavelength	nm
μ	Viscosity	cP
$\tilde{n}$	Dispersant refractive index	-
n	Number of moles	mole
N	Rotor speed	rev/min
N_A	Avogadro's number	$6.02214076 \times 10^{23}$ mol^{-1}

n_i	Polarization perpendicular to the scattering plane	$C \cdot m^2$
ζ	Zeta potential	mV
ρ	Density	kg/m3
P	Pressure	N/m^2
P_1	Original pressure	N/m^2
P_2	New pressure	N/m^2
P_{atm}	Atmospheric pressure	atm
P_e	Electrostatic pressure	$C^2 \cdot N^{-1} \cdot m^{-2}$
P_{int}	Internal pressure	atm
P_L	Laplace pressure	$N \cdot m^{-1}$
q	Scattering vector	-
Q	Electrostatic charge	C
Q_0	Electrostatic charge	C
R	Ideal gas constant	8.314 J/mol·K
r	radius	m
Re	Reynolds number	-
ri	Spherical area radius	m
σ	Surface charge density	$C \cdot m^{-2}$
S	Surface area	m^2
T	Temperature	-
t	Time	s
τ	Delay time	s
U_e	Electrophoretic mobility	μm·cm / V·s
Ut	Buoyancy	N

v	Velocity	m/s
V	Volume	m^3
V_0	Initial volume of air	m^3
V_1	Original volume	m^3
V_2	New volume	m^3
V_{out}	Output Voltage	Volt (V)
V_S	Input Voltage	Volt (V)
W_{dl}	Double layer interactions	-
W_{vdW}	Van der Waals forces	L/mol
z_i	Valence of the ion	Q/q
ϕ_e	Helmholtz energy	J
x	Mole fraction of gaseous constituent in solution	Moles/Total moles
$\bar{x}$	Mole fraction of the gas in the vapour above the solution	Moles/Total moles
ψ_0	Surface potential	-
ω_i	Angular frequency	rad/sec

Chapter I

Introduction

In recent years, three new types of nanoscale bubble systems have been reported: (i) spherical cap-shaped bubbles that form at solid-liquid interfaces called Surface Nanobubbles (NBs), with typical heights and widths of 10-20 nm and 50-100 nm; (ii) micropancakes which as well as surface nanobubbles need a solid interface to form, and are characterised from a quasi-2D gaseous domain with several microns in diameter and only 1-2 nm in height; and (iii) spherical nano bubbles reported exist in the bulk liquid and called Bulk Nanobubbles (BNBs), with a typical diameter of 100-200 nm (Seddon et al., 2010, Craig, 2011, Seddon et al., 2012).

The nanoscale bubble systems are attracting particular interest as the observed stability of NBs is inconsistent with current bubble dissolution theories, which stated that bubbles less than 1µm should dissolve very quickly in a timescale of microseconds (Epstein and Plesset, 1950, Ljunggren and Eriksson, 1997), whereas NBs has been reported to last for days and weeks (Alheshibri et al., 2016). Because of established bubble theories, early reports on stable surface nanobubbles were in the first instance not well accepted, creating scepticisms and opening debates; however as researchers were challenged and involved with this particular bubble behaviour, reports start to grow very fast, proofs of SNBs existence and stability were presented and deeply discussed as well as different models to explain their long-term stability. Nowadays, surface nanobubbles are widely accepted, in contrast with bulk nanobubbles, where their existence and stability is still causing controversy and debates (Häbich et al., 2010, Alheshibri

and Craig, 2019b, Hernandez et al., 2019). A widely accepted model for the bulk nanobubbles stability is still missing and, the origin of the scepticism of their existence could be individuated in two different aspects: (i) the controversy between the reported measurements and the life-time theories (Epstein and Plesset, 1950, Ljunggren and Eriksson, 1997), and (ii) the lack of techniques and methods designed to make a distinction between solid and gas-filled nano-entities, especially between nanoparticles, nanodroplets, hydrophobic mesoscale particles, and bulk nanobubbles.

The characterisation of bulk nanobubbles is often problematic because of their gaseous domain and size range. Countable are reports that have tried to use electron microscopies, such as Scanning Electron Microscopy (SEM) or Transmission Electron Microscopy (TEM), in studies involving bulk nanobubbles (Ohgaki et al., 2010, Li et al., 2016, Jadhav and Barigou, 2020a). However, due to the problematic characterisation and sample preparation of bulk nanobubbles with these techniques, that often brings to artefacts and modification of the bubble shell, techniques based on the light scattering are instead preferred. Such non-invasive techniques including Dynamic Light Scattering (DLS) and Nanoparticle Tracking Analysis (NTA) are often used to report information of bulk nanobubbles in term of bubble size distribution, mean bubble diameter, zeta potential and bubble number density.

Bulk nanobubbles are reported in being negatively charged with a zeta potential value of ~ -30 mV (Attard, 2013, Yasui, 2016, Nirmalkar et al., 2018a, Wang et al., 2019, Boshenyatov et al., 2019, Zhang et al., 2020a). There are three main aspects associated with the long-term stability generally linked with bulk nanobubbles, that are: (i) the predominance of the Brownian motion on their negligible buoyancy force, which prevents them from rising to the free surface (Hernandez et al., 2019); (ii) their interfacial stability that prevents them from the dissolution

(Zhang et al., 2020a); and (iii) their colloidal stability that prevents them from mechanisms such as coalescence or Ostwald ripening (Nirmalkar et al., 2018a).

Recently, bulk nanobubbles have attracted a lot of attention due to their physicochemical properties such as their gaseous domain, the high volume to surface ratio, the incredible and mysterious stability against the classic dissolution theories, their typical size range, and their negative charge. All of those properties make them promising for a vast range of applications across many fields of science and engineering, because they may provide innovative and beneficial solutions to industrial challenges where a low environmental impact is a must. Also, such properties make them a perfect allied for eco-friendly and bio-applications including the promotion of the physiological activity of living organisms (Ebina et al., 2013), the enhanced germination rate of seeds (Liu et al., 2013, Liu et al., 2016), surface cleaning (Zhu et al., 2016, Ghadimkhani et al., 2016), and for biomedical applications (Kawara et al., 2014, Wang et al., 2010, Misra et al., 2015, Meng et al., 2016, Peyman et al., 2016, Tian et al., 2015, Rapoport et al., 2007, Fan et al., 2015). Other applications have been suggested and tested in froth flotation (Etchepare et al., 2017a, Calgaroto et al., 2016, Calgaroto et al., 2014, Fan et al., 2010c) and to improve the engine efficacy using hydrogen nanobubbles (Oh et al., 2015, Oh et al., 2013).

To fully exploit these potential benefits, however, a better understanding of their formation, characterisation and long term-stability is needed, also because, especially when considering the gas nanobubbles in the bulk liquid, the question about their stability and consequently their existence inevitably arises and still represents a challenging problem.

1.1 Objectives

The objectives of this study are:

- *Generation and characterisation of nanobubbles suspensions.* Methods for generating and characterising nanobubble suspensions have not been standardized yet and are a matter of investigation. Different innovative methods for the bulk nanobubble generation will be delineated with the aim to prove the existence and the formation of bulk nanobubbles in pure water. The Malvern Nanosight model *NS300* and the dynamic light scattering (DLS) model *Zetasizer Nano ZSP* will be used principally as characterisation instruments to study bubbles in term of bubble number density, bubble size distribution, bubble mean diameter and zeta potential.

- *Stability of bulk nanobubbles*. Coalescence, bubble breakup and Ostwald ripening are the major destabilisation mechanisms of bubbles. Due to the unusual and exceptional bulk nanobubbles stability, suspensions will be analysed at different temperatures through a series of experiments to shed light on the behaviour of bulk nanobubbles, in particular how their diameter will change as a function of temperature and time.

- *Effects of gas properties.* The generation of bulk nanobubbles under different gas will be explored. Early reports reported the generation of bulk nanobubbles only in air-saturated water; thus, an investigation of the effects of different gases it is needed. The effects of inert gases will be explored and discussed. Experiments under controlled conditions of temperature will help to understand the influence of the gas

solubility on the bulk nanobubble formation. Furthermore, experiments will also be performed in degassed water to prove the indispensability of gas for their generation and thus, their existence.

- *Effects on the formation and stability of bulk nanobubbles, through an investigation of the liquid properties.* Suspensions will be analysed by altering the water pH, in different salt solutions, and at different temperatures to explore the bubble behaviours in extreme conditions. The aim of those experiments will identify the optimum conditions for the bubble generation and stability, shedding light on the stability mechanism that governs their longevity, inhibiting the coalescence or any other mechanisms of destabilisation. Additionally, nanobubble suspensions will also be monitored over time to understand how and in which particular conditions the process of destabilisation occurs.

1.2 Thesis layout

The present thesis has been organized as follows. After the present introduction section, a new-fashioned review of the existing literature of nanobubbles observed in the bulk liquid will be presented in Chapter II. The review will explore and discuss the bulk nanobubble generation methods, stabilisation mechanisms, and the potential future applications that have been suggested or tested over the last years.

Chapter III will describe the characterisation instruments adopted in the present work, individuating the advantages and shortcomings of each technique. Preliminary studies on bulk

nanobubble generation will be analysed and thoroughly discussed showing the easy-way and possibilities to generate nanoparticles during the ordinary operations, and will explain the reason why this work is focussed on generating bulk nanobubbles in pure water.

Chapter IV will introduce a bubble generation method based on the hydrodynamic cavitation, a technique commonly used in many other industrial processes but not yet reported to produce bulk nanobubbles. This generation system will create the basis of this work to consider that bulk nanobubbles do exist and exhibit exceptional stability in pure water.

Chapter V will introduce an entirely new bubble generation system, based on Henry's law, to confirm the existence of bulk nanobubbles generated in pure water through irrefutable proofs that the gas is indispensable for the bubble formation. The system was ideated with the purpose to try to simplify the bubble generation process and to reduce as much as possible the risk of introduction and creation of external impurities, which represents the main problem to study and analyse bulk nanobubbles. The automatization of the proposed generation system will be presented and discussed.

Chapter VI will focus on the experimental investigation of the mechanism that governs the stability of bulk nanobubbles. In this chapter, bulk nanobubble properties will be explored, and screening effects of the bulk nanobubble shell will be investigated, showing that in some particular conditions, mechanisms such as the bubble coalescence are possible. Findings will not only represent proofs of the existence of bulk nanobubbles but will also shed light on the primary mechanism that should affect their mysterious longevity.

The last chapter, Chapter VII, will present a general discussion of the findings reported in this work and provide suggestions for future works.

1.3 Publication arising from the thesis

Ferraro G., Jadhav A.J., and Barigou M. (2020), A Henry's law method for generating bulk nanobubbles, *Nanoscale, 2020, 12, 15869-15879*

1.4 International talks and conferences attended

Nirmalkar N., **Ferraro G.**, and Barigou M. (2017), "Microfluidic generation of bulk nanobubbles and their colloidal stability", *UK Colloids 2017*, Manchester, United Kingdom, July 10 – 12.

Ferraro G., Barigou M. (2017), "Bulk Nanobubbles: Their Existence and Longevity", *NanoInnovation 2017*, Italy, Rome, September 26-29.

Ferraro G., Barigou M. (2018), "Understanding the Properties of Bulk Nanobubble Suspensions", *CHEMENGDAYUK 2018*, Leeds, United Kingdom, March 27-28.

Ferraro G., Barigou M. (2018), "Mechanical Generation of Bulk Nanobubbles", *12th International Conference on Advances in Fluid Mechanics 2018*, Ljubljana, Slovenia, July 10-12.

Ferraro G., Barigou M. (2019), "Interfacial and Colloidal Stability of Bulk Nanobubbles", *International Conference on Nanobubbles, Nanodroplets, and their Applications*, *Nanobubble 2018*, Suzhou, China, October 16-19.

Ferraro G., Jadhav A.J., Barigou M. (2020), "A Henry's law method for generating bulk nanobubbles", *NanoInnovation 2020*, Italy, Rome, September 16-18.

Chapter II

Literature Review

2.1 Introduction

Nanobubbles are a novel class of nanomaterials characterised by a filled gaseous domain which were observed first on the surface (Surface Nanobubbles and Micropancakes) and then in the bulk liquid (Bulk Nanobubbles). While the bubbles observed on the surface were extensively studied on different surfaces and their stability widely explained and accepted, the formation and stability of the bubbles observed in the nanoscale within the bulk liquid are still object of discussion. Bulk Nanobubbles are intrinsically interesting since, in pure water, the pressure estimated from the Young-Laplace equation inside a nanobubble of 100 nm diameter will be close to ~30 atm, therefore, from diffusion theories, the bubble should dissolve on a timescale of microseconds, however, their stability was observed to last for days and months. This mysterious stability poses many challenges to our understanding of bubble physics and behaviour. This extraordinary stability attracts the attention of many researcher and industry and a wide range of industrial applications being suggested or tested, attracting much interest due to the peculiar properties of these suspensions. A review of the leading generation methods, bulk nanobubble observations and models of stability is here reported, and to conclude this chapter, a brief review of the potential bulk nanobubble applications is discussed.

2.2 Bulk nanobubble generation and characterisation

Nanobubbles (NBs) are a class of nanomaterials characterised by a gaseous filled domain. Their history is relatively recent, and the works, particularly in the early stage from their first observation, are scattered in the literature. The general tendency is to associate the name nanobubbles to all the nano-entities which are gaseous filled and with the size < 1µm. However, this class of materials has been observed both on the surface and in the bulk liquid. The first observations of NBs were probably reported in the late 1990s and were first directly imaged by Atomic Force Microscopy (AFM) in 2000 (Ishida et al., 2000, Lou et al., 2000). In the last two decades, NBs have become a hot topic due to their peculiar characteristic to show exceptional stability (days or months) against the classical dissolution theories (Epstein and Plesset, 1950, Ljunggren and Eriksson, 1997) which show that the lifetime of NBs should be of the order of microseconds. Three different classes of NBs have been identified; two observed on solid surfaces, *Surface Nanobubbles* (SNBs) and *Micropancakes*, and one within the bulk liquid named *Bulk Nanobubbles* (BNBs) (Zhang et al., 2007, Zhang et al., 2008, Zhang et al., 2009, Seddon et al., 2010, Seddon and Lohse, 2011, Seddon et al., 2011, Craig, 2011, Seddon et al., 2012, Alheshibri et al., 2016). While the existence and stability of the NBs observed on the surfaces has been accepted by the scientific community due to the broad studies of the last two decades, NBs in bulk are still object of debate, and questions arise about their existence as well as their long-term stability.

Bulk nanobubbles are also called *Ultrafine Bubbles* (UFBs) and are a fascinating bubble system which challenges conventional understanding and theories of bubble physics. The debate of their existence mostly arises due to the lack of instruments and techniques able to make a distinction between a solid nanoparticle and a bulk nanobubble. In fact, characterisation

instruments mainly used to detect and analyse the suspensions of bulk nanobubbles are non-invasive techniques based on the light scattering method such as *Dynamic Light Scattering* (DLS) and *Nanoparticle Tracking Analysis* (NTA), that will be deepened during this work, and are not able to provide information on the chemical composition of the entity observed. Beside, the physical chemistry of the interfacial stability of a single bubble and the colloidal stability between two or more bubbles in suspension is attracting considerable interest, mostly in recent years. BNBs usually are reported in size between 50-300 nm when generated in pure water.

Recently, the Malvern Panalytical Ltd. has released a highly innovative instrument called Archimedes that provides information previously unavailable to bulk nanobubbles. This instrument, illustrated in **Figure 2.1**, could make a distinction between solid nanoparticles and bulk nanobubbles in liquid suspension. The instrument is based on resonant mass measurement, where the suspension passes through a MEMS (Micro-Electro-Mechanical-Systems) resonator altering its position. By the shift of the resonator, there is a variation of the resonance frequency and it is possible to have an accurate measurement of the buoyant mass of entities which passed through it, as depicted in **Figure 2.1b-c** (Burg et al., 2007, Fujita;, 2014, Panalytical, Hernandez et al., 2019). Finding based on that measurements were reported by (Kobayashi et al., 2014), who used various methods to measure the particle size and number density of ultrafine bubbles. They generated the UFBs in the range between 100–200 nm, and they used a resonant mass measurement method to make a distinction between ultrafine nanobubbles and other particles. They compared the results obtained by this technique with the results obtained utilizing the NTA method (particle size distribution), and they concluded that results obtained by the two instruments showed a moderate correlation.

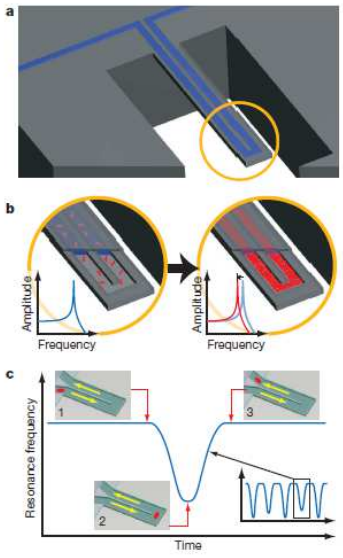

Figure 2.1. Schematic picture of Archimedes microcantilever. The figure was taken from (Burg et al., 2007).

(Alheshibri and Craig, 2018, Alheshibri and Craig, 2019a) reported papers in which they studied bulk nanobubble suspensions through Archimedes and excising high external pressure on those suspensions, showing that suspensions generated by a commercial instrument were not nanobubbles, thus, creating doubts on the real nature of the entities usually reported as BNBs in literature. On the other hand, they analysed nanobubbles of octafluoropropane (C_3F_6) armoured by a lipid shell (insoluble surfactant), schematically reported in**Figure 2.2**. In the last case reported, they concluded that the entities observed were nanobubbles due to their response to the application of external pressure.

Bulk nanobubbles is a growing topic, and different are the approaches and the methods to generate them. An upgraded review of the main methods, generally reported in the literature, is here presented. Among the various generation techniques it is possible to find electrolysis

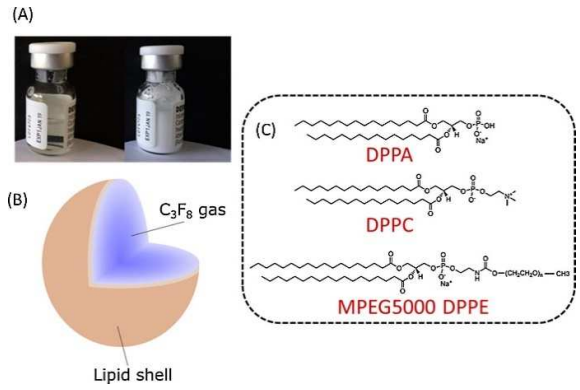

Figure 2.2. Figure A) shows the ultrasound contrast agent used, B) shows the nanobubbles generated by the activation of the contrast agent formed by octafluoropropane gas protected by a shell consisting of three lipids reported in C). Images were taken from (Alheshibri and Craig, 2019a).

(Kikuchi et al., 2009, Kikuchi et al., 2007, Kikuchi et al., 2006a, Chen et al., 2015a, Chen et al., 2015b, Chen et al., 2014), acoustic cavitation (Yasuda et al., 2019, Nirmalkar et al., 2019, Nirmalkar et al., 2018b), hydrodynamic cavitation (Etchepare et al., 2017a, Etchepare et al., 2017b, Azevedo et al., 2016, Ushikubo et al., 2010, N. et al., 2015, Maeda S., 2011), fluidic oscillation (Zimmerman et al., 2011), vibration (Fang et al., 2020), nano-membrane filtration (Ahmed et al., 2018), water-solvent mixing (Nirmalkar et al., 2018b, Qiu et al., 2017, Millare and Basilia, 2018), laser (Lombard et al., 2017, Teirlinck et al., 2018, Lukianova-Hleb et al., 2014), periodic pressure changes (Wang et al., 2019), compression and decompression of gas (Ferraro et al., 2020, Ke et al., 2019, Jin et al., 2020, Jin et al., 2019), and chemical reactions (Li et al., 2016).

2.2.1 BNBs generated mechanically

Among the first evidence that bulk nanobubbles do indeed contain gas, a notable work was presented by (Ohgaki et al., 2010). In this study, the authors using gas injection reported the generation of small bubbles of nitrogen (N_2), argon (Ar) and methane (CH_4) in water. The

bubbles resulted in having an average radius of 50 nm and were observed by the rapid freezing of a droplet that was used to form a replica of the surface and then analysed by the scanning electron microscopy (SEM). Images are reported in **Figure 2.3b**. The method used for the generation of BNBs produced a large bubble number density under atmospheric conditions; they estimated the density of nanobubbles generated to be around ~ 10^{13} bubbles/mL. A schematic diagram of the experimental apparatus used for the generation of nanobubble is reported in **Figure 2.3a**. The generated nanobubbles were reported to have high stability and persist up to 2 weeks.

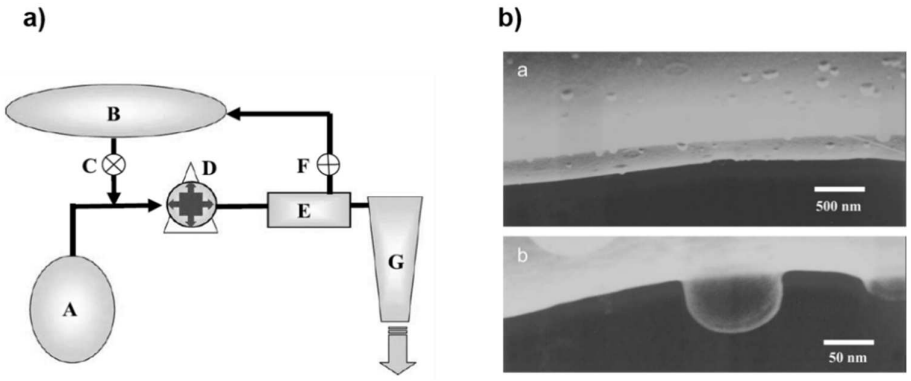

Figure 2.3. Figure a) shows a schematic of the experimental apparatus used to generate a high density of nanobubbles, where the capital letters A, B, C, D, E, F, and G represent the water tank, the reservoir, the gas flow regulator, the pump, the gas-liquid separator, the release valve and the decompression chamber respectively. Figure b) shows a scanning electron micrograph of nitrogen nanobubbles in aqueous solution. The image is taken from (Ohgaki et al., 2010).

The successful use of the Nanoparticle Tracking Analysis (NTA) to measure the bulk nanobubbles concentration and size distribution, was declared for the first time in 2010. The bulk nanobubbles analysed were produced by GALF (GAs Liquid Foam) bubble generation system, in which the authors showed the existence of ultrafine bubbles in the range between ~100-200 nm in diameter (Kobayashi et al., 2014). (Maeda S. et al., 2011) developed a new technology from the experimental apparatus GALF to produce a high bubble number density,

and this ultrafine bubble generator system was called (ultrafine-GALF). This instrument has been reported to produce a high concentration of nanobubbles (1×10^9 bubbles/mL). Schematic difference between GALF and ultrafine-GALF are shown in **Figure 2.4**.

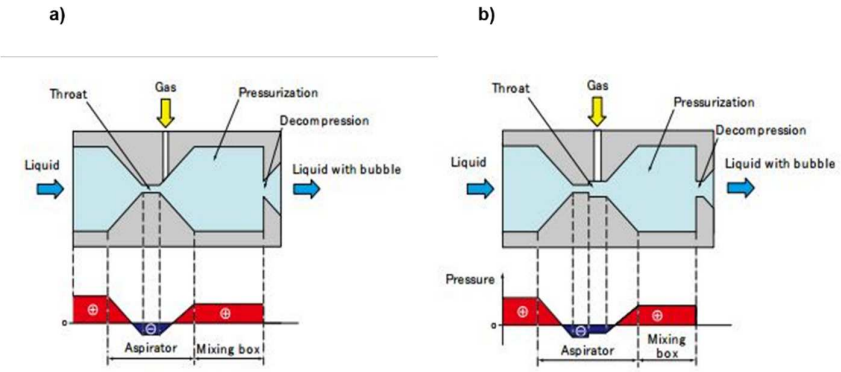

Figure 2.4. Figure a) shows a schematic diagram of GALF bubble generator, whilst b) shows the ultrafine-GALF system. Illustrations were taken from (Maeda S. et al., 2011).

(Calgaroto et al., 2014) reported the generation of stable bulk nanobubbles after rapid depressurization of air-saturated water solutions at a high flow velocity, in which the size of the nanobubbles was strongly dependent on the zeta potential value. They used a needle valve (2 mm internal diameter) into an empty glass column. As characterisation methods they used a Kruss 8451 tensiometer to measure the water/air surface tension and a Zetasizer Nano ZS to measure the size and the zeta potential of the NBs. They found that the suspension of bubbles generated in different pH water solutions had a zeta potential varying from ~ +26 mV at pH 2 to ~ –59 mV at pH 10 and they attributed the increasing value of the zeta-potential to the adsorption of negative OH^- at the gas-water interface. The bubble size was decreasing by an increase of the pH value, finding also confirmed most recently by different groups (Ferraro et al., 2020, Zhang et al., 2020b).

(Calgaroto et al., 2014) stated that the adsorption of OH^-, which caused the formation of an electric double layer, is believed to have an essential role in the stability of bulk nanobubbles inhibiting their coalescence and providing high repulsive force between bubbles. They also advanced the hypothesis, according to many other authors, that H^+ ions are more likely hydrated and thus have the tendency to stay in the bulk solution, whereas smaller less hydrated and more polarised anions would adsorb onto the surface of the bubble (Kim et al., 2000, Takahashi, 2005).

(Calgaroto et al., 2014) tried to explain the coalescence inhibition in electrolytic-aqueous solutions; however, they discarded the Deryagin-Landau-Verwey-Overbeck (DLVO) theory, which is a theory of colloidal dispersion stability (**section 2.2.2**), because it was not able to explain the experimentally observed ion-specific forces acting between the bubbles and also reported by (Marčelja, 2006, Lima et al., 2008). In contrast to this statement, (Nirmalkar et al., 2018a), who generate bulk nanobubble suspensions by hydrodynamic cavitation through a high-pressure Y-type microfluidic cell (**Figure 2.5**), reported the use of DLVO theory based on the experimental observations to explain the colloidal stability of bulk nanobubbles generated in pure water where the pH of the solution was modified after the bulk nanobubble generation.

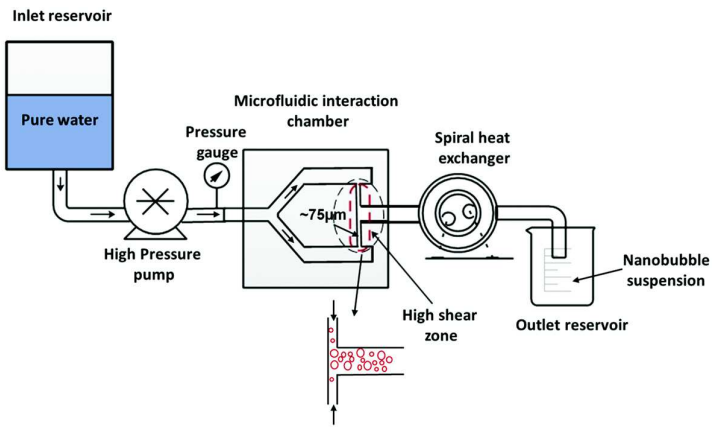

Figure 2.5. Illustration of the microfluidic cell used for the generation of bulk nanobubbles. The schematic was

taken from (Nirmalkar et al., 2018a).

(Etchepare et al., 2017b) investigated the generation of bulk nanobubbles in a semi-continuous system, where bubbles were generated with a centrifugal multiphase pump. They reported a concentration of bulk nanobubbles of 4×10^9 nanobubbles/mL, generated at 5 bar and 49 $mN\cdot m^{-1}$ surface tension. The authors observed that nanobubbles were resistant to shearing caused by pump impellers and high operating pressure, showing a not change in size. However, this paper, based only on deep cleaning of the setup before the generation, assumed that the observed nano-entities were exclusively NBs, without giving particular attention on the possible formation of oil droplets or any other contaminant detached from the apparatus used that may have been generated during the operations. Note that this study was focused on presenting a high rate bubble generation system for future applications in flotation.

Some studies have demonstrated the potential use of bulk nanobubbles in the separation of amine and sulfate precipitates by dissolved air flotation (Calgaroto et al., 2016, Amaral Filho et al., 2016). (Zhang et al., 2020b) reported an experimental study on the size distribution and zeta potential of bulk nanobubbles generated by hydrodynamic cavitation. In this recent study, they investigated the effects of pH solutions, airflow, air pressure, surfactants, and liquid flow rate on the size of bulk nanobubble suspensions. Findings reported showed that the size of NBs decreased with increasing pH value and surfactant concentration. They also concluded that at higher air-flowrates, a more significant number of gas nuclei for the formation of bulk nanobubbles were present.

2.2.2 BNBs generated from acoustic cavitation

Bulk nanobubbles have also been observed from acoustic cavitation. (Nirmalkar et al., 2018b) reported the stability of nanobubbles over periods of many months during which the

NBs size remained unchanged and thus, they suggest the absence of bubble coalescence, Ostwald ripening and bubble breakage effects. The concentration reported approaches ~10^9 bubbles/mL. In this study, they introduced an innovative method for the investigation on the entities generated, which consisted of the freezing and thawing the BNB suspensions at -18 °C. Findings revealed that the population of bulk nanobubbles analysed after thawing disappeared, suggesting that the observed entities were NBs. In this paper, they provide multiple evidence on the existence of bulk nanobubbles.

(Yasuda et al., 2019) reported the use of ultrasonic irradiation in pure water to form bulk nanobubbles. They reported that the bubble number density increased with increasing ultrasonic power and decreasing frequency. In this study, they also reported the use of ultrasound on bulk nanobubble suspensions generated by the pressurized-dissolution method. They observed that NBs were reduced, and the concentration decreased with increasing the power and frequency of the machine, thus, reporting another evidence of the existence of BNBs.

2.2.3 BNBs generated by the solvent-exchange method

Among the various generation techniques, an important role is covered by the solvent-exchange method, in fact, mixtures of water and organic compounds have been reported to produce a large number of NBs. Several studies have proven first the existence of SNBs in hydrophobic substrates with the solvent-exchange method (Lou et al., 2002, Lou et al., 2001). Most recently, that method has been reported to generate not only surface nanobubbles but also nanoscale “entities” in the bulk liquid. There are still disputes around the entities observed in the bulk liquid when a solvent is mixed with water.

(Qiu et al., 2017) by using the nanoparticle tracking analysis, reported the formation and

stability of bulk nanobubbles generated with the ethanol-water exchange. In their thorough study of the generation of bulk nanobubbles, (Qiu et al., 2017) showed a comparison of BNBs generation in degassed and not degassed ethanol-water exchange solution, suggesting that observed nanoscale entities were supposed to be gas-filled. Another interesting analysis was the influence of the temperature during the generation, where BNBs were first increasing in concentration and then slightly decrease after 4h. They conclude that it was hard to generate BNBs with a high concentration of ethanol and the maximum concentration were reported for ethanol/water ratio of 1:20, corresponding to 20% v/v ethanol.

Other authors have reported studies on the ethanol-water exchange aimed to investigate the properties and the behaviour of BNBs with the addition of salt and sugar solutions. They found that the effect of sugar addition (Glucose and Sucrose) on BNBs generation increases the bubble number density significantly, reducing the bubble size, and increasing the ζ-potential (Millare and Basilia, 2018). They explained the increase in ζ-potential due to the hydrophobic backbone structure of sugar molecules, that can promote the stabilisation of the gaseous phase. The salts addition (NaCl and Na_2SO_3), on the contrary, resulted in decreasing the bubble number density, increasing the mean bubble diameter, and reducing the ζ-potential value. They explained these findings through the interaction between salts and amphiphiles, H_2O and other species in liquid, by stating that the anion of salts (Cl^- and SO_3^{2-}) interact with the polar H-group of ethanol molecules, that create a shall that stabilize or encapsulate the gaseous domain. On the other hand, the Na^+ ions interact with the H_2O molecules and OH^- ions providing a lower ζ-potential. (Nirmalkar et al., 2019) investigated the stability of bulk nanobubbles generated from acoustically cavitated aqueous organic solvent mixtures. In their influential examinations, (Nirmalkar et al., 2019) concluded that nanobubbles generated in water-organic solvent enjoy long-term stability (> 3months). Even in this case, the BNB generation was influenced by the

solvent concentration, and they attributed that to the water gas oversaturation. The authors compared the stability of bulk nanobubbles generated in pure water with suspensions generated in the organic solvent. (Nirmalkar et al., 2019) stated that the adsorption of hydroxyl ions on the bubble interface governed the stability of BNBs in pure water, which are present in water because of self-ionization, a concept not valid in the case of pure organic solvent because they do not autoionize. Their conclusion, based on the experimental observations, was that in the case of organic solvent solutions, bulk nanobubbles were stabilized by a strong hydrogen bonding formed due to the preferential adsorption of the organic solvent molecules on the bubble interface as schematically reported in **Figure 2.6**.

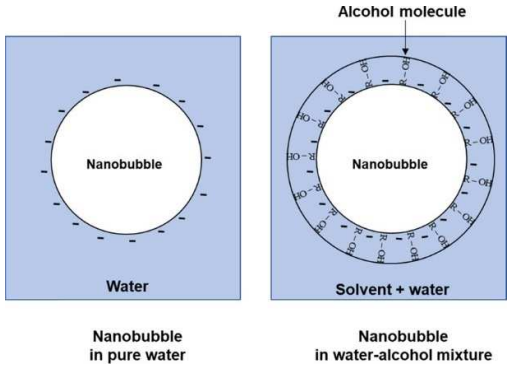

Figure 2.6. Schematic illustration of a protective shell formed around nanobubbles in water-organic solutions (Nirmalkar et al., 2019).

The above mentioned Nirmalkar's paper might have been more persuasive if he adopted spectroscopies to detect the presence of any titanium nanoparticles possibly eroded during the generation of bulk nanobubbles from the titanium probe. It is well known that acoustic cavitation is a high energy consumption technique; thus the erosion of the titanium surface during the generation could be possible, mostly in the nanoscale. This work has been subjected to heavy criticism by (Rak et al., 2019) who reported evidence of the generation of nanoparticles

created by the disintegration of the surface of the metal ultrasonic probe. Besides, they disproved the generation of nanobubbles also by mixing organic solutes to water, associating the entities formed and observed during the mixing at nanoparticles or nanodroplets originating from the mesoscale solubilization of hydrophobic compounds, which they stated being present as molecularity dissolved impurities in the solute. Thus, in both the separate cases of ultrasonication and solvent mixing, they associated the observed nano-entities using NTA method to nanoparticles and not bulk nanobubbles. Their conclusions, which presenting a drawback of studies on bulk nanobubbles, would have been much more convincing if in their experiments they had adopted the same parameters and protocols of the other authors. In fact, they used ultrasonication for 60 minutes compared to the only 180 seconds of the Nirmalkar's paper, and such a considerable time of generation leads indeed to the erosion of the probe.

To support the not existence of bulk nanobubbles by mean of mixing of ethanol and water (Alheshibri and Craig, 2019b) published a work in which they reported findings based on the density of the entities observed. They use a resonant mass measurement, a method that measures the buoyancy of particles dispersed in liquid suspension. They found that the maximum population was obtained at 20% v/v ethanol with a mean diameter of ~100nm. They concluded that the observed nano-entities were nanoparticles and not nanobubbles through two observations. The first based on the results of the resonant mass measurements, in which all the particles resulted to have a positive buoyance with a mean density of 0.91±0.01 g/cm^3 (which resulted much higher compared to the expected density for gas bubbles), and the second observation arise from the application of high external pressures (10 ±0.1 atmospheres) that did not significantly changed the mean bubble diameter of the suspension as expected. These studies would have been more relevant if it had also included studies on the screening effects of suspended entities observed in order to to detect any variation of their size.

A much more systematic approach has been published by (Jadhav and Barigou, 2020b, Jadhav and Barigou, 2020a) that trough various physical and chemical analytical techniques tried to provide conclusive proof that entities generated by ultrasonication and organic solvent mixing should be gas-filled and not nanoparticles, and thus proofs on the existence of bulk nanobubbles.

Very recently, (Chen et al., 2020), individuated and reported that during the ethanol-water mixing, three different stages happen. The authors monitored the process of the ethanol-water mixing by a light scattering equipment. Findings allowed them to conclude that the observed nano-entities must be gas-filled. The three stages that occurred during the mixing were summarized as follow. In the first moment, when the mixing begins, the scattered light drastically increases and then tends to be constant as the replacement time increases, suggesting the formation of nanobubbles or particles within the suspension. Finally, with the increase of the exchange time, the particle size decreases and tend to be constant to ~100nm. Since the particle size reduced, they assumed that the entities observed were gas-filled. These findings should help to close the debate of the generation of bulk nanobubbles with the ethanol-water mixing.

2.2.4 BNBs generate by electrolysis

Electrolysis has been reported to produce hydrogen and oxygen nanobubbles in the bulk liquid. (Kikuchi et al., 2007, Kikuchi et al., 2006b, Kikuchi et al., 2001b, Kikuchi et al., 2001a, Kikuchi et al., 2009, Kikuchi et al., 2006c) in this series of works reported the generation of bulk nanobubbles during water electrolysis. They observed that electrolysis using a low-roughness platinum surface gave a high concentration of dissolved hydrogen within the

electrolyzed solution; however, they also reported that the concentration of nanobubbles observed was a function of the type of the electrolyte used. The authors also investigated the behaviour of hydrogen nanobubbles near the cathode and in the bulk solution. Using different dissolved oxygen measurements methods, and characterizing the bubble generated in electrolyzed water effluent from anodic electrolysis, they reported the existence of oxygen nanobubbles. Those series of studies investigated different aqueous solutions and studied both the bubbles effluent from the anode and the cathode during the electrolysis of water, therefore provided a piece of evidence about the existence and generation of bulk nanobubbles through the decomposition of water into oxygen and hydrogen gas. (Takenouchi, 2010) reported the presence of hydrogen nanobubbles in alkaline electrolyzed water using dynamic light scattering and monitored their behaviour over time. The bubbles observed were stable for more than 24h. The authors speculated that the Ostwald ripening phenomena was observed since after one week from the generation few nanobubbles smaller than 300 nm were detected. Such expositions are unsatisfactory because the concentration of bulk nanobubbles generated was not reported and all the DLS entities observed were associated exclusively to hydrogen nanobubbles. It should be pointed out, however, that during the electrolysis of water, pitting[1] could occur leading to the generation of contaminations; thus characterisation based on only light scattering techniques might be not adequate for this kind of bubble generation methods (Ovarfort, 1988, Palit et al., 1993).

2.2.5 BNBs generated by chemical reactions

Processes based on chemical reactions could lead to the formation of bulk nanobubbles. (Li

[1] *Pitting* is a form of extremely localized corrosion that creates small holes in the metal.

et al., 2016) reported the generation of nitrogen bulk nanobubbles by chemical reaction directly above the TEM grid coated with carbon film. The chemical reaction used to generate bulk nanobubbles is reported below.

$$NaNO_2 + NH_4Cl \xrightarrow{H^+} NaCl + 2H_2O + N_2 \Rightarrow N_2(g)$$

They used 3µl of solution A, 10% Sodium nitrite ($NaNO_2$), which was applied to the TEM grid, and successive 3µl of solution B, 10% Ammonium chloride (NH_4Cl) plus 0.037-7.4% Hydrochloric acid (HCl), added to the same TEM grid. Using a light microscope, they did take a picture 1 minute after the mixing and then analysed it by Cryo-TEM. They observed that changing the concentration of HCl was possible to observe fewer or more nitrogen nanobubbles.

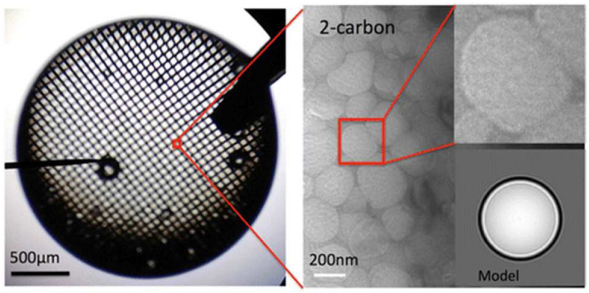

Figure 2.7. Bubbles observed by light microscope on the right, and Cryo-TEM images on the left. Images were taken by (Li et al., 2016).

Each method has its advantages and shortcomings. For example, electrochemical and chemical reaction methods are limited to specific gases; for instance, electrolysis of water can only produce hydrogen and oxygen nanobubbles. On the other hand, hydrodynamic cavitation, ultrasound cavitation and membrane filtration are more general and can be utilized with a wide

range of gases. These methods, however, if used in an uncontrolled fashion, are prone to contamination, they have a low resistance to corrosive chemicals, which restricts the use of reactive gases and solutions, and they tend to be energy-intensive. Therefore, to serve industries in many fields, such as medical or even food industries, the BNBs generation methods needs to produce the minimal amount of contaminations as possible, thus the search for nanobubbles needs to be improved in order to be cost-effective and amenable to scale-up and process control.

2.3 Bulk nanobubbles stability

Due to the lack of instruments to make a distinction between bulk nanobubbles and nanoparticles, the existence of bulk nanobubbles has been the object of dispute among the community research, since, with light scattering techniques such as DLS or NTA, floating nano-contaminations included liquid droplets or nanoparticles, can be easily mistaken as BNBs (Alheshibri and Craig, 2019b, Jin et al., 2007, Rak et al., 2019). What more important, is also a lack of a physicall accepted model able to explain their extraordinary stability (from hours to months) evinced in experimental observations (Ushikubo et al., 2010). However, it appears that such stability may be related to the existence of a negative charge on bulk nanobubbles interface (Nirmalkar et al., 2018a, Jin et al., 2019) and thus, it is correlated to the well-known phenomenon of ion enrichment at air-liquid interfaces. The ζ-potential value observed for a negative charge bubble generated in pure water usually depends on several parameters such as the method of bubble generation, the water pH, and has also been associated by the type of gas used (Wang et al., 2019, Nirmalkar et al., 2018a, Jin et al., 2019). If from one side, the stable negative ζ-potential value, experimentally reported, and thus, the negative charge surrounding

the nanobubbles does lead to the repulsion between bubbles preventing them from coalescence and/or Ostwald ripening mechanisms (Meegoda et al., 2018, Ushikubo et al., 2010, Nirmalkar et al., 2018a), on the other side, there are still disputes on which is the main mechanism behind the stabilisation of a single charged bubble and how it can be stable in the presence of high Laplace pressure. Classical physics suggests that BNBs should have a Laplace pressure about 30 bar inside a nanobubble of 50 nm radius, in which the Young-Laplace equation, for the mechanically stable gas bubble immersed in a fluid medium with constant external pressure, can be written as follows:

$$P_{int} = P_{out} + \frac{2\gamma}{r} \quad \textbf{(2.1)}$$

where P_{int}, P_{out}, γ and r are, respectively, the gas pressure in the bubble, the external pressure applied to the fluid, the surface tension, and the bubble radius. Even if the Young-Laplace equation is usually applied when the surface tension can be treated macroscopically and in the case in which the thickness of the interface is smaller than the radius of the bubbles (Goldman, 2009), it has been demonstrated recently, the validity of the Young-Laplace equation in the nanoscale (German et al., 2016, Liu and Cao, 2016). Such a bubble should immediately dissolve into the surrounding liquid due to the difference between the internal (~30 bar) and external (~ 1bar) pressure.

(Epstein and Plesset, 1950) studied the dissolution of free bubbles. In their pionerring study, they showed that a gas bubble immersed in a liquid-gas solution grow or shrink by diffusion according as the solution is oversaturated or undersaturated. They also reported the effect of the surface tension on the bubbles's growth, stating that the surface tension generates a higher

pressure inside the bubble, and consequently a higher gas concentration in the bubble (predicted by the equation of state for the gas), that drives the outward diffusion of gas in the liquid. Therefore, according to the standard theory of bubble dissolution formulated by Epstein and Plesset, which predicts that tiny bubbles should dissolve and vanish on a timescale of microseconds (Epstein and Plesset, 1950), theory also confirmed with a different mathematical approach from (Ljunggren and Eriksson, 1997), the time for a complete dissolution of a bubble with a diameter ≤ 200 nm should be ≤ 80μs (Tuziuti et al., 2018, Yasui, 2018).

Different are the models that were trying to explain the longevity of bulk nanobubbles, and nowadays, an accepted model is still missed. The primary model behind the stability of bulk nanobubbles often advocated by researchers is named *Ion-stabilized model,* also called *Electrostatic repulsion model*, which is further discussed below. Other models often reported in the literature are based on a thin layer that covers or partially covers the bubble preventing its dissolution. Among these models, it is important to cite the *Skin model,* the *"Armored" bubble model* and the *Dynamic equilibrium model*. The former, which has been used as a model for cavitation nuclei for more than 60 years, is based on a thin layer of a surfactant or organic material that covered the surface of the bubble; this "skin" which is formed around gas bubble prevents the diffusion of gas from the inlet to the outlet of the bubble and hence prevents loss of gas (Yasui, 2016, Yount, 1979, Fox and Herzfeld, 1954, Yount et al., 1984). The second model is based on a combination of surfactants and nanoparticles that form a layer around the gas bubble. (Mohamedi et al., 2012) experimentally investigated the lifetime of microbubbles, where the longevity of microbubbles coated from a thin layer of gold nanoparticles and surfactant was compared with the longevity of microbubbles covered only with a surfactant. From this study, they evinced that the bubble covered with a surfactant were lasting for 24h

compared to the others able to be stable for 30 days. The latter, thus the *Dynamic equilibrium model,* is reported and studied in many papers (Yasui et al., 2016, Yasui et al., 2018, Yasui et al., 2015), and consider the gas forming the bulk nanobubble partly covered with hydrophobic material in water. The dynamic equilibrium model of a bulk nanobubble considers a depletion layer formed on the surface of a hydrophobic material, e.g. fats or oils, with a layer thickness of 0.2-5nm by which the gas dissolved in water is trapped (Lu et al., 2012, Peng et al., 2013a, Peng et al., 2013b, Yasui et al., 2016). In this depletion layer, the density of liquid water decreases by 44-94% compared to the density of the liquid in ambient condition (Yasui et al., 2018). This model describes the diffusion of gas into a bubble near the peripherical edge of the hydrophobic material that partially covers it, hence, the balance between the gas influx and the gas outflux from the other part of the uncovered bubble surface. A schematic of the model is reported in **Figure 2.8**.

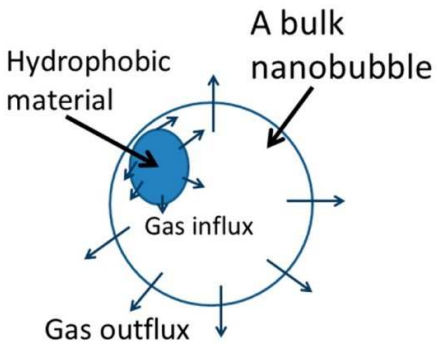

Figure 2.8. Schematic of the dynamic equilibrium model (Yasui et al., 2016).

2.3.1 Ion-stabilized model

The *Ion-stabilized model* is advocated from a significant part of the researchers in this field (Bunkin and Bunkin, 1992, Bunkin et al., 2012, Oh and Kim, 2017, Nirmalkar et al., 2018a,

Nirmalkar et al., 2018b, Jadhav and Barigou, 2020b, Ferraro et al., 2020), and very recently, using various sets of experimental data from the literature, other authors have tested the *Ion-stabilized model* (Zhang et al., 2020a). The *Ion-stabilized model* widely investigated and developed by (Bunkin and Bunkin, 1992, Bunkin and Bunkin, 2003, Bunkin et al., 2014), expressed the mechanical stability of a bubble, considering it immersed in a liquid in normal conditions and saturated by dissolved gas (e.g. atmospheric air), as:

$$P_{int} + P_e = P_{atm} + \frac{2\gamma}{r} \quad \textbf{(2.2)}$$

where P_{int}, P_{atm}, P_e, γ and r are, respectively, the gas pressure in the bubble, the external pressure applied to the fluid, the ponderomotive pressure, the surface tension, and the bubble radius. P_e represents the pressure caused by the presence of the charge, Q_0, at the spherical interface of the bubble, and is given by:

$$P_e = -\left(\frac{\partial \Phi_e}{\partial V}\right)_T \quad \textbf{(2.3)}$$

where Φ_e is the Helmholtz energy of the system, and thus, in the case of a charged bubble, it represents the energy of the electrostatic field of the system. Since the bubble was considered to be with the spherical shape of radius *r* surrounded by a spherical area of radius r_i, *with* $r_i \geq r$, the Helmholtz energy and the volume were reported to be:

$$\Phi_e = \frac{1}{2}\varepsilon \int_R^r \left[\frac{Q^2(x)}{x^2}\right] dx \quad \textbf{(2.4)}$$

$$V = \frac{4\pi}{3}\varepsilon({r_i}^3 - r^3) \quad \textbf{(2.5)}$$

where ε is the absolute permettivity, and Q the charge. Therefore, the pressure applied to the surrounding liquid (i.e. $r_i = r$) was reported to be:

$$P_e(r) = -\frac{1}{4\pi r^2}\frac{\partial \Phi_e}{\partial r} = \frac{1}{8\pi\varepsilon}\frac{Q^2}{r^4} = \frac{1}{8\pi\varepsilon}\frac{Q_0^2}{r^4} \quad \textbf{(2.6)}$$

thus, the pressure P_e, expands the bubble, and hence, it can counterbalance the squeezing surface tension force at a certain radius of the bubble. Equation **(2.6)** also implies the following equation:

$$P(r_i) = -\frac{1}{4\pi {r_i}^2}\frac{\partial \Phi_e}{\partial r_i} = \frac{1}{8\pi\varepsilon}\frac{Q^2}{{r_i}^4} \quad \textbf{(2.7)}$$

where $P(r_i)$ is the pressure applied to the outer surface of the spherical region of radius r_i, and consequently, $P(r_i)$ decreases with growing r_i. (Bunkin et al., 2012) in their studies used for their model and experiments selective adsorption of ions of the same sign on the bubble interface.

Very recently, using various sets of experimental data from the literature, other authors have tested the above ion-stabilized bubble model (Zhang et al., 2020a). In this study, based on theoretical analysis, they reported a stability mechanism for nanobubbles charged with negative ions. What stands out from this theoretical analysis is that a local minimum of system free energy raised from an additional electric field energy, caused by a surface enrichment of

charges and strong adsorption of hydroxides, that in turn is formed by the strong affinity of the negative charges envinced for bubble interfaces. The authors stated that this excess surface charges create a size-dependent coulomb force that has a key role to counterbalance the Laplace pressure. They also stated that when BNBs lose their equilibrium state, i.e. if it is thermodynamically perturbed, the excess surface charge acts to restore the force to balance the Laplace pressure and thus, preventing nanobubbles from shrinking and growing as schematically illustrated in **Figure 2.9**.

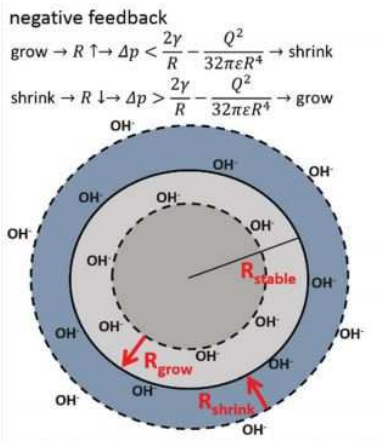

Figure 2.9. Schematic illustration of the restoring force (negative feedback mechanism) for stabilizing a bulk nanobubble with the constant adsorption of hydroxide ions onto the bubble interface.

(Zhang et al., 2020a) compared their theoretical prediction, hence, the negative feedback mechanism, with recent experimental data from different researcher groups, and they found a good agreement. However, not all the experimental data fit in their theoretical prediction, thus they arrive to the conclusion that it must exist other mechanisms for nanobubble stability.

2.3.2 DLVO theory

The Deryagin-Landau-Verwey-Overbeck (DLVO) theory was established in the 1940s, and it describes the case in which the electrostatic forces are present in combination with the van der Waals forces (Verwey et al., 1948, Derjaguin, 1993, Derjaguin and Landau, 1993). The theory was initially formulated for two identical interfaces (homoaggregation) and then extended to two different interfaces (heteroaggregation), thus in the case of nanobubbles, it can be applied to the interaction between two bubbles. It can be written as following (Trefalt et al., 2016):

$$W(h) = W_{vdW}(h) + W_{dl}(h) \quad \textbf{(2.8)}$$

where h is the surface separation between the two colloidal particles, whilst $W_{vdW}(h)$ and $W_{dl}(h)$ are the two contributions related to the van der Waals and the double layer interactions. The van der Waals forces resulting from interactions of the rotating and fluctuating dipoles of atoms and molecules can be expressed as:

$$W_{vdW}(h) = -\frac{H}{12\pi h^2} \quad \textbf{(2.9)}$$

where H define its strength and is named Hamaker constant, that usually is positive and meaning that the van der Waals force is attractive. Typical values of H are 10^{-21} – 10^{-19} J. The double-layer interactions, on the other hand, is given by:

$$W_{dl}(h) = \frac{2\sigma_+\sigma_-}{\varepsilon_0 \varepsilon} exp(-\kappa h) \quad \textbf{(2.10)}$$

where σ_+, σ_-, ε_0, ε and κ are the surface charge densities per unit area of the two surfaces, the permittivity of vacuum, the dielectric constant of water and the inverse Debye length respectively, which the latter is defined as:

$$\kappa^{-1} = \left(\frac{k_B T \varepsilon \varepsilon_0}{2e^2 N_A I_s}\right)^{1/2} = \frac{0.3\ nm}{\sqrt{I_s}} \quad \textbf{(2.11)}$$

where e, N_A, I_s, T *and* k_B are the elementary charge, the Avogadro's number, the ionic strength, the absolute temperature in kelvins, and the Boltzmann constant respectively. The ionic strength of the solution is given by:

$$I_s = \frac{1}{2}\sum_i z_i^2 c_i \quad \textbf{(2.12)}$$

where z_i is the valence of the ion of type *i*, c_i is its concentration expressed in mol/L and i runs over all types of ions in solution.

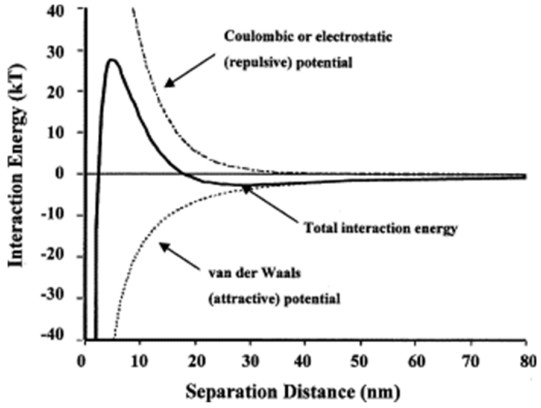

Figure 2.10. Illustration of DLVO theory. The image was taken from (Adair et al., 2001).

2.4 Bulk nanobubbles applications

While research in this area is still in its infancy, already a wide range of potential BNBs applications have been suggested or have indeed been industrially implemented including water treatment (Agarwal et al., 2011), the enhanced germination rate of seeds (Liu et al., 2013, Liu et al., 2016), promotion of the physiological activity of living organisms (Ebina et al., 2013), sterilization of bacteria (Kawara et al., 2014), therapeutic drug delivery (Wang et al., 2010, Misra et al., 2015, Meng et al., 2016), ultrasound contrast agent (Rapoport et al., 2007, Tian et al., 2015, Fan et al., 2015, Peyman et al., 2016) and the use in diagnostics and gene therapy (Zhou et al., 2012). Other applications suggested seeing them used for surface cleaning (Ushida et al., 2012c, Ghadimkhani et al., 2016, Zhu et al., 2016), for drag reduction (Ushida et al., 2012a), froth flotation (Fan et al., 2010a, Fan et al., 2010b, Fan et al., 2010c, Fan et al., 2010d, Calgaroto et al., 2014, Calgaroto et al., 2016, Etchepare et al., 2017a) and for example to improve the engine efficacy using hydrogen nanobubbles (Oh et al., 2013, Oh et al., 2015).
A review of some possible bulk nanobubbles applications already presented is reported below.

Authors generally emphasize the implementation of bulk nanobubbles in the already existing technologies, especially if they could help to reduce the impact of those technologies on the physical environment. That can be, for example, the case of fuels, since recently an improvement in fuel efficiency is required due to the environment aggravation problems. Recently, nanobubbles have become subjects of research for the reduction of fuel consumption and poisonous exhaust gases. (Nakatake et al., 2013) performed several tests on the use of air-filled nanobubbles on common-rail diesel engine and they found that by mixing the air-nanobubbles into the gas oil had improved the efficiency, but also reduced the fuel consumption. In this work, they confirmed that air-nanobubbles had advanced activated

combustion by physical and chemical action. (Oh et al., 2013) introduced a new hydrogen nanobubble gasoline blend, which resulted in improvements of the engine power, the fuel consumption and had a better impact on the reduction of the brake-specific fuel consumption. (Gobinath et al., 2019) investigated the effect of air-nanobubbles on the combustion and emission characteristics of mustard oil biodiesel in common rail direct injection (CDRI) engine. They found that the mixing of nanobubbles to mustard oil biodiesel had better emission characteristics compare to the conventional petroleum diesel and resulted in a reduction of 25% in brake-specific fuel consumption and 16% in CO emission. Similar improvements behaviour were also reported by (Liang, 2019). All in all, bulk nanobubbles both hydrogen or air-filled seems to increase the engine efficiency, reducing the poisonous exhaust gases, thus, these studies making those tiny bubbles a great ally of the environment for future applications where the emission and the aggravation issue of the environment is a must.

Other fields in which nanobubbles could become of valuable importance are the field of water treatment and surface cleaning. (Wu et al., 2008) demonstrated that nanobubbles could be used for cleaning a solid surface and particularly to remove the proteins that are already absorbed to a surface, which is an exciting aspect to prevent the absorption of nonspecific protein. In previous works, they found that nanobubbles can inhibit protein absorption on a different type of surfaces (Wu et al., 2006, Wu et al., 2007). They demonstrated that electrochemical treatment could be applied to clean a surface by the production of nanobubbles, and that is possible using nanobubbles for minimizing the fouling of a surface (Wu et al., 2008). Chen (2009) has patented a bathing pool to prevent germs. This invention consists in the use of nano-scale ozone bubbles for a rehabilitation bath, particularly to prevent germs from infecting people in a bathing pool but also to provide potable water without germs (Chen, 2009). (Ushida et al., 2012c) compared the effects on washing rate of cloth in an alternating flow by

using both bulk nanobubbles and microbubbles mixing with surfactants. They found that the NB water achieved a washing rate higher than the microbubble water, which has the same rate of the ion-exchanged water. Thus, they conclude that nanobubbles enhanced the washing effect. (Zhu et al., 2016) reported that NBs produced by electrolysis could be used as cleaning agents and for preventing surface contamination. They used protein bovine serum albumin (BSA) and lysozyme as model contaminants. They reported the use of spectroscopic ellipsometry[2] to measure the material in aqueous solutions after the adsorption of contaminants onto the hydrophilic silicon wafer surface, and they used the NTA method for measuring the size and the concentration of nanobubbles produced. Findings demonstrated that nanobubbles in the size range between 20 – 450 nm effectively remove the lysozyme molecule absorbed. They also investigated whether the nanobubbles produced can prevent the deposition of material on the surface. The authors observed that nanobubble have a key role in preventing the adsorption of BSA to the surface.

Bulk nanobubbles could have a significant impact also on the food industry since many studies have been reported they positive effects on the seeds germination or as an excellent solution to remove micro-organism from fresh vegetable, reducing, thus, the number of chemicals instead used for the same purpose. In the work published by (Yoshida et al., 1996) was demonstrated that cucumber plants grew better if the dissolved oxygen concentration was higher, thus leading to think the benefit that oxygen bulk nanobubbles could bring in this field. (Park and Kurata, 2009) demonstrated that gas-filled microbubble affects the growth of leaf lettuce and speculate that microbubbles have negative electronic charges on the surface that can attract positively charged ions present in the nutrient solution, thus, for this reason as well as

[2] *Spectroscopic ellipsometry* is a non-destructive and non-invasive optical technique based on the change in the polarization state of light.

the larger surface area, they affect the growth of plants. Most recently, (Ebina et al., 2013) studied whether oxygen nanobubbles could affect the growth of plants, mammals, and fishes. They generated nanobubbles through a nanobubble aerator in which fine microbubbles were generated with a brief sonication first and then using a gas-liquid mixing system. They reported that those nanobubbles promoted the growth of the leaves of Brassica campestris and thus, the growth of plants. In the same paper, the authors reported that the total weight of sweetfish increased in air-nanobubbles water as well as the total weight and length of mice promoted by free oral intake of oxygen-nanobubble. The use of micro-bubbles resulted in better cultivation of oysters (*Heterocapsa circularisquama*) in term of size and taste (Ohnari, 2001); thus, the use of BNBs could have similar effects. (Ushida et al., 2017) investigated the effect of UFBs on the washing rate of fresh vegetables in an alternating flow. This research aimed to show the potential benefit of using ultrafine bubbles in food industry instead of the chemicals generally used to wash fresh vegetable to remove micro-organisms. (Ushida et al., 2017) reported that all the results under no mechanical action were almost the same, so no particular benefit was found to use ultrafine bubbles, however, they found a definite improvement in the washing rate when UFBs were used under alternating flow. A similar application of BNBs in the same field was reported early by (Enomoto Naoyuki et al., 2015).

(Ushida et al., 2012b, Ushida et al., 2015) also suggested the use of BNBs on the drag reduction. Also, in that case, their use would have a positive impact on the environment. Usually, surfactants and polymers are used in drag reduction, but they are limited because of environmental concerns. The authors observed the drag reduction by using mixed nanobubbles water and glycerol, and they attributed it to interface phenomena, where the nanobubbles adhered to the surface of the wall creating a wall slip due to the probable formation of a gas phase. They compared the experimental results with numerical results and found that they were

consistent each other.

Bulk nanobubbles have shown significant advantages also in the biomedical field. Different were the areas in which they were applied. (Cavalli et al., 2012) reported the characterisation of chitosan nanobubbles for ultrasound-mediated gene delivery. They showed that the nanobubble ability to transfect DNA in vitro was triggered by 30 seconds of ultrasound treatment. In the absence of ultrasound stimuli, nanobubbles did not show this capacity. They reported that chitosan nanobubbles could be considered a new tool in the future development of the ultrasound-responsive technique for targeting DNA delivery.

(Perera et al., 2014) investigated the use of lipid-shelled Pluronic nanobubbles, and they examined them in term of size distribution, ζ-potential, biodistribution, accumulation in tumour, and treatment efficiency. Finding revealed that tumours treated with ultrasound-modulated nanobubbles showed a significant reduction in growth compared to the treatment without nanobubbles.

(Cai et al., 2015) reported the high potential of nanobubbles for ultrasonic targeted imaging and treatment in tumours. However, they stated that one of the main future challenges is to generate a uniform size distribution of BNBs. Also (Zhang et al., 2019) reported the use of nanobubbles as ultrasound contrast agents for diagnosis and as drug/gene carriers for therapy. The nanobubbles used were generated by the thin-film hydration method under centrifugation conditions and presented a low toxicity level. Findings revealed that nanobubbles *in vivo* experiments improved the video intensity signal compared to microbubbles.

Thus, it appears that there is immense scope for nanobubbles to impact and perhaps revolutionise many current industrial sectors and medical processes.

2.5 Conclusions and outlook

This chapter aimed to provide a new-fashioned review on bulk nanobubbles, and since it is a growing topic, early reports are scattered in the literature, and the new ones are published continuously on different research fields, making difficult the inclusion of all the works. Thus, some interesting new or past works may not have been included. However, a general review has been reported, including the main generation methods, the controversy about their existence and the possible stability mechanisms that could explain BNB mysterious longevity. A wide range of significant future applications has also been reviewed. Nevertheless, due to the different nature of bulk nanobubbles that could be generated with different methods, additional literature review, drawbacks of experimental techniques, and discussion to each specific study are presented in the introduction of each chapter that will follow.

Chapter III

Bulk Nanobubbles: Characterisation and Generation Methods

3.1 Introduction

Bulk nanobubbles can be considered a new class of nanomaterials since their existence is claimed in liquid suspensions, have a gaseous domain, and their dimension is generally reported in the range between 50-250 nm. Those peculiarities make this class of materials challenging to detect and analyse. Light microscopes cannot be used in this size range because the lateral resolution of the optical microscope is fundamentally limited (200 nm) due to the finite wavelength of light (Abbe limit)(Abbe, 1873). On the other hand, electron microscopies (EMs), which use electrons instead of photons to form images, could be used to observe entities in the researched range. However, the particular sample preparation required with EMs, often changing the morphological structure of the bubbles, making measurements quite complicated. Few are the reports which have tried to use EMs to observe bulk nanobubbles in different studies (Ohgaki et al., 2010, Li et al., 2016, Jadhav and Barigou, 2020a).

Nevertheless, there are a few techniques able to characterise bulk nanobubble suspensions and often used to collect information on the bubble size and bubble number density including *Dynamic Light Scattering* (DLS) and *Nanoparticle Tracking Analysis* (NTA). Those techniques are based on the light scattering principle and present some limitations, in fact, both

solid and gas-filled nano-entities, when light is shined through their suspensions, scatter light causing the effect of a visible light beam called Tyndall Effect. Thus, make a distinction between solid nanoparticles and bulk nanobubbles is not possible with light scattering based techniques. That is the most significant limitation of characterisation instruments based on light scattering often used to analyse bulk nanobubbles, and probably this limitation had originated the scepticism about their existence.

DLS and NTA provide information about the bubble number density, bubble size distribution, mean bubble diameter, and ζ-potential. These pieces of information are extrapolated by theirmotion and through the scattered signal coming from the bulk nanobubbles suspensions when a laser beam is lighted through the suspension. Both the techniques were used to characterise bulk nanobubble suspensions and are described below.

In this Chapter first preliminary studies on the generation and characterisation of bulk nanobubbles suspension will be presented and discussed.

3.1.1 Dynamic Light Scattering

Dynamic Light Scattering (DLS) also known as *Photon Correlation Spectroscopy* (PCS) studies the diffusion behaviour of particles in liquid solution. Historically known as *quasi-elastic light scattering* (QELS) because, when a colloid in liquid suspension, which moves following the Brownian motion, is illuminated by a laser beam, photons are scattered, and the

process is quasi-elastic, thus, QELS measurements providing information on the dynamics of the scatterer and hence originated the name of the acronym DLS (Arzenšek et al., 2010).

Nowadays, DLS is a widely used in R&D industry, such as biopharmaceutical industries, since, information about size, surface charge, shape or morphologies of particles are essential for developing and troubleshooting formulation of new products (Nam et al., 2002, Akagi et al., 2007). DLS is one of the most popular non-invasive light scattering techniques in physics that can be used to determine the size distribution of micro or nano-particles within the range of ~0.1 nm to ~10 μm; it also provides other relevant physics information such as the ζ-potential, and the polydisperse index of suspensions (Goldburg, 1999).

Commercial "particle-sizing" systems mostly operate at fixed detection angle (usually 90°) using a laser light source He-Ne (633) such as *Malvern Zetasizer Nano ZS90*, or they can use a Non-Invasive Backscatter optics (NIBS) with typical detection angle at 173° or 13° such as *Malvern Zetasizer Nano ZSP*, that has significantly better performance than systems using only 90°. Recently, Malvern Panalytical Ltd. released a new Multi-Angle Dynamic Light Scattering (MADLS), named *Zetasizer Ultra*, that provides a higher resolution view into the sample size distribution. Other instruments that provide information about the size and zeta potential are also available and generally based on the Field-flow fractionation (FFF) principle and Multi-Angle scattering detection, such as *Postnova EAF2000* or *Postnova AF2000*.

In this study, a Malvern Zetasizer Nano ZSP was used to characterise bubble suspensions in term of size distribution and zeta-potential.

3.1.1.1 Dynamic Light Scattering Theory

A typical setup for the scattering experiment consists of different components such as a monochromatic beam of laser light, which has the purpose to shine the suspension, generally shaped by apertures or more in general optics (i.e. lenses), and a detector or multi detectors placed at fixed angle θ to measure the intensity $I(\theta,t)$ of the scattered light. The intersection between the incident and the scattered beams defines the scattering volume *V,* called also *illuminated volume* as depicted in **Figure 3.1**.

Ideally, in a light-scattering experiment, the incident light is a plane electromagnetic wave:

$$\boldsymbol{E_i}(\boldsymbol{d}, t) = \boldsymbol{n_i} E_0 exp[\boldsymbol{i}(\boldsymbol{k_i} \cdot d - \omega_i t)] \tag{3.1}$$

where $E_i(d$,t) is the electric field at the point in space d at time t**,** n_i is the polarization perpendicular to the scattering plane, E_0 is the amplitude, k_i is the wave vector of the incident light that is $\boldsymbol{k_i} = \left(\frac{\omega_i}{c}\right)\widehat{\boldsymbol{k}}_{\boldsymbol{i}}$ with $\widehat{\boldsymbol{k}}_{\boldsymbol{i}}$ is a unit vector defining the direction of the propagation of the incident wave and ω_i represents its angular frequency (Berne and Pecora, 2000).

The particles or molecules in the illuminated region are constantly moving with motion governed by translations, rotations and vibrations by virtue of thermal interactions, and therefore, when those entities are illuminated, they scatter light. Due to the random motion of the suspended entities, the intensity of the signal received at the detector will fluctuate in time, thus, significant structural and dynamical information is obtained from the scattered field.

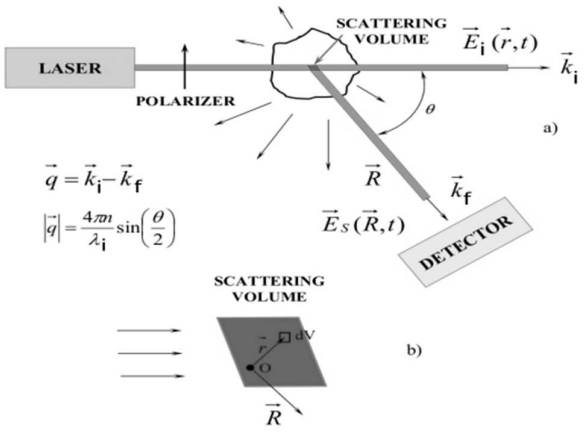

Figure 3.1 Schematic of a Dynamic Light Scattering setup; a) shows the typical light scattering setup, whilst b) shows the position of the scattering volume (Kozina, 2009).

Therefore, the intensity I(t) scattered to a point in the far-field will fluctuate randomly in time. Information of the particles can be extrapolated from their motion, in fact, a more rapid change in the intensity fluctuation signal, meaning that particles move fastest, and the rate of this motion is an information of the particles' size. Large particles cause the intensity to fluctuate more slowly than the small one (Kaszuba et al., 2008). A typical intensity fluctuation is illustrated in **Figure 3.2**.

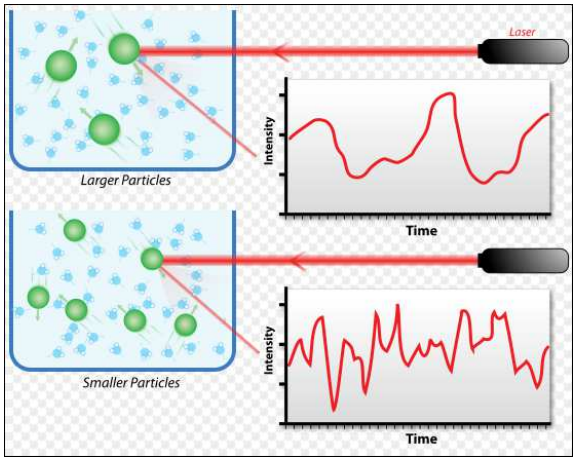

Figure 3.2. The schematic picture shows the typical intensity fluctuation according to the particles size. The image was taken from (Malvern Ltd. illustration).

The time-dependent fluctuations in the intensity of the scattered light are further analysed by using an autocorrelator, which determines the autocorrelation function of the signal, G, that is defined as:

$$G = \langle I(t_0)I(\tau)\rangle = \int_0^\infty I(t)I(t+\tau)dt \quad \textbf{(3.2)}$$

where the signal I(t) is compared with a delay version of itself $I(t+\tau)$, t is the time, and τ is the delay time.

The autocorrelation function can be modelled as:

$$G = B + Ae^{-2q^2D\tau} \quad \textbf{(3.3)}$$

where B is the baseline at infinite time, A is the amplitude, D is the translational diffusion coefficient, τ is the correlator delay time, and q the Bragg wave vector, which is proportional to the solvent refractive index n, and defined as $q = \frac{4\pi\tilde{n}}{\lambda_0} sin(\frac{\theta}{2})$, with $\tilde{n}$ the dispersant refractive index, λ_0 the laser wavelength and θ the detection angle (Kaszuba et al., 2008). The modelled correlation function permits to calculate the diffusion coefficient, D, to solve the Stokes-Einstein equation and thus, the hydrodynamic diameter of the suspended particle is given by:

$$D_H = \frac{k_B T}{3\pi\mu D} \quad \textbf{(3.4)}$$

where D_H is the hydrodynamic diameter, k_B is the Boltzmann constant, T is the absolute temperature in kelvins and μ is the dispersant viscosity. However, it should be noted that this

technique as well as the NTA, does not provide any information about the shape of the entities observed.

3.1.1.2 Zeta potential

The Zeta potential is a scientific term used for electrokinetic potential in colloidal dispersions. Colloidal chemistry literature denotes it using the letter Zeta (ζ). That potential is caused by the net charge at the particle surfaces, which affects the distribution of ions in the surround interfacial region. The increase of the concentration of the ions is characterised by an opposite charge (counter-ions) close to the surface. It is possible in the liquid discerning a double layer or two parts, that surround a particle, an inner region and an outer region. In the first region called the *Stern layer,* the ions are strongly bound. In the second region called *diffusive layer,* the ions are less firmly attached. A schematic representation is reported in **Figure 3.3**.

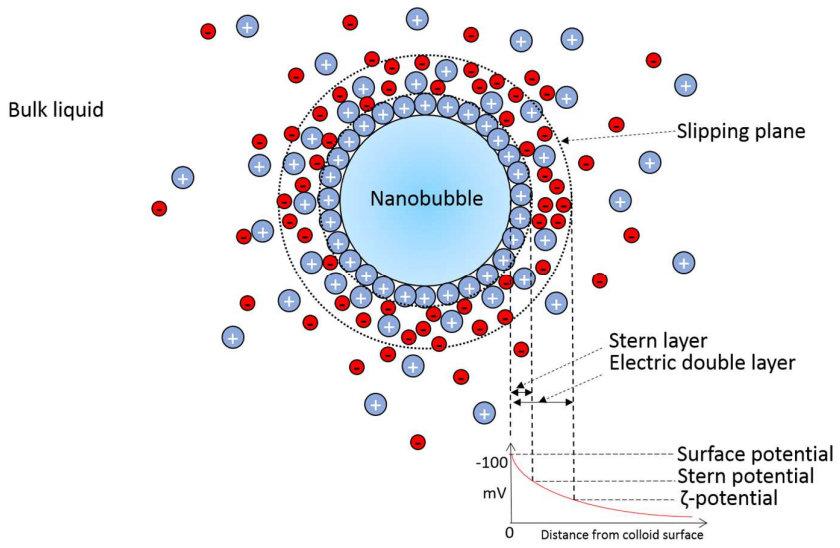

Figure 3.3. Schematic of Zeta Potential, Stern Layer and slipping plane are represented.

When an electric field is applied, particles start to move, the ions within the boundary follow this movement, but all the ions outer the boundary do not follow the movement of the particles. This boundary is named *slipping plane* and represents the surface of hydrodynamic shear, and the potential that is measured in this area is known as the ζ-potential (Hunter, 1981). ζ-potential also depends on the location of the slipping plane, and it is different from the Stern potential because the latter is measured in a different location. The ζ-potential magnitude indicates the stability of colloidal dispersions. It indicates the degree of electrostatic repulsion that exists between particles when the distance between them is very small or if they are similarly charged. With a large negative or positive ζ-potential colloids tend to coalesce, agglomerate, coagulate or flocculate. Generally, colloids with a ζ-potential value greater than ± 30 mV are considered electrically stabilised, thus, the greater is that value and the more excellent is considered the colloidal stability (Samimi et al., 2019).

One way to determine the zeta potential of a charged particle is through the electrophoretic mobility of the particle when they are subject to an electric field. The electrophoretic mobility, U_e, is given by measuring the particle velocity:

$$U_e = \frac{v}{E} \tag{3.5}$$

where v and E, are the measured velocity of the particles and the electric field strength. The ζ-potential can be determined using the Smoluchowski's equation (Smoluchowski, 1903):

$$U_e = \frac{\varepsilon_r \varepsilon_0 \zeta}{\eta} \tag{3.6}$$

where $\varepsilon_r, \varepsilon_0, \zeta$ and η are respectively the relative permittivity called also dielectric constant of the dispersion medium, the relative permittivity of the free space, the zeta potential and the viscosity of the medium.

The **3.6** is valid only in the limit of thin double layer, thus, considering k the reciprocal thickness of the double layer and i the particle radius, the **3.6** is valid only for ki »1 (Overbeek, 1950, Booth, 1948).

3.1.2 Nanoparticle Tracking Analysis (NTA)

Nanoparticle Tracking Analysis (NTA) is a non-invasive technique, which allows the visualization and characterisation of nano-entities such as nanoparticles and nanobubbles dispersed in a liquid suspension, in the range between 10-1000 nm. Each particle is individually and simultaneously tracked with video by direct observation and measurements of the diffusion events. Since the method is particle by particle, the resultant size is *high resolution*, and due to the known volume, it is possible to measure the concentration of particles within the liquid.

One of the greatest strength of the NTA is the capability to analyze the population of nano-suspensions on an individual basis simultaneously, thus, it is very suited for the real-time mono and poly-disperse suspensions in the range between 10 nm to 2μm (Paul Harrison, 2014, Ltd, 2015), thus, is particularly indicated to analyze BNB suspensions, which, due to their high polydispersity index (PI), usually greater than 0.7, are considered polydisperse suspensions. The PI is defined as a measure of the heterogeneity of a sample based on size. International standards organizations (ISOs) have classified the dispersity of the samples according to the PI. PI values < 0.05 identify monodisperse samples, while values > 0.7 are common to a wide size

distribution of particles, hence, they are common to polydisperse samples (ISO standards ISO 22,412:2017 and ISO 22,412:2017). However, the instrument itself does not provide a measurement of the PI, which is provided instead by other techniques such as the Dynimic Light Scattering, nevertheless, the samples' polydispersity can be observed from any bubble size distribution diagram, since the bubble size distribution is observed and reported in the range of ~ 50 – 300 nm.

NTA is a light scattering based technique, that exploits the properties of both light scattering and Brownian motion in order to obtain the particle size distribution and the number density of nanoparticles in liquid suspension. Particles in liquid suspension are loaded into a sample chamber, which is illuminated by a specially shaped laser beam. The laser beam passes through a prism-edge glass flat located within the sample chamber, and the scattered light from the particles suspended in the path of the laser beam, in turn, passes through a microscope objective (x20 magnification) before arriving at the CMOS/CCD camera sensor for a live video recording. The NanoSight software then analyses the video of the particles under Brownian motion, and by using the following equation, estimates the diameter and thus, the size distribution of the suspension.

$$\frac{(\overline{x,y})^2}{4} = Dt = \frac{Tk_B}{3\pi\mu D_H} \quad \textbf{(3.7)}$$

where $(\overline{x,y})^2$ is the mean square displacements in two dimensions, T is the absolute Temperature, $k_B$is the Boltzmann's constant, Dt is the particle diffusion coefficient, μ is the solvent viscosity, and D_H is the hydrodynamic diameter.

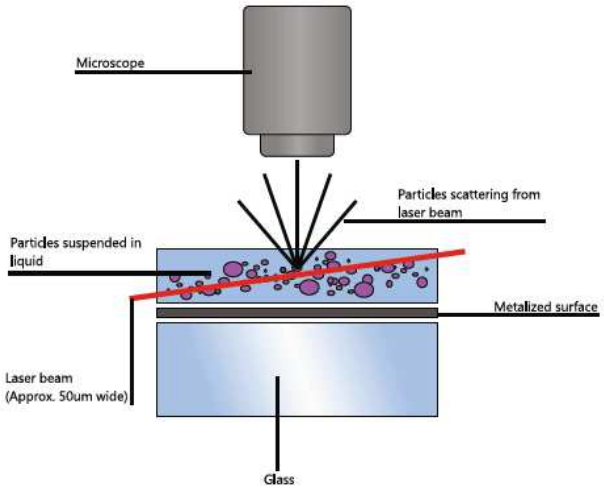

Figure 3.4. Schematic of NanoSight principle. The illustration was taken from (Malvern NS300 manual of operation).

NanoSight LM10 and NanoSight NS300 were used to characterise BNB suspensions. The LM10 comprises a small Al metal housing (92 x 66 x 47 mm) containing a solid-state, single-mode red-laser diode (<40mW, 635nm) configured to finely focussed beam through the 300 µL sample chamber (Ltd., 2008), whilst the NS300 comprises an Al laser module (140 x 74 x 68 mm), with the temperature control, and two interchangeable top plates, one in PMMA called Flow-cell top plate designed for a small amount of solution ~ 0.1 µL, and the other in anodized Al alloy called O-ring designed for ~ 600 µL of solution. The laser module of the LM10 is equipped with a red laser (<70mW, 642nm), while the NS300 is accessorised with a Violet laser (<70mW, 405nm), both suitable to studybulk nanobubbles. Besides, for the characterisation of the BNBs suspension discussed in this work, a syringe pump (accessory of the NS300) was connected directly to the NanoSight sample chamber for dynamic measurements. The Malvern Panalytical NanoSight syringe pump enabling analysis in constant flow, thus, it is beneficial for bulk nanobubbles analyses, where statistically robust data are a

must due to their polydispersity. The use of a syringe pump not only improves sampling for the size-distribution statistics and measurements, but also the data repeatability. NTA software automatically compensates for flow in the sample and, in this way, only the Brownian motion of the nano-entities is used for the size data.

Last but not least, it is recommended for analyses of low concentration samples, this is very important, because as also reported in this work, sometimes the concentration of bulk nanobubbles could be very low and difficult to analyse properly with other techniques. It has been found that the lower limit of the NTA is about ~ $5 \cdot 10^6$ particles/mL, typical value observed for pure water analysis, where, in the worst-case scenario, only a few particles per frame are observed.

A comparison between measuremets with syringe pump (dynamic measurements) and without syringe pump (static measurements) are reported in this chapter, followed by a comparison between the characterisation methods.

3.2 Materials and Methods

Different instruments were used to characterise bulk nanobubbles, particularly the Dynamic Light Scattering (DLS) technique (Malvern Zetasizer Nano ZSP model, Malvern Panalytical Ltd, Malvern, UK) was used to characterise bubble suspensions in term of size distribution and ζ-potential, whereas Nanoparticle Tracking Analysis (NTA) (NanoSight LM-10 and NanoSight NS300, Malvern Panalytical Ltd, Malvern, UK) was used to characterise bubble suspensions in term of bubble size distribution and bubble number density.

Pure water was generated by an Aquatron water still (A4000D) system, which had an electrical conductivity of 1.70 $\mu S \cdot cm^{-1}$ and a pH of 6.5, and filtered with a Corning® bottle vacuum filter, with pore size of 0.22µm prior to start the experiments.

Four different methods are here investigated to generate bulk nanobubble suspensions and they are based on acoustic cavitation, hydrodynamic cavitation, solvent mixing exchange and mixing respectively as schematically illustrated in **Figure 3.5**. Specifically, bulk nanobubbles produced by acoustic cavitation were generated through the use of a 20 kHz probe-type US processor (Sonics VCX 750 W model, Sonics & Materials, Newtown, UK), equipped with a titanium probe of 0.75 inch. in diameter, which was used to sonicate 80 mL of pure water with the US amplitude fixed at 95%, for 3 minutes as reported by (Nirmalkar et al., 2018b). The temperature of the sample was controlled at 20.0 °C by using a recirculating cooler (JULABO GmbH, Germany) (**Figure 3.5a**). The second method used was a NanoGalf bubble generator system (IDEC Corporation, Japan) which was run, with 2 L of pure water up to 4 hours; this technique was intrododuced and described by (Maeda Shigeo and Goto Kuniaki, 2014) (**Figure 3.5b**). The third technique adopted (solvent-mixing exchange) involved the mixing of 20% volume of analytical grade (99.5% pure) ethanol, purchased from Fisher Scientific (UK), and pure water. The solvent was handled in glassware in order to avoid contamination from plastic products. The % volume of the solvent here used has been reported being the optimum value in order to generate the maximum bubble number density (Millare and Basilia, 2018) (**Figure 3.5c**). Finally the last technique analysed involved the use of a magnetic stirrer (Stuart US151 Magnetic Stirrer model), equipped with a magnetic stir bar coated by PTFE (PolyTetraFluoro-Ethylene) and used to mix 40 mL of pure water at maximum speed 2000 rpm for 5 hours in 40 mL of pure water (**Figure 3.5d**).

Prior to experimentation, the pure water was examined using the NanoSight LM-10 instrument (Malvern Instruments, UK), to ascertain that no significant levels of nanoscale impurities could be detected.

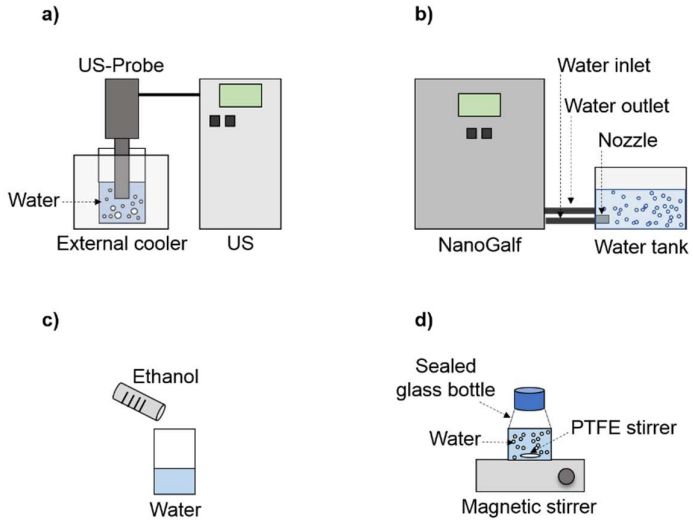

Figure 3.5. Schematics of bulk nanobubble generation methods; a) Ultrasonication; b) NanoGalf (hydrodynamic cavitation); c) Ethanol-water exchange; d) Mixing.

3.3 Comparison between characterisation methods

3.3.1 NanoSight analyses

A bulk nanobubble suspension was analysed to test the NanoSight with and without the use of the syringe pump, hence, in static and dynamic mode. The two different modalities can be described as follow. The first consists in a static measurement in which the Brownian motion of a fixed volume of a suspension is observed, tracked and analysed within the NanoSight

chamber; the second consists in a dynamic measurement obtained with the help of an external syringe pump. In the last case scenario, the fluid that contains the nanobubble suspension flows through the NanoSight chamber, and hence, a different population of the same suspension of bulk nanobubbles is observed, tracked and analysed each time. **Figure 3.6a** shows the static measurements of a fixed volume of BNBs observed and kept for 60 min inside the NanoSight chamber. Three measurements were taken at different time intervals, as reported in the figure. **Figure 3.6a** represents the bubble number density of the observed population, and it is possible to see that these measurements are characterised by a fluctuation of the value, which gradually decreases along the 60 min of observation. As the population decreases in bubble number density, most likely due to accidental contact of the bubbles against the boundaries of the NanoSight chamber, the mean bubble diameter slightly increases to ~100 nm (**Figure 3.6b**).

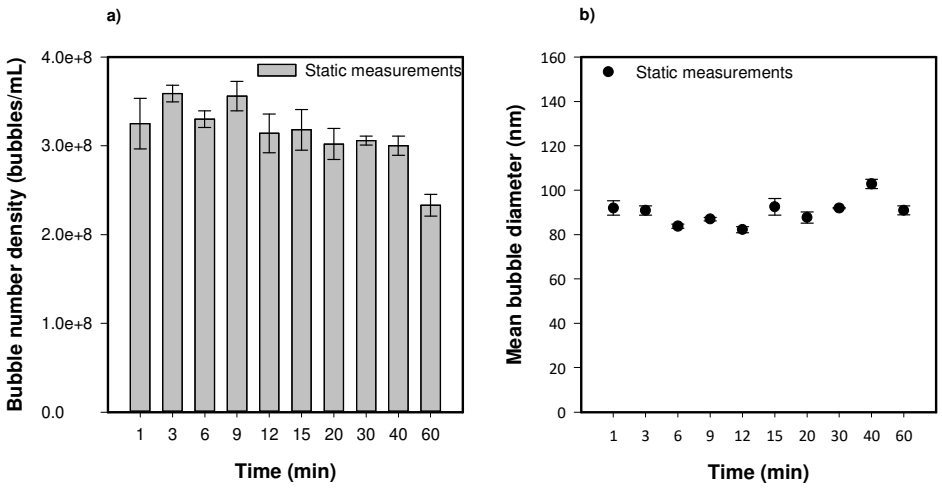

Figure 3.6. Static measurements of a bulk nanobubbles population observed and kept inside the Nanosight chamber for 60 min. Figure a) shows the bubble number density, whilst b) shows the mean bubble diameter.

The same bulk nanobubble suspension was observed with the use of a syringe pump. Results are depicted in **Figure 3.7**. In this case scenario, the samples' population analysed is always

different, and that because the pump allows the solution to flow inside the Nanosight chamber, where is recorded and analysed before to flow out directly into an external bottle. Thus, the same population could not be observed for a long interval of time and it depends from the pressure applied to the syringe, resulting in a change of the flow speed value in the NTA software. In this study, different measurements have been taken at different video recording time, fixing the syringe pump flow rate at a value of 70, and varying the recording time from 20 to 60 seconds in order to increase the statistic of the population analysed. Results are reported in **Figure 3.7a** for the bubble number density, and **Figure 3.7b** for the mean bubble diameter. Three different measurements of each recording time are here reported. It is possible to observe not a relevant improvement of the statistic by changing the recording time, and thus, consequently it is possible to conclude that the recording time seems to not significantly affect the measurements. Therefore, three measurements of 30 seconds each were chosen as the best parameter in order to analyse enough volume of BNBs suspension and to save space on the hard drive memory. Those parameters will be adopted for the entire work presented.

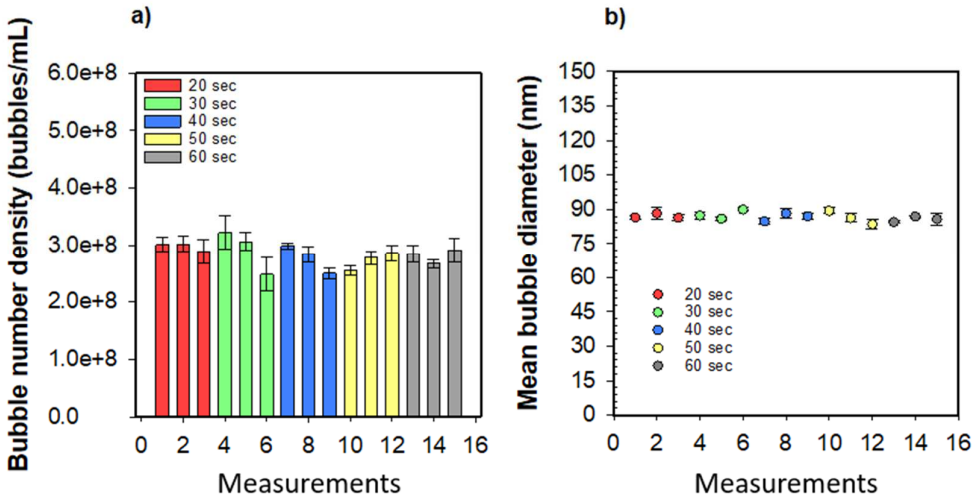

Figure 3.7. Dynamic measurements of a bulk nanobubbles population by Nanosight accessorised by a syringe pump. Figure a) shows the bubble number density of three measurements for each selected time, whilst b) shows the mean bubble diameter.

As further proof, it is possible to see that the valid tracks recorded and observed increasing linearly with the recording time, as shown from the regression line reported in **Figure 3.8**.

In conclusion, due to the polydispersity of bulk nanobubble suspensions, the use of the syringe pump is strongly recommended in order to analyze different volumes of the suspension. For all the measurements reported in this work, the parameters of the NTA software used were reported in **Table 1**. Note that measurements could be affected by the software parameters used, thus a comparison of the results should be made only for the same parameter adopted.

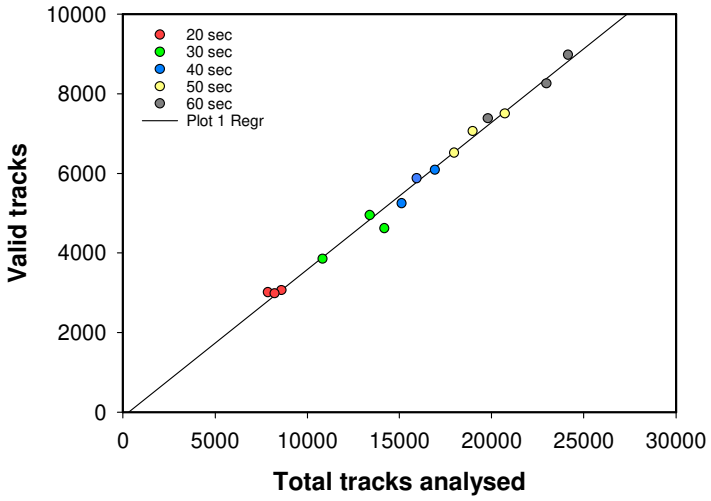

Figure 3.8. Numbers of valid tracks at different recording video time.

Parameters	Value
Syringe pump	yes
Syringe pump flow rate	70
Camera level	14-16 [3]
Detection threshold	5

Table 1. Parameters and accessories used to analyse bulk nanobubble suspensions in this work.

[3] The camera levels were selected in according to the intensity of the scattered light of the particular suspension. This parameters increase or reduce the ISO sensibility of the CMOS camera.

3.3.2 DLS vs NTA

A comparison between the two instruments (DLS and NTA), to assess which characterisation instrument is more accurate to study bulk nanobubbles is here reported. As described in the previous sections, both the instruments are based on the light scattering but use a different principle to calculate the bubble size distribution. Thus, a BNB suspension was analysed with both the methods and results are depicted in **Figure 3.9**. What is striking in this figure is the overestimation of the bubbles size distribution by DLS, resulting in a shift of the distribution on the right side of the graph. The calculated DLS size distribution is plotted against the percentage intensity, whereas the calculated NTA size distribution is reported in bubbles/mL (volume-weighted distribution). The reason why the DLS make an overestimation of the bubble size can presumably be attributed to the fact that bigger bubbles scatter more light compared to smaller one, thus the signal scattered from the smaller one is most likely overshadowed from the other, as also reported by (Nirmalkar et al., 2018b) and in a similar study by (Filipe et al., 2010).

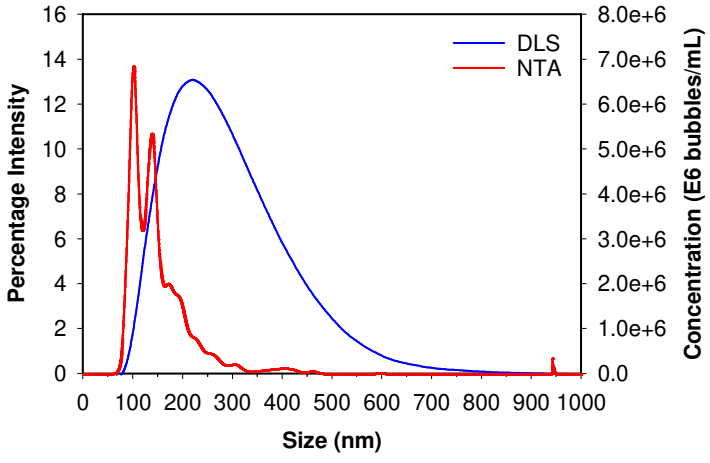

Figure 3.9. Comparison between DLS (intensity-weighted) and NTA(volume-weighted) measurements of the same bulk nanobubble suspension.

3.3.3 Freezing-Thawing

Due to the lack of instruments to make a distinction between solid nanoparticle and gas nanobubbles, in this work the freezing-thawing method, for the first time introduced by (Nirmalkar et al., 2018b) and then discussed in other papers (Nirmalkar et al., 2018a, Jadhav and Barigou, 2020a), was used here to have an estimation of the contaminations generated during the process to form bulk nanobubbles. Different could be the sources of contamination within the sample during the bulk nanobubble generation, and they strictly depend on the method chosen for their production. This method consists of freezing the BNB suspension at -18 °C, and successive analyse it when the same sample has been completely defrosted. This method resulted in being a potent tool to make a distinction between solid nanoparticles and bulk nanobubbles because the bubble number density drastically falls after a cycle of freezing-thawing at -18°C. However, it has advantages and shortcomings. Among the advantages, it provides evidence that the BNB suspensions are reduced by more than 90% in most of the experiments reported (i.e **Figure 3.10**), suggesting therefore that the observed nano-entities should be gas-filled and hence, excluding their ascription entirely at solid nanoparticles; on the other hand, it is not clear *a priori* if the bulk nanobubbles disappear during the process because are compressed with each other by the growing ice crystals, or if they shrink and become not visible to the characterisation instruments. However, if any nanoparticles are in the liquid suspension, after freezing-thawing, the same particles should remain within the liquid, hence detected by the characterisation instruments. Note that if particles form aggregates during the freezing-thawing process, the size distribution should be shifted on the right side of the size scale, and thus begin detected. This method alone could not give a proof of the existence of

bulk nanobubbles, but together with other characterisation techniques and experiments could help to shed light on their existence.

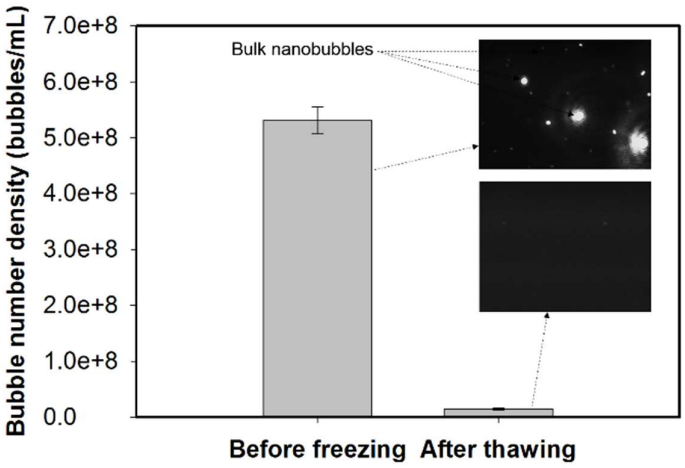

Figure 3.10. Example of bubble number density before freezing and after thawing.

3.4 Generation of Bulk Nanobubbles: preliminary studies

This section aimed to investigate and compared the formation of BNBs using different methods, where some of them are often reported in the literature. The results here reported represent a critical evaluation of the generation of bulk nanobubbles in pure water, showing the advantages and shortcomings of those methods to understand the nature of the entities observed.

3.4.1 Results

Bulk nanobubbles generated by the NanoGalf instrument were obtained with the pump pressure fixed at 160 psi, and the dissolution pressure displayed on the instrument was of 41

psi. BNBs are formed due to hydrodynamic cavitation (Kobayashi et al., 2014, Maeda S. et al., 2011) since water is pumped at high pressure in an external vessel, where the liquid is forced to pass into a nozzle, and because of the area expansion, tiny bubbles are formed within the liquid. The system is characterised by recirculation of the BNBs water, which after a few minutes from the generation becomes milky and cloudy. The continuous generation of bulk nanobubbles was performed for 4 hours. Each hour a sample of 10 mL was withdrawn and analysed with the NanoSight. Results are reported in **Figure 3.11**. The maximum BNB number density was found after 1 hour of continuous generation, and after that, it starts to decrease with time (**Figure 3.11a**), and consequently the bubble size distribution resulting in a decrease of the intensity (**Figure 3.11b**).

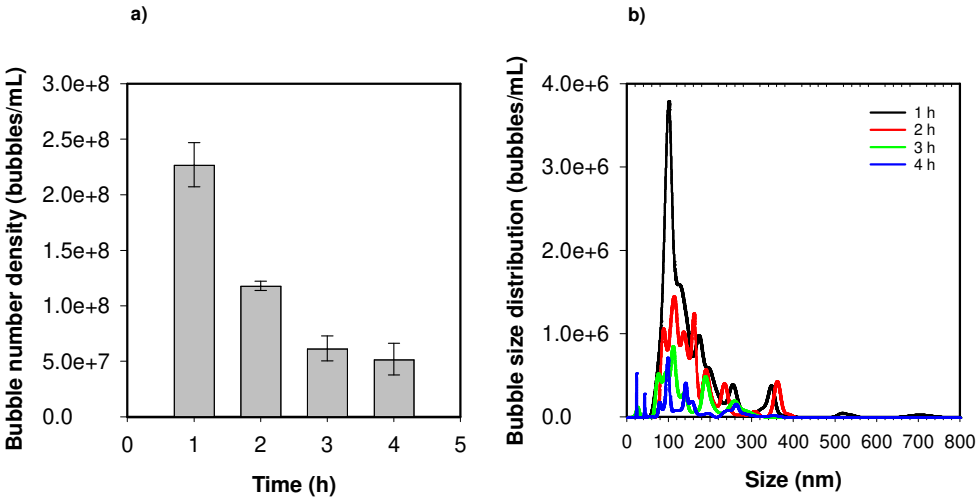

Figure 3.11. Bulk nanobubble suspensions generated by NanoGalf. a) shows the bubble number density, while b) shows the bubble mean diameter.

At the end of the experiment, the temperature rises up to ~ 60 °C, and a tiny layer of black particulate was found within the water tank. The tiny particulates found might probably affecting the stability of bulk nanobubbles (Tuziuti et al., 2018). Therefore, this instrument has

been discarded for the bulk nanobubble generation due to the impossibility to distinguish if the suspension analysed were effectively bulk nanobubbles or nanoparticles detached or eroded from any components of the instrument during the production.

In order to minimise the generation of contaminations, bulk nanobubble suspensions were generated by mixing pure water with a magnetic stirrer (Error! Reference source not found.**d)**. This method resulted in being one of the most "clean" for the production of bulk nanobubbles since a minimal number of contaminations could be generated because the pure water enters in contact only with the glass bottle and a magnetic stir bar coated by PTFE (PolyTetraFluoro-Ethylene). The mixing, at maximum speed (2000 rpm) was performed up to 5 consecutive hours, where five different suspensions were generated up to 5 consecutive hours with fresh pure water, before being analysed. Results are depicted in **Figure 3.12**.

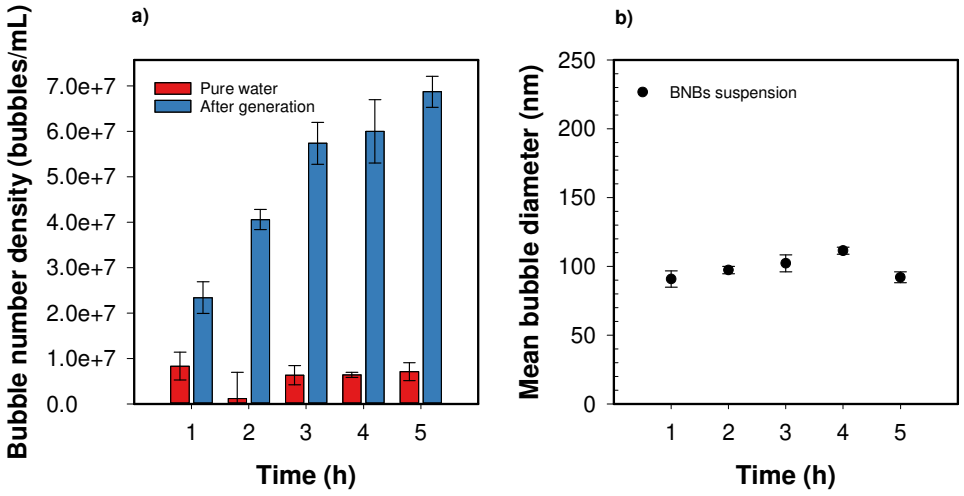

Figure 3.12. Bulk nanobubbles generated by mixing with a magnetic stirrer. a) shows the bubble number density, whilst b) shows the mean bubble diameter.

Figure 3.12a shows the bubble number density against the generation time. In this graph, pure water was analysed before each experiment. What is striking in this figure is the increase in the total concentration of bulk nanobubbles within the solution, whilst the mean bubble diameter (**Figure 3.12b**) remained constant at ~100 nm. In this experiment, contaminations are drastically reduced, suggesting that the observed nano entities should be gas nanobubbles, however after 5 hours of generation, the bubble number density was very low, making difficult to perform studies on stability and nature of the entities observed.

The other two methods investigated were the acoustic cavitation (Error! Reference source not found.**a)** and the solvent- mixing exchange (Error! Reference source not found.**c)**. Both the methods were objects of many studies and criticism in the literature. Both the methods were reported from different researcher groups, i.e. the nanobubbles generation witho solvent mixing exchange was reported by (Millare and Basilia, 2018, Nirmalkar et al., 2018b, Jadhav and Barigou, 2020b), in contrast also highly criticised by other groups (Rak et al., 2019, Alheshibri and Craig, 2019b). However, those methods were used here to make a comparison in term of bubble number density with the other generation techniques described, which are summarised in **Figure 3.13**. Results are reported in **Figure 3.14**.

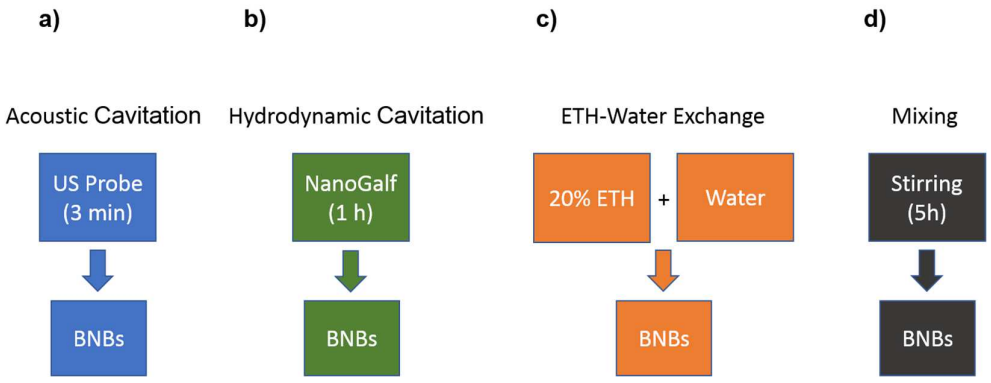

Figure 3.13. Summarisation of the parameters and methods used for a comparison of the efficiency in the generation of BNBs

As it is possible to see in **Figure 3.14**, the ethanol-water mixing is the most efficient techniques leads to the generation of ~ 5.5×10^8 bubbles/mL. Moreover, the shortcomings of the ethanol-water exchange are the debates behind the nature of the entities observed and not always associated to bulk nanobubbles; nevertheless, very recently some papers were published that should help to close the debate on their nature (Jadhav and Barigou, 2020b, Chen et al., 2020). The use of the solvent-exchange method has been discarded in this work, which aimed to show the existence and stability of bulk nanobubbles in pure water, because the addition of a chemical compound could influence the BNBs stability mechanism but also their formation.

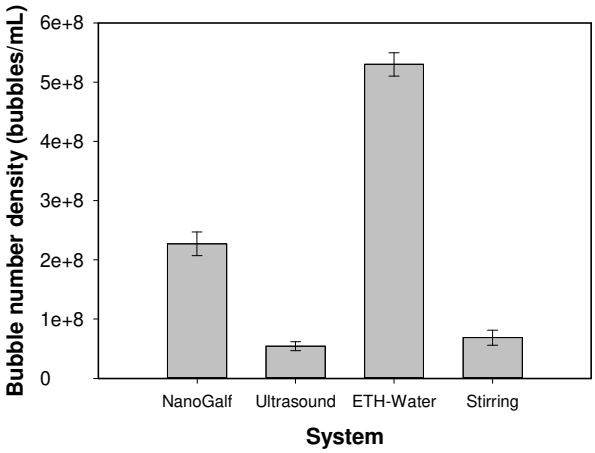

Figure 3.14. Comparison in term of bubble number density between four different BNBs generation methods.

The ultrasound method has also been discarded as BNBs generation method because the ultrasonic probe, which is continuously in contact with the sample, could lead to the generation of contaminations. In fact, the ultrasonication is characterised by high power consumption and energy dissipation that could lead to the erosion of the titanium probe if the instrument is not used carefully. The contaminations are increasing according to generation time and the US-intensity adopted. Typical eroded and damaged US-probe are depicted in **Figure 3.15a**, where

the first one on the right side represents a brand new probe. **Figure 3.15b** shows a micrograph, of contaminations found in pure water, made by an optical microscope; particles sedimented after two days from the generation at 100% of US-amplitude for 10 minutes.

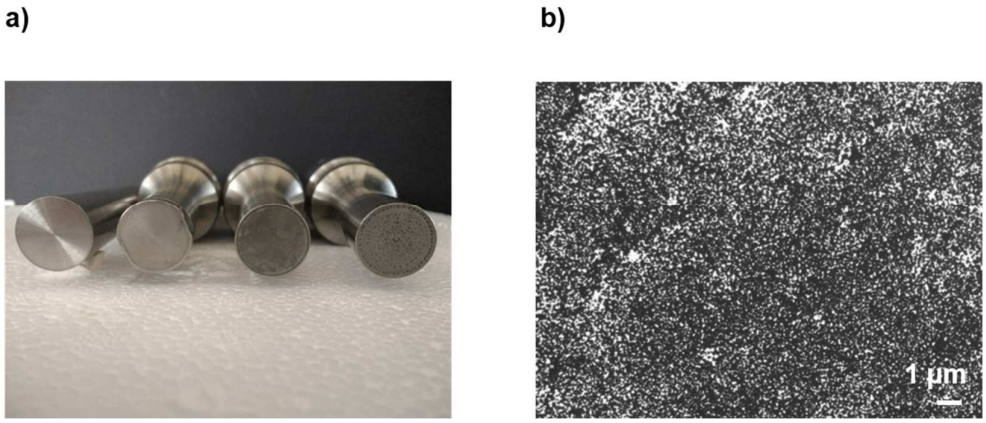

Figure 3.15. Figure a) show the typical erosion on the US-probe after an extensively use, whilst figure b) shows an optical microscopy capture of the contaminations found in a water solution after 10 min of generation at 100% amplitude.

Therefore, different generation methods were investigated and are reported in this work and well explained in the next chapters, in order to produce bulk nanobubbles in pure water, trying to reduce the number of contamination generated, and at the same time, increasing the efficiency of the bulk nanobubble generation.

3.5 Conclusions and outlook

This chapter was focussed on describing the characterisation techniques and testing four different methods for the bulk nanobubble generation. Advantages and shortcomings were presented and can be summarised as follow. The *Nanoparticle Tracking Analysis* (NTA)

resulted in being the best characterisation instrument to have information on the bubble number density and bubble size distribution compared to *Dynamic Light Scattering* (DLS) that generate an overestimation of the bubble size distribution. On the other hand, the DLS will be used for the ζ-potential measurements during this work.

Among the different generation methods tested, the Ultrasound (US) and NanoGalf could produce a sensible number of contaminats that due to the lack of methods for the distinction between solid nano-entities and bulk nanobubbles could misleading the interpretation of the results. On the other hand, the entities produced by the magnetic stirrer and observed in pure water suggesting the existence of bulk nanobubbles, with the mean bubble diameter of ~100 nm as often reported in the literature, but that method produced a limited bubble number density ~7×10^7 bubbles/mL. Last but not least, the ethanol-water exchange resulted in being the most efficient technique for the BNBs in term of total concentration generated. However, this generation method has been discarded in this work because it will introduce a further variable (addition of solvent) to the understanding of the existence, formation and stability of BNBs in pure water.

In conclusion, the need to introduce new generation methods able to generate bulk nanobubbles in pure water is necessary to shed light on their existence and mysterious stability.

Chapter IV

Mechanical generation of bulk nanobubbles

4.1 Introduction

Rotor-Stator mixers, also known as High Shear Mixers (HSMs) or High Shear Reactors (HSRs) are characterised by a micrometric gap between the rotor and the stator, usually in the range between 10 to 3000 µm (Karbstein and Schubert, 1995). Another peculiar characteristic of HSMs is the high rotor tip speeds (ranging from 10 to 50 m/s), and a high shear rate (ranging from 20,000 to 100,000 s^{-1}), hence, imposing high levels of shear and energy dissipation rates, which in comparison with the mechanically stirred vessel, are three orders of magnitude higher (Atiemo-Obeng et al., 2004, Zhang et al., 2012). There are different commercial HSMs provided by different vendors such as Silverson Ltd, Ross, Rayneri, Chemineer, Ystral IKA, and Works. The assembly of the rotor and stator is often called the working head or mixing head, however, often the stator itself has named the head (Pacek et al., 2007, Utomo et al., 2008, Utomo et al., 2009). Their peculiar characteristics make them very versatile for the industrial processes and a wide range of applications, included liquid-liquid homogenisation, emulsification processing but also in food, chemicals, cosmetic and pharmaceutical industries (Zhang et al., 2012). Silverson rotor/stator mixers and more in general HSMs have been extensively studied in the last decade, both batch and in-line HSMs are subjects of interest for many researchers. The majority of the existing studies focus on the development of scaling

rules, and effects of working head geometries on mixing efficiency, but also, aim to investigate the turbulence within the mixing head.

Nevertheless, a significant part of the studies present in literature focus on measurements of power consumption, flow visualization studies using techniques such as Particle Image Velocimetry (PIV), Laser Doppler Anemometry (LDA) and computational fluid dynamics (CFD) numerical simulations. (Padron et al., 2001) studied the power draw in different batch roto-stator mixers, characterised by a different design of the working head. They concluded that the number of holes, together with their size affects the power number, and thus the agitation power. (Utomo et al., 2009, Utomo et al., 2008) studied the flow pattern, the periodicity, the effect of the stator geometry, the effect of the hole spacing and the energy dissipation in a batch rotor-stator mixer (Silverson L4RT). In their studies, they have tried to validate CFD predictions of flow pattern and distribution energy for a batch rotor-stator assembly, and they verified the obtained results by LDA measurements performed both in the proximity of the mixing head and in the bulk liquid. They also investigated numerically the effect of stator geometry on the flow pattern and energy dissipation rate arriving at the conclusions that most of the energy supplied by the rotor during the mixing operation was dissipated in the rotor swept region. They reported a comparison between the jets emerging from stators with small hole spacing, typically it moves tangentially in the proximity of the working head, whereas the emerging jets from geometries with large hole spacing move radially as free jets. Another observation reported was that since stators with small hole spacing have more hole edges, where stagnations occur, those geometries dissipate above 10% more energy compared to those with large hole spacing which dissipate on the other hand more energy in the bulk region, thus, more suitable for bulk agitation. (John et al., 2019a) reported a comparison between a batch and in-line assembly, in which trough the CFD they investigated

and compared the power and flow characteristics for both the assemblies. (John et al., 2019b) investigated how stator geometry affects power and flow characteristics using a Silverson L5M batch lab-scale mixer and they found that the flow rates vary through each of the rows holes in the screen, whereas by increasing the hole size they found that the non-uniformity in flow between rows increased.

The majority of studies present in the literature are also focussing on the droplet break-up mechanism occurred using HSMs (De Hert and Rodgers, 2017a, De Hert and Rodgers, 2017b, James et al., 2017, Hall et al., 2011, Rodgers and Cooke, 2012, Rueger et al., 2013). (Bałdyga et al., 2008) reported some new studies of breaking up mechanisms to generate nanoparticle suspensions breaking up nanoparticle clusters, often called agglomerates, in high-shear flows. They used silica nanoparticles aggregate, and they stated that the agglomerations breakage occurs by an erosion mechanism, where small fragments were chipped off from large agglomerates.

(Gül Özcan-Taşkın et al., 2016) studied the performance of three different rotor-stator configurations on silica nanoparticles dispersed in water, to identify the mechanism and kinetics of break-up with the aim also to determine the smallest obtainable size, which was found to be in the range of 150-200nm by using a Polarisation Intensity Differential Scattering (PIDS) measurement technique. (Padron and Özcan-Taşkın, 2018) published a work aimed to study the deagglomeration of nanoparticle clusters using a Silverson 150/250MS in recirculation loop modality. They found the kinetic of the de-agglomeration process is governed from the flow conditions around the particle and not from the bulk rheology of the dispersion. In their study they reported an abnormal bimodal particle size distribution, with consistent peaks in the range

of ~ 150 nm, increasing as a function of the mixing time, however, they justified those peaks as sampling/measurements error and/or due to the recycle mode used in their experiments.

From this review emerged that all the studies on the high shear mixing paid attention to the breakage of solid nanoclusters, the effects of the stator geometries and the power consumption and the high energy dissipation of the HSMs instruments. There are no studies yet in the literature that considers the use of this technique to generate bulk nanobubbles, neither that the observed peaks at ~ 150 nm could be associated with the generation of impurities.
It is believed that due to the characteristics that the HSMs offer, such as high energy dissipation and turbulent mixing, they could be used for the generation of bulk nanobubble suspensions. Therefore, this chapter aimed to investigate the potential of the High Shear Mixer technique to generate bulk nanobubbles in pure water. The work presented here shed light on the existence of gas/vapour filled entities generated in nanoscale by exploring the use of different stator geometries and different mixing modality, i.e. batch system and recirculating in-line system. We provide multiple evidence that the observed nano-entities must be gas/vapour-filled nanobubbles by (i) generation of suspensions at different rotor speed, (ii) studying the effect of the mixing time on the bulk nanobubble generation, (iii-iv) studying the effects of different geometries and temperatures on the generation of bulk nanobubbles, (v) showing that the bubble number density gradually decreases over time, (vi) studying the suspensions before and after freezing-thawing and (vii) by sparging different gases.

The bulk nanobubble generation by using HSM could be described as a combination of four different steps as follow: (i) pure water upwards from the bottom of the vessel into the centre of the work-head; (ii) centrifugal force, that can be calculated knowing the mass, the radius and the angular speed of the shaft, drives the liquid suspension between the ends of the rotor blades

to the inner wall of the stator; (iii) liquid is forced suddenly out, radially and at high speed, through the perforations present in the stator, while (iv) fresh material is continually drawn maintaining the mixing cycle. A schematic representation of the described steps is shown in **Figure 4.1**

Error! Reference source not found.

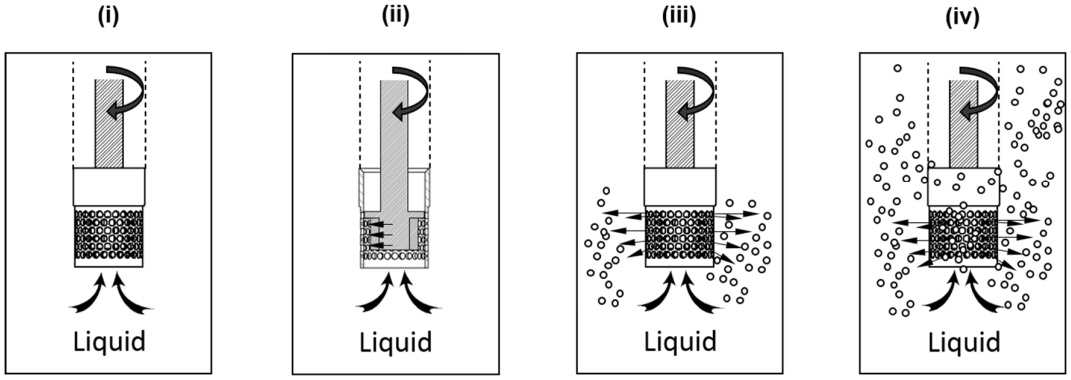

Figure 4.1. Schematic illustration of the steps that occur during the high shear mixing.

According to (Utomo et al., 2009, Utomo et al., 2008), the energy supplied by the rotor is dissipated in the rotor swept region and it depends on the geometry used. As the fluid arrives in the swept region, it is forced to pass through regions characterised by a narrow area (area reduction) before suddenly begin expelled in the bulk liquid (area expansion). During the passage into the expansion area, hence, most likely immediately after the stator perforations, the local fluid pressure falls below the water vapour pressure, and tiny bubbles are formed leading to the cavitation phenomena. In other words, hydrodynamic cavitation occurs where according to Bernoulli's principle of mechanical energy conservation, a reduction in the area of flow leads to an increase in the velocity stream and in a decrease of the fluid static pressure which leads to the nucleation of bulk nanobubbles (Nirmalkar et al., 2018a). However, cavitation could be not the only mechanism behind the formation of bulk nanobubbles. It is not

clear *a priori* if some bubble breakup mechanism could arise in order to generate bulk nanobubbles from microbubbles, or if BNBs are formed just from microbubbles collapsing (Jin et al., 2020), especially if during the generation, external gas is introduced by sparging in the system, where gas bubbles are sucked into the centre of the work head and disrupted in microscopic bubbles passing through the stator holes. Therefore, both the mechanisms, together with the cavitation, could take place leading to the BNBs formation.

4.2 Materials and Methods

Silverson Laboratory Mixers L5M-A model, 740 W (1 hp), with maximum speed 10,000 rpm (Silverson Machines Ltd., Waterside, Chesham Buckinghamshire, England) was used with water as working fluid to generate bulk nanobubbles. Standard Mixing Assembly, 1" and 3/4" Tubular Assemblies were used as accessories for the batch operations, whereas a Laboratory In-Line Mixing Assembly was used for semi-continuous in-line mixing, called also recycle mode. Ultrapure double distilled water with pH between 5.0 to 6.5, water resistivity in the range between 0.7 – 1.0 mOhm·cm and conductivity in the range between 1.0 -1.5 µS/cm, produced by an Acquatron A4000D distillation system (Cole-Parmer Ltd, Staffordshire, UK), has been used to test the method. Ultrapure water (type I) characterised by the resistivity of 18.2 MΩ·cm, the conductivity of 0.055 µS/cm, and pH of 6.7 at a temperature of 20 °C, was obtained from a water purification system (Avidity Science, UK). In this system, the feed water is purified first through reverse osmosis (RO) and then after passing through different filters (such as the Endure Purification Module) and further purified by Ultraviolet (UV) Photo Oxidation at 254 nm and 185 nm to eliminate trace organics and inactive microorganisms

present in it. Typical values are TOC < 5ppb and Endotoxin < 0.03 EU/ml. Type I water has been used in all the experiments to generate bulk nanobubbles. All the glassware was cleaned by immersion for 10 min in boiling type II water, for several times, rising with type I water, drying in a microwave oven, and flushing with a flow of high-purity dry nitrogen before being used. The use of any organic solvent was avoided in order to reduce the possible contaminations. Dry air, nitrogen (oxygen-free) and pureshield argon gases of purity > 99.5% were purchased from The BOC Group (Guildford, UK). Those gases were sparged through a fritted gas dispersion tube or a stainless steel gas sparger directly into pure water. The temperature of the water was controlled by using a recirculating cooler (JULABO GmbH, Germany), and monitored with a stainless steel thermocouple.

Silverson L5M-A model was experimentally used in order to generate BNBs. The Silverson Mixing Assemblies are explicitly designed for the different kind of applications, thus, a wide selection of stator geometries are available including Disintegrating Head (DH), Square Hole Head (SHH), Standard Emulsor Head (SEH), Fine Emulsor Head (FEH) and Vertical Slotted Head (VSH). Besides, the L5M-A is also accessorized with different rotor-stator assemblies based on the volume of fluid required to be processed and might include tubular, standard and in-line mixing assemblies, as reported in **Figure 4.2**. The tubular and standar assemblies are used here for the generation of BNBs in a batch system, while the latter is used to generate BNBs in a semi-continuous in-line sytem. All the assemblies illustrated in **Figure 4.2** were tested to create the basis to identify and develop a new system for the bulk nanobubble generation. The need to identify a system able to generate bulk nanobubbles in pure water was necessary not only to shed light on the bulk nanobubbles existence but also to find a new

generation method able to produce bulk nanobubbles on a large scale number, in order to a possible scale-up of the process from a laboratory scale to an industrial scale.

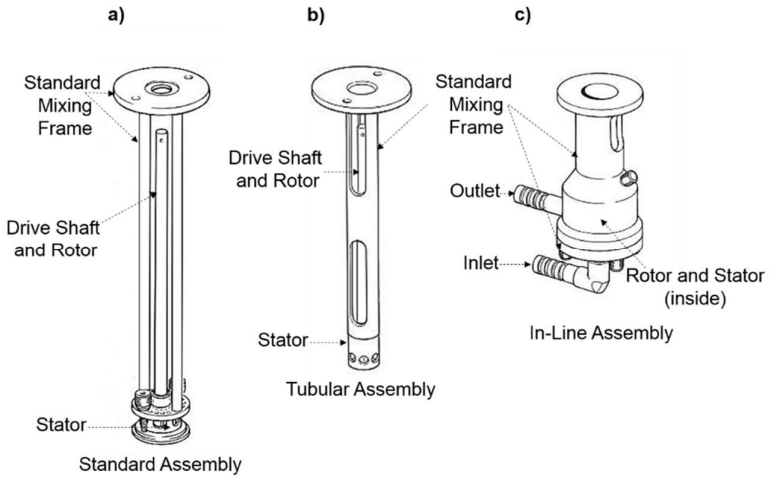

Figure 4.2. Schematics of different mixing assemblies; a) Standard assembly; b) Tubular assembly; c) In-Line assembly. Illustrations from Silverson L4RT High Shear Mixer Operating Manual (Silverson Machines Ltd.)

The assemblies reported in **Figure 4.2** are characterised by different mixing capacities, which vary from 20 mL for the tubular assemblies, up to 12 litres for the standard assembly, whereas the in-line assembly possess the ability to process flow rates up to 20 litres/minute. The properties of the assemblies used are schematically reported in **Table 2**. Each assembly is characterised by a rotor-stator pair, which has a characteristic size of rotor blade and stator holes. Stators, on the other hand, are characterised by different hole geometries and holes number.

Assembly	Shaft diameter (mm)	Overall length (mm)	Capacity depending on viscosity (mL)	Bush
Tubular 3/4”	15.6	208	20 – 250	PTFE
Tubular 1”	25	240	50 - 500	PTFE
Standard	32	292	Up to 12000	PTFE
In-Line	32	N.A.	20000/min	PTFE

Table 2. Details of the Silverson Assemblies used to generate bulk nanobubbles.

In this study, the effects of different assemblies including rotor speed, time of generation and stator geometries were analysed to identify the best parameters for the production of bulk nanobubbles, and that was study through the analysis of bubble number density, bubble size distribution and mean bubble diameter. **Figure 4.3** shows a schematic of the stator geometries used, whilst a 3D representation is depicted in **Figure 4.4**.

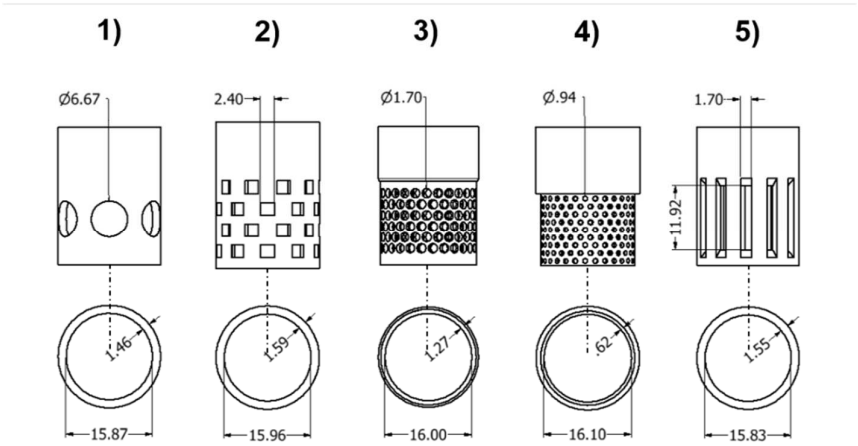

Figure 4.3. Stator geometries used to generate bulk nanobubbles. The stators illustrated are referred to a 3/4”

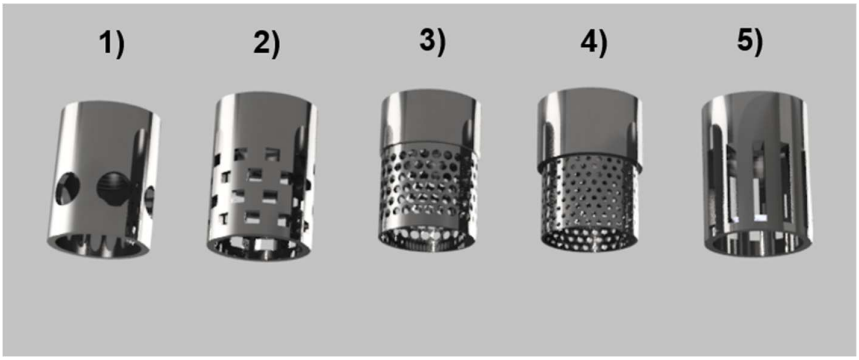

Figure 4.4. 3D - Autodesk Inventor representation of the stator geometries used with a 3/4” Tubular Assembly.

In **Table 3**, are reported the different parameters that characterise each stator used with 3/4" Tubular Assembly, while in **Table 4** are reported the properties for the stators relative to the other assemblies used.

Stators (3/4" Tubular Assembly)	**No. of hole**	**Dimension (mm)**	**Area/hole (mm2)**	**Total hole area (mm2)**
1) Disintegrating Head (DH)	6	d = 6.67	34.94	209.65
2) Square Hole Head (SHH)	48	2.40 x 2.40	5.76	276.48
3) Standard Emulsor Head (SEH)	138	d = 1.70	2.27	313.23
4) Fine Emulsor Head (FEH)	270	d = 0.94	0.70	187.37
5) Vertical Slotted Head (VSH)	12	1.70 x 11.92	20.26	243.16

Table 3. Details of the stators used for a 3/4" Tubular Assembly.

Stators (1" Tubular Assembly)	**No. of hole**	**Dimension (mm)**	**Area/hole (mm2)**	**Total hole area (mm2)**
1) Disintegrating Head	6	d = 8.28	53.84	323.07
Stators (Standard Assembly)	**No. of hole**	**Dimension (mm)**	**Area/hole (mm2)**	**Total hole area (mm2)**
1) Disintegrating Head	6	d = 9.67	73.44	440.65
Stators (In-Line Assembly)	**No. of hole**	**Dimension (mm)**	**Area/hole (mm2)**	**Total hole area (mm2)**
1) Standard Emulsor Head (SEH)	6	d = 9.67	73.44	440.65

Table 4. Details of stators used with different assemblies.

4.2.1 Possible sources of contamination

To shed light on the nature of the entities observed and discussed in the experiments here reported, the needs to understand and find the possible causes of contamination is necessary. From an accurate and meticulous observation of our system, sources of contamination might come from the mechanical setup used or any surface the liquid entered in contact with during

the mixing. The working fluid, hence, in this case the pure water used, could contain an initial amount of impurities or contaminants; thus, it is a part of a proper protocol to analyse few mL of water into the characterisation instrument before starting the new experiment. Usually, the analyses of pure water result in a black screen on the NS300 and are not more than few particles per frame.

Therefore, the possible primary sources of contamination are generated from the experimental setup used. Consequently, the two systems used, the batch rotor-stator mixing and the in-line mixing in semi-continuous mode are analysed below.

In a batch system, the possible contaminations could be attributed to different sources included abrasion, air quality and any contaminants detached from the beaker or the rubber bung, which is often used to seal the beaker to avoid contaminations such as dust to enter in contact with the working fluid during the BNB generation. The former could be generated by the accidental friction between the rotor, which is in motion at high angular speed, and the stator which is fixed at the standard mixing frame, however, also the friction between the shaft and the PTFE bush (**Figure 4.5a**) could generate other impurities. The second source of contamination concerns the air quality, and it can be attributed at dust and any other impurities suspended in the air environment but also coming out from the machine cooling fan as illustrated in **Figure 4.5a**, which in turn could be drawn and released into the suspension during the common mixing operations. The latter is concerning to a not proper rinsing and drying of the glassware and rubber bung used, which could affect the final measurement. This last source of contamination could be avoided by following a strict experimental protocol that sees all the materials involved flushed with type I water before each use.

In an In-line system, the possible sources of contamination are slightly different, and the mechanical components are depicted in **Figure 4.5a**. In this case, the liquid is mixing inside a sealed stainless steel chamber, hence, contaminations coming from the environment are drastically reduced. In this configuration, the shaft's length is optimized, therefore, the vibrations propagating along the shaft are less, and consequently, less could be the accidental frictions between the rotor and the stator. The major causes of mechanical contamination in an In-line mixing assembly are generating from the friction between the bush and the shaft, and the constant friction between the stationary seal seat and the mechanical shaft seal (in**Figure 4.5b**). However, on the top side of the stationary seal, it is present a small chamber filled with water to reduce the friction between the mechanical parts, but also a seat seal called O-ring to seal the mixing chamber properly, that also prevents the diffusion of the possible generated contaminations from entering in contact with the working fluid.

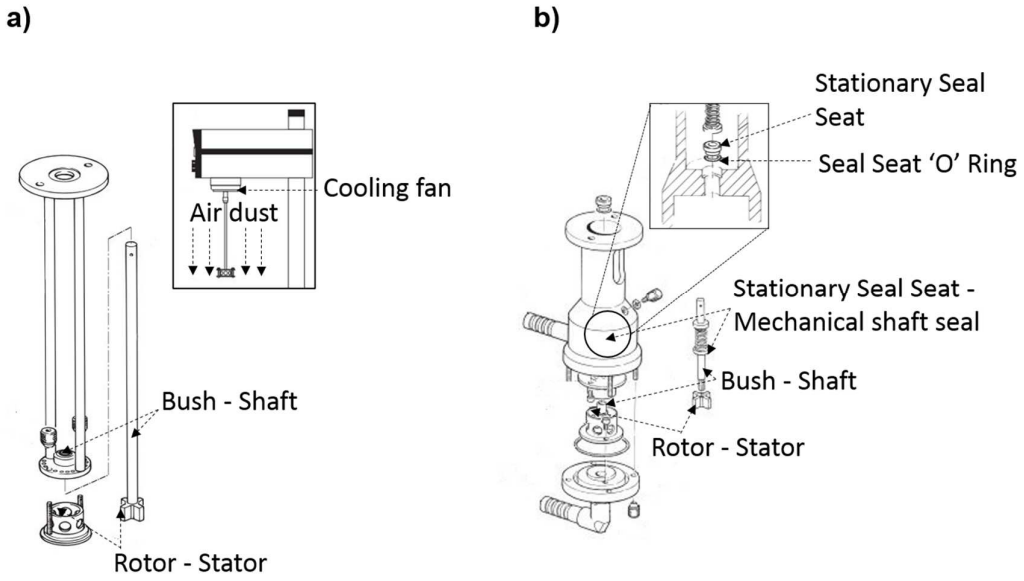

Figure 4.5. Possible causes of contamination that could be found in the suspension during the mixing in a batch system (a) or in semi-continuous mode (b).

A chamber in plexiglass was designed to reduce the contaminations coming from the cooling fan, constitutes by two sliding openings to allow the cleaning of the machine between each experiment and for sampling. Two apertures were also designed (gas inlet and outlet) to allow the sparging of fresh and clean air inside it as reported in **Figure 4.6**. In the batch system, mostly for tubular assemblies, a rubber bung was used to properly seal the vessel during the experiments, with the duplex effect of having better control of the aeration within the liquid and fixing the position of the tubular assembly for better reproducibility.

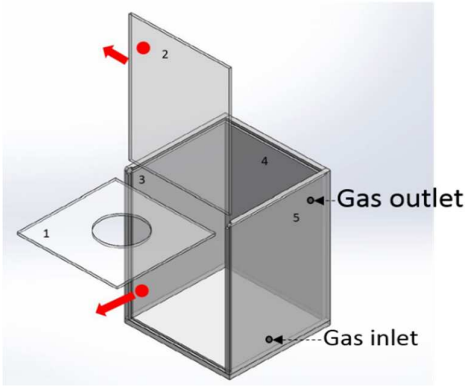

Figure 4.6. Plexiglass chamber to avoid contamination coming from the machine cooling fan and the environment.

4.3 Batch System - Preliminary studies

4.3.1 Effect of rotor speed

To investigate the generation of bulk nanobubbles produced by the HSM, pure water (PW) from Acquatron A4000D distillation system (Cole-Parmer Ltd, Staffordshire, UK) was used as

working fluid and the Standard Emulsor Head for the 3/4" tubular assembly was used at different rotor speed (rpm) for a generation time fixed at 30 minutes at room temperature ~ 20°C. Findings show that the number density increases as the rotor speed increases (**Figure 4.7**). The best operating speed was found to be 10000 rpm (maximum HSM speed in pure water), and no variations of the particles size were reported with the average value constant at ~ 90 ± 10 nm. At high rotor speed, also the power dissipation increased as the temperature of the sample raised faster. The pure water was also checked before each experiment, and the average value is reported in the graph. It should be pointed out that the Reynolds number in all the experiments was > 10000 which indicates that the mixing occurred at turbulent flow regimes, where the Reynolds number in a rotor-stator mixing instrument is calculated as:

$$Re = \frac{\rho N D_{r,o}^2}{\mu} \tag{4.1}$$

where ρ is the density, μ is the viscosity at a fixed temperature, N is the rotor speed and $D_{r,o}$ is the outer rotor diameter (Espinoza et al., 2018, Padron and Özcan-Taşkın, 2018).

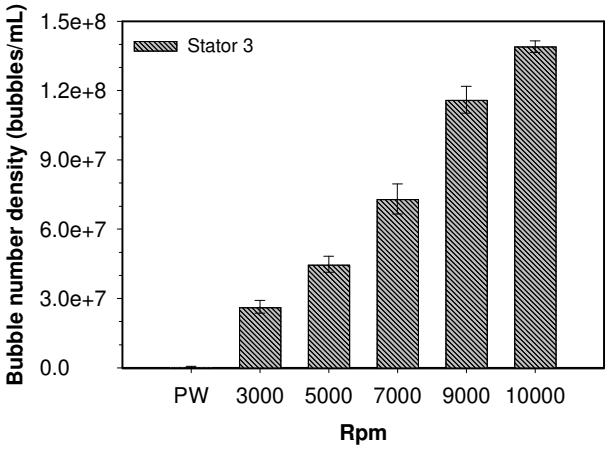

Figure 4.7. Effect of revolution per minute (rpm) on bulk nanobubble generation using the standard emulsor head.

This preliminary finding shows that nano-entities are generated during the ordinary operation with HSMs, and their number density seems to increase linearly with the rotor revolution per minutes.

4.3.2 Effect of mixing position

The position of the shaft inside the vessel is fundamental and leads to a different mixing efficiency. In order to achieve the best mixing efficiency that in this case, should result in higher bubble number density, the position of the mixing head in the vessel was investigated. One of the general rules used to build a mixing system is called "D/T ratio" where the D stands for the diameter of the mixing blade and T stands for the width of the tank as depicted in **Figure 4.8**. A right starting place to achieve an effective flow pattern with an excellent mixing efficiency is when the impeller's diameter is one-third of the tank diameter as well as the height of the mixing blade in the tank, however, it might be different according to the specific application (Özcan-Taşkin and Wei, 2003).

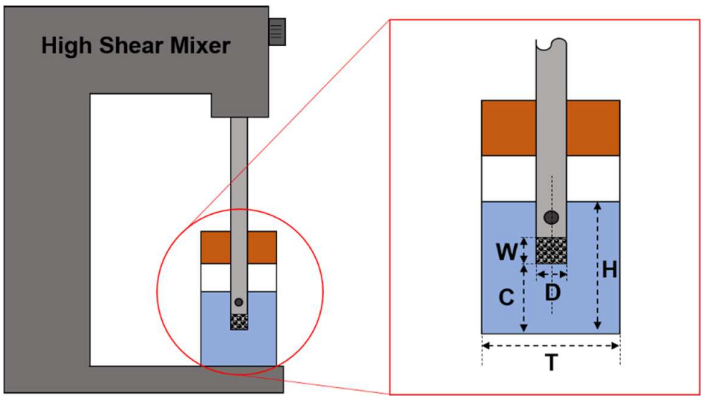

Figure 4.8. Schematic of mixing ratio.

Three different C/H ratios were analysed in order to understand the effect on the bubble generation; the position of the rotor-stator head has been considered, from the bottom to the top, respectively at 2/3, 1/2, 1/3 of H, as schematically depicted in **Figure 4.9**.

Before each measurement, 2 mL of pure water was removed from the beaker and analysed to check the presence of possible initial nano-entities or contaminations, thus, processed on the NS300. That was considered the blank, the pure water measurements, which is reported as time 0 in **Figure 4.10a**. The HSM was run for 20 minutes, and samples were characterised after approximately 10 minutes from the end of the experiment. The temperature was not controlled in this experiment.

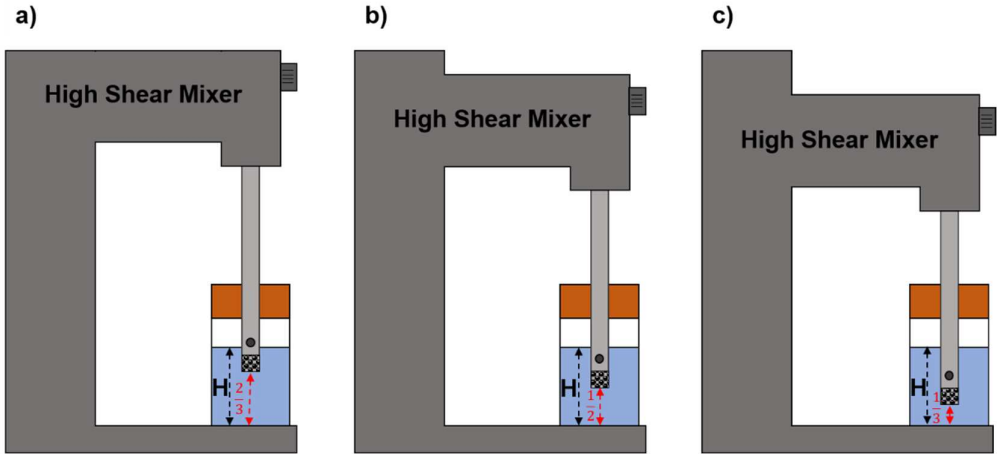

Figure 4.9. Schematic representation of C/H ratios investigated on the bulk nanobubble generation; a) C/H = 2/3; b) C/H = 1/2; c) C/H = 1/3.

Findings reported in **Figure 4.10a** shows the bubble number density obtained for three different positions of the rotor-stator head. What stands out in this chart is the best rotor-stator head position within the vessel, and it was found to be at the C/H ratio of 1/2. **Figure 4.10b** shows the bubble size distribution, which results to be unaffected by the position of the shaft

into the beaker.

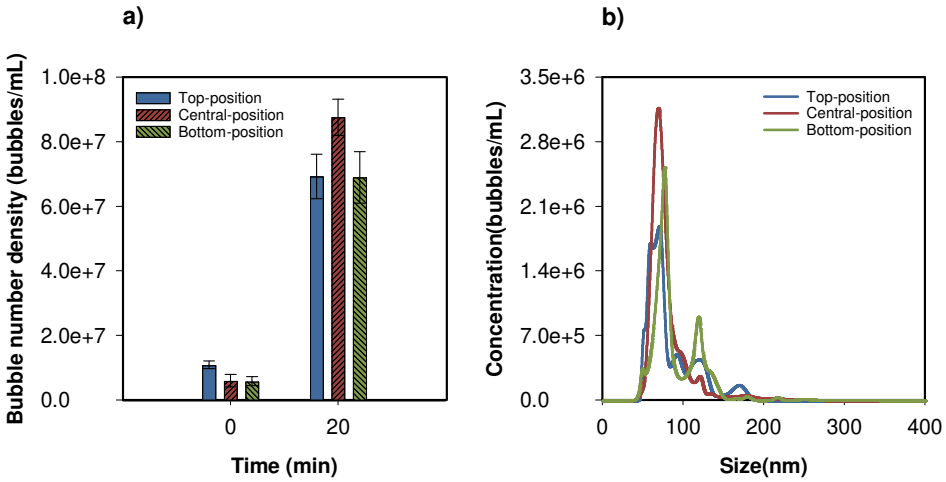

Figure 4.10. Figure a) shows the bubble number density obtained at different height-position of the rotor-stator inside the vessel, in the on-centre mixing; b) shows the unaffected bubble size distribution.

While the bulk nanobubbles research is still in its infancy and due to the vast range of mixing operations for which the HSMs are used, it is essential to understand which is the best mixing configuration to optimize the bulk nanobubbles production. Even though Silverson Ltd recommend a position of the rotor-stator head slightly off-centre in order to achieve the best mixing result and thus, avoiding vortex formation which could cause aeration, spillage or splashing according to the viscosity of the fluid, both off-centre and on-centre position were tested. Therefore, with the rotor-stator head positioned at the C/H ratio of 1/2, the axial position was investigated with the mixing head positioned respectively at 1/2 and 1/3 of T, as schematically illustrated in **Figure 4.11**.

Both the positions mentioned above were investigated by using the emulsor screening head and fixing the rotor speed at 9000 rpm. Findings are reported in **Figure 4.12**. What can be clearly seen in these charts is the no significant difference in BNBs production between the two

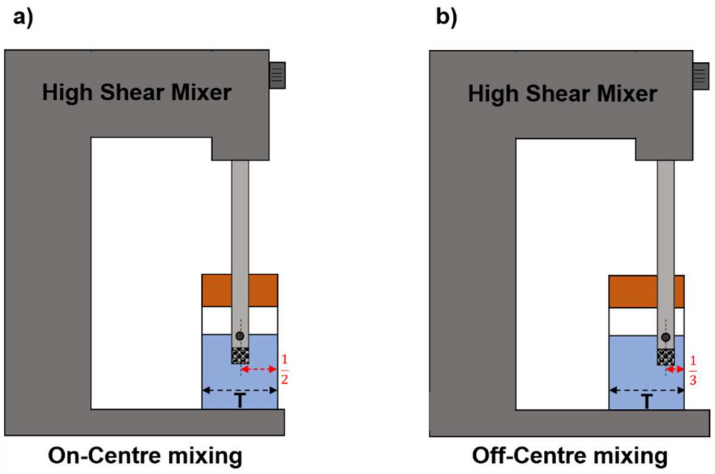

Figure 4.11. Schematic representation of the mixing position of the head/rotor inside the vessel where a) represent the on-centre mixing position and b) the off-centre mixing position.

configurations. While the bubble number density slightly rises in the case of the central mixing, most likely due to different aeration and mixing efficiency, no significant difference was found in the size distribution observed in the range between 50 and 200 nm. Hoverer, since the difference in bubble generation was not so marked, the off-centre mixing was adopted in all the other experiments as general configuration for the BNBs generation, which creates less vortex with a better bulk mixing efficiency, but also because in that configuration it has been observed a better top to bottom liquid flow pattern.

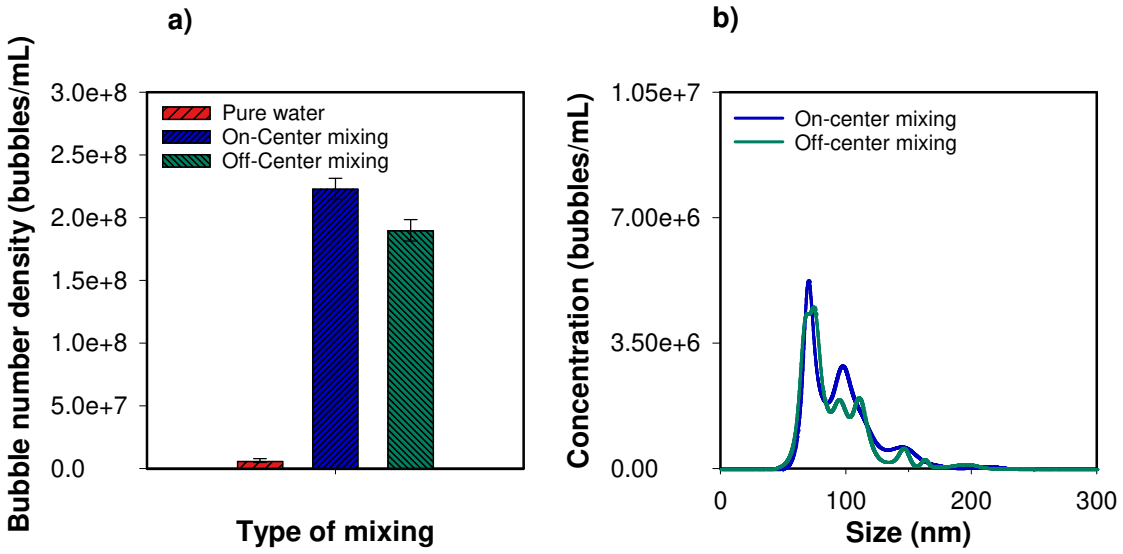

Figure 4.12. Figure a) shows the bubble number density obtained at different position-side of the rotor-stator inside the vessel; Figure b) shows the bubble size distribution for the position investigated.

4.4 Batch System - Time and Temperature effects

Findings reported in previous sections showed the best mixing position and the effect of rotor speed on the generation of nanoscale entities that we assumed to be BNBs, thus, provided preliminary information on the number density and size distribution that are possible to obtain with HSMs. This section aims to provide evidence that the nano-entities previously observed must be gas/vapour-filled. In order to show that, a strict investigation on how operating parameters influence the bubble numbers density, is indeed necessary, therefore experimental studies here presented focussing on (i) the effects of mixing time, (ii) the effects of stator geometries, (iii) the effects of operating temperatures, but also we reported here studies of (iv) the long-term stability and (v) freezing-thawing analyses of the suspension generated. The optimal mixing conditions found in previous studies are adopted for the following experiments,

thus, the off-centre mixing and the position of the mixing head at 1/2 of H. The geometries used were illustrated in **Figure 4.3.**

4.4.1 Effects of the generation time without temperature control

The HSM was run at maximum speed (10000 rpm) in 200 mL of pure water for 60 minutes, and results are reported in **Figure 4.13**. The pure water was analysed before each experiment, and it is reported as the blank at time 0 in **Figure 4.13a**. What is striking in this figure, is the dominance of the bubble number density generated by the Disintegrating Head (DH) and the Standard Emulsor Head (SEH) against the other geometries. Both configurations leading to a bulk nanobubble generation that increases accordingly to the mixing time, whilst the other geometries seems being characterised by fluctuation or at least a slowly increasing of the bubble number density. Similarly, both those geometries produced bulk nanobubbles with a mean bubble diameter in the range of ~100 ± 10nm. The mean bubble diameter is reported in **Figure 4.13b**. What stands out from the chart is that the mixing time seems do not significantly affects the size of the suspensions for almost all the stators, with the only exception made by the Square Hole Head (SSH) which produce a BNBs suspension with the mean diameter around ~150 nm that slowly decreases when the mixing time increases.

All the stators produced a polydisperse bubble suspension in the range between 50 – 250 nm, clearly evident observing the bubble size distribution reported in **Figure 4.14a**. The lower end of the bubble size distribution appears to lie on the x-axis only because of the y-axis scale and the intensity of the signal from bubbles as small as ~50 nm are included, but it only exists

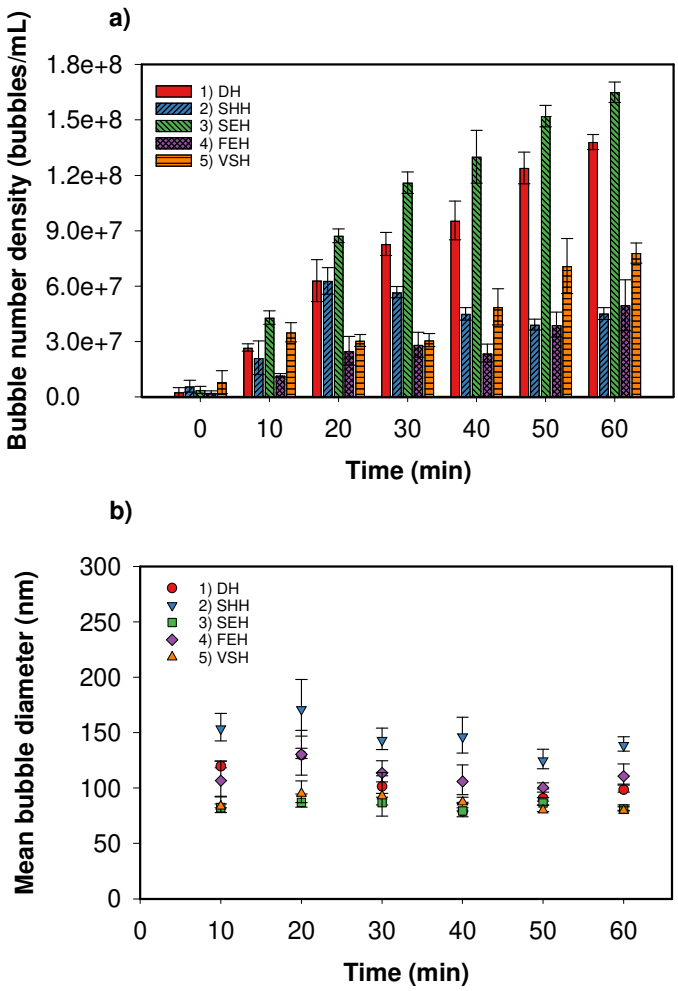

Figure 4.13. Effects of time and stator geometries on the generation of bulk nanobubbles; a) shows the bubble number density, while b) shows the mean bubble diameter.

in small numbers. Therefore, even if the lower NTA detention limit is ~10 nm, according to (MalvernPanalytical-NS300), some bubbles could exist in the range between 10–50 nm. **Figure 4.14b** shows the ζ-potential value of the suspensions analysed after 60 minutes of generation by different stators. It can be clearly seen that the ζ-potential value is not significantly affected by the different stator geometries, and the trend is almost flat at -27 ± 5mV.

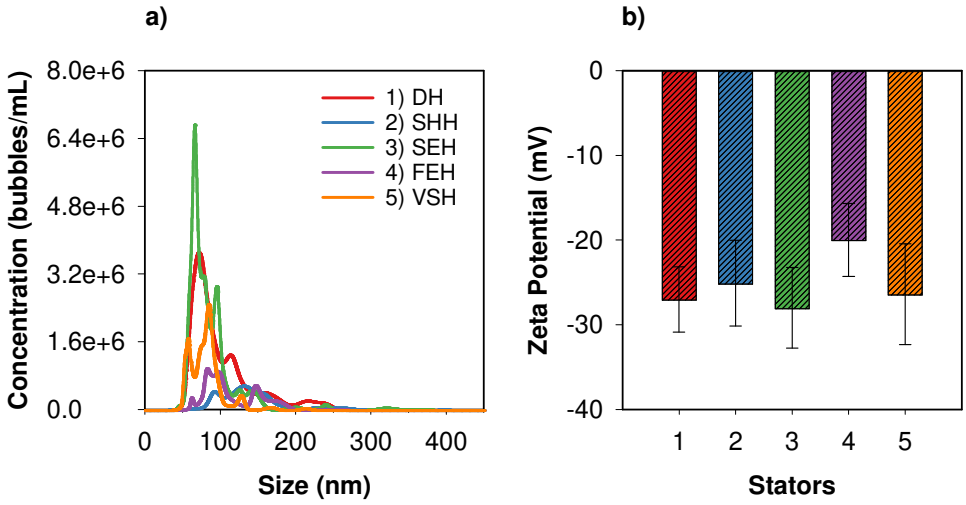

Figure 4.14. Effects of time and stator geometries on the generation of bulk nanobubbles; a) shows the bubble size distribution, while b) shows the ζ-potential of the BNBs suspension.

During the mixing, the temperature within the sample rises fast with the mixing time due to the high energy dissipation. It should be pointed out that all the stators have slightly different properties included the gap between the inner stator diameter and the outer part of the rotor blade; thus, the energy dissipation varies from stator to stator. Therefore, the temperature was monitored during the experiment by a stainless steel thermocouple inserted in the vessel and the values are summarized in **Table 5**.

Stator Geometries	Rotor/stator gap	Starting temperature	Final temperature
1) Disintegrating Head (DH)	~0.20 mm	25.2 °C ± 1 °C	34.3 °C ± 1 °C
2) Square Hole Head (SHH)	~0.25 mm	24.8 °C ± 1 °C	33.4 °C ± 1 °C
3) Standard Emulsor Head (SEH)	~0.28 mm	25.4 °C ± 1 °C	35.0 °C ± 1 °C
4) Fine Emulsor Head (FEH)	~0.30 mm	25.1 °C ± 1 °C	33.1 °C ± 1 °C
5) Vertical Slotted Head (VSH)	~0.18 mm	24.8 °C ± 1 °C	31.6 °C ± 1 °C

Table 5. Sample's temperature analysed before and after each running.

Frames from recorded videos of suspension, made by the CMOS camera mounted on the NTA, were extrapolated and micrographs were reported in the following figure (**Figure 4.15**). **Figure**

4.15 shows how BNBs increases with the mixing time, whilst **Figure 4.16** shows a comparison between the suspensions generated with the SHH and the SEH for different generation time.

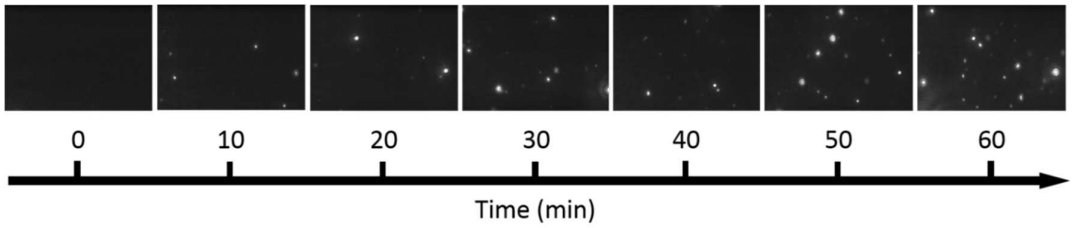

Figure 4.15. Bubble micrographs. The bubble number density increases with the generation time.

It should be pointed out that due to the high energy dissipation rate, the temperature rises within the sample, and since any external device did not control the temperature, it is not possible at this stage to state that BNBs increases only due to the mixing time. On the other hand, it was found that both the Disintegrating Head and the Standard Emulsor Head returns a relatively high number of BNBs. By the results depicted in **Figure 4.13a,** it seems that there is not a specific correlation between the number and size of the stator holes and the number of bubbles generated, therefore, suggesting that bulk nanobubbles could be generated by some breakup mechanism and most likely, their generation could also depend from the aeration of the system. For this reason, studies such as controlling the temperature of the system, and sparging gas during the mixing are necessary and could shed light or give valuable information on the formation of bulk nanobubbles.

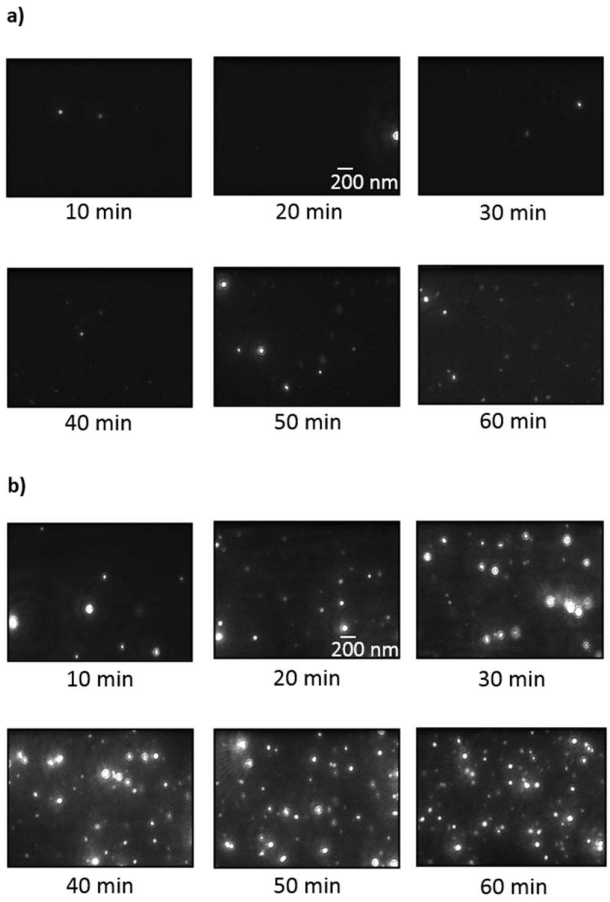

Figure 4.16. Bubble micrographs. a) shows the bubble suspension generated with the Square Hole Head, while b) shows the bubble suspension generated with the Standard Emulsor Head for different generation time.

4.4.2 Temperature effects

The effect of generation at different temperatures is here analysed. The temperature of the sample during the generation must be controlled to prevent the overall increasing temperature of the system caused by the high energy dissipation. The reason why that is an important parameter to be controlled is that to increase the efficiency of the bulk nanobubbles production is necessary to be aware of all the parameters involved during their generation. In other words,

not having control of this parameter leads to increase the overall system temperature, which is influenced by the ratio between the mixing head size and mixed fluid volume, the gap between rotor and stator, and also from the stator geometry adopted (number of holes and size), making difficult to understand the principle behind generation and nature of the observed entities. On the other hand, the knowledge of the effects of the temperature on the bubble formation, not only provide us with an understanding on the mechanisms of their formation but also give us information on the behaviour of the bubble such as the bubble size distribution and ζ-potential for different operating conditions. Understanding the role of the temperature on the BNBs generation will be helpful for a future scale-up of the system, thus, for large scale production of bulk nanobubbles; for example, it could be possible to the benefit of the high energy dissipation caused by the working head to assist the BNBs generation and thus, to reduce the cost needed to control the temperature of the system, while at the same time, increasing the efficiency of the process.

By considering the pressure constant at a fixed value, hydrodynamic cavitation in water is most likely to occur when the temperature of the water increases according to the water phase diagram. If we exclude the first transition period in which the rotor passes from the off-state to the full-working regime, as depicted in **Figure 4.17**, and also assuming homogeneous the differential pressure within the inner part of the stator, by controlling the sample temperature it is possible to understand if cavitation has a significant role in the BNBs formation or not. Several experiments were ran trying to control the temperature of samples during the generation. The temperature of the solution was controlled by an external recirculating cooler (JULABO GmbH, Germany), and in order to keep the temperature constant, the tubular 3/4" assembly equipped with SHE was used to process 200 mL of water for 60 minutes (volume selected after some trials to have a right balance between optimal temperature control and

concentration of BNBs). However, even if the temperature of the samples was still rising of ~ 3 °C in the first few minutes of mixing, it became utterly stable immediately after, hence, the temperature of the cooler has been regulated accordingly to that variation.

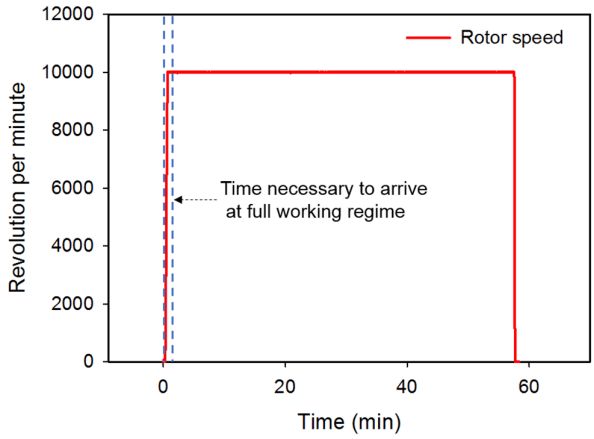

Figure 4.17. The transition between an off-state to a full working regime for an HSM.

Findings are reported in **Figure 4.19** and **Figure 4.20**, while a schematic of the experimental setup is illustrated in **Figure 4.18**. **Figure 4.19a** shows the results obtained with the rotor speed fixed at 10000 rpm. Samples were collected and analysed every 10 minutes, and the experiment was repeated for different temperatures (10 °C, 20 °C, 30 °C, 40 °C and 50 °C) ± 3 °C. As depicted in **Figure 4.19a**, the temperature seems to enhance the process yield and reaching faster the upper limit of the bulk nanobubbles generated, which was found to be 3.0 x 10^8 bubbles/mL after 50 minutes of generation at 50 °C. What is interesting in this chart is the rapid growth of bubble number density for temperatures above 30 °C suggesting that most

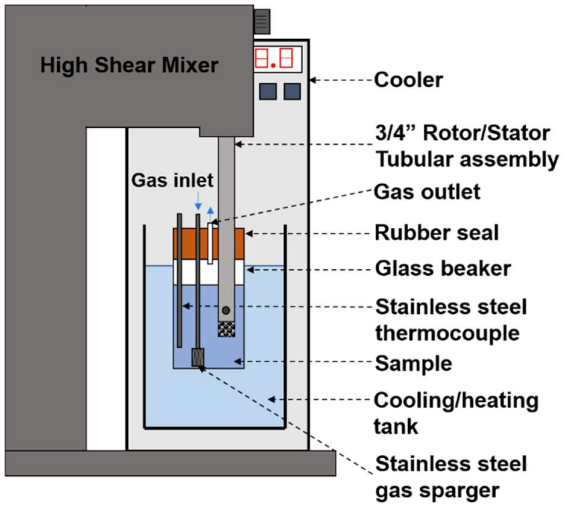

Figure 4.18. Schematic representation of the experimental setup with the temperature control and the possibility to sparge gas through a stainless-steel gas sparger.

likely hydrodynamic cavitation enhances the process yield, excluding perhaps the hypothesis that the entities observed are only solid nanoparticles. **Figure 4.19b** shows the bubble size distribution, and it is interesting to see that the shape of the bubble size distribution remained more or less unchanged, but the intensity increases as the concentration of the bubbles detected increases. For the suspensions generated at 40 °C and 50 °C, the bubble size distribution seems slightly shifted on the right, meaning that the population of the bubble with a mean diameter greater than 100 nm increases as the temperature of the system increases. That is also evident if we compare the micrographs of the suspensions for different temperatures, as illustrated in **Figure 4.21** where it is interesting to see that the bubbles generated at 50 °C were brighter than the bubbles generated at 20 °C. It should be pointed out that the NTA is a light scattered based technique; therefore, a changing in the brightness of the suspended colloids could depend on two factors including the size and the refractive index of the colloid. Due to the limits of those characterisation techniques is difficult to state if the observed nano entities are solid or filled with gas or vapour without further analyses; however, the fact that the bubble number density

increased with the temperature, represents a proof that the entities generated and analysed by the NS300 could not be attributed entirely and solely to the possible impurities generated during the mixing and already discussed in **4.2.1**; thus, they must be gas/vapour filled.

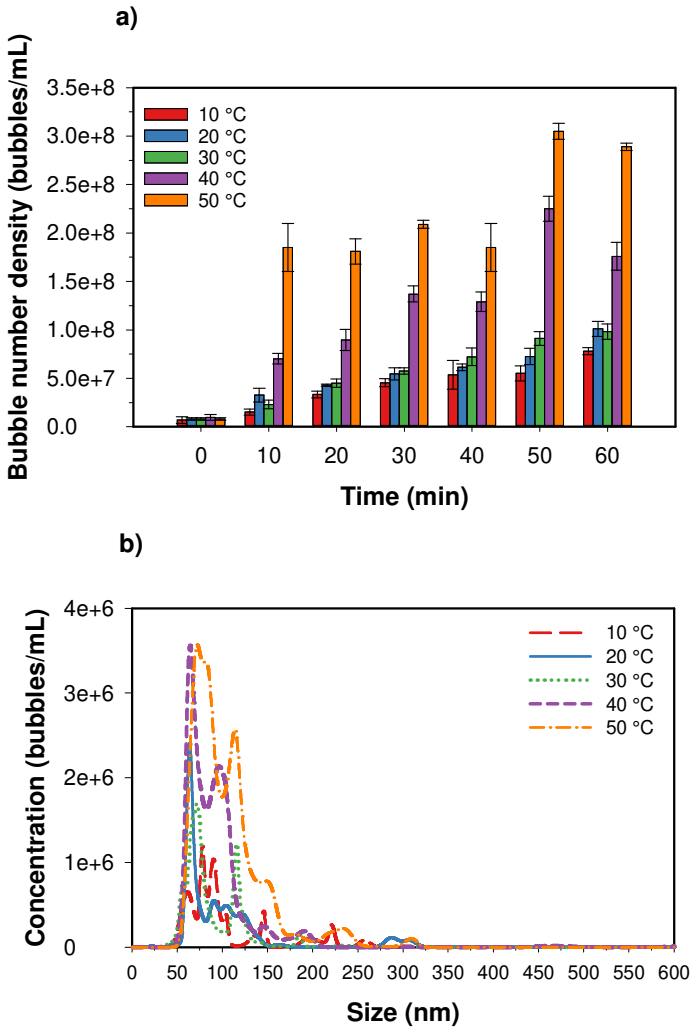

Figure 4.19. Effects of temperature and time on the generation of bulk nanobubbles; a) shows the bubble number density, whilst b) shows the bubble size distribution.

Measurements of the mean bubble diameter and ζ-potential of the bubble suspensions generated at different temperatures are instead reported in **Figure 4.20a-b**. Findings show that

the mean bubble diameter is not affected significantly during the 60 minutes of mixing either by varying the generation temperature. Also, the ζ-potential of the generated suspensions results quite stable and negatively charged with a mean ζ-potential value of ~ -28 mV.

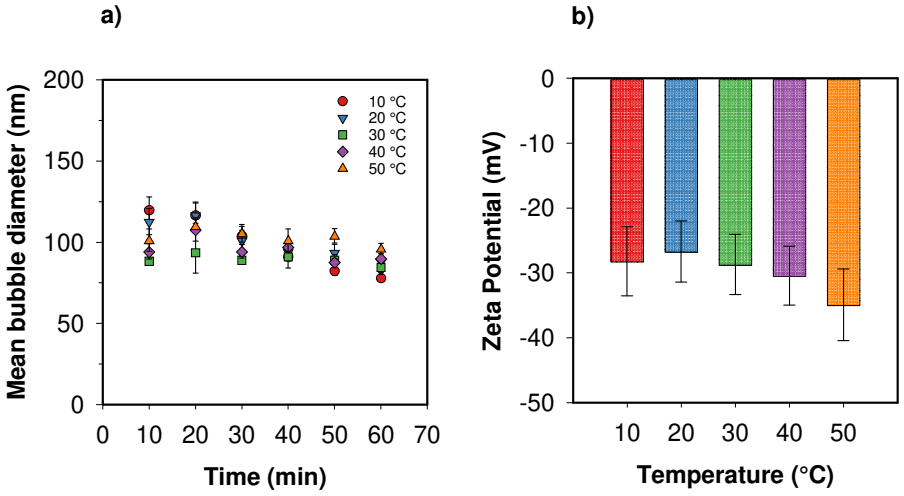

Figure 4.20. Effects of temperature and time on the generation of bulk nanobubbles; a) shows the mean bubble diameter, whilst b) shows the zeta potential at different temperatures of generation.

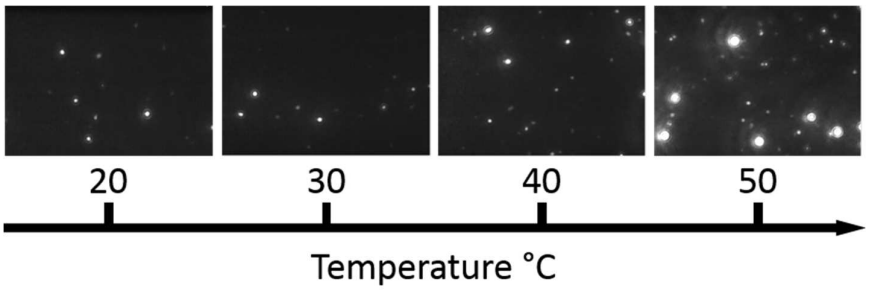

Figure 4.21. Micrographs of bulk nanobubbles generated at different temperatures.

4.5 Batch System - Gas effects

Effects of gas properties are here reported. Experiments were performed with two different stators, the Disintegrating Head and the Vertical Slotted Head respectively, by sparging different gases such as nitrogen and air at different operating temperatures and findings are reported in **Figure 4.22**, where a comparison between the generation with or without gas sparging inside pure water and between the two stators are here presented. The experimental setup is depicted in **Figure 4.18**, where the temperature was controlled by a recirculating cooler (JULABO GmbH, Germany), while the generation time was fixed at 30 minutes. What can be clearly seen in **Figure 4.22a-b** is the growth of bubble number density when gas is sparged in the water during the mixing, which leads to enhance the process yield even at a lower temperature compared to the case without gas sparging, suggesting that increasing the amount of gas during the operations is a benefit for the production of bulk nanobubbles; hence, the entities observed must be gas/vapour filled.

Therefore, it is possible to conclude from these series of experiments that aeration and temperature of the solution are essential parameters for the formation of bubbles in nanoscale, suggesting that both breakup mechanism and hydrodynamic cavitation are the leading causes behind their formation. The bubble size distribution and the ζ-potential of those suspensions were found unchanged compared to the case without sparging of gas, reported in **Figure 4.20a-b**, therefore, not significant effects on the BNBs properties (ζ-potential and bubble size) were found by sparging gases.

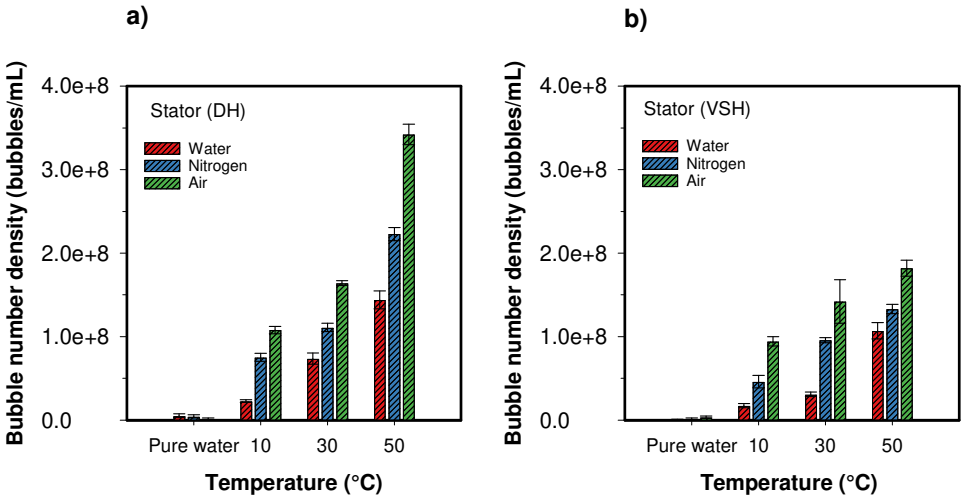

Figure 4.22. Effect of gas sparging on the bulk nanobubble generation. Figure a) shows the bubble number density obtained with the Disintegrating Head, while Figure b) shows the bubble number density obtained with the Vertical Slotted Head.

4.6 Batch mixing – Comparison of mixing assemblies

The Silverson L5 Series mixer has a capacity limited at 12 litres in a batch mode using the Standard Assembly; however, Silverson Ltd, offers a complete range of multipurpose batch mixers with the capacity of up to 30,000 litres (MODEL 700X to MX), thus, offering the possibilities to scale-up the system for the desired applications. Therefore, it has been considered useful understanding of how the working head size affects the generation of the nanobubble suspensions. Different studies were performed with the Standard Mixing Assembly (32mm rotor diameter) and the 1" Tubular Assembly (29 mm rotor diameter). Moreover, it has been found that due to the high dissipation energy of the HSM, it was not possible to control the temperature effectively maintaining the same parameters as before, such as keeping the same amount of water (200 ml), and using a bigger working head size (Standard mixing assembly and 1" tubular assembly) because temperature raised too fast within the

solution. That happened most for the Standard Mixing Assembly; hence, a not accurate comparison between the different rotors could be made.

However, since the operating temperature influences the bubble number density, the study has been done by changing the volume of the sample in order to maximize the bubble number density but keeping reasonable control of the operating temperature. To achieve that goal, the 1" Tubular Assembly was used, and the volume of 350 mL of pure water results being the lower volume possible to use in order to control the temperature effectively using this assembly. Results are reported in **Figure 4.23a-b**, where it is interesting to see that the bubble number density per mL obtained at higher temperature is almost double compared to the previous case. In contrast, the bubble size distribution remained more or less unchanged in the range between 50-300 nm, with a minimal population percentage detected at 300 nm. All of those suspensions were also characterised with the Zetasizer Nano ZSP, and the ζ-potential were constant at the value of ~ -27 ± 2 mV.

Besides, bulk nanobubbles stability was monitored over few months for some samples prepared at different temperatures, and results are depicted in **Figure 4.23c-d**. What stands out in these charts is the astonishing stability of those suspensions. However, finding shows that bubble number density gradually decreased over time (up to 60 days here reported, but observed to be stable for longer). The bubble size distribution retained its shape and did not present any shift on the right side of the nanometric scale, whileits peak gradually decreased over time, hence, suggesting the absence of significant effects from bubble coalescence, bubble breakage or Ostwald ripening. However, further discussions about the long-term stability of BNBs have postponed to Chapter VI for a full detailed explanation about their stability mechanism and physical behaviour.

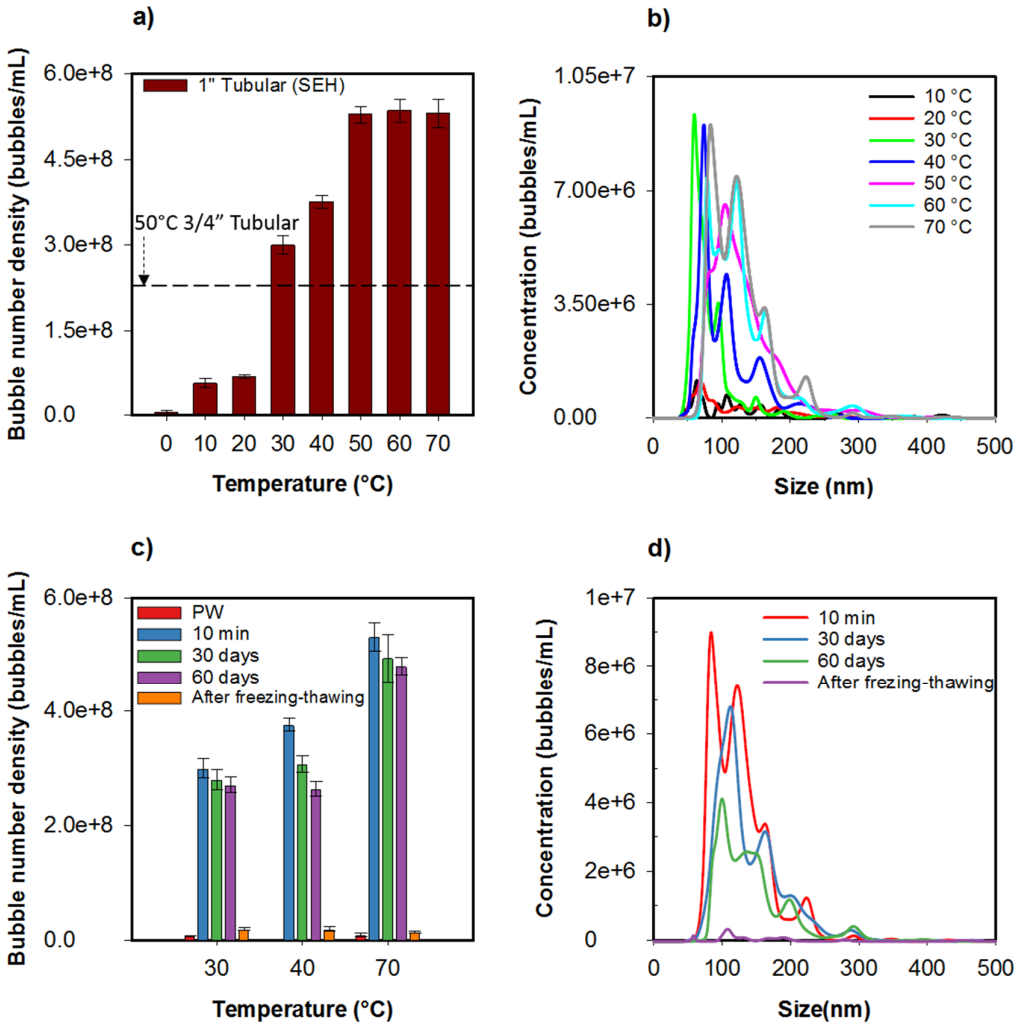

Figure 4.23. Bulk nanobubbles generated with 1" Tubular Assembly; a) bubble number density; b) bubble size distribution; c-d) bubble number density and bubble mean diameter long term study.

Here the study was limited to observe that the entities generated must be gas-filled, thus, do exist in pure water and to support that statement, results obtained by freezing and thawing the suspensions, are presented in **Figure 4.23c-d**. The bubbles suspensions were stored in sealed glass vials and then frozen at -18 °C for 24h before thawed at room temperature for almost 6h. When the samples were thawed completely, suspensions were gently stirred, and a few mL of each sample were flushed into the NS300 chamber and analysed. **Figure 4.23c** also shows the

blank (pure water) that was the sample analysed before starting the mixing operation, but also the difference between the suspensions analysed after 10 minutes from the generation and after freezing-thawing. It is interesting to see the phenomenal disappearance rate after thawing ~94% compared to the suspension generated and analysed after 10 minutes, whilst the size distribution of the suspension studied after thawing did not present any significant peak out of the bubble range. That is a piece of evidence that entities observed must be gas/vapour filled. However, the bubble number density measured after thawing is slightly higher than the value measured in pure water,thus, most likely meaning that some contaminations or impurities must be generated during the mixing operation. Therefore, since the percentage of entities detected after thawing is close to ~ 6 % is a good attitude to consider those as contaminations, even though after successive cycles of freezing-thawing this percentage could be further reduced. The freezing-thawing method could be considered a powerful procedure to estimate the amount, but not the nature, of the solid contaminations generated during the experimental procedures.

It should be pointed out that the results for the Standard Mixing Assembly are not reported since by using that assembly the temperature was difficult to control due to the larger size of the rotor for the setup used, thus, resulting in high energy dissipation within the system leading to the evaporation of the suspension. However was demonstrated that the process of bulk nanobubble generation could be scaled up and some improvements, in order to achieve a larger concentration of BNBs, could be done by reducing the volume of the processed liquid, increasing the rotor size, with the sparging of gases and operating at high temperatures. Therefore, by taking advantage of those results, it could be possible with a new setup to process up to 12L of water by using the Standard Mixing Assembly.

4.7 In-line System

For industrial applications the batch system could represent a limit for its economic edge in term of efficiency and thus as the limited amount of volume processed; therefore the possibility to switch from a batch system to an in-line system for bulk nanobubble generation should be taken into consideration for a more significant throughput and continuous operation. However, this statement is not only valid for bulk nanobubble applications but more, in general, the in-line HSMs have attracted more attention for industrial automatic production processes (Qin et al., 2017, Espinoza et al., 2018).

This section aimed to investigate the capability of the in-line mixing assembly, on a laboratory scale, to generate bulk nanobubbles by using the knowledge developed for the batch system. The in-line assembly could be used in continuous or semi-continuous mode. However, the continuous mode, characterised by only a single passage of the flow within the mixing chamber, was found in being not so fruitful for the BNBs production, since only a single passage is not enough to generate an acceptable bubble number density. Thus, the work here presented was focused on the semi-continuous operating modality.

A semi-continuous mixing consists in a multi-passages of the operating fluid into the working head where the fluid is expelled out from the holes of the stator and subsequently from the main rotor-stator chamber as depicted in **Figure 4.24**.

In addition to the possible sources of contamination already described in **4.2.1**, in this experimental setup, both the PVC tubings and all the glassware including the fritted gas dispersion tube (with micrometric pore diameters) could be possible sources of contamination

during the mixing operation. Note, all the materials were selected and cleaned adequately before each use in order to minimize possible contaminations.

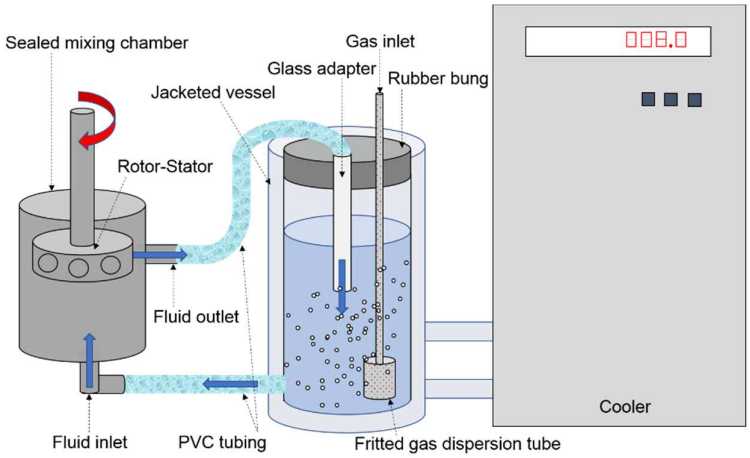

Figure 4.24. Experimental setup for in-line semi-continuous HSM.

It should also be mentioned that the stator has a diameter of 32mm, same as the Standard Mixing Assembly, thus greater compared to the tubular assemblies used and discussed for the batch system. The Standard Emulsor Head (SEH) was used in all the experiments here reported. The working fluid used was pure water (type I), inserted in a jacketed vessel of 200 mL to allow the control of the temperature, which due to the recycling, was possible to be controlled better compared to the batch system, but also allowing us to reduce the volume of the processed fluid in order to increase the bubble number density. The temperature was controlled with an error of ± 3 °C, and dry air was sparged into the water solution during the generation.

Neverthless, since the setup is slightly different from the batch system, the effects of rotor speed at (3500, 7000 and 10250 rpm) were also studied, and results were reported in **Figure 4.25**. Measurements of pure water (time 0), which were checked before starting each experiment and after the freezing-thawing of the suspensions generated, are also included in

the chart. However, due to the high bubble number density generated after 10 minutes, those measurements are not clearly visible in the scale. The chart shows that the bubble number density increases with the revolution per minute, whereas it drastically falls after the application of the freezing-thawing method. Findings suggest that the suspensions generated and observed must not be solid nanoparticles detached from the surfaces of the system used.

Temperature experiments were performed, and the findings reported in **Figure 4.26**. It should be mentioned that, with this experimental setup, the high temperatures could affect the stability of the polyvinyl chloride (PVC) that forms the tubing where the liquid flows.

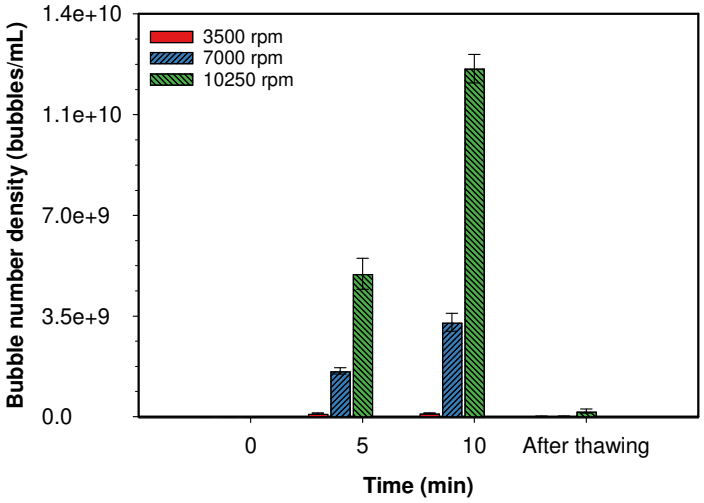

Figure 4.25. Effect of rotor speed for in-line mixing assembly.

Therefore, the experiments were limited at 50 °C for a generation time fixed at 40 minutes. **Figure 4.26a** shows the bubble number density against the time of generation. It is interesting to see the analogies of the results here reported and the findings for the batch system discussed before, however, the in-line assembly allowed us to achieve a higher bubble number density,

that was found to be $3x10^{10}$ bubbles/mL after 40 minutes at 50 °C. **Figure 4.26b** shows the bubble mean diameter obtained for the generated suspensions. It does not change significantly over time, but it slightly increased for a temperature of 50 °C at 100nm.

The suspensions generated were monitored continuously and analysed over time (10 min, 2, 3, 7, 15, 30 days), and after one month the samples were frozen for 24h at -18°C to be subsequently analysed after thawing. Results are depicted in **Figure 4.27**. Findings in **Figure 4.27a** show that the number of bulk nanobubbles decreasing faster during the first week after the generation and then the disappearance rate slowly decrease in the second and third week.

By freezing-thawing the suspensions, findings revealed a reduction between the samples measured after 10 minutes and the samples analysed after thawing ≥ 96% for all the samples analysed. This finding shows again that bubbles disappearing after the phase-changing (liquid-solid-liquid) of water, suggesting that they must be gas/vapour filled and that the contaminations generated during the process are about 4%.

Figure 4.27b shows the bubble size distribution monitored over time. It is interesting to see that the main peak falls during the three weeks, and some peaks appeared after 60 days at ~150 nm and ~200 nm, thus, suggesting the presence of some mechanisms such as agglomeration, interaction between possible contaminants and bubbles, or simply coalescence between bubbles.

In-line HSM was found to be a prominent method for bulk nanobubble generation and to enhance the process yield, specially if compared to a batch system. Instruments are commercially available for processing volumes up to 20 L/min or higher, i.e. the Silverson Verso Laboratory In-Line Mixers, which was also used for the generation of 10 L of bulk

nanobubble suspension to provide multiple evidence that the nano-entities observed and produced mechanically in pure water have indeed gas-filled domains (Jadhav and Barigou, 2020a).

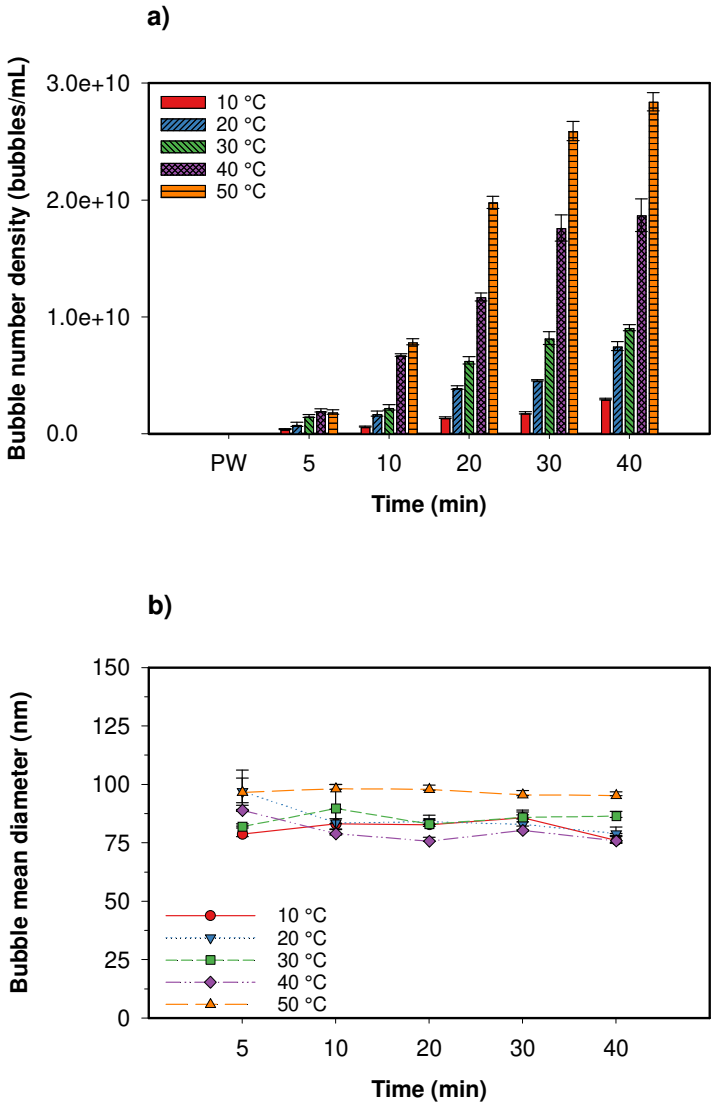

Figure 4.26. Effects of temperature on bulk nanobubble generation; a) shows the bubble number density, whilst b) shows the bubble mean diameter for different temperatures.

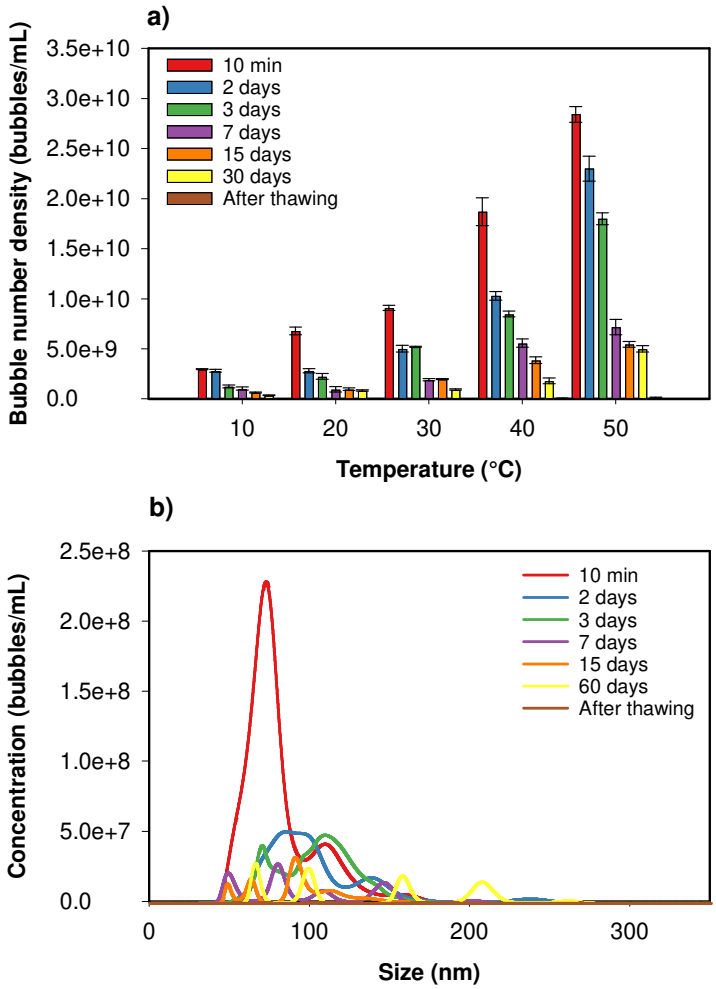

Figure 4.27. Bubble suspensions measured over time; a) shows the long term stability, whilst b) shows the bubble size distribution.

4.8 Conclusions and outlook

High Shear Mixed has been individuated as a valid technique for the bulk nanobubble generation in pure water. From strict analyses of the experimental setup, all the possible sources of contamination in both the batch mixing and semi-continuous in-line mixing were individuated and reported. It has been proved that the entities observed must be gas-filled by

experimental observations described as follow: (i) bubble number density increases by increasing the temperature of liquid during the generation; (ii) sparging different gases enhance the process; (iii) analyses of freezing-thawing revealed that the bubble number density drastically falls of a factor of ~96%, suggesting that the numbers of nanoscale impurities generated during the process are ~4% of the suspension; (iv) bubble number density gradually decreases over time maintaining the mean bubble diameter constant, suggesting that bubbles are inhibited from coalescence or other destabilisation mechanisms, and they must disappear due to the contact with the vials wall or the free surface of the liquid. The stability of the bubbles seems to be governed from a double electric layer. In fact, the bubbles generated are negatively charged with a ζ-potential value of ~ -27mV, which seems not to be affected by the gas used to generate the bubbles.

The semi-continuous mode showed a better efficiency compared to the batch system, leading to generate up to ~10^{10} nanobubbles/mL with a characteristic size of ~ 90 nm. All in all, the high shear mixing, could be used as a bubble generation method to process a high volume of liquid. The BNBs generation has been tested only for a single pair rotor-stator in semicontinuous mode with water as working fluid. However, it is believed that the bubble number density could be increased by forcing the liquid to pass through a series of rotors-stators or using double rotor-stator mixers. Moreover, the shortcomings of this technique are the high energy dissipation and high operating cost to generate bulk nanobubbles. The energy dissipation can be used to increase the local temperature in order to increase the bubble number density, but the total concentration of bulk nanobubbles obtained is still too far from the industry requirements and the cost needed to obtain that concentration on a large volume scale is too high. Thus, improvements in the technique are required to generate a large number of bubble suspensions minimising the cost and able to produce them in on a large scale.

Chapter V

A Henry's Law Method for Generating Bulk Nanobubbles

5.1 Introduction

A new method for generating bulk nanobubbles is here presented. The need to produce BNBs with a different technique arises from the contamination issues already discussed in previous chapters, but also to prove their existence and to better understand the mechanism behind their formation and stability. Among the various bulk nanobubble generation techniques, the compression and decompression of gas, have recently become of interest in the nanobubbles field. Among the various reports on the effects of compression or decompression of gas on bulk nanobubble formation and stability, (Tuziuti et al., 2017) published the influence of the increase in static pressure on bulk nanobubble suspensions. In this study, the authors reported that the bubble concentration decreases after pressurization, suggesting that the impurities present on the nanobubble surface, influenced the growth and the coalescence of the bubbles (**Figure 5.1**). They also reported that during the pressurization, the bubble size increased. Nevertheless, results were based on the effect of the static pressure on bulk nanobubble suspensions, previously generated by a shear method.

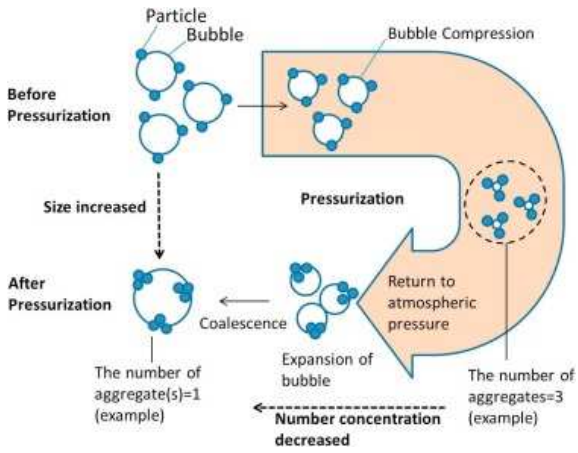

Figure 5.1. Effects of static pressure on bulk nanobubbles suspensions. .The image was taken from (Tuziuti et al., 2017)

A novel and simple method for the bulk nanobubble generation was presented by (Oh and Kim, 2017), in which bulk nanobubbles were generated by mixing DI-water and CO_2 with a linear motion piston. By the ATR-FTRI analyses, they showed that such generated entities, obtained by a mixing time of 120 minutes, were CO_2 gas-filled and they were stable for at least 24h. Previously published studies of the formation of surface and bulk nanobubbles produced by decompression are limited to a low concentration of formed bulk nanobubbles (Fang et al., 2018, Ke et al., 2019). (Fang et al., 2018) produced a very low concentration of bulk nanobubbles ~ 4.2 x 10^7 bubbles/mL, generated after more than 20 min of decompression. The authors reported that the bubble number density decreased by increasing the degassing time. Most recently (Ke et al., 2019) reported a new method of BNB generation named compression-decompression method. This method consisted of pressurization of gas at 10 atm within the solution for a duration time of 10 min, with the subsequently slow releasing of the pressure to atmospheric pressure. This approach, however, led to the generation of a low bubble number density, reported being ~5.8 x 10^7 bubbles/mL.

Research on the generation of size-adjustable bulk nanobubbles based on periodic pressure change has been published by (Wang et al., 2019). Wang's method consists of an electric motor connected to a piston used to cause the periodic change of internal pressure in U-tube. Nevertheless, the authors focussed the attention more on the size and stability of the observed bubbles rather than the concentration obtained. In this study, they also reported an investigation on the effects of the action time (up to 120 minutes) of the periodic change, where they observed that the NBs size decreases with the increase of the action time.

More recently, other authors reported the formation of bulk nanobubbles resulting from repeated compression of microbubbles (Jin et al., 2019). In this study, (Jin et al., 2019) reported a pressure-driven method, which through repeated compression of sulfur hexafluoride (SF_6) gas into water led to the formation of BNBs. They estimated a massive concentration of BNBs generated after 600 times of repeated compression ($1.92x10^{10}$ bubbles/mL); based on the same generation method they showed that microbubbles collapse and turn into bulk nanobubbles (Jin et al., 2020). A common statement in some of these papers is that the nanobubbles concentration is affected by the decompression time.

In this chapter, it is presented a new technique based on Henry's law's vacuum degasification principle for generating BNB suspensions in pure water, by means of successive expansion-compression strokes inside a sealed syringe. The bubble number density obtained is characterised by a high concentration. Multiple pieces of evidence that the observed nano-entities must be gas-filled nanobubbles are reported and discussed. The first part of this chapter will focus on the validation of the technique reported, followed by the study of the influence of expansion-compression cycles number; the type and concentration of dissolved gas in water, and its solubility on the formation of BNBs. A discussion of how sparging of added gas

enhances the process yield and how the bulk nanobubble generation is affected in degassed water will be reported. Finally, we propose a tested automated model of the technique and outline the basis for process scale-up.

5.2 Materials and Methods

Ultrapure double distilled water with pH between 5.0 to 6.5, water resistivity in the range between 0.7 – 1.0 mOhm·cm and conductivity in the range between 1.0 -1.5 µS/cm, produced by an Acquatron A4000D distillation system (Cole-Parmer Ltd, Staffordshire, UK), has been used to test the method. Ultrapure water (type I) with the resistivity of 18.2 MΩ·cm, the conductivity of 0.055 µS/cm and pH of 6.7, at a temperature of 20 °C, was obtained from a water purification system (Avidity Science, UK) in which the feed water is purified first through reverse osmosis (RO), and then after passing through different filters (such as the Endure Purification Module). The water is further purified by Ultraviolet (UV) Photo Oxidation at 254 nm and 185 nm to eliminate trace organics and inactive microorganisms present in it. Typical values are TOC < 5ppb and Endotoxin < 0.03 EU/ml. Type I water has been used in all of the experiments to generate bulk nanobubbles

Different syringes were tested for the bulk nanobubble generation in order to understand the mechanism behind their formation and the production of impurities. *BD plastic syringes* with and without Leur lock tip of 10 mL and 20 mL volume size, were bought from Becton Dickinson and Company (BD) (Franklin Lakes, New Jersey) and properly cleaned before being used to generate bulk nanobubbles. The rubber seal, typically is lubricated with medical-grade silicone oil (<0.25 mg/cm^2) to avoid the friction between the plunger (polypropylene) and the barrel (polypropylene), was removed from the plunger rod and appropriately cleaned by

immersion in 10% water – analytical grade ethanol (99.9% pure) solution for 3 hours, dried with a stream of pure nitrogen and then cleaned for several times with hot type II water and finally dried. *VacLoK syringes* (10 mL Vacuum Pressure Syringes) were purchased from MeriMedical (South Jordan UT, USA). That syringes are made to keep the vacuum inside the barrel (polycarbonate). To avoid the contamination coming from the lubrification oil, the same procedure described above was applied. Samco *glass syringes* of 5 mL volume size, manufactured by S. Murray & Co (Surrey, UK) were purchased from VWR International (Pennsylvania, USA).

All glassware was cleaned by immersion for 10 min in boiling type II water, for several times, rising with type I water, drying in a microwave oven and flushing with a flow of high-purity dry nitrogen before being used.

Air Gas Cylinder, Nitrogen (Oxygen-free) 230 bar cylinder and Pureshield Argon Cylinder and Carbon Dioxide with industrial-grade were purchased from The BOC Group (Guildford, UK). Those gases were sparged into the pure water, in a glass jacketed vessel of 100ml, and the temperature of the water was controlled by using a recirculating cooler (JULABO GmbH, Germany).

The absolute pressure sensor MPX5700AP, from the MPX5700 Series piezoresistive transducer, ideally suited for microprocessor or microcontroller-based system with A/D inputs, (700kPa and 0.2-4.7V output), purchased from RS Components Ltd., was used to monitor the pressure generated inside the syringes' barrel. The microcontroller Arduino Uno Rev3 MCU Development Board purchased from RS Components Ltd, was used to interface the transducer

to the system engineering software LabVIEW (Laboratory Virtual Instrument Engineering Workbench).

5.3 Technique Validation

This section aims to provide a validation of the innovative technique reported to generate pure nanobubbles in the bulk liquid.

5.3.1 Pressure sensor calibration

The MPX5700AP piezoresistive transducer was used before each experiment to read the pressure generated inside the closed syringe and also to test syringes from leakage since their prolonged use could allow air to get inside the barrel due to a loss of adhesion between the rubber and the barrel. The pressure sensor was connected to an external microcontroller Arduino Uno Rev3 MCU Development Board (Arduino, Italy) that was interfaced with the system engineering software LabVIEW (Laboratory Virtual Engineering Workbench, National Instruments, Texas, US). A schematic of the setup is reported in **Figure 5.2**.

The pressure sensor has been calibrated following the datasheet provided by NXP (Eindhoven, Netherlands) and implementing the transfer function in the code written in LabVIEW. The transfer function used is the following:

$$V_{out} = V_S \cdot (0.0012858 \cdot P + 0.04) \pm \delta \quad \textbf{(5.1)}$$

where V_{out} is the signal received from the microcontroller and detected by the pressure transducer, V_S is the voltage required by the transducer (Vs = 5V) that is the voltage the

microcontroller provides by default to an external A/D sensor; P is the pressure registered by the transducer, and $\delta = 0.025\ V_{out}$ is the measurement error.

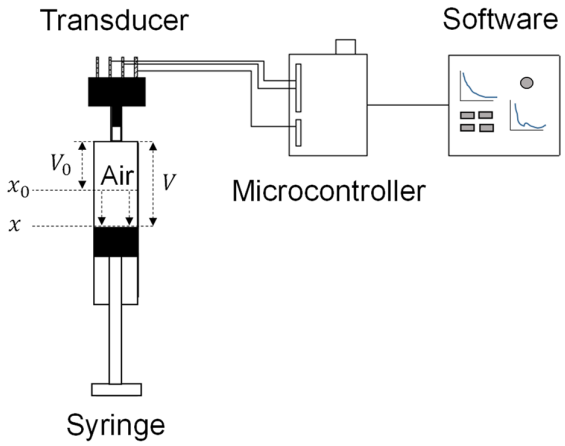

Figure 5.2. It shows the general setup used to test the syringe before starting the experiments.

To test the accuracy of the pressure sensor, a Pressure-Volume (or *P*-*V*) curve was constructed using a 10 cc empty plastic syringe. Initially, at time $t = 0$, the tip of the syringe is sealed, and the plunger is in its initial arbitrary position x_0 corresponding to a certain amount of air V_0 inside the syringe, which is at initial pressure P_0 equal to atmospheric pressure (P_{atm} = 1 atm = 101.325 kPa). By pulling out the plunger from x_0 to x, as depicted in Figure 5.3, the volume of air inside the barrel expands from V_0 to V, and the internal pressure decreases according to the ideal gas law:

$$PV = nRT \tag{5.2}$$

where P, V and T are the pressure, volume and temperature; n is the number of moles and R is the ideal gas constant (8.31441 $J \cdot mol^{-1} \cdot K^{-1}$). By running the experiment at constant room

temperature (~ 25 °C) and fixing the initial volume of air present inside the syringe V_0, it is possible to estimate the number of moles of air. Thus, the readings of the sensor could be checked against theoretical values. The most accurate experimental results, with the least deviation from the ideal gas law predictions, were obtained by making the atmospheric pressure correspond to a volume of 5 ml and changing the syringe volume by pulling or pressing the plunger in the same direction.

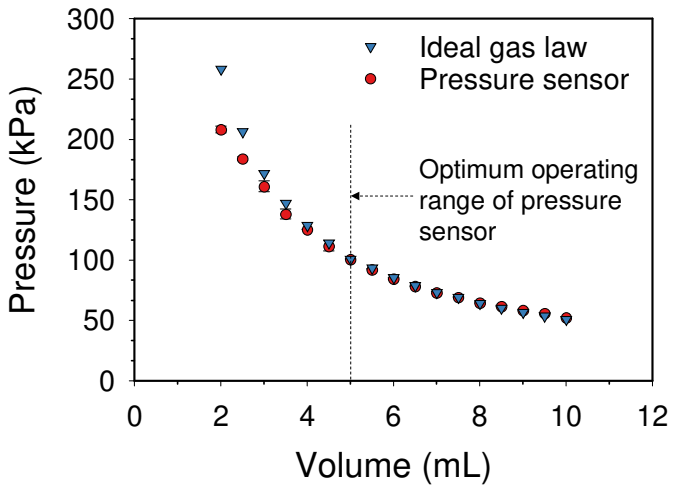

Figure 5.3. P-V diagram obtained by moving the plunger inside the barrel, containing an initial volume of air of 5 ml.

From the figure above, it is possible to see a divergence between the two curves below the volume of 3 mL and pressure above 150 kPa, that could be explained due to the not proper sealed connection between the sensor and the syringe. However, this issue is starting for pressures higher than 150 kPa, and thus, it will not affect our results since we are always below that value.

5.3.2 Expansion – Compression cycles

Considering an empty cap-sealed syringe, a vacuum condition is created inside the barrel by pulling out the plunger from the initial position. In order to quantify the vacuum level created inside a 10mL volume syringe, the sensor was directly connected to its tip, after had carefully removed the air within the barrel. Nevertheless, an experimental error is made since we are neglecting the presence of air trapped into the dead space of the syringe (0.10 mL) and the air present into the sensor since those were difficult to remove. A *P-V* diagram was obtained, and the results are shown in **Figure 5.4.**

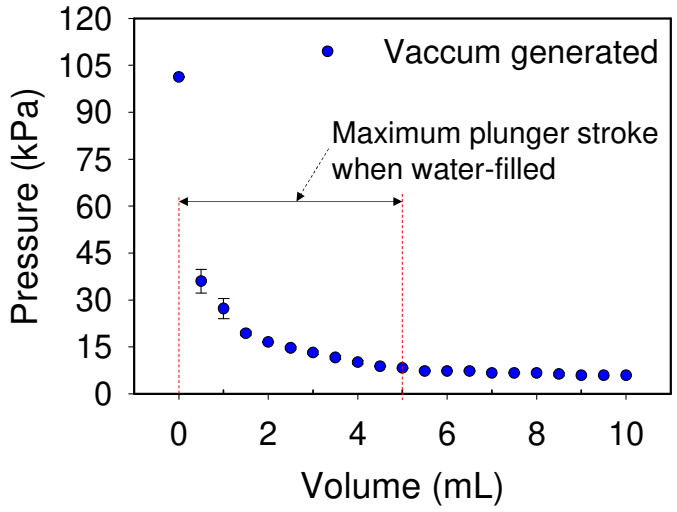

Figure 5.4. P-V diagram for a syringe without air inside. The pressure decreases faster in the first 3 mL of volume.

Figure 5.4 shows a sharp drop of pressure in the first 2 mL of syringe volume; it goes from the atmospheric value to about 15 kPa to gradually decreases until the end of the plunger stroke. What is standing out from this trend is a confirmation of the well-known phenomena that by

pulling a plunger of a closed syringe, a high vacuum level is generated. With or without water inside the syringe, the vacuum generated is comparable with the only difference that when the syringe is water-filled, the stroke of the plunger is limited due to the presence of the water; therefore, the maximum stroke corresponds to an expansion of the volume inside the barrel approximately of 5 mL (~33.90 mm) as depicted in **Figure 5.4.**

The choice of syringe material and size, as well as the volume of water used for the generation of BNBs, are critical. After a series of tests, glass and stainless steel syringes were discounted because glass syringes tended to release silica impurities, whilst stainless steel syringes generated too much friction for manual operation. Polypropylene plastic syringes with a latex-free elastomer seal are highly resistant to most solvents and chemicals (Sastri, 2010, Sastri, 2013) as well as being abrasion resistant (Wagner Jr, 2016). They generated much fewer impurities and were found to be the most appropriate for manual handling. It has been established, that the syringe size of 10 mL and the volume of water of ~ 6 mL were optimum parameters for ease of manual operation, i.e. for generating sufficient but manageable pressures, as well as providing adequate samples of BNB suspension for analysis. Three different syringes were used each time to increase the data quality, for a total of 18 mL of water processed for each sample. In order to generate BNBs, the syringe was filled with pure water and, sealed with a plastic Leur lock cap after having removed carefully all the bubbles of air trapped inside, included the gas present in the dead space (0.10 mL).

According to Henry's law, at a constant temperature, the saturation concentration of gas in a given liquid, i.e. the amount of dissolved gas, is directly proportional to the partial pressure of the gas above the liquid, thus:

$$C = K_H P \quad \textbf{(5.3)}$$

where C is the gas solubility (in units of M or mL gas/L) at a given temperature in a particular solvent, P is the pressure of the gas above the solution (often in units of atm) and K_H is Henry's law constant (often in units of M/atm).

Therefore, subjecting the liquid to reduced pressure makes the dissolved gas less soluble and, hence, leads to gas molecules being released. This principle forms the basis of the technique of vacuum degasification (Coker, 2007).

The initial pressure inside the barrel, when the water is loaded and the gas present in dead space removed, is homogeneous and it is equal to the atmospheric pressure. It is shown that subjecting the water to vacuum pressure at constant temperature inside a syringe creates gas undersaturation which, when followed by vacuum release, leads to the formation of BNBs. In order to increase the number of bulk nanobubbles generated, the plunger of the syringe was pulled down and released for several times (cycles). This has been called an expansion-compression method, and it can be described as two main steps that are replicated for the desired number of cycles: the *expansion* and the *compression*.

The expansion - Since the syringe is closed at the top from the Leur lock cap and at the bottom from a rubber seal, that could be considered a closed system. During the expansion, obtained by pulling out the plunger of the syringe, as shown in a 3D view of the syringe made by Autodesk Inventor (California, USA) in Figure 5.5**a**, a high vacuum is generated inside the syringe as reported in Figure 5.5**b**.

At this stage, the volume of the chamber increases due to the expansion and the pressure inside decreases in an inverse relationship that is given by:

$$P = \frac{c}{V} \tag{5.4}$$

where P is the pressure, V is the volume and c is a constant.

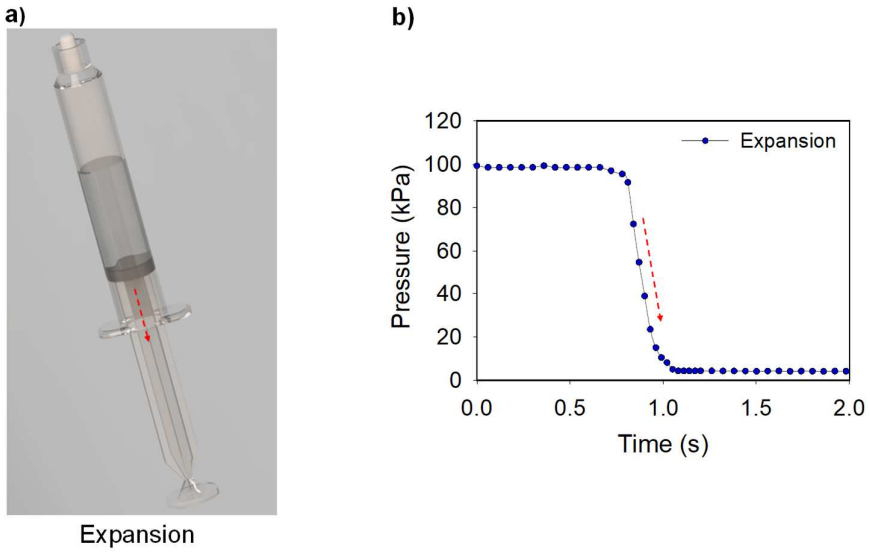

Figure 5.5. a) A 3D representation of the sealed syringe made using Autodesk Inventor (California, USA) is presented; b) It represents the typical trend for the pressure versus the time during the vacuum creation step.

Thus, a partial vacuum condition is created inside the barrel and the amount of gas (initially dissolved in the water), remains constant inside the chamber. It has been shown that subjecting the water to vacuum pressure at constant temperature inside a syringe, by pulling out its plunger, the water pressure reduces substantially much below atmospheric (~ 4.9 kPa = 0.048 atm), which results in a decrease in air solubility and creates local gas undersaturation. The released air molecules form thousands of microbubbles which, as the pressure decreases, increases their volume, hence, increases according to Boyle's Law (Boyle, 1662):

$$P_1V_1 = P_2V_2 \tag{5.5}$$

where P_1 is the original pressure, V_1 is the original volume, P_2 is the new pressure, and V_2 is the new volume.

Due to the expansion bubbles start to grow, and they become clearly visible in the syringe barrel. The expansion of microbubbles was recorded with a high-speed camera Pentax K3II (Pentax Ricoh Imaging Company Ltd., Japan) and frames of the bubble growth are reported in **Figure 5.6**. Subsequently, some bubbles rise-up and burst as soon as they reached the free surface, while other remains in the bulk liquid before the fast compression that occurs immediately after the expansion.

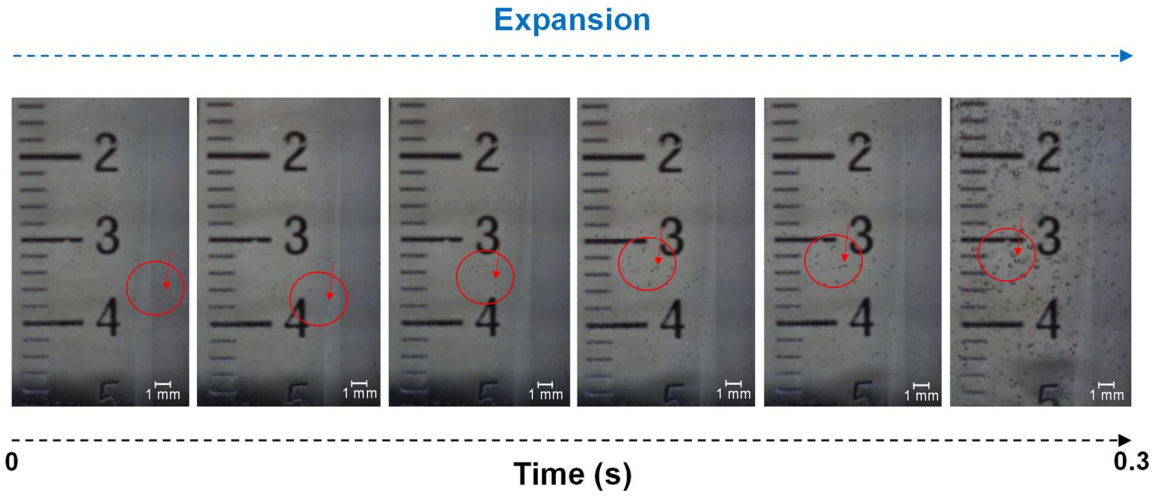

Figure 5.6. Typical frames sequence of growing bubbles during the expansion.

The compression – Whilst in the previous step, the water was depressurised by quickly pulling the syringe plunger out, during the compression the water is pressurised again by the instant release of the plunger which travels at relatively high velocity under the action of vacuum pressure (typically ~ 7 cm s^{-1}).

Figure 5.7a shows a 3D representation of the syringe during the compression, whereas **Figure**

5.7b shows the pressure versus the time as the plunger goes back to its original position. By releasing the plunger, the volume of bubbles decreases accordingly to the equation (**5.5**), and microbubbles collapse and disappear (Jin et al., 2020). In this phase, a quick compression of the fluid against the top wall of the barrel occurs, and that is recorded as a peak by the pressure sensor and reported in **Figure 5.7b**. In this step, the gas released in the previous step is mixed back to the liquid, and bulk nanobubbles are formed. A schematic of the generation process is depicted in **Figure 5.8**.

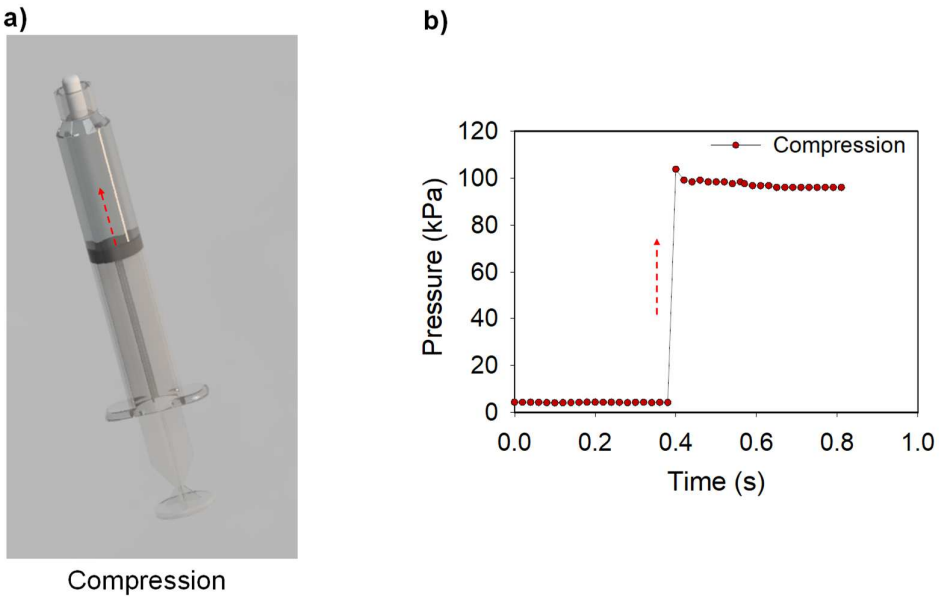

Figure 5.7. a) A 3D representation of the sealed syringe made using Autodesk Inventor (California, USA) is presented. b) It represents the typical trend for the pressure versus the time during the compression step.

It should be noted that a sufficient amount of vacuum needs to be created inside the syringe in order to cause enough dissolved gas to be released as well as have enough pressure differential during the compression stage to enable the formation of BNBs. In other words, the pressure inside the syringe during the expansion stroke needs to be as low as possible.

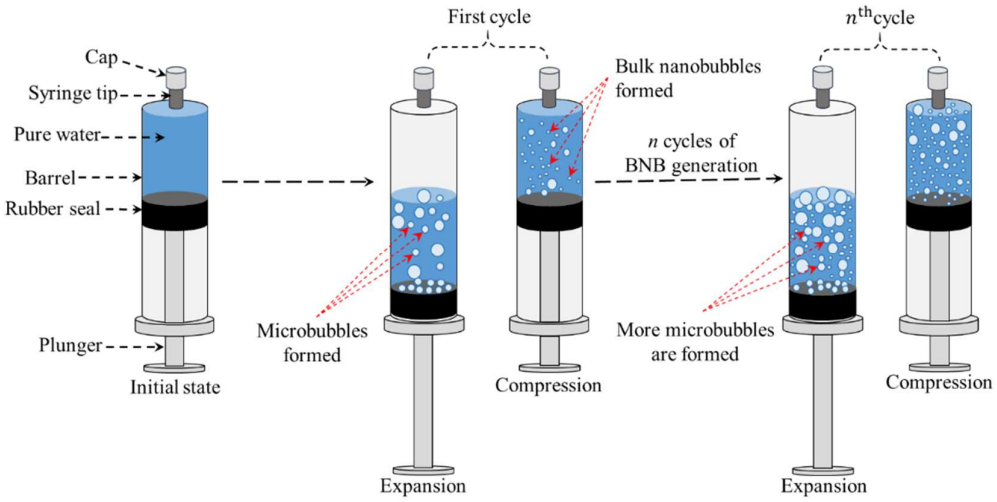

Figure 5.8. Schematic representation of the BNB generation process by means of successive expansion-compression cycles of pure water in a syringe.

It has been observed that the more are the cycles, i.e. (0, 5, 15, 30, 40), and the more are the bubbles generated inside the liquid that could be, in first approximation, observed through the Tyndall effect obtained by illuminating the suspensions with a laser source, in this case a 532 nm laser system (green laser) as reported in Figure 5.9. What stands out in **Figure 5.9** is the high rate of light scattering as the cycles number increase. The laser light goes through all the samples, from the left to the right, and it is possible to observe that it gradually increases starting from the pure water sample, which does not scatter light since it does not contain any impurities.

It should be noted, however, that if the absolute pressure of water is reduced to its vapour pressure at the prevailing temperature, it boils and vapour bubbles develop, a process commonly known as cavitation. The vast majority of the experiments were conducted at a temperature of 20 °C with a minimum absolute pressure of ~ 4.86 kPa inside the water-filled syringe, which is well above the water vapour pressure of 2.33 kPa at the same temperature (Hundy et al., 2008). Hence, cavitation did not play a role in the process of BNB generation.

Figure 5.9. Tyndall effect of bulk nanobubble suspensions. Samples were illuminated from left to right.

Some limited experiments were performed at temperatures of 5, 15, 25 and 35 °C to investigate the effects of air solubility in water. The operating vacuum pressure in the syringe was marginally below vapour pressure (5.67 kPa = 0.056 atm) only at 35 °C where air solubility was least. Any amount of cavitation which might have occurred in this case, however, would have been insignificant and did not affect the results of the temperature experiment, as discussed further below. In conclusion, whilst the method described here has been tested solely on the basis of Henry's law effects, in practice, any occurrence of cavitation can only assist the process of BNB generation. However, it is unlikely that cavitation will play any significant role even if the pressure inside the syringe falls below the vapour pressure because the time available for cavitation to take effect towards the end of the expansion stroke is very short.

(Takahashi et al., 2007b) in their research found through the Electron spin-resonance spectroscopy, that as microbubbles collapse in the absence of a dynamic stimulus, free-radicals are generated. Other authors reported the formation of hydroxyl radicals as microbubbles collapse and that might affect the stability of nanobubbles (Agarwal et al., 2011, Jin et al.,

2020). It has been observed that the bulk nanobubbles generated with the technique here presented resulted in being very stable, suggesting, as further discussed in chapter VI, that the stability of BNBs could depend from the OH^- ions absorbed on their interface, due to the negative ζ-potential measured. However, further, and specific studies on the bulk nanobubbles properties and stability mechanism are postponed to the next chapter.

5.3.3 Reproducibility

The reproducibility of the results is essential, not only because the method here presented is new, but also to understand the parameters that could affect the generation of bulk nanobubbles. Therefore, experiments were performed on different days for different cycles number. The reproducibility of the sample has been tested at room temperature with BD plastic syringe and type II water obtained by an Acquatron A4000D water distillation system (Cole-Parmer Ltd, UK). A volume of 5 mL of water was loaded into different plastic syringes, and bulk nanobubbles were generated for different cycles in the range between 5 - 45 cycles. Each bar, in Figure 5.10, represents the bubble number density at a specific number of cycles. Pure water is also included, and measurements are present but lie down on the graph origin because of the scale.

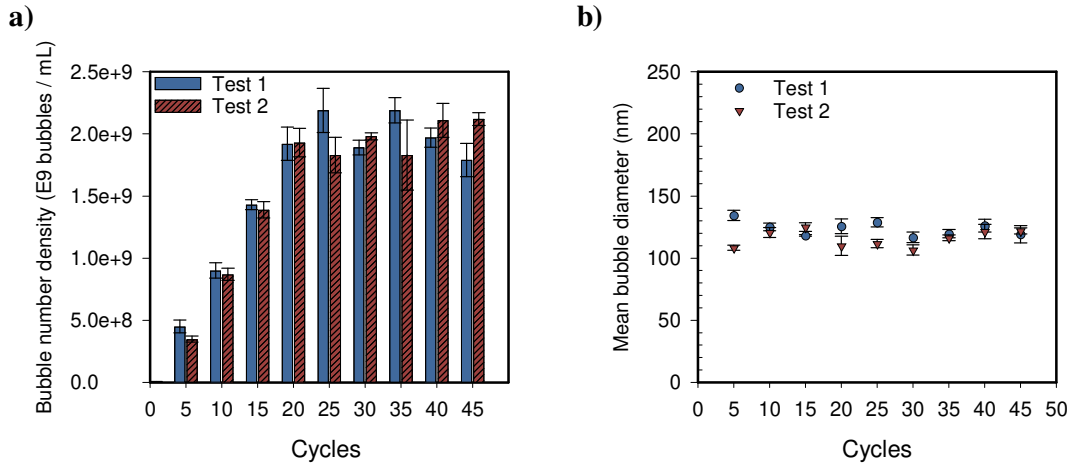

Figure 5.10. Figure on the left (a)shows the bubble number density against the cycles number, whereas the scatter plot on the right (b) shows the mean bubble diameter.

What can be clearly seen in this figure is that bubble number density increases with the cycles number, as also shown in **Figure 5.9**, before to reach a plateau. The reproducibility of the samples (test1 and test2), which were prepared in two different days, suggests that a specific process occured in order to generate BNBs. It should be noted that the size of bulk nanobubbles are not affected by the number of cycles with the mean bubble diameter constant around 120 ± 10 nm.

5.3.4 Bulk nanobubbles or solid nanoparticles?

Due to the impossibility with the light scattering-based techniques to make a clear distinction between bulk nanobubbles and solid nanoparticles, it could be claimed that the entities here analysed and reported are not nanobubbles but nano-entities detached from the friction between the rubber seal and the barrel, droplets of silicon oil not well removed from the rubber seal and the barrel or in the worst-case scenario, contaminations coming from the solution used to clean

them. Those, together with the initial possible contaminations present in pure water, are the only contaminations that we could be claimed in that system.

Therefore, in this work, we provide pieces of evidence for the existence and generation of bulk nanobubbles, and the importance of the role covered by the dissolved gas in their fabrication by (i) generation at different dissolved oxygen concentration, thus, at different temperatures of the solution for different syringe cycles; (ii) generation at different temperatures of the solution with a fixed number of syringe cycles; (iii) increasing the bubble number density with the replacement of the dissolved gas every 30 cycles of generation; (iv) generation in pure water at different degassed levels. Additionally, to prove that the entities generated by expansion-compression are bulk nanobubbles and not contamination of any type, we will discuss: (v) the generation with different syringe types and the analysis of the bubbles' suspension by freezing-thawing method, and (vi) by spectroscopy analyses, including GC-MS and IPC-MS, of bubble suspensions.

5.3.4.1 Glass syringe versus plastic syringes

Due to the reproducibility of the results generated by the expansion-compression method, a comparison between different syringes has been made to understand if the material selected could influence the results observed. One of the main reasons for that is the already discussed issue of the easy-generation of nano-entities during the production of BNBs. Therefore, due to the lack of the characterisation instruments, able to make a distinction between nanoparticles and gas-filled nanobubbles in suspension, there was the need to test different syringes made of different materials such as glass, stainless steel and plastic. In order to have a first information of the generated entities, it was considered useful to analyse the bubble number density after

the freezing-thawing method, hence, to have an estimation of the possible impurities generated. This step is crucial in the validation of a new bubble generation technique because it provides useful information, and thus, a first evaluation of the suspensions generated, trying to distinguish between solid-entities like nanoparticles, i.e. nanoparticles detached from the friction betweenthe barrel and the plunger in the absence of a lubricant, and soft-core entities like droplets or bulk nanobubbles that during the freezing of the suspension they might, for hypothesis, coalesce or collapse due to the changing phase of the water.

Ultrapure water type I has been used to generate bulk nanobubbles suspensions, the cycles number was fixed at 30, and the generation took place at room temperature. Glass syringe (Samco glass syringe) and plastic syringes (BD plastic and VacLock plastic) were used to generate the suspensions, whereas the stainless-steel syringe was revealed difficult to handle for the manual operations, therefore it was discarded. Results are reported in **Figure 5.11**. **Figure 5.11a** shows the bubble size distributions of suspensions immediately after the generation, whereas **Figure 5.11b** shows the bubble size distributions after the freezing-thawing process. What is striking in these charts is that the plastic syringe distributions behave similarly compared to the glass syringe distribution. However, it should be noted the difference between the Samco glass line and the BD plastic lines in the chart after freezing-thawing (**Figure 5.11b**).

The bubble concentration generated in plastic syringes falls close to zero, whereas the sample generated by glass syringe remains predominant, meaning that after thawing the suspension continues to scatter light. In other words, the latter was not completely affected by the change of the water phase during the freezing-thawing process, suggesting the presence of solid nanoparticles. Therefore, interesting is to compare the bubble size distribution generated

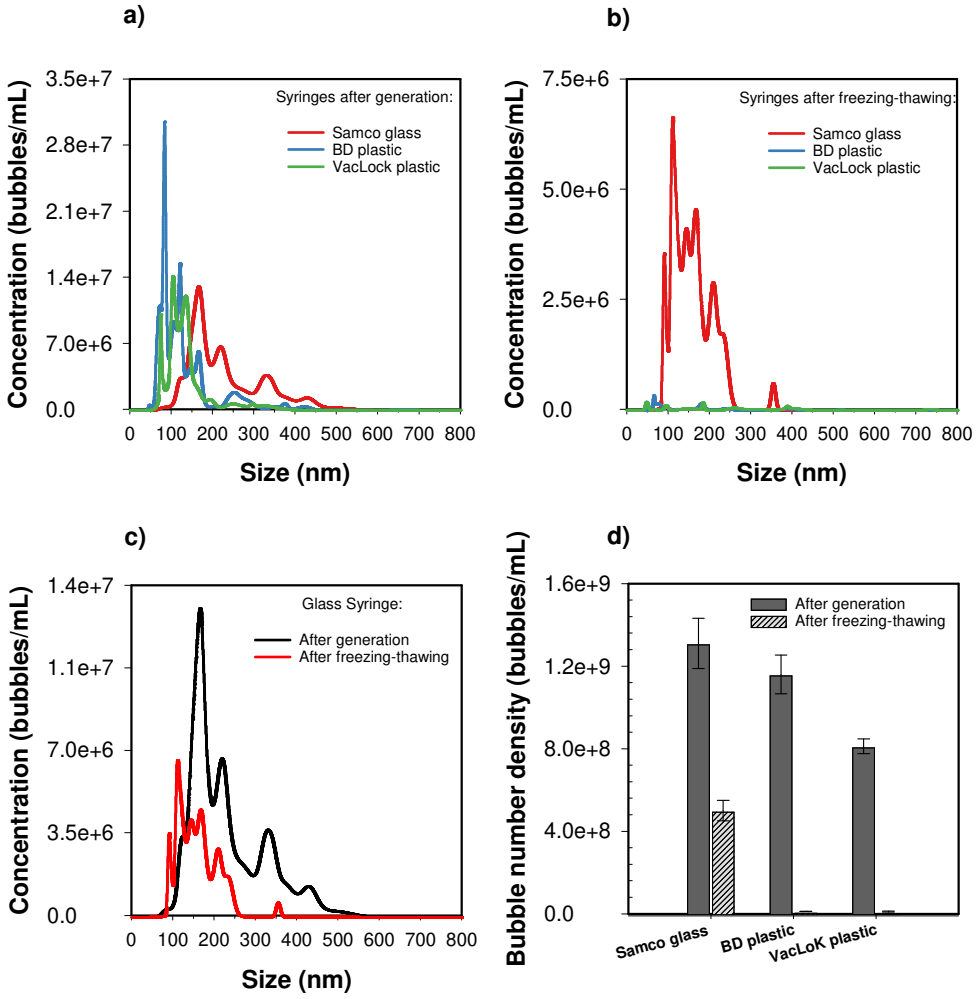

Figure 5.11. a) Bubble size distribution for different syringes after generation; b) bubble size distribution for different syringes after freezing-thawing; c) comparison between bubble size distribution before and after freezing-thawing for glass syringe; d) bubble number density obtained with different syringes.

with the glass syringe before freezing and after thawing (**Figure 5.11c**). What can be clearly seen is that the two distributions have a similar shape, but the freezing-thawing line (red line) results shifted on the left, and that could be explained if it is considered that during the BNB generation, both bulk nanobubbles and glass nanoparticles could be generated, but with the freezing-thawing process only bulk nanobubbles disappear. By analysing the bubble number density (**Figure 5.11d**) this statement is more evident. In fact, in the case of the glass syringe, after thawing, only 61% of bubbles disappeared, whereas, in the case of plastic syringes more

than 97% vanished.

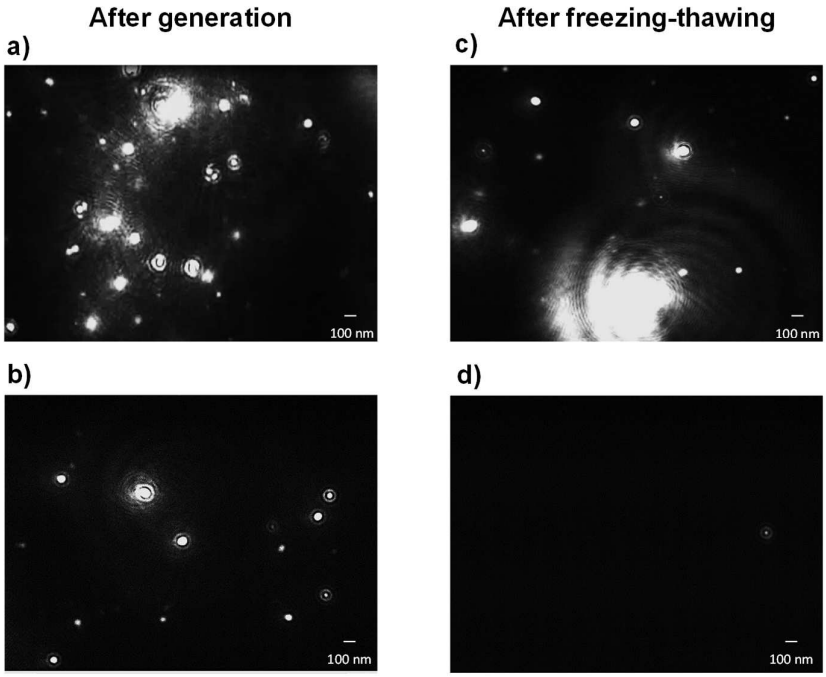

Figure 5.12. a-b) Micrographs of suspensions after generation with (a) glass syringe, and (b)plastic syringe; c-d) micrographs of suspensions after freezing-thawing, (c) glass syringe, and (d) plastic syringe samples.

Micrographs of suspensions after generation and after thawing were extrapolated from the video recorded with the NS300 and reported in **Figure 5.12**. What is interesting in these figures is not only that for the suspension generated with the glass syringe the particles remain in the sample even after the freezing-thawing but also that the light is scattered differently compared to the suspension generated with the plastic syringe, and that is clearly visible analysing the the live video during the measurements..

Therefore, since the glass syringe was not provided with any rubber seal to prevent the friction between the barrel and the plunger, it is possible to conclude that during the stroke of the plunger some silica nano-entities were detached from the glass due to the high friction

generated. Further analyses, however, have been made to understand if, the suspensions analysed and generated by the plastic syringe are effectively bulk nanobubbles or oil nanodroplets. Those analyses have been made by using the mass spectroscopy analyses and in particular, the *Gas Chromatography-Mass Spectroscopy (GC-MS)* and the *Inductively Coupled Plasma–Mass Spectroscopy (ICP-MS).*

5.3.4.2 Gas Chromatography-Mass Spectroscopy Analysis

Gas Chromatography-Mass Spectroscopy (GC-MS) is an analytical method characterised by the combination of the features of gas-chromatography and mass spectrometry to analyse and identify tiny amounts of a substance in the suspension. The analyses of water and bulk nanobubbles suspensions were performed with an Agilent 7890A gas chromatograph (Agilent Technology, UK) equipped with ZB-WAX column (30m x 0.25, thickness 0.25 um, Phenomenex, UK) coupled to a GCT Premier mass spectrometer (Waters, UK) operated in electron ionization (EI+) mode. Helium was used as a carrier, and make-up gas passed through the column at a constant flow rate of 1.0 $mL \cdot min^{-1}$. The injection volume was 1 µL, which was used with a split ratio of 1:10. The column temperature programme was as follows: the temperature was held at 50 °C for 2 min, increased to 250 °C at 5°C min^{-1} and then held at 250 °C for 118 min. A resume of the main parameter is reported in Appendix A (**Table 10**).
Results are shown in **Figure 5.13**. During the analysis, the software elaborates a graph from the signal received called a chromatogram, as shown in the figure below. Each peak of the chromatogram standing for the signal generated as a compound elutes from the GC column into the detector. The y-axis shows the intensity (abundance), whereas the x-axis represents the retention time (min).

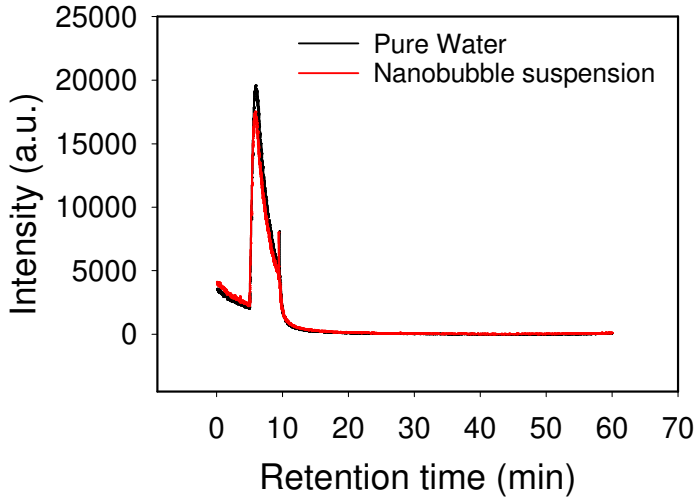

Figure 5.13. Chromatogram generated by a GC.

What stands out from **Figure 5.13** is that the retention time of pure water is superimposable with the retention time obtained for the nanobubble suspension. This finding shows that no trace of any organic contaminants was found in the suspension generated, in fact, and more in general, if the GC conditions (oven temperature, column type, etc.) are the same, a given compound, water in this case, will always elute from the column at nearly the same retention time.

5.3.4.3 Inductively Coupled Plasma-Mass Spectroscopy Analysis

Inductively Coupled Plasma–Mass Spectroscopy (ICP-MS) is a type of mass spectrometry that uses the inductively coupled plasma to atomize the sample and to create polyatomic ions, which are then detected by the instrument. This technique is well-known for its ability to detect, at low concentration, the presence of metals and inorganic elements in liquid samples. ICP-MS

analysis of pure water and bulk nanobubble suspensions generated by glass and plastic syringes has been performed with a NexION 300X ICP-MS spectrometer (PerkinElmer, UK), which was equipped with a cyclonic spray chamber and a SeaSpray concentric nebulizer, to detect the presence of any trace of inorganic particles. Analytical results were quantified by the internal and external standard addition mode. All the standards were prepared in 2% aqueous solution of HNO_3. Single element stock solutions (Sigma-Aldrich, UK) of 21 elements, namely, Na, Mg, Al, Si, P, S, K, Ca, Ti, V, Cr, Mn, Fe, Co, Ni, Cu, Zn, Rb, Sr, Zr and Hg at 1000 ppm concentration were used to prepare the standards for external calibration. The parameters used and the calibration curves, with the corresponding correlation coefficient ($R^2 > 0.99$) are reported in **Appendix A**. Indium at 1 ppm was employed as the internal standard. Samples analysed were acidified using 2% HNO_3 before ICP-MS sampling. Samples, also, were supplied to the nebulizer in continuous mode with the spectrometer peristaltic pump using flared end poly(vinyl chloride)-based tubing of 0.19 mm internal diameter.

The results obtained for the pure water and the bulk nanobubble suspensions generated with the different syringes are reported in **Figure 5.14**. As shown in the figure, there is a consistent presence of Si and Sr in the sample generated with the glass syringe and a small presence of Ca, meaning that the sample analysed differs from the blank, which in our case is the pure water (black line).

On the other hand, the presence of Si, S and Sr, was also found in the sample prepared with the BD plastic syringe, although in much smaller proportions. That finding is consistent with the results reported in **Figure 5.11d**, which shows the number density of the particles measured before and after thawing by the NS300, thus, provide also evidence that the freezing-thawing

method helps to distinguish between solid-nanoparticles detached during the generation and soft-core nano-entities.

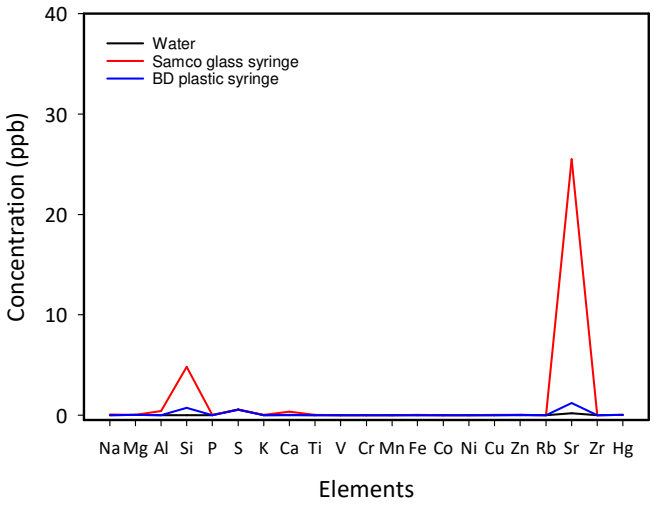

Figure 5.14. ICP-MS results for pure water (black line) and suspensions generated with Samco glass syringe (red line) and BD plastic syringe (blue line) are shown.

All the results of ICP-MS are reported in **Table 6**. Results in **Table 6** show that the BNB suspensions generated with the plastic syringe contained extremely low levels of metal traces mostly similar to pure water. The concentration of Si in the nanobubble suspension is higher than in pure water, which suggests the existence of some syringe abrasion effects. It should be pointed out that the sample analysed by ICP-MS represents a probably worst-case scenario where the syringe was deliberately overused (>400 cycles) to assess the amount of potential impurities that can be generated and, hence, the usability of the syringe. In reality, the amount of such impurities can be controlled at much lower levels by generally restricting the number of syringe cycles to less than ~200. Nonetheless, the concentration of these impurities is still far too low, and the observed nano-entities cannot, therefore, be attributed to the presence of metal/nonmetal contamination. In conclusion, these analyses combined strongly suggest that the observed nano-entities must be gas-filled bubbles.

Inductively coupled plasma mass spectrometry results			
Elements	*Pure Water (ppm)*	*Glass syringe sample (ppm)*	*Plastic syringe sample (ppm)*
Na	0.0017	0.0509	0.0012
Mg	0.0034	0.0255	0.0046
Al	0.0015	0.3835	0.0028
Si	0.0005	4.7883	0.7260
P	0.0002	0.0098	0.0015
S	0.5509	0.5148	0.5340
K	0.0008	0.0191	0.0015
Ca	0.0020	0.3236	0.0184
Ti	0.0000	0.0047	0.0003
V	0.0001	0.0000	0.0001
Cr	0.0000	0.0006	0.0001
Mn	0.0000	0.0003	0.0001
Fe	0.0047	0.0192	0.0010
Co	0.0004	0.0001	0.0000
Ni	0.0001	0.0006	0.0001
Cu	0.0000	0.0044	0.0004
Zn	0.0002	0.0206	0.0055

Table 6. ICP-MS analysis results for pure water and bulk nanobubbles suspension generated with glass and plastic syringes

5.4 Importance of dissolved gas in bulk nanobubble generation

This section aims to report further proofs of the existence of bulk nanobubbles by using BD plastic syringe that generates, as verified, very low amounts of impurities. It should be pointed out that at the moment of the BNB generation, if all the air trapped into the barrel is carefully removed, the only gas available to form bulk nanobubbles is the dissolved gas in the liquid. Therefore, to understand the BNB formation within the barrel, the attention should be focused on the dissolved gas in the liquid.

Bulk nanobubble suspensions were generated (i) starting from different water temperatures, (ii) for different cycles of generation, (iii) replacing the gas in the liquid after several cycles and (iv) in partial degassed water. All the results show that the presence of dissolved gas at the moment of generation influence the bubble number density but not the mean bubble diameter, always constant around the value of ~100 nm. The stability of bubble suspensions has also been monitored for weeks, showing the long-term stability of the NBs generated.

5.4.1 Effects of temperature and cycle numbers

It is well known that, in general, as the temperature of a gaseous solution is raised, the gas is coming out until the complete degassing occurs at the boiling point of the solution. This variation of the solubility of a solute as a function of the temperature can be reported as:

$$\left[\frac{\partial \ln(\bar{x}/x)}{\partial T}\right]_P = -\frac{\Delta H}{RT^2} \quad \textbf{(5.6)}$$

where x is the mole fraction of the gaseous constituent in solution, $\bar{x}$ is the mole fraction of the gas in the vapour above the solution, T represents the thermodynamic temperature, R is the gas constant (8.314 JK^{-1} mol^{-1}), ΔH is the heat of solution expressed in kJ mol^{-1} at a given temperature and pressure, and P is the total pressure above the solution. This equation, however, strictly holds only for solutions where all the molecular interactions are the same and therefore have ideal behaviour (Hitchman, 1978). In other words, the quantity of dissolved air is affected by the solvent temperature; the lower the water temperature, the higher is the air solubility. Based on that consideration, employing different numbers of expansion-compression cycles using water at different temperatures, bulk nanobubbles were generated. According to Henry's law **(5.3)**, different gases have different K_H values at the same temperature, thus, K_H is a function of the nature of the gas, however, it also varies with the temperature.

The temperature of the water was controlled by an external cooler (JULABO GmbH, Germany) and the air gas was sparged inside the glass beaker (80 mL) for 30 minutes with a flow rate of 227 l/h at different temperatures 5, 15, 25, 35 °C. The dissolved oxygen (DO) has been checked by a dissolved oxygen meter (Jenway 9500, Cole-Parmer, Staffordshire, UK) 1 minute after the airflow was stopped. At this point, the syringe was sunk into the pure water, loaded, and all the bubble of airs trapped inside the dead space and barrel were carefully removed before sealing the syringe and starting the generation of the suspension. The characterisation of bulk nanobubbles was done immediately after for different cycles number. A schematic of the experimental setup is shown in **Figure 5.15.**

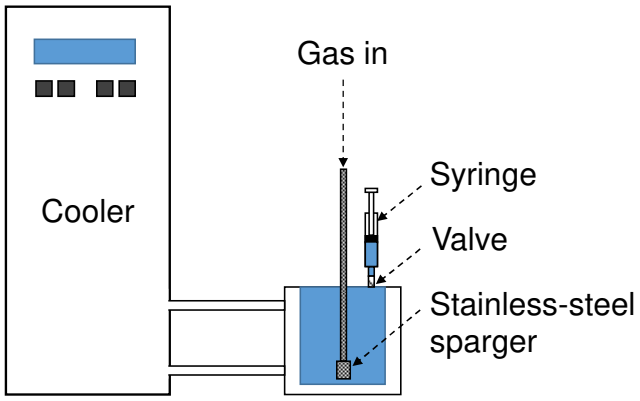

Figure 5.15. Sketch of the experimental setup for gas sparging. Gas was sparged into the water for 20 min with a 200 µm pores size stainless steel sparger, while an external cooler controlled the temperature.

Results plotted in **Figure 5.16a** shows that the number of BNBs increases with the number of generation cycles. At temperatures of 25 °C and higher, the bubble number density levels off after about 40 cycles as the available released gas is depleted. However, at lower temperatures, the curve does not reach a plateau even after 90 cycles and continues to increase, albeit at a slower rate, which implies that more released air is still available in the water which requires more cycles to convert into BNBs. As expected for gas-filled bubbles, the temperature plays a crucial role. The number density is much higher at lower temperatures and declines steeply at higher temperatures because as the temperature of a gaseous solution is raised the gas is driven off, therefore, less is the DO concentration in the liquid. The bubble number density (bubbles/mL) against the DO ($mg \cdot L^{-1}$) at different water temperature is plotted in **Figure 5.16b**; it is interesting to see the almost linear relationship between the number of bubbles generated and the amount of DO in the liquid at the moment of the generation, in fact, the bubble number density increases as the DO increases.

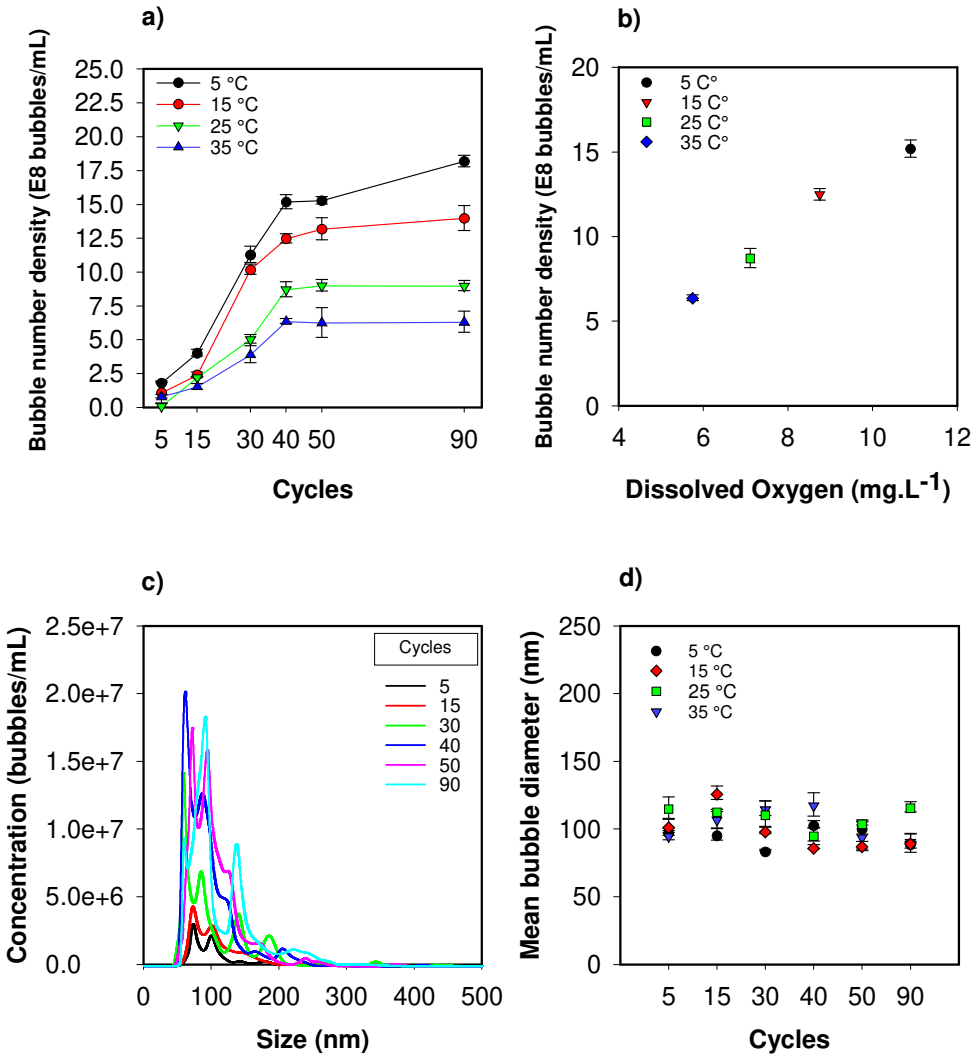

Figure 5.16. a) Bubble number density against cycles; b) bubble number density against the initial dissolved oxygen level; c-d) bubbles size distribution on the left and mean bubble diameter on the right.

While the number density increases with the number of generation cycles before reaching a situation of a plateau, the bubble size distribution, and the mean bubble diameter seems to be not affected by the number of cycles as shown in **Figure 5.16c-d**. The size distribution reported refers to bubbles generated at 25°C, and it is distributed in the range between 50 - 250 nm for all the cycles, whilst the mean diameters, for different temperatures and different cycles, are always around 100nm ± 20nm.

5.4.2 Effects of temperature at fixed cycle numbers and stability

The effects of the temperature for different generation cycles have been explored and discussed previously. Due to the significant positive correlation between the dissolved oxygen and the bubble number density, by fixing the number of cycles, mostly for high cycle numbers, the relation between the dissolved gas held by the liquid at different temperatures and the number of bubbles generated becomes more evident. The results here reported show the bubble number density against the temperature. Similar trends are well known for the gases solubility in water against the temperature (Garde et al., 1999). The number of generation cycles is here fixed at 40, which was the optimal value for the BNB generation for almost all the temperatures previously reported. Results are depicted in **Figure 5.17**. **Figure 5.17a** shows a gradual drop in the bubble number density as the temperature rises from 5 °C to 40 °C. The temperature study was limited at 40 °C, since after that temperature, the properties of the plastic materials start to change (i.e. deformation of the plastic barrel) and was not possible to generate reliable measurements. What is striking in **Figure 5.17b** is that the mean bubble diameters are not affected by the temperature, and is always 100 ± 20nm. Bulk nanobubbles expressed a negative charge according to the ζ-potential measured by DLS instrument.

It is interesting to see that the ζ-potential of all the suspensions is very stable around -35 ± 5 mV, meaning that the bulk nanobubbles generated by expansion-compression of microbubbles are very stable as depicted in **Figure 5.17c**. A likely explanation of the formation of the electric double layer around each bubble could be the adsorption of OH^- at the gas/liquid interface, which could be formed during the collapsing of microbubbles (Takahashi et al., 2007b, Masuda

et al., 2015). Last but not least are the results reported in **Figure 5.17d**, where the bubble suspensions generated were studied before and after the freezing-thawing method.

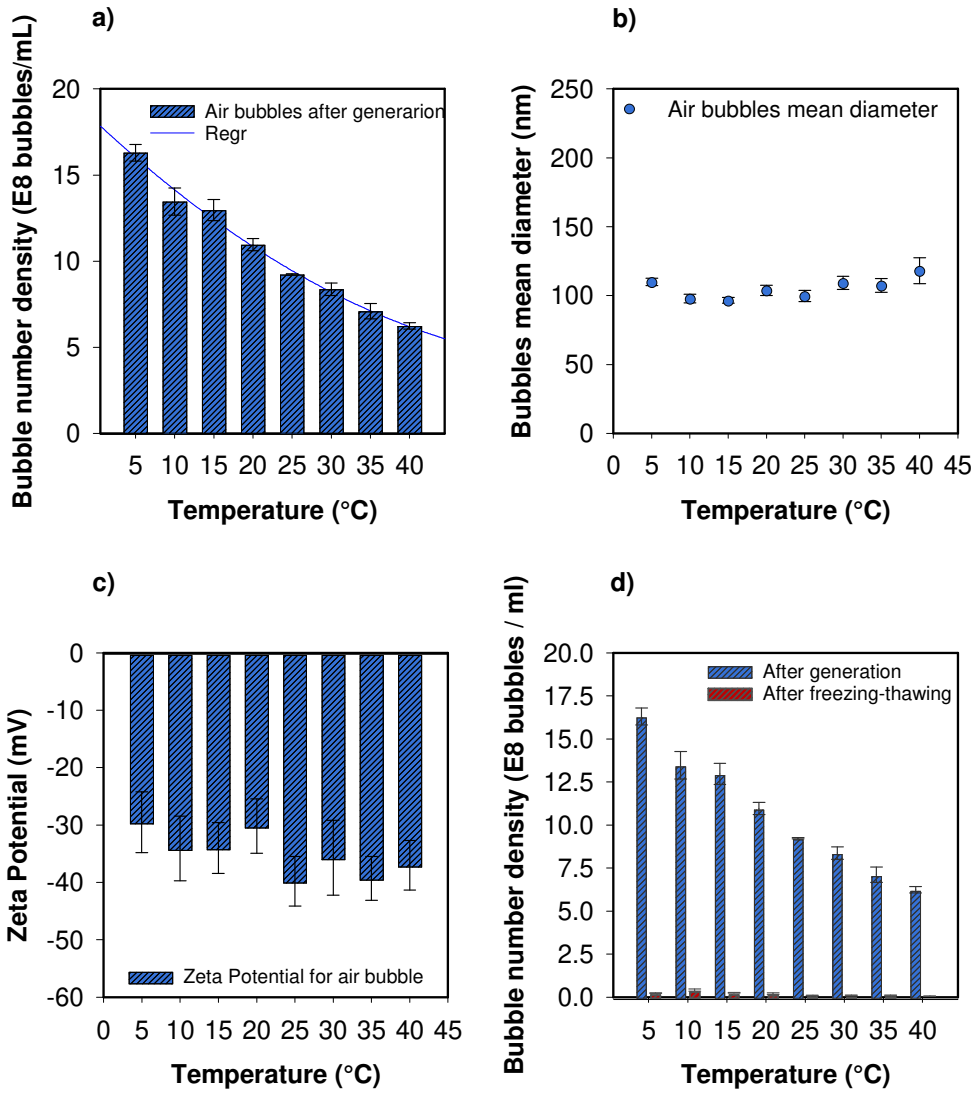

Figure 5.17. Bulk nanobubbles generated ad fixed cycles number (40 cycles) versus temperature. a) Bubbles number density against temperature; b) mean bubble diameter; c) ζ-potential; d)freezing-thawing analyses.

All the suspensions were frozen at -18°C for 24h and thawed for 6h at room temperature before being analysed again. What stands out in this figure is the dramatic decline of the bubble

number density, more than 96% of all the suspension disappeared after thawing as also reported in **Table 7**.

Temperature	***b.n.d.* before freezing***	***b.n.d.* after thawing***	***Percentage difference (%)***
5°C	1.63E+09 ± 4.89E+07	2.47E+07 ± 1.86E+06	-98.48
10°C	1.35E+09 ± 7.95E+07	4.17E+07 ± 6.66E+06	-96.91
15°C	1.30E+09 ± 6.06E+07	2.53E+07 ± 2.27E+06	-98.05
20°C	1.10E+09 ± 3.56E+07	2.05E+07 ± 4.84E+06	-98.13
25°C	9.23E+08 ± 4.23E+06	1.14E+07 ± 4.62E+05	-98.76
30°C	8.38E+08 ± 3.61E+07	1.07E+07 ± 2.51E+06	-98.72
35°C	7.11E+08 ± 4.46E+07	1.09E+07 ± 2.48E+06	-98.46
40 °C	6.25E+08 ± 1.80E+07	6.50E+06 ± 1.61E+06	-98.96
***bubble number density (b.n.d.)**			

Table 7. The bubble number density of the generated suspensions at different temperatures before freezing and after thawing. The disappearance rate is also reported as a percentage difference.

The suspension generated at 5, 15, 25 and 35 °C were analysed over time (**Figure 5.18**). **Figure 5.18Figure 5.18a** shows the bubble size distribution monitored up to 40 days. It should be noticed the bulk nanobubbles stability due to the high zeta potential value. The bubble concentration slowly declined as the bubble size distribution collapsed over time, as shown in **Figure 5.18**, indicating that the nano-entities were gradually disappearing whilst their average diameter and zeta potential retained their initial values previously reported (**Figure 5.17b-c**).

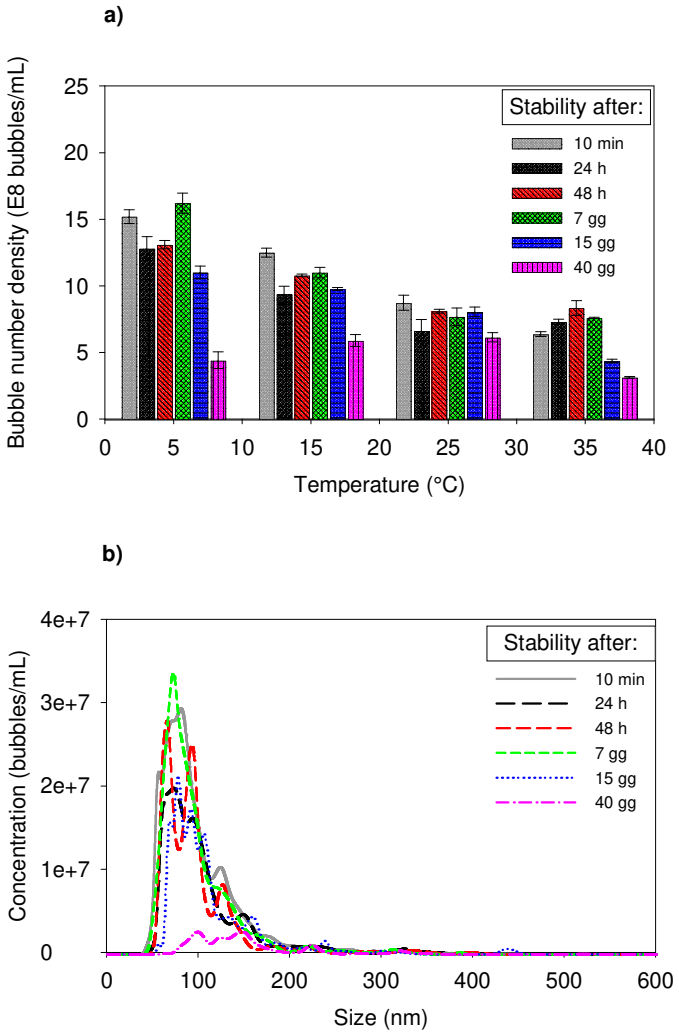

Figure 5.18. Long term stability of bulk nanobubbles generated at different temperatures. a) Bubble number density; b) bubble size distribution.

The gradual depletion in time of the nano-entities observed supports the hypothesis that they must be gas-filled. Such behaviour is characteristic of the stable bubbles, which vanishing over time through no apparent breakage, coalescence, or Ostwald ripening. A possible reason behind their depletion could be attributed at the collision between the bubbles and the vial walls, where they were stored, or due to the interaction with the free surface. Similar observations were argued with BNBs produced by other generation methods (Nirmalkar et al., 2018a, Nirmalkar

et al., 2018b, Jadhav and Barigou, 2020a); such conjecture has been experimentally confirmed by a more recent paper (Kanematsu et al., 2020), in which the influence of the storing system was studied.

Based on these observations, it is possible to safely discount the possibility that the observed nano-entities are solid nanoparticles, since their disappearance should occur through a growth in size, showing peaks on the right side of the size distribution graph due to their aggregation or sedimentation. Note that all the samples were stirred before the NTA analyses. Thus, since no peaks or sedimented particles were observed, the reported nano-entities must be nanobubbles.

In conclusion, all the data presented show the dominance of the bubble number density at a lower temperature but also the high disappearance rate generated as a consequence of the freezing-thawing technique. BNBs generated at different dissolved oxygen level showed a gradual disappearance over time, which in addition to the results reported in **Figure 5.13** and **Figure 5.14**, represents further proof of the existence of bulk nanobubbles.

5.4.3 Generation in degassed water

In this section, we report the effects of the degassing time on the bulk nanobubble generation in pure water. Therefore, if the dissolved oxygen plays a crucial role in nanobubble formation, by partial degassing the pure water, we should generate fewer bubbles. The experimental setup designed for the degasification of the pure water and the direct generation of bulk nanobubbles inside that system has been schematically illustrated in **Figure 5.19**

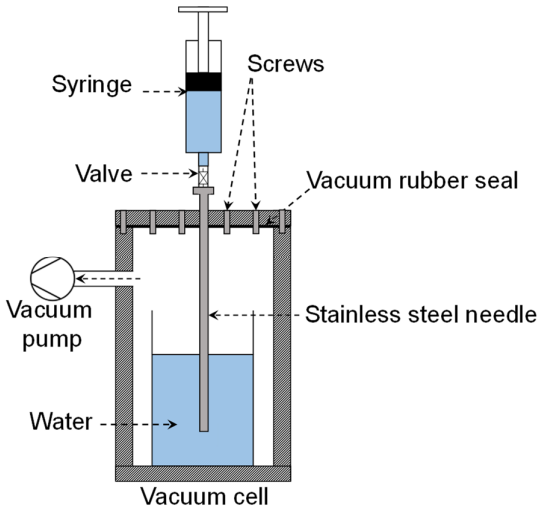

Figure 5.19. Schematic of the BNB generation in degassed water.

A beaker with pure water was placed within an airtight plexiglass box, where the lid was fixed to the base through several screws and a sealed rubber as depicted in **Figure 5.19**. On the side of the box, a pipe was directly connected to the vacuum pump. A stainless steel needle was inserted inside the beaker and connected to a valve, which was shut before the generation of the BNBs. A vacuum of 15 mbar was created inside the box chamber, and the water was degassed for different hours. Findings are reported in Figure 5.20. Figure 5.20**a** shows the bubble number density against the degassing time. Whilst, the mean diameter remains more or less unaffected throughout, results show that the longer the water degassing time, and the fewer were the nano-entities observed per unit volume. This experiment aimed to show the importance and the influence of the dissolved gas in the water on the generation of bulk nanobubbles. Findings show that after a degassing time of 5 h, there was about 50% reduction in the number density compared to the entities generated in non-degassed water. It means that the gas dissolved at the beginning in pure water is essential for the formation of the bulk nanobubbles.

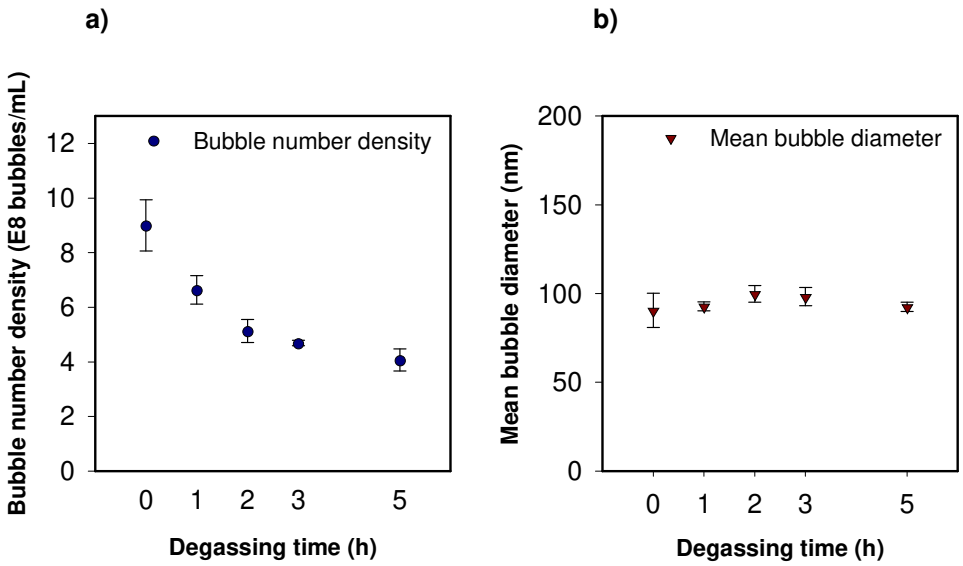

Figure 5.20. Bulk nanobubbles generation in degassed water; a) bubble number density versus degassed time, b) mean bubble diameter versus degassed time.

The considerable dependence of the bubble number density with the degassing time is another strong indication that the entities observed must be gas-filled nanobubbles. However, questions arise spontaneously from that conclusion: can we go beyond the plateau shown in **Figure 5.16a** ?. Is it possible to increase the bubble number density per unit volume? Those questions are analysed in the following section.

5.4.4 Effects of gas replacement on bulk nanobubble generation

It was demonstrated in the previous sections that the dissolved gas is a key parameter behind the generation of bulk nanobubbles; however, it was also reported that after some cycles of generation a situation of the plateau was reached and the bubble number density did not increase significantly beyond that limit. This section aims to answer at the following question: is it possible to increase the bubble number density per unit volume?

A study was performed replacing the gas in the barrel of the syringe after a specific number of cycles, fixed at 30 (~ the beginning of the plateau reported in **Figure 5.16a**). After the first 30 cycles, the sample was placed in a glass vial of 20 mL and sparged with the pure air for 2 minutes at room temperature. The same sample was loaded again into the syringe, the gas in excess well removed, and the syringe was closed again with the male Luer lock cap. The generation of bulk nanobubbles was done for other 30 cycles, and this process was repeated for four times. The bubble number density reached the value of ~4.18 x 10^9 bubbles/mL, whereas the mean diameter of the generated suspensions remained unchanged and always constant at 100 ± 10 nm. Results are shown in **Figure 5.21a-b**.

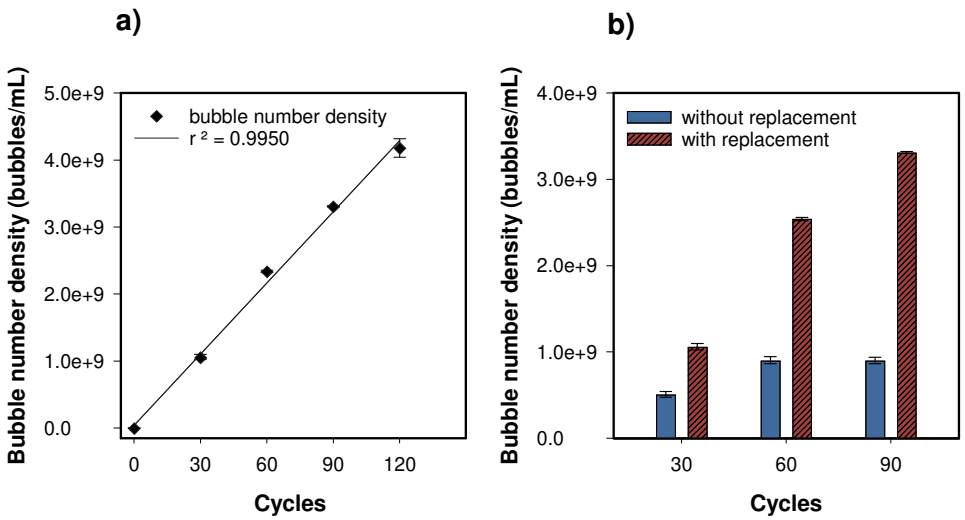

Figure 5.21. Effect of repeated additional air sparging on the generation of bulk nanobubbles. a) bubble number density as the gas is replaced during the cycles; b) bubble number density with and without gas replacement.

Results displayed in **Figure 5.21a-b** show that sparging enables water to be resaturated with air, thus, allowing the concentration of BNBs to increase linearly well above the bubble concentration obtained without sparging. Therefore, repeated sparging of air might provide a mechanism for producing a significantly higher concentration of bulk nanobubbles, which has so far been elusive. Furthermore, these findings represent further evidence that the number of

nano-entities being significantly augmented by the supply of additional air, hence, they must be bubbles.

5.4.5 Generation of bulk nanobubbles with different gas

The effects of type of dissolved gas on the formation of BNBs were explored by pre-sparging nitrogen, argon and carbon dioxide in pure water for 20 min with a flow rate of ~200 l/h at a controlled temperature in the range 5–35 °C. The experimental setup used is illustrated in **Figure 5.15**. The DO has been checked by a dissolved oxygen meter (Jenway 9500, Cole-Parmer, Staffordshire, UK) before and after sparging the gasses into the water. However, when nitrogen, argon and carbon dioxide were sparged into the water, they replaced the oxygen gas content and therefore the value read by the meter was 0% for 15, 25, and 35 °C and 7% (DO 0.83mg/L) for water at 5 °C, thus, it could be considered that the suspensions of bulk nanobubbles are made by bubbles filled with the relative gas sparged within the liquid.

It should be reported that due to the high solubility of carbon dioxide, during the expansion, the gas dissolved in water was fast released affecting the following compression cycle. Therefore, there was not enough pressure difference to drive the plunger up in order to compress the microbubbles and form bulk nanobubbles, thus, carbon dioxide was excluded from the results.

Since different gases have different solubility, under the pressure of 101.325 kPa at room temperature, the solubilities of nitrogen, oxygen and argon are respectively, 1.11 mM, 2.31 mM, 2.51 mM (Fernández-Prini et al., 2003). By volume dry air contains approximately

78.09% of nitrogen, 20.95% of oxygen, 0.93% of argon, 0.03% of carbon dioxide and small amounts of other gasses (Cox, 2000); gasses dissolve in water according to their partial pressure and absorption coefficient. If the gas is a mixture of more gasses like air, each gas of this mixture will dissolve according to its partial pressure and absorption coefficient, therefore, the percentage composition of the mixture in solution is different from the percentage composition in the vapour phase. Excluding the minor components of air, if we assume that its approximate percentage composition in volume is: N_2 80% and O_2 20%, at the atmospheric pressure of 1,0 atm, it will correspond the partial pressure of P_{N_2}= 0.8 atm and P_{O_2}= 0.2 atm. When air is dissolving in water, it happens proportionally to the partial pressure of the constituents and to their absorption coefficients, thus, the ratio O_2/N_2 in water will be around O_2 33.5 % and N_2 66.5% of (Silvestroni, 1997). Therefore, in the case of air, it is expected to find different gas-filled bubbles.

The effects of air sparging have already been discussed, and results reported in **Figure 5.17**, whilst the results for nitrogen and argon are reported in **Figure 5.22. Figure 5.22a** shows the bubble number density obtained for argon and nitrogen. It is interesting to see that even in that case, the trend is similar to the one obtained and already discussed for the air in **Figure 5.17a**. That can be explained due to the solubility of the gases at different temperatures Ar > air > N2. Findings show a greatest slope of the curve for the argon, and that was expected as the solubility of argon (similar to the solubility of O2) in water is higher than the solubility of nitrogen. A second-order regression was used to fit the data; results and polynomial coefficients adopted are reported in **Table 8.**

Figure 5.22b shows that the mean bubble diameter is not affected by the gas used, and it is constant at ~100 ± 10 nm. The ζ-potential of the generated suspensions is not affected, as well

Gas	r^2	Adj r^2	b_0	b_1	b_2	Confidence interval
Nitrogen	0.9947	0.9841	15.99±0.77	-0.48±0.09	5.37e-3± 2.24e-3	95%
Argon	0.9994	0.9982	20.56±0.36	-0.70±0.04	8.10e-3±1.05e-3	95%
Air	0.9910	0.9848	18.08±0.59	-0.42±0.06	3.18e-3±1.30e-3	95%

Table 8. Parameters of the second-order regression used to fit the istograms in figure 5.22a and figure 5.17a.

as for the air, by the initial temperature of water, and also it is similar for both the gas, meaning that this generation technique produce stable bulk nanobubble with the ζ-potential constant around -35 ± 5 mV.

Figure 5.22 is a comparison between the bubble number density obtained for different gases at 5°C and the bubbles generated in pure water without any sparging.

What is striking from that figure is that the bulk nanobubble generation is affected by two parameters that are the solubility of the gas but also the gas saturation. It can be clearly seen if we compare the blue and the green histograms, that by sparging air, it is possible to increase the bubble number density by approximately 25%.

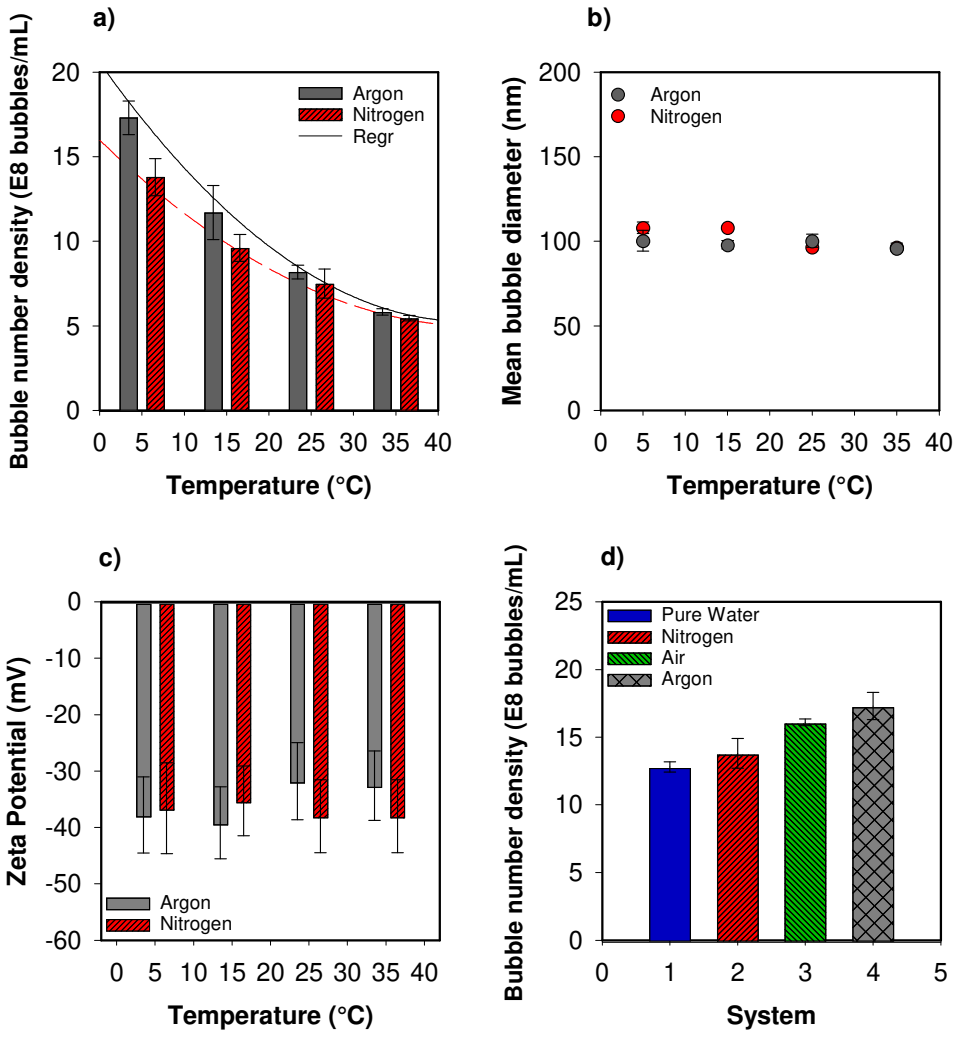

Figure 5.22. Gases effects on bulk nanobubbles generation. a) bubble number density of argon and nitrogen versus temperature; b) mean bubble diameter; c) zeta-potential; and d) comparison of gases at 5°C.

5.5 Automatization of sealed syringe technique

Given the potentially large number of BNBs per unit volume that this expansion-compression method can generate, especially with additional gas sparging **(Figure 5.21),** we

considered automating the technique to enable easy operation as well as scale-up of the BNB production process. The automation requires studies and investigation such as the design of the lines of the process, the study of the plunger speed in expansion and compression, the vacuum generated in an automatized system, the components necessary to make the process automatic etc. For example, it could be possible put syringes is series to produce more nanobubbles, put two valves (inlet and outlet) for the gas sparging and therefore to enhance the process yield, but also to choose a better material like stainless steel, to increase the durability of the components over time such as the barrel due to its constant friction with the rubber seal. Plastic syringes are subject to deterioration and plastic deformation after many cycles of use, therefore, the generation of the vacuum inside the barrel would be affected, but also the temperature could affect the properties of the material after extended use of it. In this section are presented the preliminary studies necessary for future research and development.

5.5.1 Components necessary for the automatization

To automatize the entire process the following components were used: (i) a pneumatic cylinder compact 16x30 TN Twin Piston; (ii) a trigger timer delay switch 12 V; (iii) a solenoid valve (5 way 2 positions Pneumatic Air operating at 12V in a pressure range of 0.15 – 0.8 MPa); (iv) a dry compressed air gas cylinder; (v) a holder for the syringe.

The pneumatic 16 x 30 twin-piston, **Figure 5.23a**, was modified to allow the connection with the syringe plunger, which was loaded and fixed to the syringe holder. The trigger timer delay switch, **Figure 5.23b**, was used to change the number of cycles and the speed of expansion and compression; the switch was connected directly to the two-position solenoid valve, **Figure 5.23c**, which has a key role since it driven the pneumatic-twin piston by

regulating the airflow going into it. The airflow, necessary to move backwards and forwards the pneumatic rods, was also regulated with the fine regulator valves illustrated in **Figure 5.23d**. The gas cylinder was connected directly to the solenoid valve and used at different pressure (from 1 to 2.5 bar).

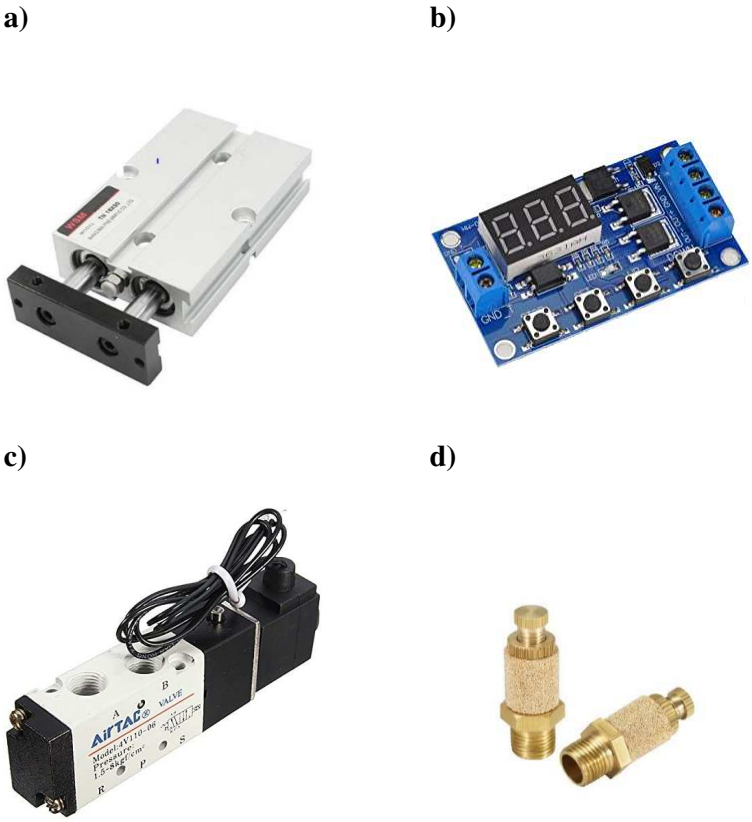

Figure 5.23. Components used for the automation of the syringe method; a) pneumatic cylinder two rods; b) trigger timer delay switch; c) solenoid valve two positions; d) airflow silencer valve.

A schematic diagram of an automated model is depicted in **Figure 5.24**. A scale identical to that of the manual process discussed in this study was used, i.e. a 10 mL syringe, to illustrate

the automation of the system but the design can be readily scaled up using the same design concept. In order to make the process the same of the manual one, the stroke of the two pneumatic rods must be exactly the same as the stroke of the syringe plunger when the liquid is loaded inside. The syringe is housed inside a cylinder and needs to be well-fixed in a syringe holder to avoid the possible axials movements of the syringe barrel, due to the force that the two rods applied at that system.

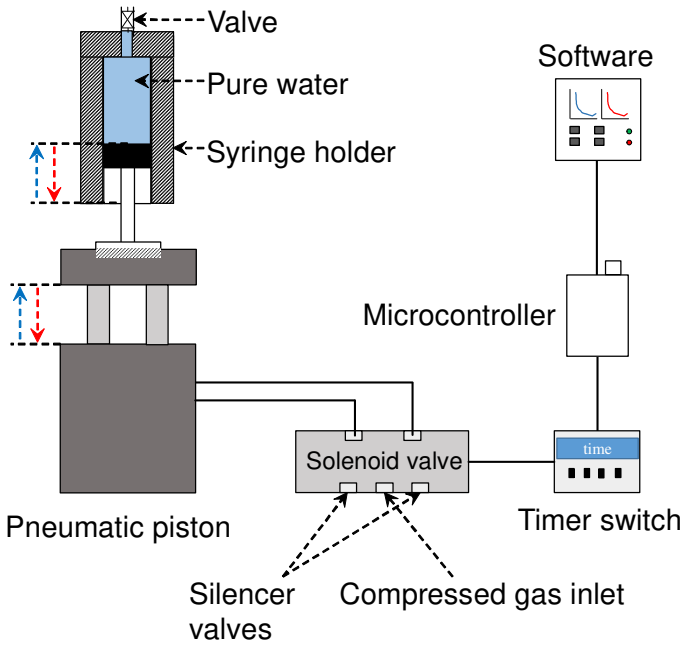

Figure 5.24. Schematic of the automation process.

While in a manual case, the driven force of the syringe plunger is the ΔP generated inside the barrel as the vacuum is created during the expansion, here, is necessary to calculate the force that is applied to the syringe plunger. Therefore, if we neglect the sliding friction forces, in expansion and compression cycles, the forces required to pull the plunger of a conventional plastic syringe of 10mL in volume or to push the aspiration plunger is calculated by the

measured vacuum pressure multiplied times the cross-sectional surface area of the inner barrel of the syringe used. Therefore, $F = PS$ with F the force required to move the plunger, P the pressure applied and S the surface area $S = \pi r^2$, where r represents the radius of the plunger.

5.5.2 Plastic barrel deformation and presence of air inside the barrel

The effect of air traped inside the barrel was considered to understand if during the BNB generation any leakage of the syringe barrel could affect their generation. Therefore, the following experiment was done by moving the plunger manually. Three scenarios are presented with a different initial volume of air inside the barrel. It was considered the generation in the absence of air (results already discussed), and the generation starting with the presence of 0.5 and 1 mL of air inside the barrel as depicted in **Figure 5.25**. Results of the bubble number density and ζ- potential are reported in **Figure 5.26**. Findings show that by increasing the volume of air before starting the BNB generation bring the bubble number density to decrease, thus, fewer bubbles are generated, and those have a smaller zeta potential value. It means that the bubbles generated are weakness if any presence of air is inside the barrel before starting the BNB generation. In this scenario, it is most likely that the vacuum level and thus, the negative pressure generated inside the syringe is smaller, therefore, by reducing the ΔP inside the barrel there is a reduction of the efficiency in BNB generation. In other words, the presence of air inside the syringe barrel before the expansion cycle leads to the generation of fever microbubbles, which they will collapse or burst in a limited number, thus the process is slowed down. That likely means less production of OH^- and therefore, the formation of fewer stable bulk nanobubbles (Jin et al., 2020).

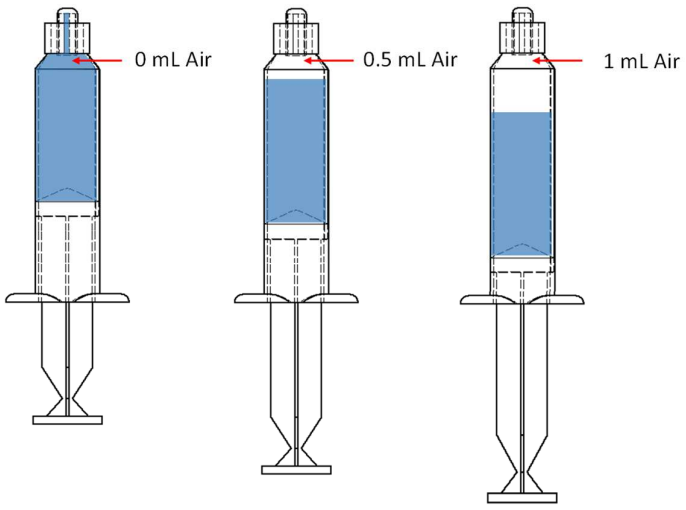

Figure 5.25. Schematic of the generation of BNBs with a different initial volume of air inside the barrel.

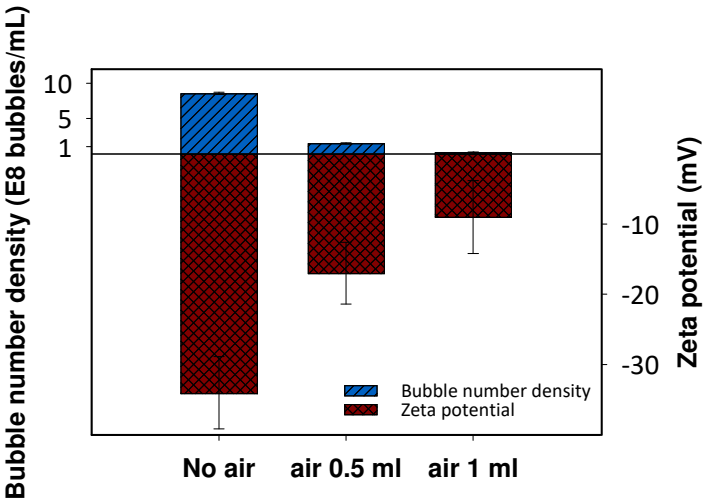

Figure 5.26. The figure shows the bubble number density (blue histograms), and the zeta potential (red histograms) obtained with the presence of different volume of air inside the syringe barrel at the moment of the generation.

Another important consideration needed for the realization of the automation process is considering the wear of the material, in fact, due to the continuous production, plastic is subjected to the plastic deformation of the barrel, especially if a not proper alignment between the plunger and the barrel is made.

Figure 5.27 shows a comparison of the pressure registered of two different plastic syringes during ~30 manual cycles of generation. **Figure 5.27a** represents the signal obtained with a brand-new syringe, and it is possible to see that the pressure value reached in compression and decompression is constant. **Figure 5.27b** reported the signal obtained by an old syringe already used for more than 200 cycles. What is striking here is that the pressure registered decreases with the cycles of generation. That can be explained because, after many cycles of generation, the plastic deformation of the barrel occurs, and the system, not adequately sealed anymore, start to leaks. Therefore, air enters from the bottom of the syringe inside the barrel, and affects the differential pressure generated.

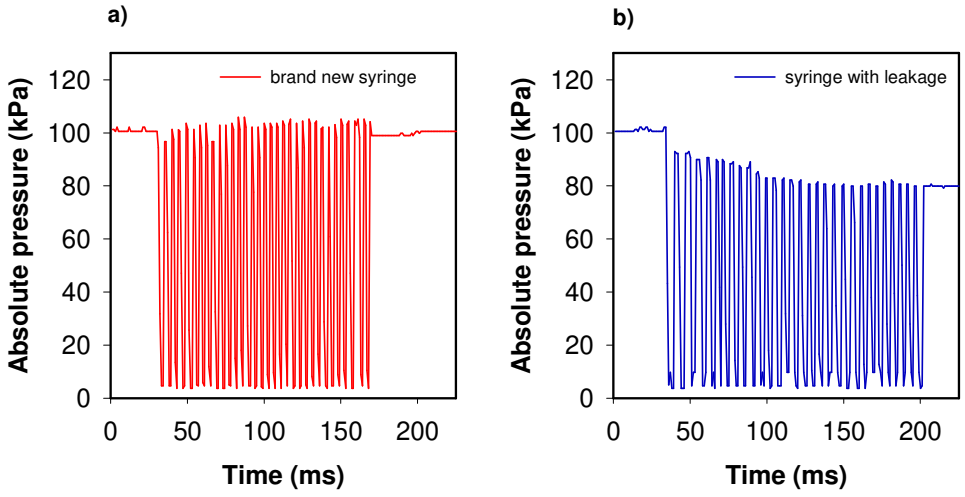

Figure 5.27. Absolute pressure inside the syringe barrel; a) syringe cycles generated by a brand-new plastic syringe; b) syringe cycles generated by a plastic syringe already used for more than 200 cycles.

5.5.3 Effect of compression and decompression time

In this section, the plunger speed velocity is analysed. The speed of expansion and compression of the plunger was changed by regulating the time on the trigger delay switch. **Figure 5.28a** shows the data of the expansion and compression, alternately fixing one of the two steps at 0.1 second and changing respectively the other with a different speed time. It is interesting to see that a slower compression decreases the bubble number density, whilst a slower expansion increases the bubbles concentration. Another parameter that has been changed was the pressure of the gas cylinder. In fact, it has been noted that the optimization of the operating pressure of the solenoid valve, is essential to optimise the working condition of the pneumatic rods, and consequently, the force applied to the syringe plunger. As reported in **Figure 5.28b,** the best pressure in order to increase the efficiency of the solenoid valve was found to be at a value of ~2.5 bar of the gas cylinder.

Once the best operating gas pressure (2.5 bar) was selected within the operating range of the solenoid valve to yield the maximum bubble number density without causing mechanical damage to the syringe, then, by keeping this gas pressure constant, the linear piston velocity was varied, as shown in **Figure 5.28c.** The most effective piston velocity was found to be 6 $cm \cdot s^{-1}$. Higher velocities did not improve the bubble number density but caused instead increasingly more friction and mechanical stresses leading to mechanical damage of the syringe. **Figure 5.28d** shows the bubbles size distribution related to the data showed in **Figure 5.28c**. It is possible to see that the bulk nanobubbles are generated in the range between 50 and 250 nm.

In conclusion, it should be noted that the bubble number density reached with the automation is similar to the bubble number density reached handling the syringe manually at room temperature; therefore we demonstrated that the process could be automated and further studies are required to improve that system and scale it up.

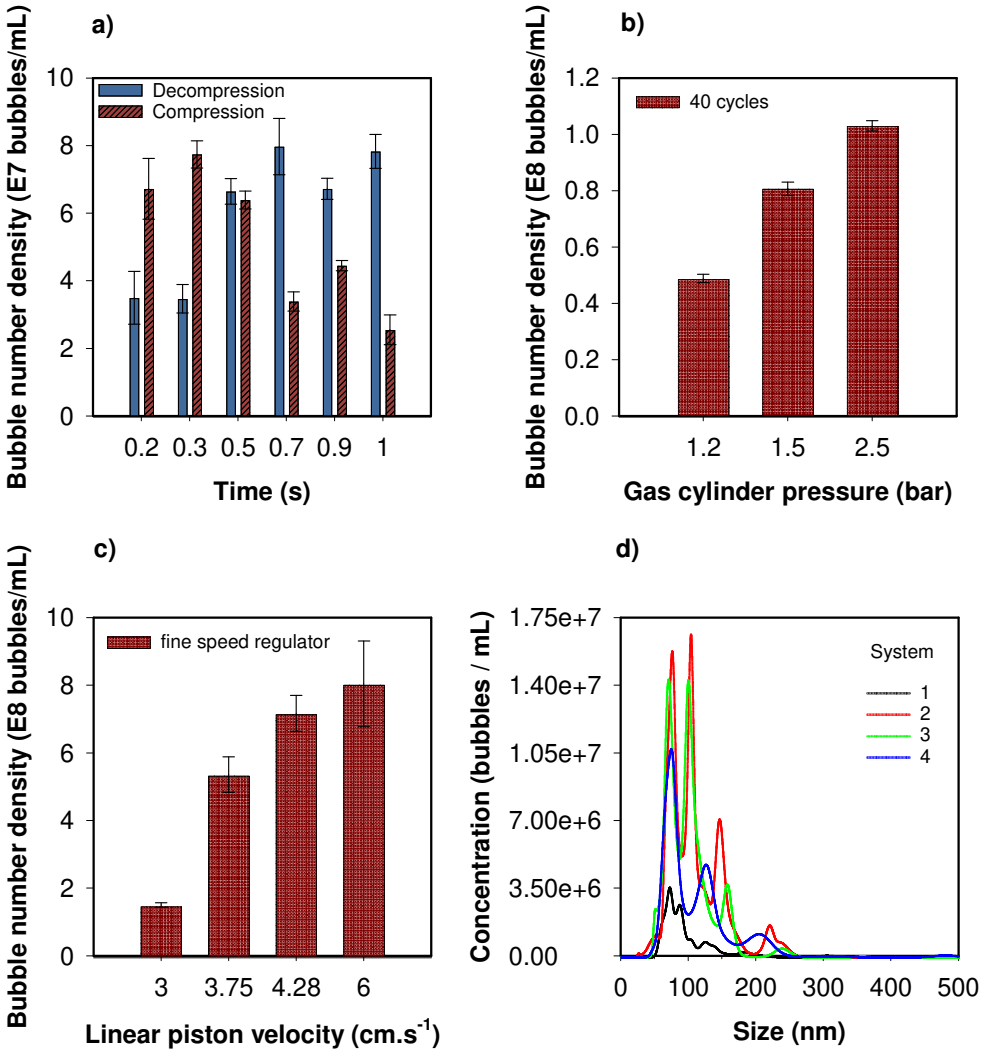

Figure 5.28. a) Compression and decompression as a function of the trigger switch time; b) effects of gas cylinder pressure on the bulk nanobubble generation; c) bubble number density versus linear piston velocity, and d) bubble size distribution.

5.6 Conclusions and outlook

In this chapter, a new technique based on Henry's law's vacuum degasification principle has been developed to generate high concentrations in excess of 10^9 bubble.mL^{-1} of stable bulk nanobubbles in pure water, through successive expansion -compression strokes inside a sealed syringe.

To understand if the entities observed were nanoparticles generated by the constant friction between the syringe plunger and the barrel or any other contaminants, different techniques were used. It has been shown that the observed nano-entities must be gas-filled as: (i) the *freezing-thawing method* showed that 96% of bulk nanobubbles disappeared after thawing the suspensions at room temperature; (ii) for plastic syringes they cannot be attributed, as proven by several spectroscopy analyses, to the presence of organic or inorganic impurities (i.e. droplets of medical oil present in the brand-new syringe and not well removed during the cleaning); (iii) they gradually disappear over time whilst their mean bubble size remains unchanged; (iv) the amount of dissolved gas and its solubility have a direct bearing on their number density; and (v) added sparging of gas enhances their number density.

Bulk nano-entities generated with glass syringe were not completely vanished after the freezing-thawing method (only 50%), suggesting that since the glass plunger was not provided by any rubber seal, the friction between the syringe plunger and its barrel were producing nanoscale entities, as confirmed by spectroscopy analyses.

The experiments reported were aimed to show the importance of the dissolved gas in the liquid at the moment of the BNB generation. Bulk nanobubbles were generated for that purpose

in degassed water, starting from different water temperature, for different type of dissolved gas and by replacing the dissolved gas every 30 cycles of generation. The number of bubbles increases as a function of the number of expansion-compression cycles up to a point and then levels off as the available dissolved gas is depleted. However, sparging additional gas allows improved yield to be achieved. It has been shown that it is possible to generate more than $4.50 \cdot 10^9$ bulk nanobubbles$\cdot mL^{-1,}$ but it is expected that the concentration of bulk nanobubbles with a proper automatization system could be over the power of 10 after ~ 200 cycles of generation in 10 mL since the bubble number density seems to increase linearly with the gas replacement into the solution.

Reported findings show that bulk nanobubbles, generated by expansion–compression method, are very stable with the ζ-potential ~ -35 mV ± 5mV when generated in optimal conditions.

The type of dissolved gas seems to have some effects on BNB generation. For example, more BNBs are generated with Argon than with air than with nitrogen. The difference in bubble number density can be qualitatively explained by the differences in solubility of these gases.

The proposed syringe technique has potential for large scale production of BNB suspensions. A successfully developed and tested automated 1:1 scale model were presented, and the basis for process scale-up was outlined, but further studies are required to test it using more resistance materials (i.e. stainless steel syringes) and sparging gas through an automatic valve after a specific number of cycles.

Chapter VI

Bulk Nanobubble Properties

6.1 Introduction

This chapter aims to elucidate parts of the bulk nanobubbles properties and to investigate about their mysterious stability, that has fascinated researchers mostly in the last decade, advocating the use of the *Ion-stabilized bubble model* (described in **2.3.1**). Among the fascinating properties of bulk nanobubbles there are: (i) their incredible long-term stability against the classical theory of bubble dissolution (Epstein and Plesset, 1950, Ljunggren and Eriksson, 1997) which was observed and reported experimentally to last for days or months (Ohgaki et al., 2010, Weijs et al., 2012, Ebina et al., 2013, Nirmalkar et al., 2018b, Meegoda et al., 2018, Nirmalkar et al., 2019, Jadhav and Barigou, 2020a, Ferraro et al., 2020); (ii) their high surface to volume ratio; (iii) their bio-compatibility and (vi) their negative charge observed. All those properties make them a perfect allied for eco-friendly and bioapplications such as water treatment (Tasaki et al., 2009, Agarwal et al., 2011), the enhanced germination rate of seeds (Liu et al., 2013, Liu et al., 2016), promotion of the physiological activity of living organisms (Ebina et al., 2013), sterilisation of bacteria (Kawara et al., 2014), therapeutic drug delivery (Wang et al., 2010, Misra et al., 2015, Meng et al., 2016), ultrasound contrast agent (Peyman et al., 2016, Tian et al., 2015, Rapoport et al., 2007, Fan et al., 2015) and the use in diagnostics and gene therapy (Zhou et al., 2012). Other applications suggested seeing them used for surface cleaning (Ghadimkhani et al., 2016, Zhu et al., 2016, Ushida et al., 2012c), for

drag reduction (Ushida et al., 2012a), froth flotation (Etchepare et al., 2017a, Calgaroto et al., 2016, Calgaroto et al., 2014, Fan et al., 2010a, Fan et al., 2010b, Fan et al., 2010c, Fan et al., 2010d) and for example to improve the engine efficacy using hydrogen nanobubbles (Oh et al., 2015, Oh et al., 2013). Thus, bulk nanobubbles could be applied in a wide range of areas, and it appears that there is immense scope for nanobubbles to revolutionise many current industrial and medical processes.

Despite the multitude of scientific reports (>150), a number that is growing faster in the recent years, the mystery behind the BNBs longevity is still causing scepticisms about their existence, leading to speculation and controversy on the BNBs nature and their origin. The small minority of works which dispute the BNBs existence have tended to attribute them to solvent/oil contamination, solid impurities, mesoscale aggregates or supramolecular structures (Alheshibri and Craig, 2019b, Alheshibri et al., 2019, Häbich et al., 2010, Rak et al., 2019, Jin et al., 2007, Sedlák and Rak, 2013, Leroy and Norisuye, 2016). While direct evidence is still missing, recently, however, a significant body of indirect corroborative evidence has been reported that BNBs do exist and they are stable in pure water as well as in aqueous organic solvent solutions (Oh and Kim, 2017, Nirmalkar et al., 2018b, Nirmalkar et al., 2018a, Nirmalkar et al., 2019, Wang et al., 2019, Jadhav and Barigou, 2020a, Jadhav and Barigou, 2020b, Michailidi et al., 2020). Thus, all the evidence present in literature should help to close the debate about the existence of bulk nanobubbles, and further studies focused on their properties are indeed necessary to understand the mechanism of formation and stabilisation.

There are three main aspects associated with the long-term stability of bulk nanobubbles also observed and reported in previous chapters for different generation techniques, that are: (i) the predominance of the Brownian motion on their negligible buoyancy force, which prevents them

from rising to the free surface (Hernandez et al., 2019); (ii) their interfacial stability that prevents them from the dissolution (Zhang et al., 2020a); and (iii) their colloidal stability that prevents them from mechanisms such as coalescence or Ostwald ripening (Nirmalkar et al., 2018a).

The colloidal stability of bulk nanobubbles was explained in the published work of (Nirmalkar et al., 2018a) that applied the Deryagin-Landau-Verwey-Overbeck (DLVO) theory to bulk nanobubbles produced in pure water by hydrodynamic cavitation. The authors reported the effects of the pH, different salts valence and surfactants on the generated suspensions. The DLVO theory, discussed in **2.3.2**, can be applied to describe the interaction (attraction and repulsion forces), thus the colloidal stability, between two charged bubbles in suspension. On the other hand, the interfacial stability, and hence the mechanical stability of a single bubble in the bulk liquid is still subject of discussion, and an accepted model is still missed.

This chapter intended to explore and to investigate the properties of bulk nanobubbles. Experiments were performed to prove the validity of the ion-stabilized bubble model and the role of OH^- and H^+ ions on the bulk nanobubble stability. Bulk nanobubbles were also generated in different salts solution, and their stability monitored over time. The effects of different temperatures on a BNBs suspension, ranging from –196 °C to +90 °C, were also investigated and analysed.

6.2 Materials and Methods

Ultrapure water (type I), henceforth referred to as pure water or simply water, from a Millipore purification system (Avidity Science, UK), of electrical conductivity 0.055 μS cm−1

and pH 6.7 at a temperature of 20 °C, was used in all experiments. Sodium chloride (NaCl, ≥ 99.5%), calcium chloride ($CaCl_2$, ≥ 99%), aluminium chloride ($AlCl_3$, 99.9%), and sodium sulfite (Na_2SO_3, ≥ 98%) were obtained from Sigma-Aldrich. Potassium hydroxide (KOH, 98%) and hydrochloric acid (37% HCl AR grade) were purchased from VMR Chemicals (UK).

BD plastic syringes with Leur lock tip of 10 mL volume size, were bought from Becton Dickinson and Company (BD) (Franklin Lakes, New Jersey) and properly cleaned before being used to generate bulk nanobubbles. Silverson Laboratory Mixers L5M-A model, 740 W (1 hp), with maximum speed 10,000 rpm (Silverson Machines Ltd., Waterside, Chesham Buckinghamshire, England) was used in batch mode with water as working fluid to create bulk nanobubble suspensions, the instrument was equipped with 3/4" Tubular Assembly and Standard Emulsor Head (SEH).

Before experimentation, the purified water and all stock solutions were examined using the Nanosight NS300 instrument, to verify the complete absence of any significant levels of nanoscale impurities. In all cases, the BNB suspensions formed were stored in 20 mL air-tight glass vials for further analysis. All glassware was cleaned by immersion for 10 min in boiling type II water, for several times, rinsing with type I water, drying in a microwave oven, flushing with a flow of high-purity dry nitrogen, and after the final rinsing with ultrapure water they were used.

6.3 Effects of OH^- and H^+ ions on the stability of bulk nanobubbles

Starting from the point of view, in which bulk nanobubbles do exist in pure water, a top-down approach (from macro and micro-scale to nano-scale) could help in the understanding of the behaviour of these tiny colloids observed in the nanoscale. In the past, controversy, disputes and a considerable disagreement have arisen over whether the gas/liquid surface of the water is negative due to the presence of surface-active hydroxyl ions (OH^-) or positive due to the presence of surface-hydrogen ions (H^+) (Yates et al., 1974, Chaplin, 2009, Chaplin, 2011, Khatib et al., 2016, Khaled Abdella Ahmed et al., 2018). The current and general understanding is that the surface of neutral water is negatively charged, which suggests that water molecules at the interface possess the dangling O–H group pointing out of the water at a certain angle, hence, conferring a negative charge on the air-water interface (Chaplin, 2009, Chaplin, 2011). (Graciaa, 2002) extensively studied the ζ-potential of air-deionized water bubble and found it to be -65mV. This high negative value seemed to be caused by hydroxide ions as it depended on the hydroxide concentration, and was not influenced by the presence and identity of any other co-anions or counter ions (Chaplin, 2011). (Takahashi, 2005) used microbubbles for the investigation of the gas-water interface electrical charge. This work revealed that the microbubbles were negatively charged for pH > 4 and positively charged in acidic medium, hence, the surface charge of the gas-water interface was strongly affected by the pH of the water, suggesting the importance of the hydroxide and hydrogen ions for the charging mechanism. In contrast, other anions and cations resulted in having a secondary effect on the zeta potential value. Takahashi stated that the negative zeta potential value for the microbubbles was a piece of clear evidence that OH^- was more effective than H^+ at influencing the microscopic structure of the gas-water interface. Similar effects have been observed in the nanoscale, where the longevity, or permanent presence of NBs in the bulk liquid, were

associated with the negative charge of the gas/liquid interface (Khaled Abdella Ahmed et al., 2018, Nirmalkar et al., 2018a, Boshenyatov et al., 2019, Zhang et al., 2020a).

(Ohgaki et al., 2010) using infrared spectroscopy measurements, reported the presence of hydrogen bonds on bulk nanobubble interfaces. (Nirmalkar et al., 2018b) reported that many of the bulk nanobubbles generated could not survive at low pH value because of a lack of OH^-, which are needed to form a stabilizing electric double layer around the bubble interface, similar findings were also reported earlier by (Calgaroto et al., 2014). (Jin et al., 2019) published an extensive study of nanobubbles generated by compression of microbubbles, and they studied the possible formation mechanisms involved in the generation of BNBs by using optical microscopy and ATR-FTIR[4] techniques. In this work, they speculated the presence of stronger hydrogen bonds which are formed at the nanobubble interface.

All in all, the negative charge of bulk nanobubbles is often associated and presumably created by OH^- ions that confer a negative zeta-potential reported to be usually around ~ -30 mV (Boshenyatov et al., 2019, Zhang et al., 2020a). A schematic is reported in **Figure 6.1**. Besides, several studies reported the generation of hydroxyl radical (OH) from the collapsing of microbubbles or nanobubbles but also suggesting that adsorbed OH^- and H^+ are crucial factors influencing the gas-water interface charge. (Jin et al., 2020, Yasui et al., 2018, Takahashi et al., 2007b, Takahashi et al., 2007a, Kurahashi et al., 1997).

Therefore, the following experiments aim to clarify the role of H^+ and OH^- on the formation and stabilisation of bulk nanobubbles by (i) studying the effects and stability on BNB formation and generation in different water pH; and (ii) monitoring the effects and stability on nanobubble

[4] Attenuated total reflectance Fourier transform infrared (ATR-FTIR)

suspensions generated at neutral pH and subsequently modified with the addition of OH^- and H^+ to the BNB suspensions.

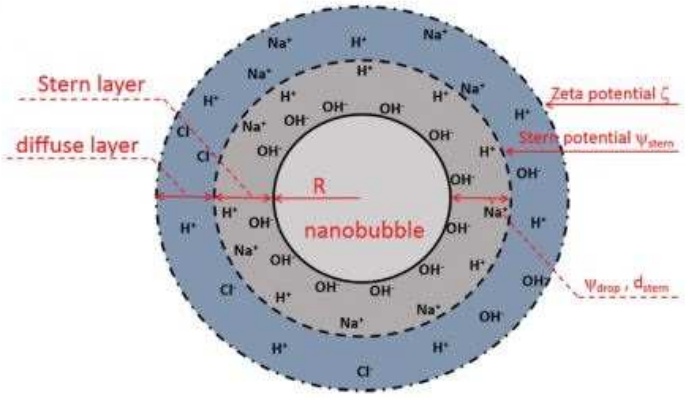

Figure 6.1. Schematic representation of the electrical double layer formed around a bulk nanobubble. This image was taken from (Zhang et al., 2020a).

6.3.1 Effects of water pH on BNB generation and stability

Nanobubble suspensions were generated in pure water with the pH in the range 2–12 by addition of HCl to make acidic solutions and KOH to make basic solutions. Two different scenarios are here presented, the first is the generation of bulk nanobubble suspensions in pure water at pre-adjusted pH, whereas the latter is the variation of pH on bulk nanobubble suspensions generated at neutral pH in pure water. Those experiments aimed to show the influence of positive and negative ions (H^+ and OH^-) on the bulk nanobubble generation and stability.

Bulk nanobubble suspensions were prepared with the method described in Error! Reference source not found., hence, by expansion and compression using a sealed syringe. The bubble generation was fixed at 30 cycles at room temperature and suspensions analysed after 1 hour from the generation.

In the first case scenario, pure water with the pH pre-adjusted was loaded into the syringe, where the bulk nanobubble generation was made only after the careful removal of all the air trapped within the barrel and the sealing. Results are plotted in **Figure 6.2**, which shows the effects on bubble number density, mean bubble diameter and ζ-potential. The bubble number density increases sharply as a function of pH (**Figure 6.2a**). It is interesting to see that a large bubble number density can be achieved in acidic solutions, but these BNBs, which have a relatively small positive ζ-potential (~ +10 mV; **Figure 6.2c**), are relatively short-lived and generally disappear within a day or two. Their disappearance is preceded by a significant increase in the mean bubble diameter (**Figure 6.2b**). The ζ-potential changes to negative at a pH between 4 and 5, which is expected to correspond to the isoelectric point of the solution. In these basic solutions, the bubble number density is much (up to an order of magnitude) higher and the absolute value of the zeta potential increases steadily with pH to reach −63 mV at pH 12. Whilst the acidic BNB suspensions are short-lived, these alkaline BNBs enjoy more long-term stability, and the vast majority were still in suspension after several weeks, while the mean bubble size remains approximately constant.

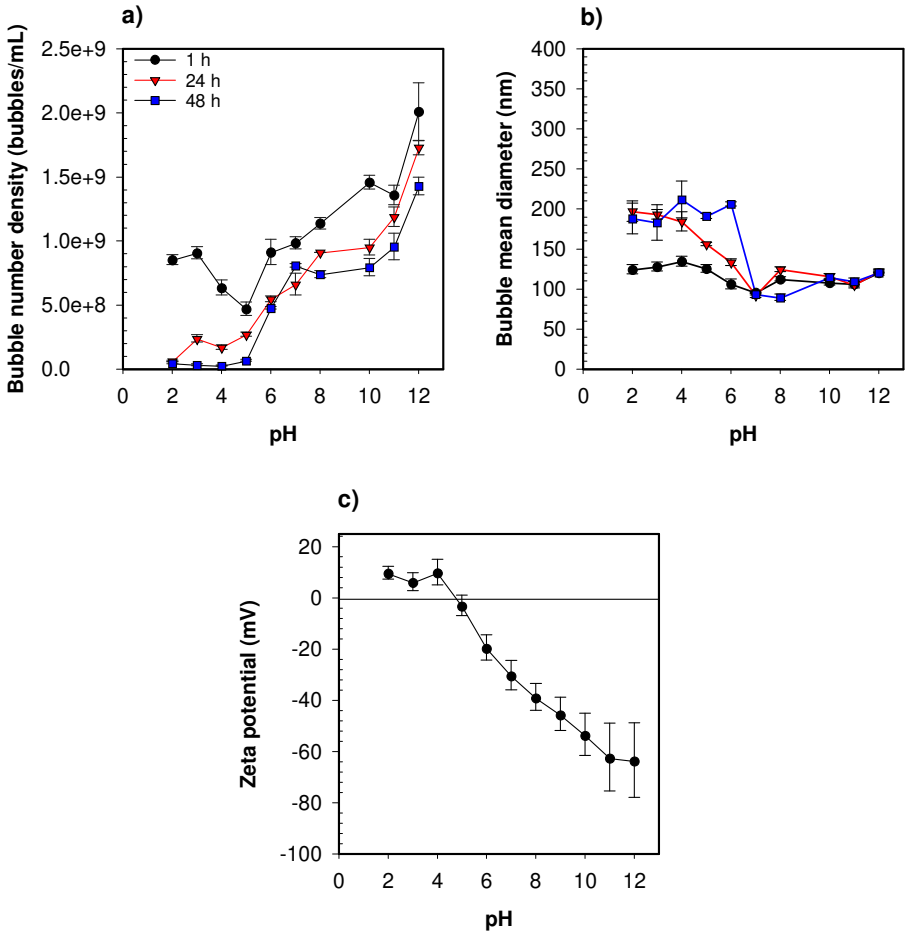

Figure 6.2. Effects of pre-adjustment of water pH on the generation and stability of bulk nanobubbles: (a) bubble number density; (b) zeta potential; (c) mean bubble diameter.

A plausible reason for the relatively weak stability of BNBs in acidic solutions may be advanced as follows. During the production of BNBs the auto-ionisation process of water, which in a neutral pH environment, produces an equal number of hydroxyl ions (OH^-) and hydronium ions (H_3O^+). In an acidic solution, such a process becomes heavily biased towards the production of the latter positive ions (Moqadam et al., 2018). Since there is a shortage in hydroxyl ions which generally attach to bubble interfaces to stabilise them, the H^+ ions emanating from the added HCl take over and attach to the bubble interfaces causing a positive

surface potential instead, as shown in **Figure 6.2c**. The plateaus of the ζ-potential visible at high and low pH values could be explained by saturation of ions adsorbed around the bubble interface, thus, in other words, H^+ and OH^- moving back to the bulk liquid of water due to the increased chemical potential at the bubble interface.

Above the isoelectric point, the nanobubble interfaces are negatively charged (**Figure 6.2c**). Thus, an electric double layer is expected to form around the nanobubbles, similar to that observed around solid nanoparticles (Nirmalkar et al., 2018a). According to the previously postulated ion-stabilised model (Nirmalkar et al., 2018a, Bunkin and Bunkin, 1992), the charged nanobubble interface gives rise to an external electrostatic pressure which balances the internal Laplace pressure and, hence, no net diffusion of gas occurs at equilibrium. Where the electrostatic pressure P_e in the proximity of a charged BNB is given by:

$$P_e = \frac{2\pi\sigma^2}{\varepsilon} \quad \textbf{(6.1)}$$

where ε is the permittivity of the suspending medium and σ is the surface charge density, while the Laplace pressure, P_L, within the bubble, is given by the Young-Laplace equation that can be written as:

$$P_L = \frac{2\gamma}{r} \quad \textbf{(6.2)}$$

where γ is the surface tension, and r is the nanobubble radius. It should be pointed out that the Young-Laplace equation was recently reported to be applicable at the nanoscale (Liu and Cao, 2016) and it is valid assuming the spherical shape of bulk nanobubbles. Therefore, from a

balance between the two pressures, at equilibrium, it should be $P_e = P_L$, and hence, the radius r of a nanobubble is given by (Nirmalkar et al., 2018a):

$$r = \frac{\gamma\varepsilon}{\pi\sigma^2} \tag{6.3}$$

where ε is the permittivity of the suspending medium, γ is the surface tension and σ is the density of surface charge which is related to the surface potential ψ_0 via the Grahame equation, thus (Israelachvili, 1985):

$$\sigma = \sqrt{8k_BT\varepsilon\varepsilon_0 c_\infty}\,\sinh\left(\frac{ze\psi_0}{2k_BT}\right) \tag{6.4}$$

where, k_B, T, ε_0, c_∞, z, e and ψ_0 are the Boltzmann constant, temperature, the permittivity of vacuum, the concentration of co-ions in the bulk, the charge on ion or valence of the ionic species, the elementary charge and surface potential respectively.

It can be inferred from equation **(6.3)** that a lower surface charge density, caused by a lower surface potential (**6.4**), will cause the nanobubble to expand to maintain equilibrium between the inner and outer counterbalancing pressures, which probably explains why at low pH values the mean nanobubble diameter increases with time (**Figure 6.2b**). Furthermore, it seems that beyond some critical nanobubble diameter, further reduction in electrostatic pressure at low pH promotes outward gas diffusion and, hence, the disappearance of the BNBs, which explains the sharp drop as a function of time in bubble number density observed in **Figure 6.2a**, and that seems to find agreement with the ion-stabilized bubble model reported by (Zhang et al., 2020a).

In the second scenario, bulk nanobubble suspension was generated at neutral pH (pH = 7) and then divided into five different vials. The pH of each vial was immediately modified in order to obtain acidic and basic solutions. Results are plotted in **Figure 6.3** showing as previously, the effects on bubble number density, mean bubble diameter and ζ-potential. It is interesting to see, even in this case, the dependence of the bubble number density as a function of the pH and the stability of the suspensions monitored over time. The bubble number density slightly increases by increasing the pH, and that can be explained by a rearrangement of the internal equilibrium of the suspension after the introduction of new OH^- ions, which confer stability at the bubbles generated at pH = 7. It should be pointed out that usually after the generation, the observed bubble number density is not very stable, which meaning that it results in high measurements error, hence, in a fluctuation of its value. In order to reduce that measurement error, it is a good practice to define a strict time-strategy before analysing the samples according to the experiment to be performed. That is the reason why it has been decided to analyse all the sample prepared after 1h from the generation. By moving on the chart to lower pH values, it can be observed that the bubble number density sharply decreases in acidic medium (**Figure 6.3a**) and the mean diameter of these suspensions sharply increases (**Figure 6.3b**), confirming, therefore, the previous findings (**Figure 6.2**), and thus, it seems to agree with the ion-stabilised model. The results in **Figure 6.3c,** showing that the zeta potential of the suspensions decreases with the pH (increases its negative value); similar findings were also reported for bulk nanobubble and microbubble suspensions (Takahashi, 2005, Jin et al., 2019, Nirmalkar et al., 2018a).

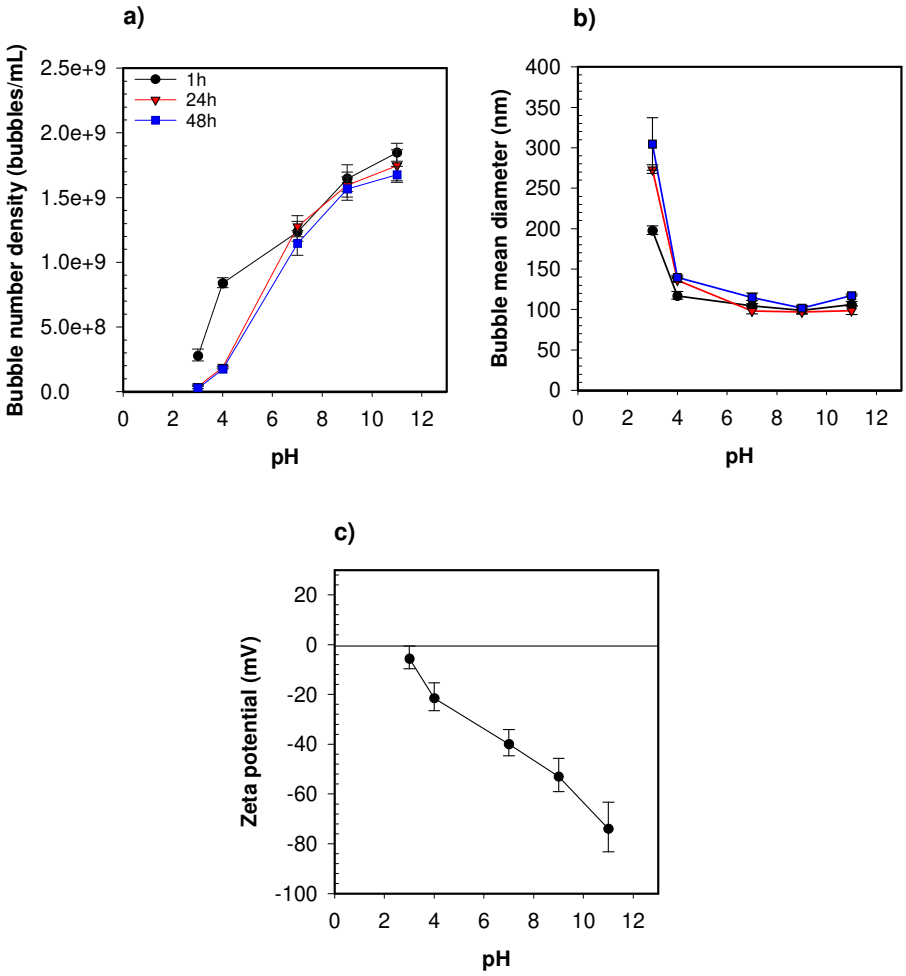

Figure 6.3. Effects of post-adjustment of water pH on generation and stability of bulk nanobubbles: (a) bubble number density; (b) zeta potential; (c) mean bubble diameter.

It is interesting to see how the BNBs size evolves over time, thus, the samples prepared by adjusting the pH of water in post-addition at pH 3 and 11, were analysed as a function of the scattered light intensity after 1h, 3h, 24h and 48 hours from the generation. Only the valid tracks reported by NS300 were taking into consideration, whilst the false tracks were excluded from the following chart. Results are reported in **Figure 6.4**. Findings show a shift on the right for bubbles with the lower ζ-potential, and that is more evident after 3h from the generation. It is also interesting to see that between the samples analysed after 24h, the suspension at pH3

scatters more light compared to the suspension at pH 11, which coincides with a decreasing in concentration as previously reported in **Figure 6.3a**. After 48h, the bubble suspension at pH 11 starts to spread in the plot and scatters more light comparing to the day before, and that can be explained again with a decreasing of the bubble number density. Analyses of the ζ-potential obtained by the DLS were also reported in **Figure 6.4,** and it is possible to see that the ζ-potential value slightly decreases after 48h for the suspension at pH 11, whilst it is remaining approximately constant for pH 3. Further investigations between the scattered light and the disappearance rate of bulk nanobubbles will be needed in future investigations.

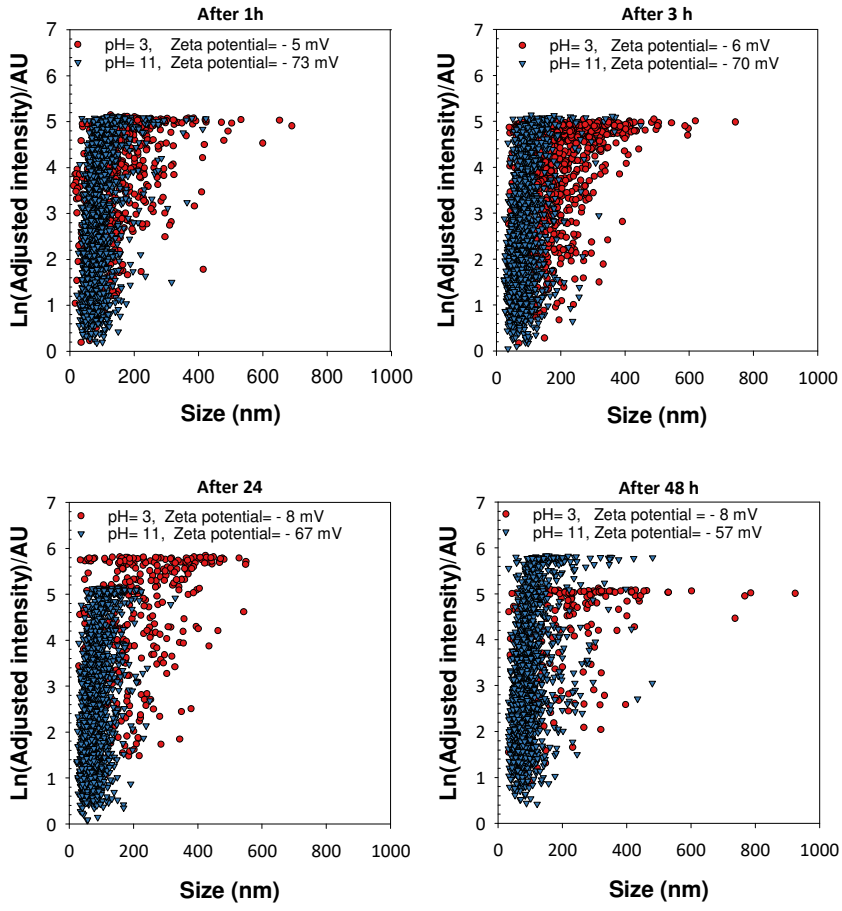

Figure 6.4. Comparison between suspensions of BNBs at pH3 and pH11. Results are reported in term of scattered light intensity against the bubble size (nm).

6.3.2 Effects of salts on bulk nanobubbles stability

The effects of pre-addition of varying concentrations of salts with different valence to pure water, namely NaCl (monovalent), $CaCl_2$ (divalent) and $AlCl_3$ (trivalent), on the generation and stability of BNBs was investigated. Results for NaCl and $CaCl_2$ are presented in **Figure 6.5**. In both cases, the presence of salt leads to a sharp drop in bubble number density which is accompanied by a considerable rise in mean bubble diameter with increasing salt concentration. In addition, the presence of either salt dramatically reduces, even if with a different rate, the lifetime of BNBs.

The magnitude of the negative ζ-potential decreases considerably but stays negative in the case of NaCl, as shown in **Figure 6.5c-f**. In the presence of $CaCl_2$, however, the ζ-potential is positive and increases in magnitude with salt concentration (note ζ-potential for concentrations higher than 50 mM cannot be measured due to the conductivity of the solution exceeding the instrument's limit). The addition of $AlCl_3$ leads to a very acidic solution (pH ~ 2.0) due to the formation of an aqueous solution of hydrogen halide[5] (HCl) which made it impossible to generate BNB suspensions that are sufficiently stable for further analysis.

As pointed out above and as discussed in a recently published work (Nirmalkar et al., 2018a), owing to the presence of counter-ions (OH^-) and co-ions (H^+), charged BNBs in water form an electric double layer, the thickness of which is known as the Debye length κ^{-1} that can be written as combination of the (**2.11** and **2.12**) as following:

[5] *Hydrogen halides* are diatomic inorganic compounds with the formula HX in which X is one of the halogens, and it can include chlorine, fluorine, bromine, iodine or astatine.

$$\kappa^{-1} = \sqrt{\frac{\varepsilon\varepsilon_0 k_B T}{2z_i^2 e^2 c_\infty}} \quad \textbf{(6.5)}$$

where ε, ε_0, z_i, c_∞, e, k_B, and T are the permittivity of the medium and the vacuum, the valence of the ion of type I (in this case the salt valence), the concentration of co-ions in the bulk, the elementary charge, the Boltzmann constant, and the absolute temperature in kelvins. In pure water, κ^{-1} = 961 nm and, according to equation (**6.5**) it will reduce with increasing co-ion concentration and salt valance, leading to the so-called *screening of the electric double laye*r (Bunkin and Bunkin, 1992). As the screening of the electric double layers occurs, the external negative electrostatic pressure decreases, causing a pressure imbalance across the nanobubble interfaces leading it to an expansion, hence, explaining the observed growth in mean bubble diameter.

The observed drastic impact of the divalent salt on the ζ-potential compared to the monovalent salt can, therefore, be explained by the deterioration of the electric double layer around the BNBs (i.e. κ^{-1} decreases) in case of the divalent salt. That is reflected in the comparatively much less stable BNBs generated in the $CaCl_2$ solutions compared to the NaCl solutions (**Figure 6.5a-d**) at any concentration; the rate of BNB disappearance being at least an order of magnitude faster in the divalent salt solution, in fact, it is interesting to see in **Figure 6.5a-d** that for the NaCl solutions bubbles are quite stable even after few hours from the generation, whilst in the $CaCl_2$ bubbles disappeared drastically in the first hour. **Figure 6.5b-e** showing the mean bubble diameter of the suspensions marking the difference between the suspensions in the NaCl and $CaCl_2$.

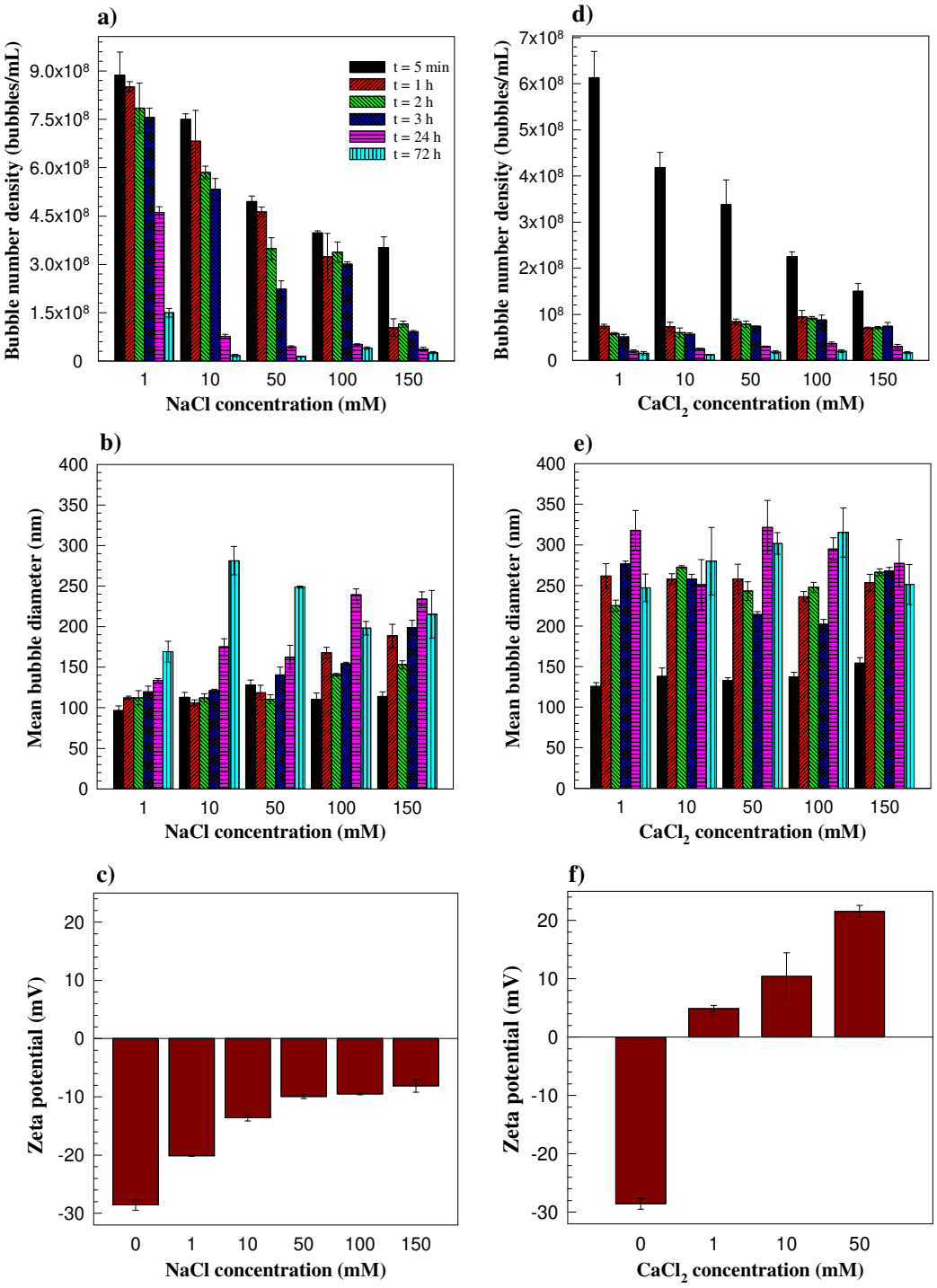

Figure 6.5. Effects of pre-addition of salts on generation and stability of bulk nanobubbles: (a)-(c) NaCl solution; (d)-(f) $CaCl_2$ solution.

6.4 Thermal effects on bulk nanobubble suspensions

Some properties of bulk nanobubbles were investigated, such as their resistance and behaviour at different temperatures. Bulk nanobubble suspensions were analysed in extreme conditions included freezing with liquid nitrogen (-196 °C) and heating the suspension up to 90 °C; also the liquid suspensions were evaporated to understand the bubble rising effect whenever a degasification of the liquid occurs.

6.4.1 Freezing – thawing at different temperatures

Experiments were conducted to study the suspensions of a known concentration and mean diameter exposing the bubble suspensions to freezing at different temperatures (- 18 °C, -80 °C and -196 °C) followed by thawing at room temperature (~ 20 °C) for 6h before being analysed. Experiments were performed with 20 mL of bulk nanobubble suspensions stored in glass vials of 30 mL. Results are depicted in **Figure 6.6.** Suspensions were generated by different methods, already discussed in other previous chapters, including HSM, expansion-compression, ethanol-water mixing at 20% v/v of ethanol and by mixing. What is striking in this figure is the unusual behaviour of bulk nanobubbles at high freezing temperatures. As the freezing temperature goes from -196 °C (liquid nitrogen) to -18 °C (standard freezer), the bubble number density drastically drops. The only exception has been observed for the ethanol-water mixing suspensions in which bubbles increases at -196 °C. Similar results were recently published by (Jadhav and Barigou, 2020a) where the authors explained it with an increase of the air saturation in the ethanol-water mixture enhanced by the cooling of the suspension (Rettich et al., 1981, Cargill, 1993) and the successive generation of nanobubbles on thawing,

where the temperature of the suspension rises again causing a spontaneous releasing of the air from both ethanol and water with the following generation of NBs.

On the other hand, results are slightly different from those reported from (Jadhav and Barigou, 2020a) since in the case presented here bubble still survive after thawing at -196 °C. This difference could be caused by the different setup used to generated bulk nanobubbles, but most likely from the timing used to analyse the suspensions after defrosting. It is hard to say if nanobubbles generated in pure water and subjecting at fast freezing could survive or if there is a possible formation of supramolecular structure around the nanobubbles caused by the fast freezing of the suspension (Devlin and Monreal, 2010) or the formation of ice nano-crystals (Pan et al., 2011). Findings are shown in **Figure 6.6** for the freezing temperature of -18 °C, suggesting that when the freezing rate in pure water is very low, nanobubbles or nano-entities present in the suspension are pressed to move, agglomerate and eventually to coalesce by growing ice crystals (Jadhav and Barigou, 2020a, Nirmalkar et al., 2018b). All in all, the bubble size distribution shape is not significantly affected by the freezing-thawing and usually is reduced in intensity with some peaks formed at the right end of the size distribution, suggesting, therefore, some agglomeration (impurities or bubbles), as reported in **Figure 6.7**, where lines for measurements after thawing at -18°C and -80 °C are reported but not clearly visible due to their lower scale, however, no significant peaks were present.

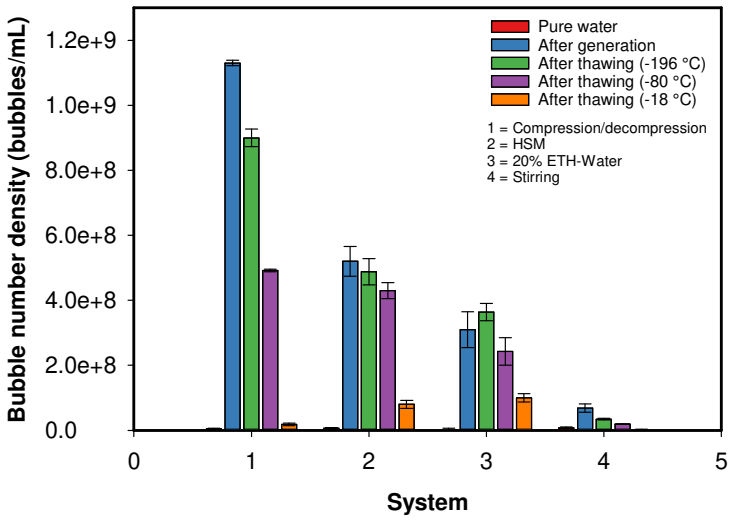

Figure 6.6. Effects of freezing at different temperatures for different bulk nanobubbles suspension.

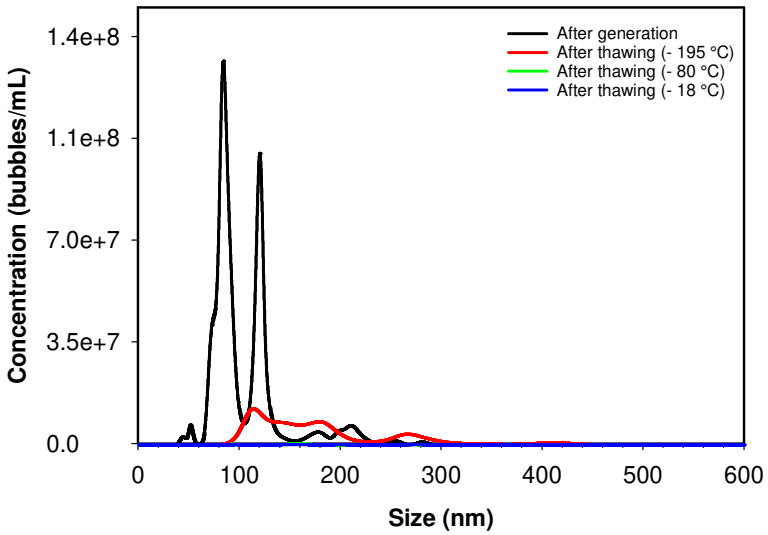

Figure 6.7. Effects of freezing at different temperatures on the bubble size distribution for suspension generated by HSM.

6.4.2 Evaporation of bubble suspension and rising time

The effect on the evaporation of bulk nanobubbles suspension is here reported. 20 mL of a suspension of BNBs prepared by the expansion-compression method in pure water, with an initial number density of 1.19×10^9 bubbles/mL and mean bubble diameter of ~119 nm was loaded inside a glass flask and evaporated for half of its volume on a hot magnetic stirrer. The sample was analysed before replacing the evaporated volume of the medium by addition of ultrapure water. The same process was repeated twice on the same suspension. Results are depicted in **Figure 6.8**. What stands out in these graphs is the incredible resistance of the bulk nanobubbles to the evaporation process. That is a quite unusual behaviour since the gas should be escaped from the liquid as the temperature rises, thus, in the first instance, it is expected a decreasing in bubble number density, however, it is quite logical if we consider that bulk nanobubbles following the Brownian motion and do not rise as larger bubbles. (Alheshibri et al., 2016) calculated the no-slip terminal rise velocity for nanobubbles of 50 and 500 nm to be 2.7 nm s^{-1} and 272 nm s^{-1} respectively, and they concluded that the extremely low rise velocities found most likely mean that the buoyancy effect on nanobubbles is insignificant compared to Brownian motion. They estimated the terminal rise velocity due to the buoyancy U_t, by using the following equation:

$$U_t = \frac{2r^2\Delta\rho g}{9\mu} \qquad \textbf{(6.6)}$$

where U_t is dependent on the boundary condition and is valid for a no-slip boundary condition, $\Delta\rho$ represents the difference in density between the bubble and the solution, g is the acceleration due to gravity and μ is the viscosity of the fluid.

Figure 6.8a shows the bubble number density during steps of evaporation and dilution. It is possible to see that bubble number density increases during the evaporation of the suspension and decreases during dilution by ~ 40%. However, the bubble number density was gradually decreasing from the first measurements, and that could be explained since during the process some bubbles were lost due to the measurements or likely vanished in contact with the vial walls. **Figure 6.8b** shows the bubble mean diameter of the analysed suspension and reveals no significant effects of the evaporation on the bubble diameter. It should be pointed out that all the measurements were carried when the suspensions were completely cooled down.

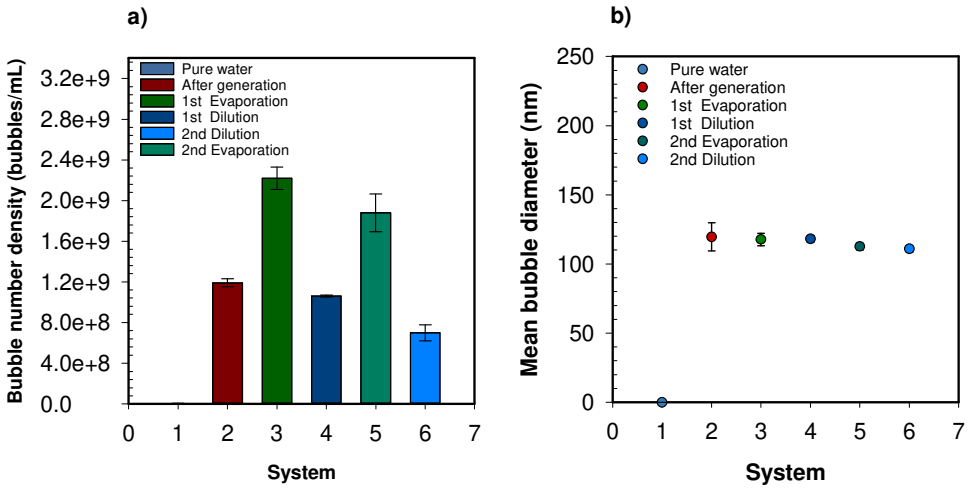

Figure 6.8. Effects of the evaporation on bulk nanobubbles suspension; a) shows the bubble number density, whilst b) the mean bubble diameter.

6.4.3 Effects of high temperatures on bulk nanobubble suspensions

The reported experiments aimed to investigate the properties of BNBs at high temperature, and more in general, to study what happens to BNB suspensions as the temperature of the solution increasing. Thus, 1mL sample of nanobubble suspensions generated in type I water

by HSM, operated in semi-continuous mode, was deposited into a 12 mm square glass cell (PCS8501, Malvern Panalytical Ltd.) for analyses with DLS instrument. The experiments were conducted with the temperature control range of 10-90 °C directly inside the DLS machine, which has a temperature module allowing to control the temperature in the range (0°C - 90°C +/-0.1) during the experiments. By taking advantage of this function, the temperature of the bubble suspension was initially fixed at 10 °C and sample equilibrated for 10 minutes before starting the measurements. The equilibration time was calibrated at 10 minutes, the time necessary to allow the suspension to cool down from 20°C to 10°C (~1 °C/ min) before starting the experiment. Same equilibration time was used for all the other measurements, where the sample was brought from 10 °C to 90 °C by steps of 10 °C, and then on the way back from 90 °C to 10 °C. A schematic of the experiment is illustrated in **Figure 6.9a**, whereas findings are reported in **Figure 6.9b**.

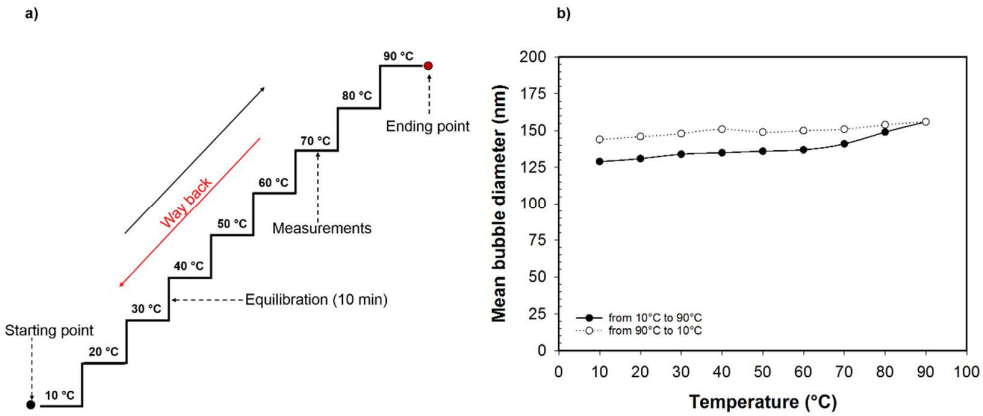

Figure 6.9. Effects of temperature on bulk nanobubbles suspension; a) shows the experimental setup, whilst b) shows the effects of temperature on the mean bubble diameter of the suspension.

It is interesting to see the trend in **Figure 6.9b**, where the mean bubble diameter seems to follow a hysteresis as the temperature rise and decrease back to the starting point. Initially, at 10 °C the measured mean bubble diameter resulted in being ~129 nm and then reaching the

value of ~156 mm at 90 °C; by cooling the suspension back at 10 °C the bubble mean diameter resulted increased by a factor of 14% (**Figure 6.9b)**. The day after the same suspension was analysed again, but this time it was brought directly at 90 °C, where the bubble mean diameter obtained for the suspension was found to be of ~153 nm, suggesting, therefore, the hysteresis trend. A plausible reason for these findings may be advanced as follows. As temperature rises, several effects happen within the suspension such as the solubility of gas decreases and the kinetic energy of the system increases, and that leads to more vapour pressure and the breaking of intermolecular bonds. On the other hand, the surface tension of water decreases as the temperature increases because cohesive forces decrease with an increase of molecular thermal activity, leading the bubbles to expand, and thus, to growth (Robinson et al., 2010). On the temperature way back, the surface tension increases, thus, the bubbles shrinking reaching a new equilibrium. However, it is not clear *a priori* if the mean bubble diameter increased due to a gas expansion or due to the Ostwald ripening which is a thermally activated process, and so its rate should increase with increasing temperature (Ostwald, 1896, Ostwald, 1897).

As the temperature rises, it is interesting to observe also the diffusion distribution of the nanobubble suspension, reported in **Figure 6.10**. The peak formed at 90°C seems to be more narrow and taller compared to the others that result shifted on the right side as the temperature of the system increases. It is not clear *a priori* if the light scattering intensity increases with the incrementing temperature, most for the sample at 90 °C, because of a measurement error due to the high temperature involved, and thus, the signal could be disturbed by bubbling into the system or if it could be associated entirely to an increase of the mean diameter of the suspension. Also, however, it is not excluded the possibility of nucleation of new nanobubbles during the experiments at higher temperatures, and that could also explain the greater intensity at 90°C. In

support of that hypothesis, in fact, temperature changes have been reported to produce bulk nanobubbles of ~290 nm in diameter (Najafi et al., 2007).

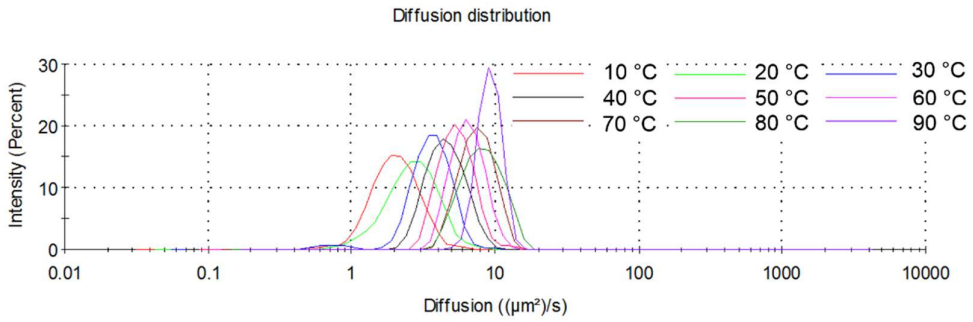

Figure 6.10. Diffusion distribution at different temperatures.

6.5 Conclusions and outlook

Results on the pre-adjustment and post-adjustment of water pH showed that BNBs enjoy much higher stability in alkaline solutions than acidic ones. The mean size of nanobubbles increased with a decrease in pH, whereas the bubble number density decreased. Perhaps, it can be conjecture that in pure water, due to the adsorption of OH^- ions an electric double layer, similar to that observed around nanoparticles and microbubbles and reported in the literature, forms around the negatively charged nanobubbles. The charged nanobubble interface is postulated to create an external negative electrostatic pressure which balances the internal Laplace pressure so that, at equilibrium, no net gas diffusion occurs. The disruption of this equilibrium due to a lower surface potential at low pH is believed to be behind the expansion and destabilisation of BNBs in acidic environments. Besides, results on the pre-adjustment of water pH, for an acidic medium, shows that bulk nanobubbles could be generated in large number also for acidic pH, suggesting perhaps that there is an excess of H^+ over OH^- at the

interface. However, bubbles with an excess of H^+ at the interface are not able to survive for more than 24h. Those findings show perhaps the perfect match with the *ion-stabilized bubble model*.

The presence of even small amounts of salts of any valence causes a drastic reduction in bubble number density and a sharp increase in mean bubble size, as it leads to the screening of the electric double layer formed by the co-ions. As a result, the external negative electrostatic pressure decreases leading to a pressure imbalance across the interface of nanobubbles which then expand and grow in size; this situation is exacerbated in the case of a high salt valence. Even in that case, the *ion-stabilized bubble model* seems to agree with the findings reported. Similar behaviour was also reported for microbubbles (Bunkin and Bunkin, 2003, Bunkin et al., 2016).

When the bubble suspensions are frozen slowly, bubbles disappear almost entirely after thawing, suggesting, therefore, a slow compression that brings them to move, agglomerate, to coalesce by growing ice crystals or eventually to stick on the iced bulk liquid. On the other hand, the fast freezing leads to reduce those phenomena allowing several bubbles to survive at the freezing-thawing cycle, and it still remains an open question to solve. Bubbles also show a peculiar characteristic when subjected to an increasing temperature, that leads the bubble to expand the mean diameter.

Results for the evaporation of bulk nanobubbles suspension show the predominance of the Brownian motion on their negligible buoyancy force, which prevents them from rising to the free surface, and thus, concentrating the bulk nanobubbles suspension. Despite the cost to evaporate a large amount of liquid, that could be an exciting way to increase the concentration

of bulk nanobubbles suspensions for future applications. It would be interesting to use that property to use nanobubbles, i.e. in heat transfer applications or within nanofluids.

However, it should be pointed out that if from a strictly theoretical point of view, the stability of a bulk nanobubble seems to be governed solely by the ion-stabilization model, as experimentally demonstrated here, where particular attention was given at the not generation of contaminants during the experimental operations, from an experimental point of view, is very easy to generate nanoscale entities that could affect the stability of part of the bubbles suspension differently, and other stabilisation mechanisms could also be present.

Chapter VII

General Conclusions and Future Recommendations

In-depth conclusions of each of the studies here presented can be found at the end of each chapter. However, in this final chapter are presented overall concluding remarks and recommendations for future works.

7.1 Characterisation instruments

The lack of instruments to distinguish between nanoparticles and nanobubbles in the bulk liquid could lead to misinformation of bulk nanobubbles. The primary characterisation instruments used are based on the light scattering and are Dynamic Light Scattering (DLS) and Nanoparticle Tracking Analysis (NTA). However, those techniques are not able to make that distinction, thus are not enough to support alone the existence of bulk nanobubbles. Misleading information could arise by using only scattering based techniques, and they could result in serious side effects, especially in applications involving the use of bulk nanobubbles in biomedical, agricultural or food fields. In every case, one should keep in mind that nanoscale contaminations are very easy to generate including chemical precipitates, oil nanodroplets, metal nanoparticles, hydrophobic mesoscale particles, and nanoplastics could be confused and reported as bulk nanobubbles. Thus, direct and multi-proofs are always needed regarding whether the nano-entities observed are bulk nanobubbles or not. Those proofs could derive

from a combination of methods and techniques, as also described in this work. To summarise is strongly recommended study the bulk nanobubble suspension before freezing and after thawing. This method does not require any additional cost and the analyses can be done in any freezer. However, it is suggested to use a slow freezing rate, in fact, it has been reported here that the bubble number density decreases faster if the suspension is freezing at (- 18 °C). It has also been reported that in the case of solid silica nanoparticles, generated in a glass syringe, the suspension analysed after freezing-thawing shows a higher bubble number density compared to bulk nanobubbles generated in a plastic syringe, suggesting that this method could be a powerful tool to make a first estimation of the entities observed. However, this method alone is not enough to state that the entities observed are exclusively bulk nanobubbles; thus, additional analyses are required, i.e. spectroscopy analyses, degassing experiments or shell screening experiments.

7.2 Bulk nanobubble generation and stability

In this work, we presented in the Chapter IV and Chapter V, two new methods for the bulk nanobubble generation, based on mechanical generation using a High Shear Mixer, and on Henry's law, using a sealed plastic syringe. This work aimed to generate bulk nanobubbles in pure water to shed light on their existence and formation mechanism. Thus the methods presented were used exclusively with pure water as working fluid, and are based on two different generation principles, the hydrodynamic cavitation and the expansion-compression of microbubbles formed by the dissolved gas in the liquid. Multiple evidence of their existence in pure water has been provided, and their long term stability monitored.

The BNBs generated presented long-term stability, which was measured for hours, days and months in different conditions. In order to shed light and investigate the stability mechanism that governs this mysterious stability, studies on the shell destabilisation were presented. Bulk nanobubbles were studied in different pH solution, under effects of salts with different valence, and in different operating conditions. Findings revealed that bulk nanobubbles present much higher stability in alkaline solutions than acidic ones. The mean size of nanobubbles increased with a decrease in pH, whereas the bubble number density decreased.

Bulk nanobubbles resulted in being characterised in having an electric double layer that forms on the gas/water interface and findings suggest, but also it is beleived that it is formed due to the adsorption of OH^- ions, that confers to a bulk nanobubble the typical negative charge. The charged nanobubble interface is postulated to create an external negative electrostatic pressure which balances the internal Laplace pressure so that, at equilibrium, no net gas diffusion occurs. The ion-stabilised bubble model is here advocate, due to the experimental findings reported, to explain the stability mechanism that governs a bulk nanobubble generated in pure water. It should be pointed out, however, that different bulk nanobubble generation techniques could lead to the generation of different contaminations, i.e. organic solvent or nanoparticle, that could affect the stability mechanism of bulk nanobubbles.

7.3 Future recommendations

This work has shown that bulk nanobubbles do exist in pure water, and they are characterised by incredible stability, which makes them intrinsically interesting as they pose many challenges to our understanding of bubble physics and behaviour. However, even if the research in this

area is still in its infancy, a wide range of industrial applications has been suggested and reported to be very prominent. There is immense scope, as discussed in this work, for nanobubbles to impact and consequently revolutionise a wide range of industrial processes in many fields. However, there are many unexplained phenomena, reported in the literature, which must be understood in order to fully and reasonably use bulk nanobubbles. The bubble number density of the generated suspensions is still too far for having a high impact for the most significant part of the industrial process; thus a continuous investigation in order to increase the efficiency of the bubble generation methods are necessary.

Since the interest in this topic is growing very fast, the attention should be focussed more on possible applications and scale-up mechanisms in order to process a higher volume of liquid. Studies are required on the stabilisation mechanisms, that are often not well accepted and is still subject of debates and disputes.

All in all, there are excellent chances for those tiny bubbles to impact and become a powerful biocompatible and eco-friendly system to improve already existing processes by reducing the environment aggravation problems such as fuel emission and water pollution, but also having a significant impact on the food, medical and pharmaceutical industries.

Appendix A

ICP-MS Parameters and Calibration Curves

Spectroscopy analyses were performed on bulk nanobubble suspensions to detect the presence of elements that could be attributed to contamination or impurities formed during the bulk nanobubble generation. In particular, the *Gas Chromatography-Mass Spectroscopy (GC-MS)* and the *Inductively Coupled Plasma–Mass Spectroscopy (ICP-MS)*, were used in this work. Those techniques, together with the results obtained, were reported in **(5.3.4)**.

The operating parameters of the instruments are summarised in the following table, whereas the calibration curves for each element investigated are reported in

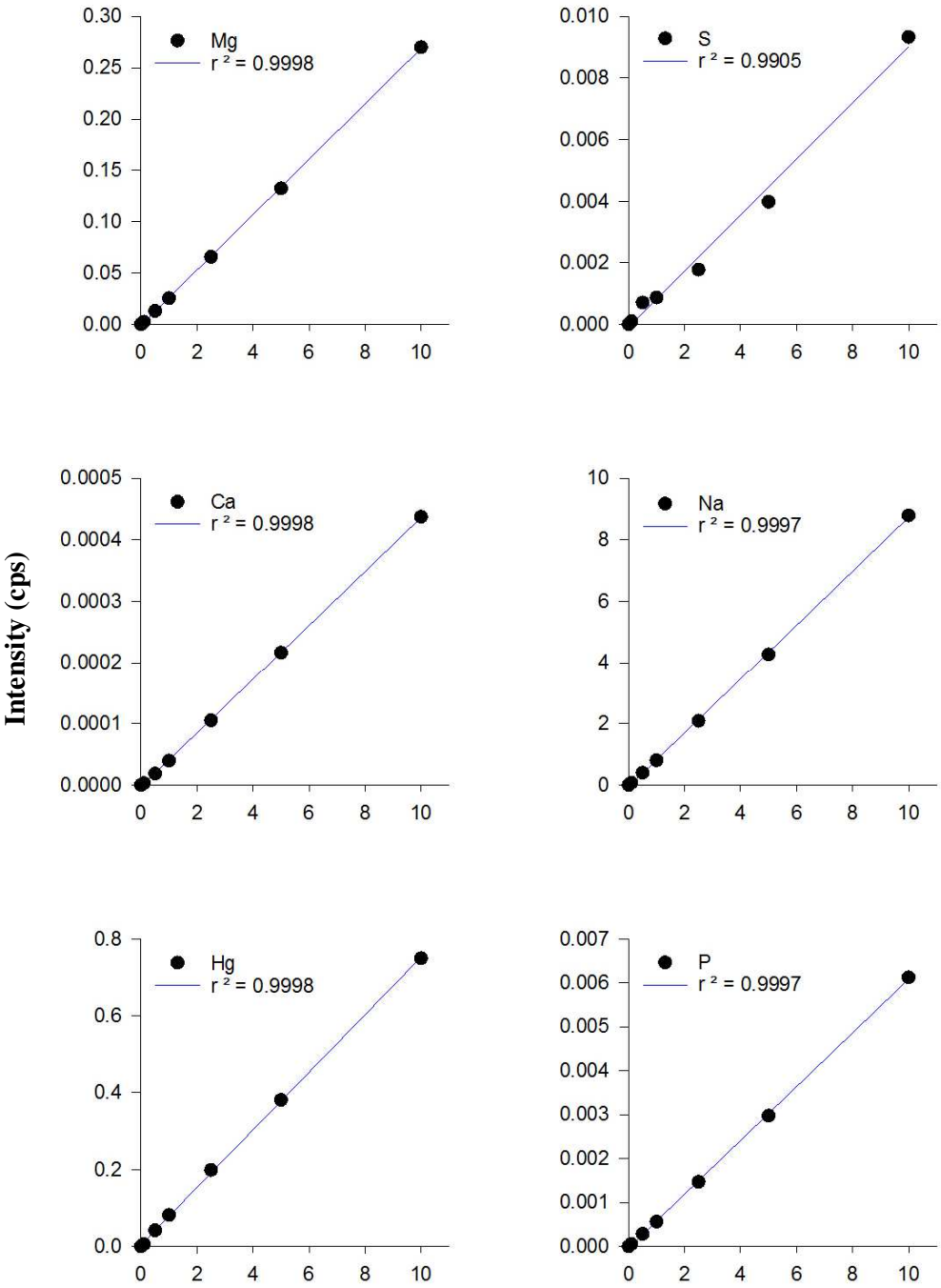

Figure A.8.1-8.4.

Gas chromatography

Instrument	7809A (Agilent)
Column	ZB-WAX 30m × ϕ 0.25 mm, 0.25µm (Phenomenex, UK)
Injection method	Split (1:10)
Injection volume	1 µL
Carrier gas	Helium
Flow rate	1 mL/min
Injection temperature	250 °C
Over temperature program	50 °C (2 min) → 5 °C/min →250 °C (118 min)
Transfer line temperature	250 °C

Mass spectrometry

Instrument	GCT Premier (Waters, UK)
Mode	Selected-ion monitoring
Ion source temperature	250 °C
Ionization mode	Electron impact (EI^+)
Electron energy	70 eV
Trap current	100 µA
Emission current	179 µA

Table 9. GC-MS operating parameters.

Inductively coupled plasma mass spectrometry

Parameters	*Value*	*Parameters*	*Value*
RF applied power (kW)	1.6 kW	*Deflector voltage*	-10 V
Auxiliary gas flow rate (Argon)	1.2 L min^{-1}	*Quadrupole rod offset*	-12 V
Plasma gas flow (Argon)	18 L min^{-1}	*Cell entrance voltage*	-9 V
Nebulizer gas flow (Argon)	0.95 L min^{-1}	*Cell exit voltage*	-20 V
Sample flow rate	0.3 mL min^{-1}	*Cell rod offset*	-15 V
KED Gas Flow (Helium)	4 mL min^{-1}	*Axial field voltage*	475 V
Nebulizer type	Sea Spray concentric	*Analog stage voltage*	-1675
Interface cone material	Nickel	*Pure stage voltage*	1050 V
Discriminator threshold	12 mV		

Table 10. ICP-MS operating parameters.

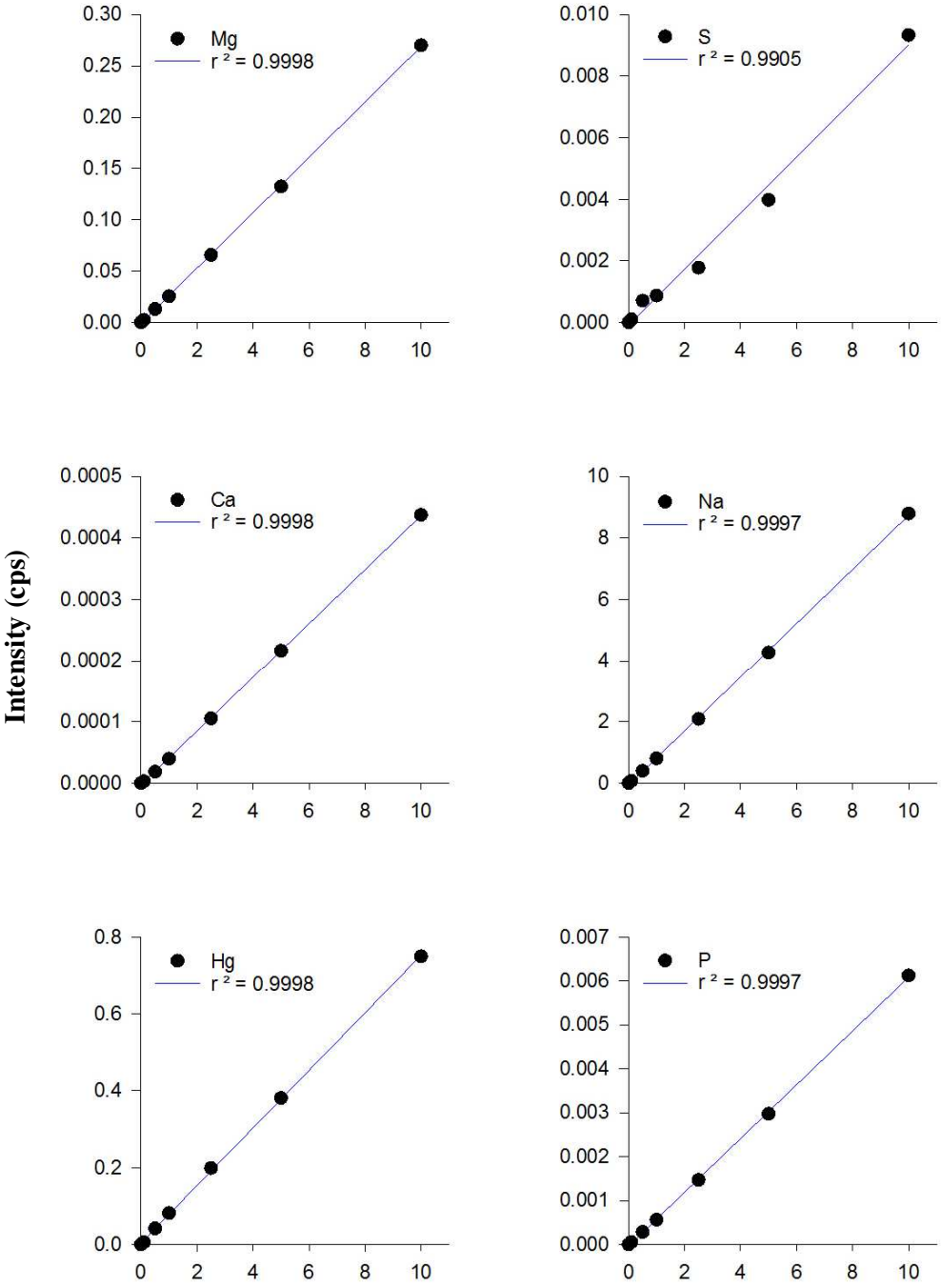

Figure A.8.1. Calibration curves for individual elements measured by ICP-MS with solution-based calibration (standard addition mode)

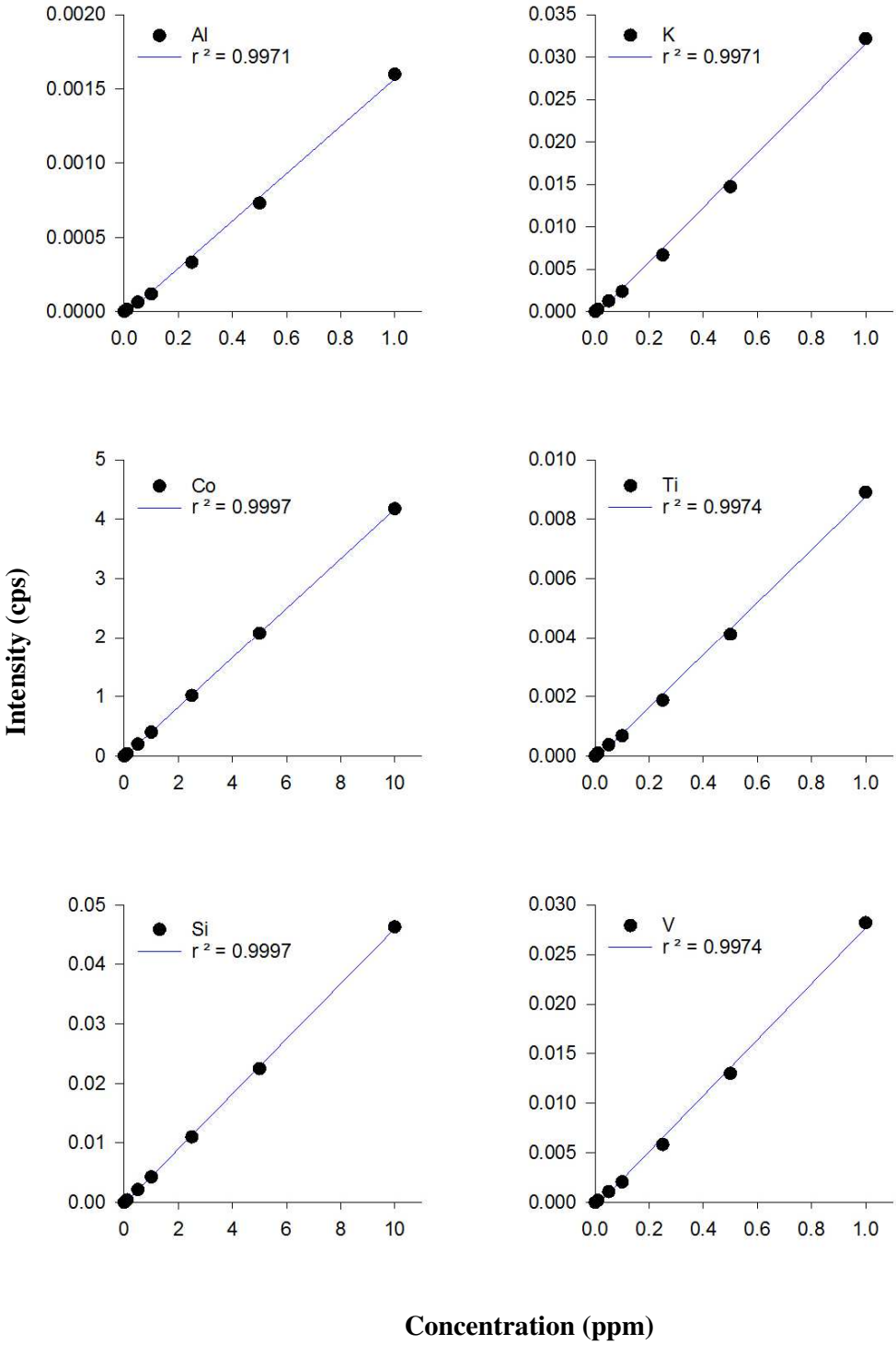

Figure A.8.2. Calibration curves for individual elements measured by ICP-MS with solution-based calibration (standard addition mode)

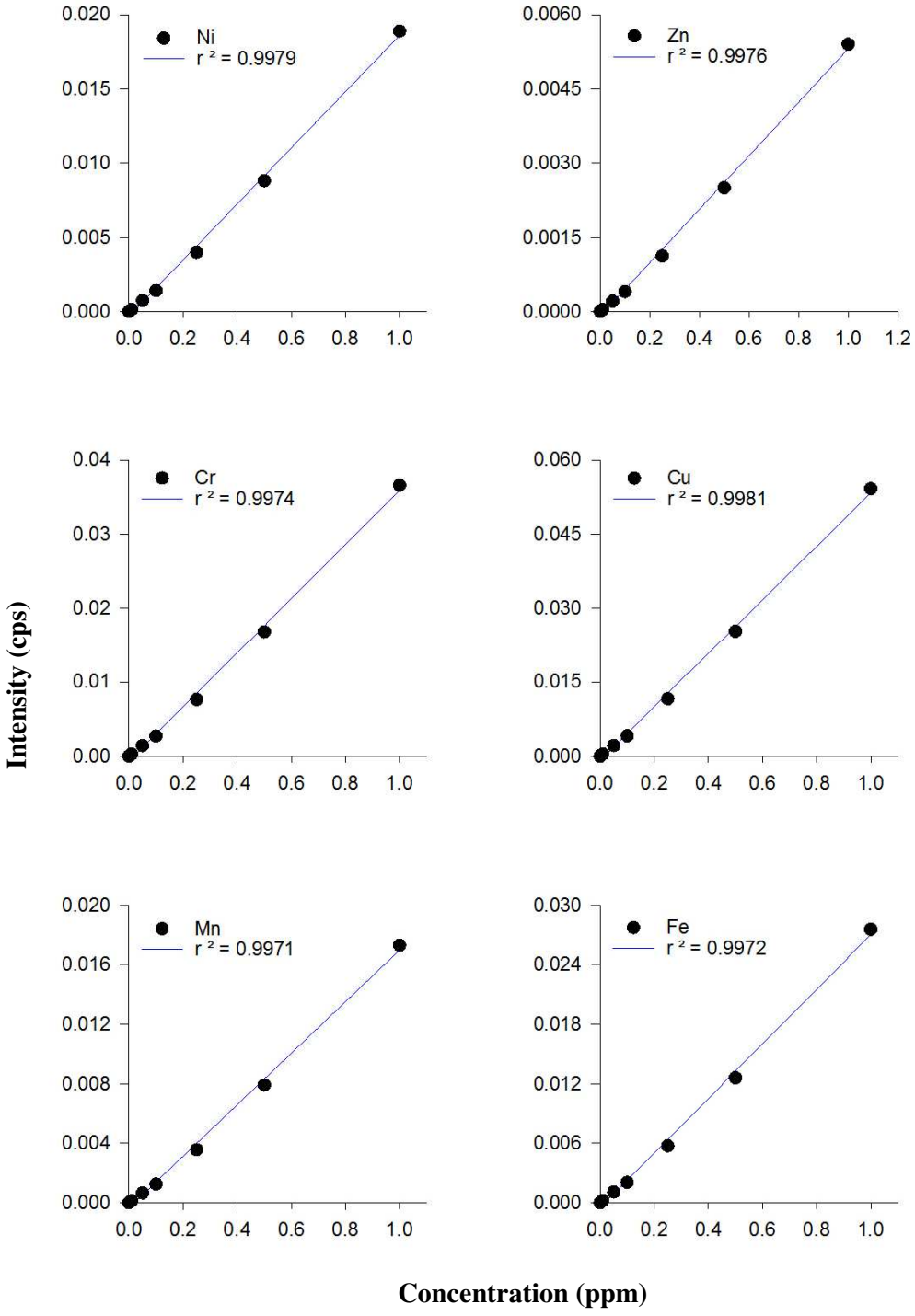

Figure A.8.3. Calibration curves for individual elements measured by ICP-MS with solution-based calibration (standard addition mode)

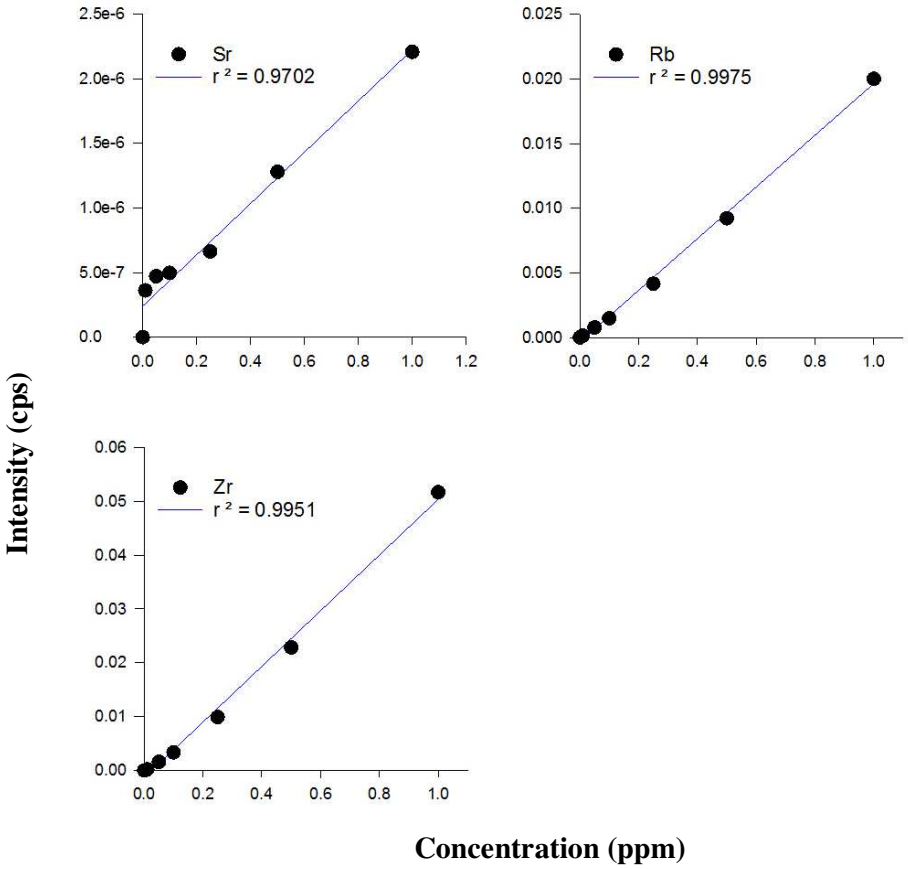

Figure A.8.4. Calibration curves for individual elements measured by ICP-MS with solution-based calibration (standard addition mode)

Appendix B

Publication from the thesis

Ferraro G., Jadhav A.J., and Barigou M. (2020), A Henry's law method for generating bulk nanobubbles, *Nanoscale, 2020, 12, 15869-15879*

References

ABBE, E. J. A. F. M. A. 1873. Beiträge zur Theorie des Mikroskops und der mikroskopischen Wahrnehmung. 9**,** 413-468.

ADAIR, J. H., SUVACI, E. & SINDEL, J. 2001. Surface and Colloid Chemistry. *In:* BUSCHOW, K. H. J., CAHN, R. W., FLEMINGS, M. C., ILSCHNER, B., KRAMER, E. J., MAHAJAN, S. & VEYSSIÈRE, P. (eds.) *Encyclopedia of Materials: Science and Technology.* Oxford: Elsevier.

AGARWAL, A., NG, W. J. & LIU, Y. 2011. Principle and applications of microbubble and nanobubble technology for water treatment. *Chemosphere,* 84**,** 1175-1180.

AHMED, A. K. A., SUN, C., HUA, L., ZHANG, Z., ZHANG, Y., ZHANG, W. & MARHABA, T. 2018. Generation of nanobubbles by ceramic membrane filters: The dependence of bubble size and zeta potential on surface coating, pore size and injected gas pressure. *Chemosphere,* 203**,** 327-335.

AKAGI, T., WANG, X., UTO, T., BABA, M. & AKASHI, M. 2007. Protein direct delivery to dendritic cells using nanoparticles based on amphiphilic poly(amino acid) derivatives. *Biomaterials,* 28**,** 3427-3436.

ALHESHIBRI, M. & CRAIG, V. S. J. 2018. Differentiating between Nanoparticles and Nanobubbles by Evaluation of the Compressibility and Density of Nanoparticles. *The Journal of Physical Chemistry C,* 122**,** 21998-22007.

ALHESHIBRI, M. & CRAIG, V. S. J. 2019a. Armoured nanobubbles; ultrasound contrast agents under pressure. *Journal of Colloid and Interface Science,* 537**,** 123-131.

ALHESHIBRI, M. & CRAIG, V. S. J. 2019b. Generation of nanoparticles upon mixing ethanol and water; Nanobubbles or Not? *Journal of Colloid and Interface Science,* 542**,** 136-143.

ALHESHIBRI, M., JEHANNIN, M., COLEMAN, V. A. & CRAIG, V. S. J. 2019. Does gas supersaturation by a chemical reaction produce bulk nanobubbles? *Journal of Colloid and Interface Science,* 554**,** 388-395.

ALHESHIBRI, M., QIAN, J., JEHANNIN, M. & CRAIG, V. S. J. 2016. A History of Nanobubbles. *Langmuir,* 32**,** 11086-11100.

AMARAL FILHO, J., AZEVEDO, A., ETCHEPARE, R. & RUBIO, J. J. I. J. O. M. P. 2016. Removal of sulfate ions by dissolved air flotation (DAF) following precipitation and flocculation. 149**,** 1-8.

ARZENŠEK, D., PODGORNIK, R. & KUZMAN, D. Dynamic light scattering and application to proteins in solutions. Seminar; University of Ljubljana: Ljubljana, Slovenia, 2010. 1-18.

ATIEMO-OBENG, V. A., CALABRESE, R. V. J. H. O. I. M. S. & PRACTICE 2004. Rotor-stator mixing devices. Wiley Online Library.

ATTARD, P. J. T. E. P. J. S. T. 2013. The stability of nanobubbles.

AZEVEDO, A., ETCHEPARE, R., CALGAROTO, S. & RUBIO, J. 2016. Aqueous dispersions of nanobubbles: Generation, properties and features. *Minerals Engineering,* 94**,** 29-37.

BAŁDYGA, J., ORCIUCH, W., MAKOWSKI, Ł., MALIK, K., ÖZCAN-TAŞKIN, G., EAGLES, W. & PADRON, G. 2008. Dispersion of Nanoparticle Clusters in a Rotor−Stator Mixer. *Industrial & Engineering Chemistry Research,* 47**,** 3652-3663.

BERNE, B. J. & PECORA, R. 2000. *Dynamic light scattering: with applications to chemistry, biology, and physics*, Courier Corporation.

BOOTH, F. 1948. Theory of electrokinetic effects. Nature Publishing Group.

BOSHENYATOV, B. V., KOSHARIDZE, S. I. & LEVIN, Y. K. 2019. On the Stability of Nanobubbles in Water. *Russian Physics Journal,* 61**,** 1914-1921.

BOYLE, R. 1662. *A defence of the doctrine touching the spring and weight of the air [electronic resource] / propos'd by Mr. R. Boyle in his new physico-mechanical experiments, against the objections of Franciscus Linus*
wherewith the objector's funicular hypothesis is also examin'd, by the author of those experiments, London, London : Printed by F.G. for Thomas Robinson ...

BUNKIN, N. F. & BUNKIN, F. V. 1992. Bubbstons: Stable microscopic gas bubbles in very dilute electrolytic solutions. *Soviet Physics - JETP,* 74**,** 271-278.

BUNKIN, N. F. & BUNKIN, F. V. 2003. Screening of strongly charged macroparticles in liquid electrolyte solutions. *Journal of Experimental and Theoretical Physics,* 96**,** 730-746.

BUNKIN, N. F., SHKIRIN, A. V., BURKHANOV, I. S., CHAIKOV, L. L. & LOMKOVA, A. K. 2014. Study of the nanobubble phase of aqueous NaCl solutions by dynamic light scattering. *Quantum electronics (Woodbury, N.Y.),* 44**,** 1022-1028.

BUNKIN, N. F., SHKIRIN, A. V. & KOZLOV, V. A. 2012. Cluster Structure of Dissolved Gas Nanobubbles in Ionic Aqueous Solutions. *J. Chem. Eng. Data,* 57**,** 2823-2831.

BUNKIN, N. F., SHKIRIN, A. V., SUYAZOV, N. V., BABENKO, V. A., SYCHEV, A. A., PENKOV, N. V., BELOSLUDTSEV, K. N. & GUDKOV, S. V. 2016. Formation and Dynamics of Ion-Stabilized Gas Nanobubble Phase in the Bulk of Aqueous NaCl Solutions. *The Journal of Physical Chemistry B,* 120**,** 1291-1303.

BURG, T. P., GODIN, M., KNUDSEN, S. M., SHEN, W., CARLSON, G., FOSTER, J. S., BABCOCK, K. & MANALIS, S. R. 2007. Weighing of biomolecules, single cells and single nanoparticles in fluid. *Nature,* 446**,** 1066.

CAI, W. B., YANG, H. L., ZHANG, J., YIN, J. K., YANG, Y. L., YUAN, L. J., ZHANG, L. & DUAN, Y. Y. 2015. The Optimized Fabrication of Nanobubbles as Ultrasound Contrast Agents for Tumor Imaging. *Scientific Reports,* 5**,** 13725.

CALGAROTO, S., AZEVEDO, A. & RUBIO, J. 2016. Separation of amine-insoluble species by flotation with nano and microbubbles. *Minerals Engineering,* 89**,** 24-29.

CALGAROTO, S., WILBERG, K. Q. & RUBIO, J. 2014. On the nanobubbles interfacial properties and future applications in flotation. *Minerals Engineering,* 60**,** 33-40.

CARGILL, R. W. 1993. The solubility of gases in water–alcohol mixtures. *Chemical Society Reviews,* 22**,** 135-141.

CAVALLI, R., BISAZZA, A., TROTTA, M., ARGENZIANO, M., CIVRA, A., DONALISIO, M. & LEMBO, D. J. I. J. O. N. 2012. New chitosan nanobubbles for ultrasound-mediated gene delivery: preparation and in vitro characterization. 7**,** 3309.

CHAPLIN, M. 2011. Water structure and science.

CHAPLIN, M. J. M. R. J. 2009. Theory versus experiment. What is the charge at the surface of water. 2**,** 1-28.

CHEN, K.-K. 2009. Bathing pool assembly with water full of nano-scale ozone bubbles for rehabilitation. Google Patents.

CHEN, M., PENG, L., QIU, J., LUO, K., LIU, D. & HAN, P. 2020. Monitoring of Ethanol-water Exchange Process to Produce Bulk Nanobubbles Based on Dynamic Light Scattering. *Langmuir*.

CHEN, Q., LUO, L., FARAJI, H., FELDBERG, S. W. & WHITE, H. S. 2014. Electrochemical Measurements of Single H2 Nanobubble Nucleation and Stability at Pt Nanoelectrodes. *The Journal of Physical Chemistry Letters,* 5**,** 3539-3544.

CHEN, Q., LUO, L. & WHITE, H. S. 2015a. Electrochemical Generation of a Hydrogen Bubble at a Recessed Platinum Nanopore Electrode. *Langmuir,* 31**,** 4573-4581.

CHEN, Q., WIEDENROTH, H. S., GERMAN, S. R. & WHITE, H. S. 2015b. Electrochemical Nucleation of Stable N2 Nanobubbles at Pt Nanoelectrodes. *Journal of the American Chemical Society,* 137**,** 12064-12069.

COKER, A. 2007. Physical Properties of Liquids and Gases.

COX, A. N. 2000. *Allen's astrophysical quantities*.

CRAIG, V. S. J. J. S. M. 2011. Very small bubbles at surfaces—the nanobubble puzzle. 7**,** 40-48.

DE HERT, S. C. & RODGERS, T. J. C. E. S. 2017a. Continuous, recycle and batch emulsification kinetics using a high-shear mixer. 167**,** 265-277.

DE HERT, S. C. & RODGERS, T. L. J. C. E. S. 2017b. On the effect of dispersed phase viscosity and mean residence time on the droplet size distribution for high-shear mixers. 172**,** 423-433.

DERJAGUIN, B. & LANDAU, L. J. P. I. S. S. 1993. Theory of the stability of strongly charged lyophobic sols and of the adhesion of strongly charged particles in solutions of electrolytes. 43**,** 30-59.

DERJAGUIN, B. J. P. I. S. S. 1993. A theory of interaction of particles in presence of electric double layers and the stability of lyophobe colloids and disperse systems. 43**,** 1-14.

DEVLIN, J. P. & MONREAL, I. A. 2010. Clathrate–hydrate ultrafast nucleation and crystallization from supercooled aqueous nanodroplets. *Chemical Physics Letters,* 492**,** 1-8.

EBINA, K., SHI, K., HIRAO, M., HASHIMOTO, J., KAWATO, Y., KANESHIRO, S., MORIMOTO, T., KOIZUMI, K. & YOSHIKAWA, H. 2013. Oxygen and Air Nanobubble Water Solution Promote the Growth of Plants, Fishes, and Mice. e65339. *PLoS ONE,* 8.

ENOMOTO NAOYUKI, KOBAYASHI HIDEAKI, MAEDA SHIGEO, IDA KATSUSHISA, NISHIHARA IKKAN & TOSHIHIRO, F. 2015. Improvement of cleaning effect of vegetables using ultrafine bubble water generated by ultrafineGALF.

EPSTEIN, P. S. & PLESSET, M. S. 1950. On the Stability of Gas Bubbles in Liquid-Gas Solutions. *The Journal of Chemical Physics,* 18**,** 1505-1509.

ESPINOZA, C. J. U., SIMMONS, M. J. H., ALBERINI, F., MIHAILOVA, O., ROTHMAN, D. & KOWALSKI, A. J. 2018. Flow studies in an in-line Silverson 150/250 high shear mixer using PIV. *Chemical Engineering Research and Design,* 132**,** 989-1004.

ETCHEPARE, R., AZEVEDO, A., CALGAROTO, S. & RUBIO, J. 2017a. Removal of ferric hydroxide by flotation with micro and nanobubbles. *Separation and Purification Technology,* 184**,** 347-353.

ETCHEPARE, R., OLIVEIRA, H., NICKNIG, M., AZEVEDO, A. & RUBIO, J. 2017b. Nanobubbles: Generation using a multiphase pump, properties and features in flotation. *Minerals Engineering,* 112**,** 19-26.

FAN, M., TAO, D., HONAKER, R. & LUO, Z. 2010a. Nanobubble generation and its application in froth flotation (part I): nanobubble generation and its effects on properties of microbubble and millimeter scale bubble solutions. *Mining Science and Technology (China),* 20**,** 1-19.

FAN, M., TAO, D., HONAKER, R. & LUO, Z. 2010b. Nanobubble generation and its applications in froth flotation (part II): fundamental study and theoretical analysis. *Mining Science and Technology (China),* 20**,** 159-177.

FAN, M., TAO, D., HONAKER, R. & LUO, Z. 2010c. Nanobubble generation and its applications in froth flotation (part III): specially designed laboratory scale column flotation of phosphate. *Mining Science and Technology (China),* 20**,** 317-338.

FAN, M., TAO, D., HONAKER, R. & LUO, Z. 2010d. Nanobubble generation and its applications in froth flotation (part IV): mechanical cells and specially designed column flotation of coal. *Mining Science and Technology (China),* 20**,** 641-671.

FAN, X., WANG, L., GUO, Y., TU, Z., LI, L., TONG, H., XU, Y., LI, R. & FANG, K. 2015. Ultrasonic Nanobubbles Carrying Anti-PSMA Nanobody: Construction and Application in Prostate Cancer-Targeted Imaging. *PLOS ONE,* 10**,** e0127419.

FANG, Z., WANG, L., WANG, X., ZHOU, L., WANG, S., ZOU, Z., TAI, R., ZHANG, L. & HU, J. 2018. Formation and Stability of Surface/Bulk Nanobubbles Produced by Decompression at Lower Gas Concentration. *The Journal of Physical Chemistry C,* 122**,** 22418-22423.

FANG, Z., WANG, X., ZHOU, L., ZHANG, L. & HU, J. 2020. Formation and Stability of Bulk Nanobubbles by Vibration. *Langmuir,* 36**,** 2264-2270.

FERNÁNDEZ-PRINI, R., ALVAREZ, J. L. & HARVEY, A. H. 2003. Henry's Constants and Vapor–Liquid Distribution Constants for Gaseous Solutes in H2O and D2O at High Temperatures. *Journal of Physical and Chemical Reference Data,* 32**,** 903-916.

FERRARO, G., JADHAV, A. J. & BARIGOU, M. 2020. A Henry's law method for generating bulk nanobubbles. *Nanoscale*.

FILIPE, V., HAWE, A. & JISKOOT, W. 2010. Critical Evaluation of Nanoparticle Tracking Analysis (NTA) by NanoSight for the Measurement of Nanoparticles and Protein Aggregates. *Pharmaceutical Research,* 27**,** 796-810.

FOX, F. E. & HERZFELD, K. F. 1954. Gas Bubbles with Organic Skin as Cavitation Nuclei. *The Journal of the Acoustical Society of America,* 26**,** 984-989.

FUJITA;, H. K. S. M. M. K. T. 2014. Measurement and identification of ultrafine bubbles by resonant mass measurement method. *SPIE*.

GARDE, S., GARCíA, A. E., PRATT, L. R. & HUMMER, G. 1999. Temperature dependence of the solubility of non-polar gases in water. *Biophysical Chemistry,* 78**,** 21-32.

GERMAN, S. R., EDWARDS, M. A., CHEN, Q. & WHITE, H. S. 2016. Laplace Pressure of Individual H2 Nanobubbles from Pressure-Addition Electrochemistry. *Nano Lett,* 16**,** 6691-6694.

GHADIMKHANI, A., ZHANG, W. & MARHABA, T. 2016. Ceramic membrane defouling (cleaning) by air Nano Bubbles. *Chemosphere,* 146**,** 379-384.

GOBINATH, S., SENTHILKUMAR, G. & BEEMKUMAR, N. 2019. Air nanobubble-enhanced combustion study using mustard biodiesel in a common rail direct injection engine. *Energy Sources, Part A: Recovery, Utilization, and Environmental Effects,* 41**,** 1809-1816.

GOLDBURG, W. I. 1999. Dynamic light scattering. *American Journal of Physics,* 67**,** 1152-1160.

GOLDMAN, S. 2009. Generalizations of the Young–Laplace equation for the pressure of a mechanically stable gas bubble in a soft elastic material. *The Journal of chemical physics,* 131**,** 184502.

GRACIAA, A., CREUX, P., LACHAISE, J., 2002. Electrokinetics of bubbles. *In:* DEKKER, M. (ed.) *Encyclopedia of Surface and Colloid Science.*

GÜL ÖZCAN-TAŞKıN, N., PADRON, G. A. & KUBICKI, D. 2016. Comparative performance of in-line rotor-stators for deagglomeration processes. *Chemical Engineering Science,* 156**,** 186-196.

HÄBICH, A., DUCKER, W., DUNSTAN, D. E. & ZHANG, X. 2010. Do Stable Nanobubbles Exist in Mixtures of Organic Solvents and Water? *The Journal of Physical Chemistry B,* 114**,** 6962-6967.

HALL, S., COOKE, M., EL-HAMOUZ, A. & KOWALSKI, A. J. 2011. Droplet break-up by in-line Silverson rotor–stator mixer. *Chemical Engineering Science,* 66**,** 2068-2079.

HERNANDEZ, C., ABENOJAR, E. C., HADLEY, J., COYNE, R., PERERA, R., GOPALAKRISHNAN, R., BASILION, J. P., KOLIOS, M. C. & EXNER, A. A. J. N. 2019. Sink or float? Characterization of shell-stabilized bulk nanobubbles using a resonant mass measurement technique. 11**,** 851-855.

HITCHMAN, M. L. 1978. *Measurement of dissolved oxygen*, John Wiley & Sons Canada, Limited.

HUNDY, G. F., TROTT, A. R. & WELCH, T. C. 2008. Air and Water Vapour Mixtures.

HUNTER, R. J. 1981. Zeta potential in colloid science : principles and applications / Robert J. Hunter. London: Academic Press.

ISHIDA, N., INOUE, T., MIYAHARA, M. & HIGASHITANI, K. 2000. Nano bubbles on a hydrophobic surface in water observed by tapping-mode atomic force microscopy. *Langmuir,* 16**,** 6377-6380.

ISRAELACHVILI, J. N. 1985. Intermolecular and surface forces : with applications to colloidal and biological systems / Jacob N. Israelachvili. London: London : Academic.

JADHAV, A. J. & BARIGOU, M. 2020a. Bulk Nanobubbles or Not Nanobubbles: That is the Question. *Langmuir : the ACS journal of surfaces and colloids,* 36**,** 1699-1708.

JADHAV, A. J. & BARIGOU, M. 2020b. Proving and interpreting the spontaneous formation of bulk nanobubbles in aqueous organic solvent solutions: effects of solvent type and content. *Soft Matter,* 16**,** 4502-4511.

JAMES, J., COOKE, M., KOWALSKI, A., RODGERS, T. J. C. E. R. & DESIGN 2017. Scale-up of batch rotor-stator mixers. Part 2—Mixing and emulsification. 124**,** 321-329.

JIN, F., YE, J., HONG, L., LAM, H. & WU, C. 2007. Slow Relaxation Mode in Mixtures of Water and Organic Molecules: Supramolecular Structures or Nanobubbles? *The Journal of Physical Chemistry B,* 111**,** 2255-2261.

JIN, J., FENG, Z., YANG, F. & GU, N. 2019. Bulk Nanobubbles Fabricated by Repeated Compression of Microbubbles. *Langmuir,* 35**,** 4238-4245.

JIN, J., WANG, R., TANG, J., YANG, L., FENG, Z., XU, C., YANG, F. & GU, N. 2020. Dynamic tracking of bulk nanobubbles from microbubbles shrinkage to collapse. *Colloids and Surfaces A: Physicochemical and Engineering Aspects,* 589**,** 124430.

JOHN, T. P., FONTE, C. P., KOWALSKI, A. & RODGERS, T. L. 2019a. A comparison of power and flow characteristics between batch and in-line rotor-stator mixers. *Chemical Engineering Science,* 202**,** 481-490.

JOHN, T. P., PANESAR, J. S., KOWALSKI, A., RODGERS, T. L. & P. FONTE, C. 2019b. Linking power and flow in rotor-stator mixers. *Chemical Engineering Science,* 207**,** 504-515.

KANEMATSU, W., TUZIUTI, T. & YASUI, K. 2020. The influence of storage conditions and container materials on the long term stability of bulk nanobubbles — Consideration from a perspective of interactions between bubbles and surroundings. *Chemical Engineering Science,* 219**,** 115594.

KARBSTEIN, H. & SCHUBERT, H. 1995. Developments in the continuous mechanical production of oil-in-water macro-emulsions. *Chemical Engineering and Processing: Process Intensification,* 34**,** 205-211.

KASZUBA, M., MCKNIGHT, D., CONNAH, M. T., MCNEIL-WATSON, F. K. & NOBBMANN, U. 2008. Measuring sub nanometre sizes using dynamic light scattering. *Journal of Nanoparticle Research,* 10**,** 823-829.

KAWARA, F., INOUE, J., TAKENAKA, M., HOSHI, N., MASUDA, A., NISHIUMI, S., KUTSUMI, H., AZUMA, T. & OHDAIRA, T. 2014. The Influences of Pepsin Concentrations and pH Levels on the Disinfective Activity of Ozone Nanobubble Water against Helicobacter pylori. *Digestion,* 90**,** 10-17.

KE, S., XIAO, W., QUAN, N., DONG, Y., ZHANG, L. & HU, J. 2019. Formation and Stability of Bulk Nanobubbles in Different Solutions. *Langmuir,* 35**,** 5250-5256.

KHALED ABDELLA AHMED, A., SUN, C., HUA, L., ZHANG, Z., ZHANG, Y., MARHABA, T. & ZHANG, W. J. E. E. S. 2018. Colloidal properties of air, oxygen, and nitrogen nanobubbles in water: Effects of ionic strength, natural organic matters, and surfactants. 35**,** 720-727.

KHATIB, R., BACKUS, E. H. G., BONN, M., PEREZ-HARO, M.-J., GAIGEOT, M.-P. & SULPIZI, M. 2016. Water orientation and hydrogen-bond structure at the fluorite/water interface. *Scientific Reports,* 6**,** 24287.

KIKUCHI, K., IOKA, A., OKU, T., TANAKA, Y., SAIHARA, Y., OGUMI, Z. J. J. O. C. & SCIENCE, I. 2009. Concentration determination of oxygen nanobubbles in electrolyzed water. 329**,** 306-309.

KIKUCHI, K., NAGATA, S., TANAKA, Y., SAIHARA, Y. & OGUMI, Z. 2007. Characteristics of hydrogen nanobubbles in solutions obtained with water electrolysis. *Journal of Electroanalytical Chemistry,* 600**,** 303-310.

KIKUCHI, K., TAKEDA, H., RABOLT, B., OKAYA, T., OGUMI, Z., SAIHARA, Y. & NOGUCHI, H. 2001a. Hydrogen concentration in water from an Alkali-Ion-Water electrolyzer having a platinum-electroplated titanium electrode. *Journal of Applied Electrochemistry,* 31**,** 1301-1306.

KIKUCHI, K., TAKEDA, H., RABOLT, B., OKAYA, T., OGUMI, Z., SAIHARA, Y. & NOGUCHI, H. 2001b. Hydrogen particles and supersaturation in alkaline water from an Alkali–Ion–Water electrolyzer. *Journal of Electroanalytical Chemistry,* 506**,** 22-27.

KIKUCHI, K., TANAKA, Y., SAIHARA, Y., MAEDA, M., KAWAMURA, M. & OGUMI, Z. 2006a. Concentration of hydrogen nanobubbles in electrolyzed water. *Journal of Colloid and Interface Science,* 298**,** 914-919.

KIKUCHI, K., TANAKA, Y., SAIHARA, Y., MAEDA, M., KAWAMURA, M. & OGUMI, Z. 2006b. Concentration of hydrogen nanobubbles in electrolyzed water. *J Colloid Interface Sci,* 298**,** 914-9.

KIKUCHI, K., TANAKA, Y., SAIHARA, Y. & OGUMI, Z. J. E. A. 2006c. Study of hydrogen nanobubbles in solution in the vicinity of a platinum wire electrode using double-potential step chronoamperometry. 52**,** 904-913.

KIM, J. Y., SONG, M. G. & KIM, J. D. 2000. Zeta Potential of Nanobubbles Generated by Ultrasonication in Aqueous Alkyl Polyglycoside Solutions. *J Colloid Interface Sci,* 223**,** 285-291.

KOBAYASHI, H., MAEDA, S., KASHIWA, M. & FUJITA, T. Measurements of ultrafine bubbles using different types of particle size measuring instruments. International Conference on Optical Particle Characterization (OPC 2014), 2014. International Society for Optics and Photonics, 92320U.

KOZINA, A. 2009. *Crystallization kinetics and viscoelastic properties of colloid binary mixtures with depletion attraction.* PhD thesis.

KURAHASHI, M., KATSURA, S. & MIZUNO, A. 1997. Radical formation due to discharge inside bubble in liquid. *Journal of Electrostatics,* 42**,** 93-105.

LEROY, V. & NORISUYE, T. 2016. Investigating the Existence of Bulk Nanobubbles with Ultrasound. *ChemPhysChem,* 17**,** 2787-2790.

LI, M., TONGGU, L., ZHAN, X., MEGA, T. L. & WANG, L. 2016. Cryo-EM Visualization of Nanobubbles in Aqueous Solutions. *Langmuir : the ACS journal of surfaces and colloids,* 32**,** 11111.

LIANG, J. Effects of Air-fuel Ratio and Hydrogen Fraction on Combustion Characteristics of Hydrogen Direct-Injection Gasoline Engine. IOP Conference Series: Earth and Environmental Science, 2019. IOP Publishing, 042012.

LIMA, E., BOSTRÖM, M., SERNELIUS, B., HORINEK, D., NETZ, R. R., JR, E. C., KUNZ, W. & TAVARES, F. 2008. Forces between air-bubbles in electrolyte solution. *Chemical Physics Letters,* 458**,** 299-302.

LIU, H. & CAO, G. 2016. Effectiveness of the Young-Laplace equation at nanoscale. *Scientific Reports,* 6**,** 23936.

LIU, S., KAWAGOE, Y., MAKINO, Y. & OSHITA, S. 2013. Effects of nanobubbles on the physicochemical properties of water: The basis for peculiar properties of water containing nanobubbles. *Chemical Engineering Science,* 93**,** 250-256.

LIU, S., OSHITA, S., MAKINO, Y., WANG, Q., KAWAGOE, Y. & UCHIDA, T. 2016. Oxidative Capacity of Nanobubbles and Its Effect on Seed Germination. *ACS Sustainable Chemistry & Engineering,* 4**,** 1347-1353.

LJUNGGREN, S. & ERIKSSON, J. C. 1997. The lifetime of a colloid-sized gas bubble in water and the cause of the hydrophobic attraction. *Colloids and Surfaces A: Physicochemical and Engineering Aspects,* 129–130**,** 151-155.

LOMBARD, J., BIBEN, T. & MERABIA, S. 2017. Threshold for Vapor Nanobubble Generation Around Plasmonic Nanoparticles. *The Journal of Physical Chemistry C,* 121**,** 15402-15415.

LOU, S.-T., OUYANG, Z.-Q., ZHANG, Y., LI, X.-J., HU, J., LI, M.-Q., YANG, F.-J. J. J. O. V. S., MICROELECTRONICS, T. B., NANOMETER STRUCTURES PROCESSING, M. & PHENOMENA 2000. Nanobubbles on solid surface imaged by atomic force microscopy. 18**,** 2573-2575.

LOU, S., GAO, J., XIAO, X., LI, X., LI, G., ZHANG, Y., LI, M., SUN, J. & HU, J. 2001. Nanobubbles at the liquid/solid interface studied by atomic force microscopy. *Chin. Phys.,* 10**,** S108-S110.

LOU, S., GAO, J., XIAO, X., LI, X., LI, G., ZHANG, Y., LI, M., SUN, J., LI, X. & HU, J. J. M. C. 2002. Studies of nanobubbles produced at liquid/solid interfaces. 48**,** 211-214.

LTD, M. I. 2015. Operating Manual NS300.

LTD., N. 2008. NanoSight LM10 Nanoparticle Analysis System & NTA 1.5 Analytical Software.

LU, Y.-H., YANG, C.-W. & HWANG, I.-S. 2012. Molecular Layer of Gaslike Domains at a Hydrophobic–Water Interface Observed by Frequency-Modulation Atomic Force Microscopy. *Langmuir,* 28**,** 12691-12695.

LUKIANOVA-HLEB, E. Y., VOLKOV, A. N. & LAPOTKO, D. O. 2014. Laser Pulse Duration Is Critical For the Generation of Plasmonic Nanobubbles. *Langmuir,* 30**,** 7425-7434.

MAEDA S., TOKUDA JUN, FUJITA TOSHIHIRO, TERASAKA KOICHI & SUSUMU, K. 2011. Measurement of nano-bubble generated by nanoGALF using three types of particle size measuring equipment.

MAEDA S., K. M., ISHIDA Y., KIMURA H., KOBAYASHI H., TOKUDA J., FUJITA T. Generation of High Density Nano-Bubbles by nanoGALF Technology and Laser Induced Quantitative Measurement. 1st international symposium on Multiscale Multiphase Process Engineering (MMPE), 2011.

MAEDA SHIGEO, K. H., KASHIWA MASAKAZU, IDA KATSUHISA, NISHIHARA IKKAN, FUJITA TOSHIHIRO, & GOTO KUNIAKI, A. N., TERASAKA KOICHI 2014. Measurement of number density of ultrafine bubbles generated by ultrafineGALF using two types of measurement methods.

MALVERNPANALYTICAL-NS300 Nanosight NS3000.

MARČELJA, S. 2006. Selective Coalescence of Bubbles in Simple Electrolytes. *The Journal of Physical Chemistry B,* 110**,** 13062-13067.

MASUDA, N., MARUYAMA, A., EGUCHI, T., HIRAKAWA, T. & MURAKAMI, Y. 2015. Influence of Microbubbles on Free Radical Generation by Ultrasound in Aqueous Solution: Dependence of Ultrasound Frequency. *The Journal of Physical Chemistry B,* 119**,** 12887-12893.

MEEGODA, J. N., ALUTHGUN HEWAGE, S. & BATAGODA, J. H. 2018. Stability of Nanobubbles. *Environmental Engineering Science,* 35**,** 1216-1227.

MENG, M., GAO, J., WU, C., ZHOU, X., ZANG, X., LIN, X., LIU, H., WANG, C., SU, H., LIU, K., WANG, Y., XUE, X. & WU, J. 2016. Doxorubicin nanobubble for combining ultrasonography and targeted chemotherapy of rabbit with VX2 liver tumor. *Tumor Biology,* 37**,** 8673-8680.

MICHAILIDI, E. D., BOMIS, G., VAROUTOGLOU, A., KYZAS, G. Z., MITRIKAS, G., MITROPOULOS, A. C., EFTHIMIADOU, E. K. & FAVVAS, E. P. 2020. Bulk nanobubbles: Production and investigation of their formation/stability mechanism. *Journal of Colloid and Interface Science,* 564**,** 371-380.

MILLARE, J. C. & BASILIA, B. A. 2018. Nanobubbles from Ethanol-Water Mixtures: Generation and Solute Effects via Solvent Replacement Method. *ChemistrySelect,* 3**,** 9268-9275.

MISRA, S. K., GHOSHAL, G., GARTIA, M. R., WU, Z., DE, A. K., YE, M., BROMFIELD, C. R., WILLIAMS, E. M., SINGH, K., TANGELLA, K. V., RUND, L., SCHULTEN, K., SCHOOK, L. B., RAY, P. S., BURDETTE, E. C. & PAN, D. 2015. Trimodal Therapy: Combining Hyperthermia with Repurposed Bexarotene and Ultrasound for Treating Liver Cancer. *ACS Nano,* 9**,** 10695-10718.

MOHAMEDI, G., AZMIN, M., PASTORIZA-SANTOS, I., HUANG, V., PÉREZ-JUSTE, J., LIZ-MARZÁN, L. M., EDIRISINGHE, M. & STRIDE, E. 2012. Effects of Gold Nanoparticles on the Stability of Microbubbles. *Langmuir,* 28**,** 13808-13815.

MOQADAM, M., LERVIK, A., RICCARDI, E., VENKATRAMAN, V., ALSBERG, B. K. & VAN ERP, T. S. 2018. Local initiation conditions for water autoionization. *Proceedings of the National Academy of Sciences,* 115**,** E4569.

N., E., H., K., S., M., K., I., I., N. & T., F. 2015. Improvement of cleaning effect of vegetables using ultrafine bubble water generated by ultrafineGALF.

NAJAFI, A. S., DRELICH, J., YEUNG, A., XU, Z., MASLIYAH, J. J. J. O. C. & SCIENCE, I. 2007. A novel method of measuring electrophoretic mobility of gas bubbles. 308**,** 344-350.

NAKATAKE, Y., KISU, S., SHIGYO, K., EGUCHI, T. & WATANABE, T. J. E. 2013. Effect of nano air-bubbles mixed into gas oil on common-rail diesel engine. 59**,** 233-239.

NAM, Y. S., PARK, J. Y., HAN, S.-H. & CHANG, I.-S. 2002. Intracellular drug delivery using poly(d,l-lactide-co-glycolide) nano- particles derivatized with a peptide from a transcriptional activator protein of HIV-1. *Biotechnology Letters,* 24**,** 2093-2098.

NIRMALKAR, N., PACEK, A. W. & BARIGOU, M. 2018a. Interpreting the interfacial and colloidal stability of bulk nanobubbles. *Soft Matter,* 14**,** 9643-9656.

NIRMALKAR, N., PACEK, A. W. & BARIGOU, M. 2018b. On the Existence and Stability of Bulk Nanobubbles. *Langmuir,* 34**,** 10964-10973.

NIRMALKAR, N., PACEK, A. W. & BARIGOU, M. 2019. Bulk Nanobubbles from Acoustically Cavitated Aqueous Organic Solvent Mixtures. *Langmuir,* 35**,** 2188-2195.

OH, S. H., HAN, J. G. & KIM, J.-M. 2015. Long-term stability of hydrogen nanobubble fuel. *Fuel,* 158**,** 399-404.

OH, S. H. & KIM, J.-M. 2017. Generation and Stability of Bulk Nanobubbles. *Langmuir*.

OH, S. H., YOON, S. H., SONG, H., HAN, J. G. & KIM, J.-M. 2013. Effect of hydrogen nanobubble addition on combustion characteristics of gasoline engine. *International Journal of Hydrogen Energy,* 38**,** 14849-14853.

OHGAKI, K., KHANH, N. Q., JODEN, Y., TSUJI, A. & NAKAGAWA, T. 2010. Physicochemical approach to nanobubble solutions. *Chemical Engineering Science,* 65**,** 1296-1300.

OHNARI, H. J. J. O. T. H. T. S. O. J. 2001. Fisheries experiments of cultivated shells using micro-bubbles technique. 40**,** 2-7.

OSTWALD, W. 1896. Lehrbuch der Allgemeinen Chemie, vol. 2, part 1. Engelmann, Leipzig, Germany. German.

OSTWALD, W. J. Z. F. P. C. 1897. File: Wilhelm Ostwald-Studien über die Bildung und Umwandlung fester Körper. pdf. 22**,** 289-330.

OVARFORT, R. 1988. New electrochemical cell for pitting corrosion testing. *Corrosion Science,* 28**,** 135-140.

OVERBEEK, J. T. G. J. A. I. C. S. 1950. Quantitative interpretation of the electrophoretic velocity of colloids. 3**,** 797-823.

ÖZCAN-TAŞKIN, G. & WEI, H. 2003. The effect of impeller-to-tank diameter ratio on draw down of solids. *Chemical Engineering Science,* 58**,** 2011-2022.

PACEK, A. W., DING, P. & UTOMO, A. T. 2007. Effect of energy density, pH and temperature on de-aggregation in nano-particles/water suspensions in high shear mixer. *Powder Technology,* 173**,** 203-210.

PADRON, G., KOCH, E. & CALABRESE, R. 2001. *Measurement and Comparison of Power Draw in Batch Rotor-Stator Mixers*.

PADRON, G. A. & ÖZCAN-TAŞKıN, N. G. 2018. Particle de-agglomeration with an in-line rotor-stator mixer at different solids loadings and viscosities. *Chemical Engineering Research and Design,* 132**,** 913-921.

PALIT, G., KAIN, V. & GADIYAR, H. J. C. 1993. Electrochemical investigations of pitting corrosion in nitrogen-bearing type 316LN stainless steel. 49**,** 977-991.

PAN, D., LIU, L.-M., SLATER, B., MICHAELIDES, A. & WANG, E. 2011. Melting the Ice: On the Relation between Melting Temperature and Size for Nanoscale Ice Crystals. *ACS Nano,* 5**,** 4562-4569.

PANALYTICAL, M. *Resonant Mass Measurement* [Online]. Available: https://www.malvernpanalytical.com/en/products/technology/resonant-mass-measurement/?gclid=CjwKCAjw75HWBRAwEiwAdzefxNq_5WHpeE08IktuvNKOG_IRN4hVhxQN6ZNjYe3tUryjoKy54cIMlhoCBegQAvD_BwE [Accessed].

PARK, J.-S. & KURATA, K. J. H. 2009. Application of microbubbles to hydroponics solution promotes lettuce growth. 19**,** 212-215.

PAUL HARRISON, C. G., IAN L.SARGENT 2014. *Extracellular Vesicles in Health and Disease*, Pan Stanford.

PENG, H., BIRKETT, G. R. & NGUYEN, A. V. 2013a. Origin of Interfacial Nanoscopic Gaseous Domains and Formation of Dense Gas Layer at Hydrophobic Solid–Water Interface. *Langmuir,* 29**,** 15266-15274.

PENG, H., HAMPTON, M. A. & NGUYEN, A. V. 2013b. Nanobubbles Do Not Sit Alone at the Solid–Liquid Interface. *Langmuir,* 29**,** 6123-6130.

PERERA, R. H., SOLORIO, L., WU, H., GANGOLLI, M., SILVERMAN, E., HERNANDEZ, C., PEIRIS, P. M., BROOME, A.-M. & EXNER, A. A. J. P. R. 2014. Nanobubble ultrasound contrast agents for enhanced delivery of thermal sensitizer to tumors undergoing radiofrequency ablation. 31**,** 1407-1417.

PEYMAN, S. A., MCLAUGHLAN, J. R., ABOU-SALEH, R. H., MARSTON, G., JOHNSON, B. R., FREEAR, S., COLETTA, P. L., MARKHAM, A. F. & EVANS, S. D. 2016. On-chip preparation of nanoscale contrast agents towards high-resolution ultrasound imaging. *Lab Chip,* 16**,** 679-87.

QIN, H., XU, Q., LI, W., DANG, X., HAN, Y., LEI, K., ZHOU, L. & ZHANG, J. 2017. Effect of Stator Geometry on the Emulsification and Extraction in the Inline Single-Row Blade-Screen High Shear Mixer. *Industrial & Engineering Chemistry Research,* 56**,** 9376-9388.

QIU, J., ZOU, Z., WANG, S., WANG, X., WANG, L., DONG, Y., ZHAO, H., ZHANG, L. & HU, J. 2017. Formation and Stability of Bulk Nanobubbles Generated by Ethanol–Water Exchange. *ChemPhysChem*.

RAK, D., OVADOVÁ, M. & SEDLÁK, M. 2019. (Non)Existence of Bulk Nanobubbles: The Role of Ultrasonic Cavitation and Organic Solutes in Water. *The journal of physical chemistry letters,* 10**,** 4215-4221.

RAPOPORT, N., GAO, Z. & KENNEDY, A. 2007. Multifunctional Nanoparticles for Combining Ultrasonic Tumor Imaging and Targeted Chemotherapy. *JNCI: Journal of the National Cancer Institute,* 99**,** 1095-1106.

RETTICH, T. R., HANDA, Y. P., BATTINO, R. & WILHELM, E. 1981. Solubility of gases in liquids. 13. High-precision determination of Henry's constants for methane and ethane in liquid water at 275 to 328 K. *The Journal of Physical Chemistry,* 85**,** 3230-3237.

ROBINSON, A., JUDD, R. L. & LESAGE, F. 2010. Numerical Method for Spherical Bubble Growth in Superheated Liquids. *Computational Thermal Sciences,* 2**,** 19-31.

RODGERS, T. & COOKE, M. Correlation of drop size with shear tip speed. 14th European Conference on Mixing, 2012. 407-412.

RUEGER, P. E., CALABRESE, R. V. J. C. E. R. & DESIGN 2013. Dispersion of water into oil in a rotor–stator mixer. Part 1: Drop breakup in dilute systems. 91**,** 2122-2133.

SAMIMI, S., MAGHSOUDNIA, N., EFTEKHARI, R. B. & DORKOOSH, F. 2019. Chapter 3 - Lipid-Based Nanoparticles for Drug Delivery Systems. *In:* MOHAPATRA, S. S., RANJAN, S., DASGUPTA, N., MISHRA, R. K. & THOMAS, S. (eds.) *Characterization and Biology of Nanomaterials for Drug Delivery.* Elsevier.

SASTRI, V. R. 2010. Chapter 6 - Commodity Thermoplastics: Polyvinyl Chloride, Polyolefins, and Polystyrene. *In:* SASTRI, V. R. (ed.) *Plastics in Medical Devices.* Boston: William Andrew Publishing.

SASTRI, V. R. 2013. *Plastics in medical devices: properties, requirements, and applications*, William Andrew.

SEDDON, J. R., KOOIJ, E. S., POELSEMA, B., ZANDVLIET, H. J. & LOHSE, D. J. P. R. L. 2011. Surface bubble nucleation stability. 106**,** 056101.

SEDDON, J. R. T., BLIZNYUK, O., KOOIJ, E. S., POELSEMA, B., ZANDVLIET, H. J. W. & LOHSE, D. 2010. Dynamic Dewetting through Micropancake Growth. *Langmuir,* 26**,** 9640-9644.

SEDDON, J. R. T. & LOHSE, D. 2011. Nanobubbles and micropancakes: gaseous domains on immersed substrates. *J Phys Condens Matter,* 23**,** 133001.

SEDDON, J. R. T., LOHSE, D., DUCKER, W. A. & CRAIG, V. S. J. 2012. A Deliberation on Nanobubbles at Surfaces and in Bulk. *ChemPhysChem,* 13**,** 2179-2187.

SEDLÁK, M. & RAK, D. 2013. Large-Scale Inhomogeneities in Solutions of Low Molar Mass Compounds and Mixtures of Liquids: Supramolecular Structures or Nanobubbles? *The Journal of Physical Chemistry B,* 117**,** 2495-2504.

SILVESTRONI, P. 1997. *Fondamenti di Chimica*.

SMOLUCHOWSKI, M. V. J. B. I. A. S. C. 1903. Contribution to the theory of electro-osmosis and related phenomena. 3**,** 184-199.

TAKAHASHI, M. 2005. ζ Potential of Microbubbles in Aqueous Solutions: Electrical Properties of the Gas−Water Interface. *The Journal of Physical Chemistry B,* 109**,** 21858-21864.

TAKAHASHI, M., CHIBA, K. & LI, P. 2007a. Formation of Hydroxyl Radicals by Collapsing Ozone Microbubbles under Strongly Acidic Conditions. *The Journal of Physical Chemistry B,* 111**,** 11443-11446.

TAKAHASHI, M., CHIBA, K. & LI, P. 2007b. Free-Radical Generation from Collapsing Microbubbles in the Absence of a Dynamic Stimulus. *The Journal of Physical Chemistry B,* 111**,** 1343-1347.

TAKENOUCHI, T. J. J. O. A. E. 2010. Behavior of hydrogen nanobubbles in alkaline electrolyzed water and its rinse effect for sulfate ion remained on nickel-plated surface. 40**,** 849-854.

TASAKI, T., WADA, T., BABA, Y., KUKIZAKI, M. J. I. & RESEARCH, E. C. 2009. Degradation of surfactants by an integrated nanobubbles/VUV irradiation technique. 48**,** 4237-4244.

TEIRLINCK, E., XIONG, R., BRANS, T., FORIER, K., FRAIRE, J., VAN ACKER, H., MATTHIJS, N., DE RYCKE, R., DE SMEDT, S. C., COENYE, T. & BRAECKMANS, K. 2018. Laser-induced vapour nanobubbles improve drug diffusion and efficiency in bacterial biofilms. *Nature Communications,* 9**,** 4518.

TIAN, J., YANG, F., CUI, H., ZHOU, Y., RUAN, X. & GU, N. 2015. A Novel Approach to Making the Gas-Filled Liposome Real: Based on the Interaction of Lipid with Free Nanobubble within the Solution. *ACS Applied Materials & Interfaces,* 7**,** 26579-26584.

TREFALT, G., BEHRENS, S. H. & BORKOVEC, M. 2016. Charge Regulation in the Electrical Double Layer: Ion Adsorption and Surface Interactions. *Langmuir,* 32**,** 380-400.

TUZIUTI, T., YASUI, K. & KANEMATSU, W. 2017. Influence of increase in static pressure on bulk nanobubbles. *Ultrasonics Sonochemistry,* 38**,** 347-350.

TUZIUTI, T., YASUI, K. & KANEMATSU, W. 2018. Influence of addition of degassed water on bulk nanobubbles. *Ultrasonics Sonochemistry*.

USHIDA, A., HASEGAWA, T., NAKAJIMA, T., UCHIYAMA, H. & NARUMI, T. 2012a. Drag reduction effect of nanobubble mixture flows through micro-orifices and capillaries. *Experimental Thermal and Fluid Science,* 39**,** 54-59.

USHIDA, A., HASEGAWA, T., NAKAJIMA, T., UCHIYAMA, H., NARUMI, T. J. E. T. & SCIENCE, F. 2012b. Drag reduction effect of nanobubble mixture flows through micro-orifices and capillaries. 39**,** 54-59.

USHIDA, A., HASEGAWA, T., NARUMI, T., KOURAKATA, I., NAKAMOTO, Y. J. J. O. F. C., MEASUREMENT & VISUALIZATION 2015. Flow Properties of Ultra-Fine Bubble Mixtures Passing through Micro-Apertures. 3**,** 111.

USHIDA, A., HASEGAWA, T., TAKAHASHI, N., NAKAJIMA, T., MURAO, S., NARUMI, T. & UCHIYAMA, H. 2012c. Effect of Mixed Nanobubble and Microbubble Liquids on the Washing Rate of Cloth in an Alternating Flow. *Journal of Surfactants and Detergents,* 15**,** 695-702.

USHIDA, A., KOYAMA, T., NAKAMOTO, Y., NARUMI, T., SATO, T. & HASEGAWA, T. 2017. Antimicrobial effectiveness of ultra-fine ozone-rich bubble mixtures for fresh vegetables using an alternating flow. *Journal of Food Engineering,* 206**,** 48-56.

USHIKUBO, F. Y., FURUKAWA, T., NAKAGAWA, R., ENARI, M., MAKINO, Y., KAWAGOE, Y., SHIINA, T. & OSHITA, S. 2010. Evidence of the existence and the stability of nano-bubbles in water. *Colloids and Surfaces A: Physicochemical and Engineering Aspects,* 361**,** 31-37.

UTOMO, A., BAKER, M. & PACEK, A. W. 2009. The effect of stator geometry on the flow pattern and energy dissipation rate in a rotor–stator mixer. *Chemical Engineering Research and Design,* 87**,** 533-542.

UTOMO, A. T., BAKER, M. & PACEK, A. W. 2008. Flow pattern, periodicity and energy dissipation in a batch rotor–stator mixer. *Chemical Engineering Research and Design,* 86**,** 1397-1409.

VERWEY, E. J. W., OVERBEEK, J. T. G. & VAN NES, K. 1948. *Theory of the stability of lyophobic colloids: the interaction of sol particles having an electric double layer*, Elsevier Publishing Company.

WAGNER JR, J. R. 2016. *Multilayer flexible packaging*, William Andrew.

WANG, Q., ZHAO, H., QI, N., QIN, Y., ZHANG, X. & LI, Y. 2019. Generation and Stability of Size-Adjustable Bulk Nanobubbles Based on Periodic Pressure Change. *Scientific Reports,* 9**,** 1118.

WANG, Y., LI, X., ZHOU, Y., HUANG, P. & XU, Y. 2010. Preparation of nanobubbles for ultrasound imaging and intracelluar drug delivery. *International Journal of Pharmaceutics,* 384**,** 148-153.

WEIJS, J. H., SEDDON, J. R. T. & LOHSE, D. 2012. Diffusive Shielding Stabilizes Bulk Nanobubble Clusters. *Chemphyschem,* 13**,** 2197-2204.

WU, Z., CHEN, H., DONG, Y., MAO, H., SUN, J., CHEN, S., CRAIG, V. S. J. & HU, J. 2008. Cleaning using nanobubbles: Defouling by electrochemical generation of bubbles. *Journal of Colloid and Interface Science,* 328**,** 10-14.

WU, Z., ZHANG, X., ZHANG, X., LI, G., SUN, J., ZHANG, Y., LI, M. & HU, J. 2006. Nanobubbles influence on BSA adsorption on mica surface. *Surface and Interface Analysis,* 38**,** 990-995.

WU, Z., ZHANG, X., ZHANG, X., SUN, J., DONG, Y. & HU, J. J. C. S. B. 2007. In situ AFM observation of BSA adsorption on HOPG with nanobubble. 52**,** 1913-1919.

YASUDA, K., MATSUSHIMA, H. & ASAKURA, Y. 2019. Generation and reduction of bulk nanobubbles by ultrasonic irradiation. *Chemical Engineering Science,* 195**,** 455-461.

YASUI, K. 2016. Mechanism for Stability of Ultrafine Bubbles. *JAPANESE JOURNAL OF MULTIPHASE FLOW,* 30**,** 19-26.

YASUI, K. 2018. *Acoustic cavitation and bubble dynamics*, Springer.

YASUI, K., TUZIUTI, T. & KANEMATSU, W. 2018. Mysteries of bulk nanobubbles (ultrafine bubbles); stability and radical formation. *Ultrasonics Sonochemistry,* 48**,** 259-266.

YASUI, K., TUZIUTI, T., KANEMATSU, W. & KATO, K. 2015. Advanced dynamic-equilibrium model for a nanobubble and a micropancake on a hydrophobic or hydrophilic surface. *Physical Review E,* 91**,** 033008.

YASUI, K., TUZIUTI, T., KANEMATSU, W. & KATO, K. 2016. Dynamic Equilibrium Model for a Bulk Nanobubble and a Microbubble Partly Covered with Hydrophobic Material. *Langmuir,* 32**,** 11101-11110.

YATES, D. E., LEVINE, S. & HEALY, T. W. J. J. O. T. C. S., FARADAY TRANSACTIONS 1: PHYSICAL CHEMISTRY IN CONDENSED PHASES 1974. Site-binding model of the electrical double layer at the oxide/water interface. 70**,** 1807-1818.

YOSHIDA, S., KITANO, M. & EGUCHI, H. Water uptake and growth of cucumber plants (Cucumis sativus L.) under control of dissolved O2 concentration in hydroponics. International Symposium on Plant Production in Closed Ecosystems 440, 1996. 199-204.

YOUNT, D. E. 1979. Skins of varying permeability: A stabilization mechanism for gas cavitation nuclei. *The Journal of the Acoustical Society of America,* 65**,** 1429-1439.

YOUNT, D. E., GILLARY, E. W. & HOFFMAN, D. C. 1984. A microscopic investigation of bubble formation nuclei. *The Journal of the Acoustical Society of America,* 76**,** 1511-1521.

ZHANG, H., GUO, Z. & ZHANG, X. 2020a. Surface enrichment of ions leads to the stability of bulk nanobubbles. *Soft matter,* 16**,** 547-5477.

ZHANG, J., CHEN, Y., DENG, C., ZHANG, L., SUN, Z., WANG, J., YANG, Y., LV, Q., HAN, W. & XIE, M. 2019. The Optimized Fabrication of a Novel Nanobubble for Tumor Imaging. 10.

ZHANG, J., XU, S. & LI, W. 2012. High shear mixers: A review of typical applications and studies on power draw, flow pattern, energy dissipation and transfer properties. *Chemical Engineering and Processing: Process Intensification,* 57-58**,** 25-41.

ZHANG, L., ZHANG, X., FAN, C., ZHANG, Y. & HU, J. 2009. Nanoscale Multiple Gaseous Layers on a Hydrophobic Surface. *Langmuir,* 25**,** 8860-8864.

ZHANG, X.-Y., WANG, Q.-S., WU, Z.-X., TAO, D.-P. J. I. J. O. M., METALLURGY & MATERIALS 2020b. An experimental study on size distribution and zeta potential of bulk cavitation nanobubbles. 27**,** 152-161.

ZHANG, X. H., MAEDA, N. & HU, J. 2008. Thermodynamic Stability of Interfacial Gaseous States. *The Journal of Physical Chemistry B,* 112**,** 13671-13675.

ZHANG, X. H., ZHANG, X., SUN, J., ZHANG, Z., LI, G., FANG, H., XIAO, X., ZENG, X. & HU, J. 2007. Detection of Novel Gaseous States at the Highly Oriented Pyrolytic Graphite−Water Interface. *Langmuir,* 23**,** 1778-1783.

ZHOU, M., CAVALIERI, F., CARUSO, F. & ASHOKKUMAR, M. 2012. Confinement of Acoustic Cavitation for the Synthesis of Protein-Shelled Nanobubbles for Diagnostics and Nucleic Acid Delivery. *ACS Macro Letters,* 1**,** 853-856.

ZHU, J., AN, H., ALHESHIBRI, M., LIU, L., TERPSTRA, P. M., LIU, G. & CRAIG, V. S. 2016. Cleaning with Bulk Nanobubbles. *Langmuir,* 32**,** 11203-11211.

ZIMMERMAN, W. B., TESAŘ, V. & BANDULASENA, H. C. H. 2011. Towards energy efficient nanobubble generation with fluidic oscillation. *Current Opinion in Colloid & Interface Science,* 16**,** 350-356.